

STRATEGIC FUNCTIONALIZATION OF SINGLE WALLED CARBON NANOTUBES TO
MANIPULATE THEIR ELECTRONIC AND OPTICAL PROPERTIES

A Dissertation
Submitted to the Graduate Faculty
of the
North Dakota State University
of Agriculture and Applied Science

By
Brendan Joel Gifford

In Partial Fulfillment of the Requirements
for the Degree of
DOCTOR OF PHILOSOPHY

Major Department:
Chemistry and Biochemistry

November 2017

Fargo, North Dakota

North Dakota State University
Graduate School

Title

STRATEGIC FUNCTIONALIZATION OF SINGLE WALLED CARBON
NANOTUBES TO MANIPULATE THEIR ELECTRONIC AND
OPTICAL PROPERTIES

By

Brendan Joel Gifford

The Supervisory Committee certifies that this *disquisition* complies with
North Dakota State University's regulations and meets the accepted
standards for the degree of

DOCTOR OF PHILOSOPHY

SUPERVISORY COMMITTEE:

Dr. Svetlana V. Kilina

Chair

Dr. Wenfang Sun

Dr. John Hershberger

Dr. Dean Webster

Approved:

November 15, 2017

Date

Dr. Gregory Cook

Department Chair

ABSTRACT

Single-walled carbon nanotubes (SWCNTs) are unique materials that exhibit chirality-specific properties due to their one-dimensional confinement. As a result, they are explored for a wide range of applications including single-photon sources in communications devices. Despite progress in this area, SWCNTs still suffer from a relatively narrow range of energies of emission features that fall short of the ~ 1500 nm desired for long-distance lossless data transfer. One approach that is frequently used to resolve this involves chemical functionalization with aryl groups. However, this approach is met with a number of fundamental issues. First, chirality-specific SWCNTs must be acquired for subsequent functionalization. Synthesis of such samples has thus far eluded experimental efforts. As such, post-synthetic non-covalent functionalization is required to break bundles and create disperse SWCNTs that can undergo further separation, processing, and functionalization. Second, a number of low-energy emission features are introduced upon functionalization across a 200 nm range. The origin of such diverse emission features remains unknown.

The research presented here focuses on computationally addressing these issues. A series of polyfluorene polymers possessing sidechains of varying length are explored using molecular mechanics to determine the impact of alkyl sidechains on SWCNT-conjugated polymer interaction strength and morphology. Additionally, density functional theory (DFT) and linear-response time-dependent DFT (TDDFT) are used to explore the effect of functionalization on emission features. A prerequisite to these calculations involves constructing finite-length SWCNT systems with similar electronic structure to their infinite counterparts: a methodological approach for the formation of such systems is presented. The optical features for aryl-functionalized SWCNTs are then explored. It is shown that the predominant effect on the

energies of emission features involves the configuration of functionalization, with the identity of the functional group only playing a minor role. While the qualitative effect of such functionalization is determined, a quantitative comparison to experiment requires correction for several sources of computational error. A model to correct for such effects is also developed. This research not only explains the origin of the multiple emission features in functionalized SWCNTs for the first time but also lays the groundwork for their further computational exploration.

ACKNOWLEDGEMENTS

First and foremost, I would like to thank my graduate research advisor Dr. Svetlana Kilina for everything she has done for me. Throughout my four years in her group, she has provided knowledge, motivation, and has continually encouraged me to strive for excellence. She was always willing to spend countless hours meeting and discussing my research progress, and her invaluable feedback guided me every step of the way. Without her gentle leadership, there is no way I would have ever made it this far and I am forever grateful! Thank you, Svetlana!

In addition, I would like to thank my committee members Dr. John Hershberger, Dr. Wenfang Sun, and Dr. Dean Webster for listening to my progress over the past four years. They have always provided constructive feedback during our annual committee meetings, and I am grateful for their willingness to meet with me and discuss my research. I also thank Dr. Dmitri Kilin for his willingness to hear and discuss my research. He always provided valuable feedback that improved my projects.

I thank the top-notch scientists at Los Alamos National Laboratory that I have worked with for the past two years including my mentor Dr. Sergei Tretiak and experimental collaborators Dr. Stephen Doorn and Dr. Han Htoon. Working with these people has been the experience of a lifetime, and I hope our collaborations continue long into the future.

I thank the faculty at the University of Wisconsin Stevens Point for providing the knowledge and guidance leading me to graduate school. I am especially grateful to Dr. Robin Tanke for allowing me to perform research in her group as an inexperienced Freshman: those early experiences were the seed of my love for research. I thank Dr. John Droske for inviting me to join his group, spending countless hours meeting with me one-on-one to provide guidance,

and seeding the idea of pursuing a doctorate. I also thank Dr. Paul Hladky and Dr. James Brummer for their excellent instruction in Physical Chemistry and encouraging me to pursue a career in it.

My time spent at Cameron Middle School and High School were perhaps the most influential in developing me into the individual I am today, and my experience would not have been complete without the contribution of a significant number of people. I thank Mrs. Valorie Pumala and Mr. Daric Klabunde for their effective instruction in middle school Math and Science. They planned joint self-guided STEM projects in which students discovered the science behind pulleys and levers: these were ultimately the most effective educational activities I have ever participated in. I also thank Mrs. Carla Kuffel and Mr. David Gerber for their science and math education throughout my high school years. I thank Mrs. Kathy Krizan for her memorable English and Composition instruction. The mnemonics she taught us for proper comma usage saved me thousands of dollars in testing out of college English classes as an undergraduate, and I still to this day use BOYFANS to recall the coordinating conjunctions. In addition, I thank Mrs. Kimberly Sanborn for all the guidance with the college application process. Without her assistance, I wouldn't have even known where to start when applying and would have likely procrastinated and never pursued higher education. I thank Mrs. Peggy Hansen for allowing me to sit in the library for study hall and for all the discussion: the library was my favorite place to work when I had things to do. When I didn't, conversing with her was infinitely more enjoyable than staring at the clock waiting for the bell to ring!

This dissertation is dedicated to Mr. Ronald Fanetti, my High School Chemistry teacher and the most influential person in my early career. On the first day of class, Mr. Fanetti wrote “molecular mass, molecular weight, molar mass, formula weight, grams/mole, AMU” on the

board and said, “All these words mean the same damn thing.” He then proceeded to explain the concept of the mole by drawing circles on the board and indicating he couldn’t draw Avogadro’s number circles, but if he could it would be a very large constant number. Keeping things simple was his strong suit. He spent his own lunch time allowing me to complete experiments to determine the empirical formula of hydrates, and he told me I had done a good job when I determined the molar mass of a salt to within a 1000% error. Because of his unique teaching style and simplifications, I understood the concepts of chemistry and was able to tutor my peers. This convinced me to pursue a degree in Chemistry and led me to the point I am today. My father was in Mr. Fanetti’s first class in 1968, and I was in his last class before he retired in 2005, a testament to his dedication to teaching. His students over all these years owe him a great debt of gratitude.

I thank Mrs. Patricia Schroeder, Mrs. Lisa Beth Hafstad, Mrs. Donna Linsmeyer, Mrs. Rebecca Ness, Mr. Michael Correll, and Mr. Wayne Czynson for each teaching me for a year throughout my childhood at Cameron Elementary School and effectively providing me with the fundamentals that would guide my success. I especially thank Mrs. Susan King, my third grade teacher, for providing intriguing scientific experiments that sparked my curiosity very early on. Science became my favorite subject after Mrs. King’s class, a theme that would continue into my adult life.

I thank Colleen Bender, Phyllis Cook, and Marla Hall for all the early memories in Youth Group and Sunday School. Their caring support early in my life would shape me into the person I am today. I thank David Burke for all the guidance in Boy Scouts and all the valuable lessons. In addition, I thank the entire Village of Cameron. The phrase “it takes a village” is entirely accurate, and I am glad to have called Cameron my home!

Last but not least, I thank my family including parents, Martha and Bimbo Gifford, sisters Danielle Hankins and Brianna Gifford, and in-laws Nathan Hankins and Tyler Gagner for their support over all these years. I thank my nieces Leonna Gifford-Gagner and Louise Hankins for being so adorable and constantly reminding me of the things in life that matter. I can't wait to meet you, Louise! I also thank my Aunt Gail Gifford for being a dedicated kayaking partner and all the conversation over these years. Finally, I thank my many extended family members for all the support and encouraging words. I couldn't have done this without you, and I love you all!

DEDICATION



In memory of Mr. Ronald Fanetti, dedicated instructor of Chemistry at
Cameron High School from 1968 to 2005.

His influence motivated me to pursue a higher degree in the subject we both
loved so much, and he will always be remembered!

TABLE OF CONTENTS

ABSTRACT	iii
ACKNOWLEDGEMENTS	v
DEDICATION	ix
LIST OF TABLES	xix
LIST OF FIGURES	xxi
LIST OF ABBREVIATIONS.....	xxxv
LIST OF SYMBOLS	xxxviii
1. INTRODUCTION.....	1
1.1. Single Walled Carbon Nanotube Structure & Properties	2
1.1.1. Forming a Tubule from a Graphene Sheet	2
1.1.2. SWCNT Chirality	2
1.1.3. Diameter Dependent Electronic & Optical Properties: Particle in a 1-D Box	4
1.1.4. Chiral Angle	5
1.1.5. Electronic Structure based on Chiral Indices	5
1.1.6. Optical Properties of SWCNTs	6
1.2. Practical Application & Limitations of SWCNTs	7
1.2.1. Challenges Generating Chirality Pure SWCNT Samples	7
1.3. Tuning SWCNT Properties by Covalent Functionalization	9
1.3.1. Chlorine Functionalization	10
1.3.2. Functionalization with Aryl Groups	11
1.4. The State of Computational Methodology for SWCNTs	12
1.4.1. Classical Methods: Molecular Mechanics.....	13
1.4.2. Electronic Structure Calculations	14

1.4.2.1. Basic Introduction to Quantum Chemical Calculations.....	14
1.4.2.2. Hartree-Fock & Semiempirics	14
1.4.2.3. Density Functional Theory	15
1.4.2.4. Time-Dependent Density Functional Theory	18
1.4.3. Approximation in the Models: Finite Computational Cells	19
1.4.4. Analytical Model for Correcting for Computational Error	20
1.5. References.....	21
2. SINGLE WALLED CARBON NANOTUBE – POLYMER SIDECHAIN INTERACTIONS AND MORPHOLOGY.....	40
2.1. Motivation.....	40
2.2. Computational Methodology	41
2.2.1. Reparametrizing the Force Field	41
2.2.2. Optimization of the SWCNT-PFO Composites w/ Different Length Sidechains	43
2.2.3. Analysis of the Binding Strengths of Polymer to SWCNT.....	43
2.2.4. Analysis of the Morphologies of the Systems.....	44
2.3. Evaluation of the Role of Sidechains in PFO-SWCNT Binding	45
2.3.1. Short Alkyl Sidechains	47
2.3.1.1. $n=0 \rightarrow n=1$ Increased Vander Waals Interactions without a Cost.....	47
2.3.1.2. $n=1 \rightarrow n=3$ Vander Waals Interactions Induce Twisting & Instability	49
2.3.2. Intermediate Length Sidechains	52
2.3.2.1. $n=3 \rightarrow n=8$ Little Impact on Morphology for Longer Sidechains.....	52
2.3.2.2. Increased number of Vander Waals Interactions Increases Adsorption	52
2.3.3. Long Sidechains	53
2.3.3.1. $n=8 \rightarrow n=12$: Decreased Stability Due to Increased Wrapping Angle	53
2.3.3.2. Binding Energy Dependence on Wrapping Angle.....	54

2.4.	Conclusions.....	55
2.5.	References.....	57
3.	CAPPING OF FINITE SWCNT SYSTEMS FOR ELECTRONIC STRUCTURE CALCULATIONS.....	59
3.1.	Motivation.....	59
3.2.	The Menagerie of Capping Schemes	60
3.2.1.	Bonds at the SWCNT Terminus.....	61
3.2.1.1.	Three Distinct types of Bonds in SWCNTs.....	61
3.2.1.2.	Possible Capping Positions	61
3.2.1.3.	Distance Between Capping Groups	62
3.2.2.	Atoms at the SWCNT Terminus	62
3.2.2.1.	Different Capping Functionalities.....	62
3.2.2.2.	Prevalence of sp^2 Hybridized Capping Groups	64
3.2.2.3.	Differentiation Between Carbon Atoms Vicinal to Capping.....	64
3.3.	Computational Methodology	64
3.3.1.	Generation of the Systems.....	64
3.3.2.	Optimization of the Geometries of the Systems.....	65
3.3.3.	Calculation of the Electronic Structure	65
3.3.3.1.	Justification of Chosen Basis Sets	65
3.3.3.2.	Justification of Chosen Density Functionals.....	66
3.3.4.	Calculation of Excited State Properties	66
3.4.	The Role of Functionalization Position	67
3.4.1.	Electronic Structure	67
3.4.2.	Molecular Orbitals.....	69
3.4.3.	Bond Lengths at the SWCNT Edges Adjacent to Methylene Functionalization	71

3.4.4. Charges on Carbon Atoms Adjacent to Methylene Functionalization	71
3.4.5. Summary the Role of Functionalization Position.....	72
3.5. The Role of Prevalence of sp^2 -hybridized Functionality	72
3.5.1. Electronic Structure & Electron Density.....	72
3.5.2. Bond Lengths & Charges on Carbon Atoms Adjacent to the Edge	75
3.5.3. Summary of the Role of Prevalence of sp^2 -hybridized Functionality.....	76
3.6. The Role of the Electron Donating/Withdrawing Groups at the SWCNT Cap.....	77
3.6.1. Class-Dependent Electronic Structure & Electron Localization in Frontier MOs	77
3.6.2. Interclass Trends of Electronic Structure	80
3.6.3. Bond Lengths & Local Charges: Justification of the Electronic Structure	83
3.6.4. Electronic Structure: Expanding beyond the Frontier MOs	85
3.6.5. Summary of the Role of Electron Donating/Withdrawing Groups	86
3.7. Optical Properties.....	87
3.7.1. Dependence on Methodology.....	87
3.7.2. Class Dependence of Optical Properties	87
3.7.3. Length Dependence on Optical Properties	89
3.7.4. Summary of Optical Properties	91
3.8. Conclusions.....	92
3.9. References.....	94
4. DOPING CHARACTER OF SINGLE-WALLED CARBON NANOTUBES FUNCTIONALIZED WITH CHLORINE	98
4.1. Motivation.....	98
4.2. Computational Methodology	99
4.2.1. Generation of the Computational Cells	99
4.2.2. Consideration of Multiple Binding Configurations.....	101

4.2.3. Methodologies Used.....	101
4.2.4. Characterization of the Systems	102
4.2.4.1. Binding Energies.....	102
4.2.4.2. Geometries	102
4.2.4.3. Electronic Structures & Optical Features	103
4.3. Evaluation of the Methodologies	103
4.3.1. Benchmarking of Basis Set and Functional.....	103
4.4. Correlation between Binding Energies and Geometries	106
4.4.1. Neutral Systems: Favorable Binding Interactions on a Single Hexogonal Ring.....	106
4.4.2. Charged Systems: Preferential Binding on Separate Rings	108
4.5. Analysis of Electronic Structure & Electron Density	111
4.5.1. Neutral SWCNTs.....	111
4.5.1.1. Molecular Orbitals and Density of States	111
4.5.1.2. Projected Density of States	116
4.5.2. Charged SWCNTs: The Emergence of n-Doped Behavior.....	117
4.6. Absorption Spectra.....	120
4.6.1. Neutral Species: Reduced Gaps → Lower Energy Emission.....	120
4.6.2. Charged Species	122
4.7. Effects of Increasing Cl Concentration.....	122
4.7.1. Effects of Chlorine Concentration on Binding Energy	124
4.7.2. Density of States: Higher Chlorine Concentrations Closes the Gap	124
4.7.3. Optical Features of Increasing Chlorine Concentration	124
4.8. Conclusions.....	125
4.9. References.....	126

5. DEDUCING THE ORIGIN OF RED-SHIFTED OPTICAL FEATURES IN CARBON NANOTUBES FUNCTIONALIZED WITH ARYL GROUPS	131
5.1. Motivation.....	131
5.2. A Menagerie of Functionalization Configurations	132
5.2.1. Synthetic Considerations	132
5.2.1.1. Dissociation of Diazonium Salt to Diatomic Nitrogen & an Electrophilic Aryl Species	132
5.2.1.2. Generation of a Reactive Carbocation Intermediate on the SWCNT	132
5.2.1.3. Formation of Product from Addition of Nucleophilic Species	133
5.2.1.4. Functionalization at the Same Hexagonal Ring.....	134
5.2.1.5. Bridging Synthetic and Computational Considerations.....	135
5.2.2. Non-equivalent Bonds in Chiral SWCNTs	135
5.2.3. Interchange of Two Functional Groups.....	135
5.2.4. Functionalization with Different Groups.....	136
5.3. Computational Methodology	137
5.3.1. Generation & Optimizing of Functionalized SWCNT Geometries in Vacuum	137
5.3.2. Solvent Dependent Geometries: a Marginal Role	138
5.3.3. Molecular Orbitals.....	139
5.3.4. Determination of Optical Properties with TDDFT.....	139
5.3.5. Quantification of Vibrational Reorganization	140
5.3.6. Calculation of Radiative Lifetimes.....	141
5.3.7. Determination of the Bond Character of Functionalization	141
5.4. Relative Stabilities and Geometries of Binding Configurations.....	142
5.4.1. Indistinguishable Stabilities for Left vs. Right SWCNTs	142
5.4.2. Ortho vs. Para: Relative Similarities in Binding Energies	142

5.4.3. Basis Set Dependence: Slight Stabilization with Larger Basis w/o Change in Trends	143
5.4.4. Geometrical Characteristics as a result of Functionalization	144
5.4.4.1. Computed Geometrical Deviation from Pristine	144
5.4.4.2. Experimental Expectations	146
5.4.5. Solvent Independence for Geometries & Relative Stabilities	147
5.5. Electronic Structure Heavily Dependent on Functionalization Configuration	149
5.5.1. Configuration Effects on Electron Localization	149
5.5.2. Origin of Configuration Dependence: Splitting of Degenerate Molecular Orbitals	150
5.5.3. Functional Group Independence on Electronic Structure	151
5.5.4. Basis Set Dependence: Similar Trends.....	153
5.6. Optical Properties Arising from Functionalization.....	156
5.6.1. The Introduction of Defect-Localized Low Energy Features.....	156
5.6.1.1. Delocalized Higher Energy States with Familiar Nodal Structure	157
5.7. Optical Properties for Different Rotational Conformation and Solvents.....	162
5.7.1. Most Stable Dihedral Conformations	162
5.7.2. A Significant Rotational Barrier.....	164
5.7.3. Rotational Conformation has Little Influence on Optical Characteristics	164
5.7.4. Insignificant Bathochromic Shifts due to Small Static Dipoles	165
5.8. Emission Features: Trending with Absorption	167
5.8.1. Emission Energies	167
5.8.2. Stokes Shifts due to Vibrational Reorganization.....	167
5.8.3. Exciton Localization in the Excited State	168
5.9. Reorganization Energies & Radiative Lifetimes	170
5.9.1. Configuration Dependent Reorganization Energies.....	170

5.9.2. Radiative Lifetimes: More Closely Correlated with Red Shifts.....	172
5.10. Role of the Chemical Species of Functionalization.....	174
5.10.1. Functional Stabilities.....	174
5.10.2. Electronic Structure due to Different Functionalization.....	174
5.10.3. Optical Properties from Different Functionalization.....	179
5.10.4. Natural Charge and Bond Character Due to Different Functionalization.....	179
5.11. Conclusions.....	182
5.12. References.....	186
6. CHIRALITY DEPENDENCE ON FUNCTIONALIZED CARBON NANOTUBE & ANALYTICAL SHIFT.....	190
6.1. Motivation.....	190
6.2. Computational Methodology.....	191
6.2.1. Details on the Computational Systems.....	191
6.2.2. Density Functional Choice: Comparison of Localization.....	192
6.2.3. Computing Length Dependence.....	193
6.2.4. Scheme for Shifting Energies of Computed Emission Features.....	193
6.2.5. Determining the Impact of Confinement vs. Methodology Errors.....	194
6.3. Influence of Chirality.....	195
6.3.1. Relative Stabilities: Trends within Near-Armchair vs Near-Zigzag Chiralities.....	195
6.3.2. Optical Features: Dependence on Functionalization Configuration.....	197
6.3.2.1. Optical Features for E_{11} : Diameter Dependence from Across Axis Localization.....	197
6.3.2.2. E_{11}^* Optical Features: Configuration Dependence due to Localization Along the Axis.....	197
6.3.3. Conclusions of Influence of Chiralities.....	199
6.4. Analytical Shift of Functionalized SWCNT Energies.....	200

6.4.1. Length Dependence of Computational Cells.....	200
6.4.2. Density Functional Dependence of Length Dependence	205
6.4.3. Linear Regression vs Kuhn	207
6.4.4. Methodology vs. Confinement Errors	208
6.4.5. Accuracy of 3-unit Cells vs. Extrapolated Energies.....	211
6.4.6. Shifted Emission Energies: Comparison with Experimental Values	213
6.5. Conclusions.....	217
6.6. References.....	218
7. CLOSING REMARKS	221

LIST OF TABLES

<u>Table</u>	<u>Page</u>
4.1. Molecular orbitals for the HOMO and LUMO of the chlorinated neutral finite SWCNTs optimized with PBE1 functional and 6-31G* basis set plotted with an isovalue of 0.02. No is the significant localization of the electron density around the chlorine atoms in the LUMO of the neutral species, showing that this state is primarily chlorine and defect character.	114
4.2. Molecular orbitals for the HOMO and LUMO of charged chlorinated finite tubes optimized with PBE1 functional and 6-31g* basis set, plotted with an isovalue of 0.02. The HOMO is localized around the Cl atoms and the sp ³ defect, while the LUMO is localized on the edges of the tube. The HOMO of the charged chlorinated tubes is very similar to the LUMO of the neutral chlorinated tubes, showing that this state introduced by chlorination becomes occupied by the addition of a charge.	119
5.2. Carbon-Carbon bond lengths (in Å) adjacent to aryl functionalization structure for Ar↑ aryl-H and di-aryl isomers calculated using the CAM-B3LYP functional and either the STO-3G basis set in vacuum. The highlighted lengths indicate those bonds that underwent the maximum elongation after functionalization.	146
5.3. Natural transition orbitals (NTOs) representing the photoexcited electron-hole pair contributing to the lowest energy transition S ₁ in the E ₁₁ * absorption band of aryl-H (Ar↑) structures and compared to the brightest transition in the E ₁₁ absorption band of pristine (6,5) SWCNT in vacuum. The left column presents information on the transition number and its oscillator strength. Only the NTO pairs that dominantly contribute to the optical transition are shown, with the percent of their contribution depicted at the bottom of each NTO image. In these cases, a few electron-hole pairs have to be taken as a linear combination to correctly describe the optical transition.....	158
5.4. Natural transition orbitals (NTOs) representing the photoexcited electron-hole pair contributing to the bright transitions in the first peak in the split E ₁₁ absorption band of aryl-H (Ar↑) structure. The left column presents information on the transition number, its oscillator strength, and the percent of the NTO pair contributing to the transition. Calculations are performed using CAM-B3LYP and STO-3G basis set.	160
5.5. Natural transition orbitals (NTOs) representing the photoexcited electron-hole pair contributing to the brightest transitions in the second peak in the split E ₁₁ absorption band of aryl-H (Ar↑) structures. The left column presents information on the transition number and its oscillator strength and the percent of the NTO pair mostly contributing to the transition.....	161

5.6. Natural transition orbitals (NTOs) representing the photoexcited electron-hole pair contributing to the lowest energy emission state of aryl-H (Ar↑) structures and compared to the emission state of pristine (6,5) SWCNT in vacuum. The left column represents information on the state number and its oscillator strength. Only the NTO pairs that dominantly contribute to the transition (>60 %) are shown. 169

LIST OF FIGURES

<u>Figure</u>	<u>Page</u>
1.1. Schematic representing the orientation of rolling a graphene sheet to form a SWCNT. The “chiral vector” is labeled by C_h	3
1.2. “Particle in a Box” model, where the wave function is considered to be confined in a one dimensional well with edges of an infinitely high potential. The energy of each level is described by the equation on the right, where h is Plank’s constant, m is the mass of the particle, L is the length of the box, and n is an integer corresponding to the quantum state.	4
1.3. Density of States (DOS) in the 1-D confined SWCNT systems.	5
2.1. (a) A single unit of monomer for poly(9,9-di-n-octylfluorenyl-2,7-diyl) (PFO) where n represents the number of methylene groups in the alkyl side chain and m represents the degree of polymerization, (b) the parameter used to quantify “twisting” of the polymer backbone in the SWCNT-PFO systems. A value of zero indicates that the normal vector to the polymer unit intersects with the axis of the SWCNT, thereby maximizing π - π overlap. A value of one indicates that the polymer unit is perpendicular to the surface of the SWCNT, and therefore the minimum distance between the vector normal to the unit and the SWCNT axis is equal to the radius of the SWCNT + the distance between the SWCNT and the center of mass of the polymer unit, and (c) the pentamer ($m=5$) optimized with DFT using the B3LYP functional and the 6-31G* basis set from which the force field was reparametrized. The torsion angle at the central unit of this oligomer is 37.5°	42
2.2. Adsorption energies per unit length of PFO to the SWCNT as a function of (a) number of methylene groups in the alkyl chain, and (b) diameter of the SWCNT. For panel a, larger circles indicate larger diameter SWCNTs, filled circles indicate a chiral angle $\theta > 20^\circ$, and empty circles indicate a chiral angle $\theta < 20^\circ$. For panel b, the size of the data point correlates to the length of the alkyl sidechain on PFO.	46
2.3. Characterization of the geometry of the PFO polymer optimized in the presence of the SWCNT, including (a) the average wrapping angle of the PFO units and (b) the average torsion angle between polymer units. Larger circles indicate larger diameter SWCNTs, filled circles indicate a chiral angle $\theta > 20^\circ$, and empty circles indicate a chiral angle $\theta < 20^\circ$	48
2.4. Top: (8,6) SWCNT with PFO where side chains are replaced with methyl groups. Due to the lack of steric hindrance between side groups and the SWCNT, polymer backbone interacts with the SWCNT via π - π stacking. Bottom: SWCNT with PFO where side chains are replaced with propyl groups. The introduction of the relatively bulkier side groups results in twisting in the backbone and reduced π - π stacking.	49

2.5. Characterization of the interaction of the PFO side chains with the SWCNT, including (a) average distance between the SWCNT surface and the atoms of the PFO alkyl group, and (b) the fraction of carbon atoms in the alkyl group that are within range to interact with the SWCNT surface via van der Waals interactions. Larger circles indicate larger diameter SWCNTs, filled circles indicate a chiral angle $\theta > 20^\circ$, and empty circles indicate a chiral angle $\theta < 20^\circ$	50
2.6. Characterization of the interaction of the PFO backbone with the SWCNT, including (a) average distance between the SWCNT surface and the PFO backbone, (b) average closest approach distance between a vector normal to each polymer unit and the axis of the SWCNT, and (c) the number of PFO units that are both planar to the surface and have all backbone C atoms within pi-pi stacking range. Larger circles indicate larger diameter SWCNTs, filled circles indicate a chiral angle $\theta > 20^\circ$, and empty circles indicate a chiral angle $\theta < 20^\circ$	51
2.7. Binding energy vs final wrapping angle for all optimized geometries of (9,1) SWCNT with n=7 PFO. All geometries with stronger binding exhibit a steeper final wrapping angle.....	54
2.8. The slope of binding energy vs final wrapping angle for all geometries with different number of side groups. For very short side groups, little dependence of wrapping angle on binding energy is observed. For longer side chains, from n=10 to n=12, a strong dependence of wrapping angle on binding energy is observed.	55
3.1. Structural parameters for the edge-functionalized (10,5) SWCNT and different capping schemes possible for this nanotube. Positions labeled by R ₁ and R ₂ are those that are used for calculations of 14 different functional schemes shown in 2. Bonds highlighted in the same color represent the same symmetry position at the tube's edge referred to as A ₁ (blue), A ₂ (green), and B (red).	60
3.2. Functional groups attached to the edge of the (10,5) SWNT. Class I compounds are those where both functional groups, R ₁ and R ₂ , have connectivity to the SWCNT via double bonds (sp ² -connectivity), Class II compounds have one connectivity via a double bond and the other via a single bond (mixed sp ² -and sp ³ -connectivity), and Class III compounds have connectivity exclusively through single bonds (sp ³ -connectivity).	63

3.3. Comparison of the electronic and geometrical parameters of the (10,5) SWCNT capped only by hydrogens (compound 14), as a reference point, and by hydrogens and one CH ₂ group (compound 7) with the CH ₂ group attached at various positions (A ₁ , A ₂ , and B) along the nanotube edge, according to 1. Position of the group at the other tube's edge is identified either by O or S, when the CH ₂ groups are either at the opposite or the same sides with respect to the nanotube axis. The geometries are optimized by AM1 for all structures. (a) The energy gaps computed by AM1 and DFT using the CAM-B3LYP functional. (b) The bond lengths between the carbon atom of the SWCNT to that the CH ₂ group is attached (C) and the adjacent carbon atom (C ₁ or C ₂). (c) The NBO charge on C, C ₁ , and C ₂ atoms of SWCNT calculated by the CAM-B3LYP. (d) Highest Occupied Molecular Orbital (HOMO) for each capping case calculated by the CAM-B3LYP. The dashed green line indicates the average bond length and charge for the central portion of the SWCNT where perturbation by capping groups is absent. There is insignificant difference between energies and orbital delocalization for either the same or opposite A-positions, while B-position results in localization of HOMO at the edges and noticeable decreasing in the energy gap.....	68
3.4. Molecular orbital diagrams and ground state molecular orbitals for two units of (10,5) SWCNT functionalized by a single sp ² -hybridized CH ₂ group (compound 7) on different positions of the tube edge using AM1 methodology. The number listed in the HOMO-LUMO gap of the MO diagram (the top panel) is the energy of the gap in eV.....	70
3.5. The electronic structure of (10,5) SWNT capped by different numbers of CH ₂ groups along A-direction and calculated by DFT within the CAM-B3LYP functional. The number listed in the HOMO-LUMO gap of the energy diagram is the energy gap in eV. For the compound 14 with no CH ₂ groups at the edge (0), the HOMO and HOMO-1, as well as the LUMO and LUMO+1, are two-fold degenerate. Addition of the CH ₂ groups breaks this degeneracy.	73
3.6. Molecular orbital diagrams and ground state molecular orbitals for two units of (10,5) SWCNT functionalized by different numbers of sp ² -hybridized CH ₂ groups on the caps using AM1 methodology. The number listed in the HOMO-LUMO gap of the MO diagram is the energy gap in eV.....	74
3.7. The electronic and geometrical characteristics of (10,5) SWCNT capped by different numbers of CH ₂ groups. Top panel: The HOMO-LUMO gaps computed by AM1 and DFT within the CAM-B3LYP functional. Middle panel: The averaged bond lengths between the carbon atom of the SWCNT to that the CH ₂ group is attached (C) and the adjacent carbon atom (C ₁ or C ₂). Bottom panel: The averaged charge on C, C ₁ , and C ₂ atoms of SWCNT using NBO calculated by the CAM-B3LYP functional.....	76

3.8. The electronic structure and geometrical parameters for the edge-functionalized (10,5) SWCNT optimized by AM1 method. (a) The HOMO-LUMO gap and (d) electronic levels calculated by semiempirical AM1 and DFT using CAM-B3LYP and BLYP functionals and 3-21G basis set. (b) Bond lengths for the AM1 optimized ground state geometry. (c) The charge on C, C ₁ , and C ₂ carbons at the nanotube's edge using NBO analysis calculated by the CAM-B3LYP functional and 3-21G basis set. The dashed green line indicates the average C-C bond length and charge for the central portion of the SWCNT where perturbation by capping groups is absent.	78
3.9. Plots of LUMO and HOMO for the (10,5) SWCNTs with functional groups 2 (Class I, sp ² -capping) and 11 (Class III, sp ³ -capping) calculated by different methods (AM1 and CAM-B3LYP), while geometries are obtained by AM1.	79
3.10. Molecular orbitals for compounds 7 (Class II) and 14 (class III) using AM1 and CAM-B3LYP methods. For class II compounds, more electron density is located near the SWCNT edges for CAM-B3LYP than for AM1, resulting in a reduced gap. This effect is not as significant for Class III compounds.	81
3.11. The electronic structure of (10,5) SWCNTs capped with fourteen different capping groups and calculated with different methods. All different methods represent single point energy calculations after the geometry is obtained using AM1.	82
3.12. Schematic representation of hybrid resonance structures for the different types of capping groups used as a model for the (10,5) SWCNT with various side-groups attached at the tube's edges.	83
3.13. Absorption spectra (in arbitrary units) of the edge-functionalized (10,5) SWCNT of several lengths. Absorption spectra of the compound 6 of class II (a), 11 of class III (b), and 1 (c) and 2 (d) of class I computed with the TDDFT/B3LYP (dotted blue lines) and TDDFT/CAM-B3LYP (solid blue lines). TDDFT/B3LYP spectra are blue shifted to align the most intensive peak (S _B) for both methods. Vertical red lines denote each optical transition calculated by CAM-B3LYP functional with the oscillator strength shown at the right Y-axis (red), with the black arrows depicting the lowest-energy transition (S ₁). In four top panels (a)-(d), the nanotube is of 2 lattice units in length. In bottom panels, the nanotube is of 9 units (e) and 7 units (f) in length. S _B defines the brightest transition associated with the E ₁₁ main band.	88
3.14. Natural transition orbitals (NTOs) contributing to the lowest energy (S ₁) and the most bright (S _B) optical transitions for the capped SWCNTs (10,5) calculated using the CAM-B3LYP functional and 3-21G basis set for capping structures 2, 6, and 11. Geometries are optimized by AM1 semiempirical approach.	90
3.15. Molecular orbitals for compound 2 constructed with 7 unit cells of SWCNT. A transition from HOMO to LUMO is $\pi \rightarrow \pi^*$ in nature, with LUMO density having more localization at the central portion of the SWCNT with negligible involvement of capping groups.	91

4.1. Overview of tube properties and defect arrangements. The upper left shows the characteristics of the pristine SWCNTs used. The bottom shows the different arrangements of Cl pairs with respect to each other. Ortho and para arrangements have two Cl atoms bound to the same ring, and 1,4, 1,6, and 1,8 arrangements have two Cl atoms bound to different rings. The upper right shows the different directions of the defects on the tube: along the tube's chiral axis, around the circumference of the tube, or diagonally wrapped around the tube.....	100
4.2. Comparison of binding energies for different methodologies. The data for the comparison between different functional (a,c) was computed with a consistent basis set of 6-31G*. The data for comparison between different basis sets (b,d) was computed with PBE1 consistently. Solid points indicate that the data was for finite tubes, whereas hollow points indicate are used for the data from calculations with PBC. Panels (a) and (b) are for neutral systems, and panels (c) and (d) are present data from systems with a negative charge.	104
4.3. Bond character of chlorinated tubes at the chlorination site with respect to methodology. The upper part of each panel shows the average C-Cl bond length, and the lower part shows the C-C bond length alternation. Bond length alternation is the average difference between the C-C bonds adjacent to the chlorine defect, which are expected to be elongated, and C-C bonds two bonds away from the chlorine defect, which are expected to be shortened. Panels a and b describe neutral tubes, while panels c and d describe charged tubes. Panels a and c show how the bond character changes with different functionals, all optimized with a 6-31G* basis set. Panels b and d show the bond character changes with different basis sets, all optimized with the PBE1 functional.	105
4.4. Binding energy of different configurations with varying distance between the two chlorine atoms for (a) neutral chlorinated SWCNTs and (b) charged chlorinated SWCNTs. Binding energy determined for finite tubes functionalized with the PBE1 functional and 6-31G* basis set. Hollow data points are for functionalized SWCNTs of length 5 units, and filled data points are for functionalized SWCNTs of length 2 units. For neutral cases, the most favorable binding occurs when two Cl atoms are bound on the same ring. For charged cases, monochlorination is most favorable, with dichlorination only becoming favorable as the distance between Cl atoms increases.	107

4.5. Bond length data for all 2-unit chlorinated finite tube arrangements optimized with PBE1 functional and 6-31G* basis set. Panels a and b describe the bond character of neutral chlorinated tubes, while panels c and d describe the bond character of charged tubes. Panels a and c show the C-Cl bond length with respect to the Cl arrangement, and panels b and d show the C-C bond length alternation with respect to the Cl arrangement. Bond length alternation is the average difference between the C-C bonds adjacent to the chlorine defect, which are expected to be elongated, and C-C bonds two bonds away from the chlorine defect, which are expected to be shortened. The top panel shows the data for neutral cases and the bottom panel shows charged cases. For neutral cases, the bond lengths for arrangements where Cl are bonded to different rings are similar to the monochlorinated case, while cases where Cl are bonded to the same ring show much smaller C-Cl bonds and generally much greater bond length alternation. For charged cases, a similar trend appears, where dichlorinated cases become more like monochlorinated case as the Cl separation increases. The main outlier is the diagonal para arrangement, which shows much weaker bonding than other arrangements with 2 Cl atoms bonded to the same ring..... 110

4.6. Density of states of selected chlorinated tubes generated by broadening about the states using a Gaussian function of linewidth of 0.06 eV. The zero energy for charged and pristine tubes is the center of the HOMO-LUMO gap. For neutral tubes, the DOS was aligned with higher energy states in the conduction band of the pristine tube. The top row shows tubes functionalized with neutral Cl, and the bottom row shows tubes functionalized with charged Cl. The tubes functionalized with a pair of neutral Cl atoms show the introduction of an unoccupied state in the band gap. This state gets closer to the Fermi energy the greater the separation of Cl atoms. Charged cases show a much greater change in band structure, but distinctly show occupied states near the conduction band, particularly in the longer tubes. 112

4.7. (a) Density of States (DOS) for neutral dechlorinated SWCNTs with PBC calculated using PBE functional and PAWS basis set. The top panel is for ortho substitution, and the bottom panel is for para substitution. For ortho substitution, the HOMO-LUMO gap decreases from functionalization with chlorine atoms along the chiral axis. (b) For para substitution, circumferential and diagonal functionalization results in a decreased gap. (c) Density of States (DOS) for neutral finite tubes calculated using PBE1 functional and 6-31G* basis set. The top panel is for ortho substitution, and the bottom panel is for para substitution. For ortho substitution, the HOMO-LUMO gap decreases from functionalization with chlorine atoms along the chiral axis. (d) For para substitution, circumferential and diagonal functionalization results in a decreased gap. 113

4.8. Molecular orbital diagram for chlorine doped SWCNTs calculated using PBE1 functional and 6-31G* basis set. The number in each diagram indicates the band gap for each arrangement. P doping is clearly observed for neutral chiral ortho and circumferential and diagonal para configurations. N doping is clearly observed in all charged cases. This is consistent in both the long capped systems (5 SWCNT units) as well as the short capped systems (2 SWCNT units).	115
4.9. Projected density of States (pDOS) for neutral finite tubes calculated using PBE1 functional and 6-31G* basis set. The Cl DOS was multiplied by 10 to better illustrate the contribution of Cl, due to the much larger number of carbon atoms. The left panels are for ortho substitution, and the right panels are for para substitution. For all configurations, the states with the strongest chlorine influence are located deep in the valence band, although there is significant contribution to the LUMO from Cl.	116
4.10. Projected density of States (pDOS) for charged finite tubes calculated using PBE1 functional and 6-31g* basis set. The Cl DOS was multiplied by 10 to better illustrate the contribution of Cl, due to the much larger number of carbon atoms. The pDOS shows a substantial Cl contribution in states well below the band gap. However, there is also significant Cl contribution in the HOMO, especially in the circumferential para configuration.	117
4.11. (a) Calculated absorption spectra of selected neutral chlorinated SWCNTs. Peaks were broadened about the transition using a Gaussian function with line width 0.04 eV., and (b) Calculated absorption spectra of selected charged chlorinated tubes. Peaks were broadened about the transition using a Gaussian function with line width 0.04 eV.	121
4.12. (a) Binding energy of chlorine on a CNT with respect to chlorine concentration. Binding energy was determined for tubes optimized with PBE1 functional and 6-31G* basis set. Concentration was increased by binding multiple Cl pairs in circumferential para configuration in different locations on the tube. (b) Density of states for chlorinated 2-unit finite tubes optimized with PBE1 functional and 6-31G* basis set with varying surface concentrations of chlorine. DOS was generated by broadening around the states with a Gaussian function with a linewidth of 0.06 eV. DOS for the chlorinated tubes were shifted to align with the first two unoccupied peaks in the pristine tube. (c) Absorption spectra for chlorinated 2-unit finite tubes optimized with PBE1 functional and 6-31G* basis set with varying surface concentrations of chlorine.....	123
4.13. Density of states for neutral 2-unit finite tubes calculated with PBE1 functional and 6-31G* basis set with varying Cl surface concentrations. Higher Cl concentrations shows an increase in midgap states.	125
5.1. Reaction mechanism between a SWCNT and electrophilic species generating reactive carbocations.	133

5.2. Possible orientations of functional groups with respect to the (6,5) SWCNT axis. (a) Ortho denotes functionalization on adjacent carbon atoms, while para refers to functionalization in the (1,4) positions on the same hexagonal ring. L_{30} , L_{90} , and L_{-30} refers to bonds that lie along a vector 27° , 87° , and -33° from the SWCNT axis, respectively. $Ar\uparrow$ and $Ar\downarrow$ refer to the order of functionalization along a chosen vector. Sample representations of a SWCNT functionalized with an aryl bromide group and a hydrogen along the ortho L_{30} bond in the $Ar\uparrow$ configuration (b) and two aryl bromide groups in the para L_{30} configuration (c).....	134
5.3. Functional groups considered in this chapter. For monovalent non-bridging species, a second location on the SWCNT was functionalized with a hydrogen group to maintain a closed-shell system.	136
5.4. Representation of the theoretical potential energy surfaces for ground and first-excited states in the defected SWCNT systems.....	140
5.5. Relative total energies of each functionalized configuration with respect to the lowest energy isomer for (a) aryl-H and (b) di-aryl structures optimized with the CAM-B3LYP functional and STO-3G basis set in vacuum. Black squares represent ortho configurations, while blue circles represent para configurations.	142
5.6. Dependence of structural and energetic changes on the functional group conformation calculated in vacuum using CAM-B3LYP functional and 3-21G basis set. (a) Relative total energies of functionalized isomers with respect to the most stable structure compared between (6,5) SWCNT functionalized with an aryl bromide group and a hydrogen (aryl-H) and two aryl bromide groups (di-aryl). (b) The averaged difference between Carbon-Carbon bond lengths adjacent to aryl functionalization and those in the pristine SWCNT. Black squares represent ortho configurations, while blue circles represent para configurations.	143
5.7. Relative total energies of each configuration with respect to the lowest energy structure for (a) $Ar\uparrow$ aryl-H configurations and (b) diaryl configurations. The panel on the left and right compares the results obtained by STO-3G and 3-21G basis sets, respectively. Black squares represent ortho configurations, while blue circles represent para configurations.....	144
5.8. Relative total energies of each functionalized configuration with respect to the lowest energy isomer for aryl-H configurations optimized in a dielectric environment equivalent to (a) vacuum, (b) heptane, (c) acetonitrile, and (d) water using the CAM-B3LYP functional and STO-3G basis set. Black squares represent ortho configurations, while blue circles represent para configurations. The red box at the bottom of each panel represents the amount of energy available at room temperature (298K).....	147
5.9. Electrostatic dipole moment and its x, y, and z components for aryl-H configurations calculated using the CAM-B3LYP functional and STO-3G basis set in vacuum.....	148

- 5.10. The ground state electronic structure comparing Ar \uparrow aryl-H and di-aryl functionalized (6,5) SWCNT in vacuum. Highest occupied molecular orbitals (HOMOs) (a) and the electronic level diagram (b) for functional groups bounded along a vector 27° (L₃₀), 87° (L₉₀), and -33° (L₋₃₀) from the SWCNT axis. The values placed between the HOMO and LUMO are the HOMO-LUMO gaps in eV. 149
- 5.11. Molecular orbital diagrams for 12 aryl-H conformations calculated by the CAM-B3LYP functional and STO-3G basis set in vacuum. (a) The electronic levels in the range of -5.0 to 1.0 eV. (b) Electronic levels at the reduced energy region with only several frontier molecular orbitals of Ar \uparrow configurations. Due to functionalization, the sp³-defect at the tube surface breaks the degeneracy of frontier orbitals of the nanotubes resulting in destabilization of the HOMO and stabilization of the LUMO. As a result, the energy gap of functionalized SWCNTs is smaller than in pristine (6,5) nanotube. The decrease in the energy gap is more pronounced in isomer structures with higher degree of localization around the defect site. 151
- 5.12. Comparison of the molecular orbital diagram of the pristine (6,5) SWCNT and covalently functionalized (6,5) SWCNT by aryl bromide and hydrogen (Ar-H) and aryl bromide and OH (Ar-OH) covalently attached to a single carbon-ring at the tube surface in ortho L₃₀ and ortho L₋₃₀ positions. Calculations are performed using CAM-B3LYP functional and 3-21G basis set and compared to the similar calculations performed with extended mixed basis with 6-31G* basis set used for OH, LANL2DZ for Br atom in aryle bromide group, and 3-21G applied to all other atoms in the system. Neither the increase in the basis set nor the substitution of H to OH-group results in any noticeable change in the electronic structure of the functionalized SWCNT. Thus, the electronic structure of the SWCNT is not sensitive to the chemical composition of the second functional group attached to the same carbon-ring of the tube surface as the aryl bromide. Instead, the position of the functional groups (L₃₀ vs. L₋₃₀) has a significant effect on the molecular orbitals of the functionalized nanotubes..... 152
- 5.13. The ground state electronic structure diagrams for Ar \uparrow conformations of aryl-H functionalized (6,5) SWCNT calculated by CAM-B3LYP functional and (a) STO-3G basis set, (b) 3-21G basis set, and (c) the mixed basis set with LANL2DZ used for Br atom and 3-21G for all other atoms of the system in vacuum. The stated values are the energy gaps in eV. (d) Images of the related highest occupied molecular orbitals (HOMO) calculated by similar methods. 154
- 5.14. Absorption spectra of the (a) pristine (6,5) SWCNT, and its functionalized counterpart with the (b) ortho L₃₀, (c) ortho L₉₀, (d) ortho L₋₃₀, (e) para L₃₀, (f) para L₉₀, and (g) para L₋₃₀ Ar \uparrow conformations calculated in vacuum using CAM-B3LYP and either STO-3G (black lines) or 3-21G basis sets (blue lines). The vertical black lines correspond to the optical transitions with the height related to their oscillator strength, which values are shown at the right Y-axis. Spectra calculated by 3-21G were consistently blueshifted by 0.20 eV to coincide in E₁₁ peak with those obtained by STO-3G basis set. 155

- 5.15. Absorption spectra of the pristine (6,5) SWCNT (a), and its functionalized counterpart in ortho L₃₀ (b), ortho L₉₀ (c), ortho L₋₃₀ (d), para L₃₀ (e), para L₉₀ (f), and para L₋₃₀ (g) Ar↑ conformations calculated in vacuum. The vertical black lines correspond to the optical transitions with the height related to their oscillator strength, which values are shown at the right Y-axis. The dashed line indicates the reference point for the energy of the E₁₁ transition in the pristine SWCNT..... 156
- 5.16. Potential energy surface (PES) as a function of rotational angle about the C-C bond between the aryl bromide group and (6,5) SWCNT for different aryl-H configurations (left panels) and absorption spectra calculated for geometries corresponding to the lowest energy (red curve) and to the highest energy (black curve) of the PES (right panels). (a) ortho L₃₀, (b) ortho L₉₀, (c) ortho L₋₃₀, (d) para L₃₀, (e) para L₉₀, and (f) para L₋₃₀ Ar↑ conformations in vacuum. Because PES of the ortho L₉₀ isomer in (b) shows two local minima and maxima, four spectra are shown with the blue and green lines depicting the spectra of ortho L₉₀ geometries at the second local minimum (torsion angle ~90°) and the second maximum (torsion angle ~130°), respectively. Since all curves in right panels nearly coincide, the absorption spectra are independent on the torsional angle between the aryl and the nanotube for all defect structures. 163
- 5.17. Absorption spectra calculated using the CAM-B3LYP functional and 3-21G basis set in vacuum (black lines) and in the dielectric environment of heptane (red lines), acetonitrile (green lines), and water (blue lines) for pristine (6,5) SWCNT and its functionalized counterpart with aryl-H configurations. Note that the results for acetonitrile and water coincide, so that the green line (acetonitrile) is covered by the blue line (water) and is not seen. The vertical black lines correspond to the optical transitions in vacuum with their height related to the transition oscillator strength, which values are shown at the right Y-axis. In all cases, the E₁₁ band has diminishing bathochromic shift in different solvents. The most red-shifted E₁₁* band associated with the defect shows more noticeable bathochromic shift, but still very small. 166
- 5.18. Absorption and emission transitions of the Ar-H isomers calculated in various solvents. (a) ortho L₃₀, (b) ortho L₉₀, (c) ortho L₋₃₀, (d) para L₃₀, (e) para L₃₀, and (f) para L₋₃₀ configurations. The black curves are absorption spectra in vacuum. Vertical lines with symbols of black, red, green, and blue colors represent the lower energy optically active transitions in the E₁₁* band of functionalized SWCNTs in vacuum, heptane, acetonitrile, and water, respectively. The height of the vertical lines corresponds to the values of the oscillator strength of these transitions, shown at the right Y-axis. Triangles depict the lowest energy transitions contributing to the absorption (calculated at the ground state, GS, geometry) and squares the emission (calculated at the optimized excited state, ES, geometry)..... 168

5.19. Calculated reorganization of different functionalization configurations with respect to the SWCNT axis compared to the energetic shift of the E_{11}^* transition from the E_{11} transition of the pristine SWCNT. In this , the hexagon represents the pristine SWCNT, filled points represent ortho, empty points represent para, squares, triangles, and circles represent Ar-H, Ar-Ar, and Aryl bridging configurations respectively, and red, green, and blue represent L_{30} , L_{90} , and L_{-30} respectively.	171
5.20. Calculated radiative lifetime of different functionalization configurations with respect to the SWCNT axis as a function of (a) transition dipole, and (b) redshift of emission features. Filled points represent ortho, empty points represent para, squares, triangles, and circles represent Ar-H, Ar-Ar, and Aryl bridging configurations respectively, and red, green, and blue represent L_{30} , L_{90} , and L_{-30} respectively.....	173
5.21. Stabilities of (6,5) SWCNTs functionalized with different chemical species.	175
5.22. The electronic structure for (6,5) SWCNTs functionalized with different chemical groups. (a) Represents the energies of the HOMO and LUMO for each species. The break in the plot is at the HOMO-LUMO gap. For nearly all species, functionalization with methyl is the highest energy in both the HOMO and LUMO (b) Difference in energies for the MO of the species functionalized with the different species versus that functionalized with methyl.	176
5.23. Optical properties of all structures in this chapter. Black vertical droplines represent the absorption oscillators, and the solid black curve is for those lines broadened by a Gaussian curve of linewidth 0.01 eV to simulate the absorption spectra. The calculated energies of emission features are represented by red drop lines.	177
5.24. Optical properties of all structures in this chapter. Black vertical droplines represent the absorption oscillators, and the solid black curve is for those lines broadened by a Gaussian curve of linewidth 0.01 eV to simulate the absorption spectra. The calculated energies of emission features are represented by red drop lines.	178
5.25. Natural charge analysis as a function of experimental redshift for the functionalized species.	180
5.26. (a) Natural charge on the carbon atom adjacent to functionalization versus red shift of the species, and (b) s character versus red shift. The dashed blue lines indicate the asymptotically decreasing trend for the alkyl groups with varying degrees of electron donating/withdrawing ability.	181
6.1. Configurations of functionalization for the different chiralities of SWCNTs explored in this chapter.....	192

6.2. Relative stabilities for functional configurations of different chiralities including (a) (11,0), (b) (9,1), (c) (6,5), and (d) (5,4). All values were acquired by subtracting the total energy of the individual chirality and functionalization configuration from the lowest energy value for that particular chirality.	196
6.3. Full optical properties for functionalized (a) zigzag (11,0), (b) near-zigzag (9,1), (c) near-armchair (6,5), and (d) near-armchair (5,4) SWCNTs. The black droplines represent the absorption transitions, the blue droplines represent emission transitions, and the solid lines the simulated absorption spectrum acquired by broadening absorption oscillators with a linewidth of 0.01 eV.	198
6.4. Energies of emission features for functionalized (a) zigzag (11,0), (b) near-zigzag (9,1), (c) near-armchair (6,5), and (d) near-armchair (5,4) SWCNTs. The unshifted values are for three unit-cells of SWCNT as calculated using CAM-B3LYP/STO-3G methodology. Shifted values are as corrected using the scheme presented in section 7.2.4 of this chapter.	199
6.5. Regressions for emission energies of different length functionalized (5,4) systems using CAM-B3LYP (panels a and b) and B3LYP (panels c and d). The dashed and solid regression lines in the left panels represents the fit using the linear method and Kuhn’s method respectively, and the formula listed is for the linear fit. The right panels contain the least-squares linear regression between the emission energies extrapolated for the infinite length systems versus the red-shift in the 3-unit cell long systems.	201
6.6. (a) Correlation between unit cell length and E_{11}^* energy for different functional configurations of aryl-functionalized (6,5) SWCNTs computed using the CAM-B3LYP density functional. The inset represents the region centered around where the most delocalized species intersect the y-axis. Dashed and solid lines represent the least-squares linear regression of the data points and the fit using Kuhn’s formula respectively. (b) Computed red-shifts for the emission of the 3-unit cell systems computed with the CAM-B3LYP density functional correlated to the expected E_{11}^* (∞) values from panel (a) using a least-squares linear regression. (c) and (d) represent the same data as panels (a) and (b) respectively when calculated using B3LYP density functional.	202
6.7. Regressions for emission energies of different length functionalized (9,1) systems using CAM-B3LYP (panels a and b) and B3LYP (panels c and d). The dashed and solid regression lines in the left panels represents the fit using the linear method and Kuhn’s method respectively, and the formula listed is for the linear fit. The right panels contain the least-squares linear regression between the emission energies extrapolated for the infinite length systems versus the red-shift in the 3-unit cell long systems.	203

6.8. Regressions for emission energies of different length functionalized (11,0) systems using CAM-B3LYP (panels a and b) and B3LYP (panels c and d). The dashed and solid regression lines in the left panels represents the fit using the linear method and Kuhn’s method respectively, and the formula listed is for the linear fit. The right panels contain the least-squares linear regression between the emission energies extrapolated for the infinite length systems versus the red-shift in the 3-unit cell long systems.....	204
6.9. Linear fitting parameters for the different SWCNTs of different lengths and functionalization configurations. Solid points and lines represent the parameters acquired from CAM-B3LYP results, and open points and dashed lines represent the parameters from B3LYP.....	206
6.10. Difference between predicted E_{11}^* using either a linear regression or the Kuhn formula for correlating the effect of exciton localization on energy shifts. Black and red points represent optical features using the CAM-B3LYP and B3LYP density functional respectively.....	208
6.11. Confinement error vs methodology error in systems exhibiting different degrees of exciton localization and red-shifts. The greatest exciton delocalization is observed in pristine for all chiralities, while the species with strongest exciton localization is chirality dependence.....	210
6.12. (a) Calculated E_{11} energies for pristine SWCNTs of different diameter and chirality, including (11,0), (9,1), (6,5), and (5,4). Solid square points represent the energies as calculated using three unit cell computational cells, while the open circles represent the energies extrapolated from the infinite length linear regressions (LR) of length dependence of E_{11} . Blue and red points represent those calculated using CAM-B3LYP versus B3LYP respectively. Black (x) points represent the experimental values to which all trends were shifted for the purpose of correcting the computed values. (b) Difference between the E_{11} as calculated from three unit cell long systems versus the linear regression, using either CAM-B3LYP (open data points) or B3LYP (closed data points).	212
6.13. Computed energies of E_{11}^* for the six different functional configurations of aryl-functionalized(11,0) (top) and (9,1) (bottom) SWCNTs (a) as calculated using the specified methodology, (b) shifted by a constant energy value, (c) corrected for confinement errors using linear regression to determine the effect of exciton localization on E_{11}^* values, and (d) by using a fit to Kuhn’s formula to determine the effect of exciton localization on E_{11}^* values. Square, triangular, and circular markers represent functionalization for different functionalization configurations. Blue markers denote values for ortho functionalization, while red markers denote para. The left and right columns present the results as calculated using CAM-B3LYP and B3LYP respectively. The dashed vertical lines represent the experimental E_{11} values.....	215

6.14. Computed energies of E_{11}^* for the six different functional configurations of aryl-functionalized (5,4) (top) and (6,5) (bottom) SWCNTs (a) as calculated (b) shifted by a constant energy value, (c) corrected for confinement errors using linear regression to determine the effect of exciton localization on E_{11}^* values, and (d) by using a fit to Kuhn's formula. The left and right columns present the results as calculated using CAM-B3LYP and B3LYP respectively. The area of the plots highlighted in yellow is the range of energies where emission features were observed experimentally, and the dashed vertical lines represent the experimental E_{11} values..... 216

LIST OF ABBREVIATIONS

1-D	One Dimensional
Abs	Absorption
AM1	Austin Method 1
Arb	arbitrary
B3LYP	Becke, Three Parameter, Lee-Yang-Par
BLA.....	Bond Length Alternation
BO	Born Oppenheimer
BSE	Bethe-Salpeter Equation
CAM-B3LYP	Coulomb Attenuated Method-B3LYP
Ch.....	Chiral
Cir	Circumferential
CNT.....	Carbon Nanotube
CPCM	Conductor-like Polarizable Continuum
DFT	Density Functional Theory
D.....	Debye
Di.....	Diagonal
DNA.....	Deoxyribonucleic Acid
DOS.....	Density of States
e.....	electron
E	Energy
EN	Electronegativity
ER	Electromagnetic Radiation
ES	Excited State
eV	Electronvolt

GGA	Generalized Gradient Approximation
GPS	Global Positioning System
GS	Ground State
HF	Hartree-Fock
HK.....	Hohenberg Kohn
HOMO	Highest Occupied Molecular Orbital
INDO.....	Intermediate Neglect of Differential Overlap
KS	Kohn Sham
LANL2DZ.....	Los Alamos National Laboratory Double Zeta
LDA	Localized Density Approximation
LED.....	Light Emitting Diode
LUMO.....	Lowest Unoccupied Molecular Orbital
MD	Molecular Dynamics
MM	Molecular Mechanics
MM3	Molecular Mechanics 3
MO	Molecular Orbital
MOPAC	Molecular Orbital PACKage
NBO	Natural Bond Orbital
nm	Nanometer
ns.....	Nanosecond
NTO	Natural Transition Orbital
n-type	Negative Type
OS	Oscillator Strength
PAW.....	Projector-augmented Wave
PBC.....	Periodic Boundary Conditions

PBE	Perdew-Burke-Ernzerhof
pDOS.....	Projected Density of States
PES.....	Potential Energy Surface
PFO	poly(9,9-di-n-octylfluorenyl-2,7-diyl)
PL.....	Photoluminescence
p-type	Positive Type
PV	Photovoltaic
RG.....	Runge-Gross
STO.....	Slater Type Orbitals
SWCNT.....	Single-walled Carbon Nanotube
TDDFT.....	Time-dependent Density Functional Theory
VASP	Vienna Ab initio Simulation Package
VDW	Vander Waals
VMD	Visual Molecular Dynamics
VSEPR	Valence Shell Electron Pair Repulsion Model
XC.....	Exchange-Coorelation

LIST OF SYMBOLS

(n,m).....	Chirality of the SWCNT, where n and m are integers denoting the number of units a_1 and a_2 are transversed along the hexagonal lattice.
Δ	“Change in”
$^\circ$	Degrees
a.....	Length of SWCNT unit vector.
a_1	Chirality unit-vector with a positive y-component.
A_1	Terminal bonds along the chiral angle adjacent to B type bonds.
a_2	Chirality unit-vector with a negative y-component.
A_2	Terminal bonds along the chiral angle not adjacent to B type bonds.
Ar.....	aryl
Ar \uparrow	Functionalization configuration in which two distinct species are used to functionalize the SWCNT and the aryl-group is placed in the top position of the hexagonal ring with the SWCNT axis placed left to right.
Ar \downarrow	Functionalization configuration in which two distinct species are used to functionalize the SWCNT and the aryl-group is placed in the bottom position of the hexagonal ring with the SWCNT axis placed left to right.
B.....	Terminal bonds across along a vector 30° removed from the chiral vector.
C.....	Carbon
c.....	Speed of light
C_h	Vector corresponding to the chiral angle of a SWCNT.
Cl.....	Chlorine

C_n	Specific carbon atom, where the index refers to the atom number.
d	Diameter
d_i	two
e^-	Electron
e	Elementary charge
E	Energy
E_{ij}	Transition between the i and j Van Hove singularities in pristine SWCNTs.
E_{ij}^*	Lowest energy transition between the i and j Van Hove singularities in functionalized SWCNTs.
F	Fluorene
f_{ij}	Oscillator strength where the subscripts indicate the relevant states.
H	Hydrogen
h	Plank's constant.
I	Class of functionalization scheme involving two functional groups bonded through sp^2 hybridized atoms.
i	Integer
II	Class of functionalization scheme involving a functional group bonded through an sp^2 hybridized atom and one functional group bonded through a sp^3 hybridized atom.
III	Class of functionalization scheme involving two functional groups bonded through sp^3 hybridized atoms.
K_b	Boltzmann constant
L	Length

L_n	Longitudinal axis, where the index refers to the approximate angle with respect to the axis of the SWCNT.
m	Integer
m	Mass
m_e	Mass of an electron
n	Integer
o	Ortho
O	Oxygen
p	para
π	Orbital involving single p orbital left over after sp^2 hybridization of atomic orbitals.
q	Integer
r	Radius
R_n	Functional group where “n” denotes the index of specifically reference groups.
S_n	Specific singlet state, where the index refers to the state.
sp^2	Hybridized molecular orbital consisting of one s atomic orbital and two p atomic orbitals.
sp^3	Hybridized molecular orbital consisting of one s atomic orbital and three p atomic orbitals.
T	Temperature
ϵ_0	Permittivity of free space
θ	Angle
π	p type bonding orbital
π^*	p type antibonding orbital
Ψ	Wavefunction

ωAngular frequency

1. INTRODUCTION

The past three decades have been met with the introduction of remarkable technologies that connect people with information from opposing corners of the globe. Whether it's using Skype to video conference with distant family members, finding an incredible bargain on Amazon.com, or being guided to our destination by the GPS in our smartphones, few innovations have shaped modern life to the same degree as the internet. As anyone suffering from slow data speeds or a complete network outage would certainly be aware, this vital data connection plays a role in practically every aspect of our life in the twenty first century. Due to this, scientists and engineers have spent the greater part of the past three decades increasing the speed and reliability of internet.

One of the most significant advancements toward rapid increase in data transfer rates involves the use of fiber optical technologies. Early in the days of the internet, getting data from one place to another relied on electrical pulses travelling through wires made of conductive copper. While this was sufficient for the short term when the internet was a barely known concept, copper wires suffer from high cost, susceptibility to corrosion, and limitations in theoretical bandwidth due to signal losses.¹ Increasing the data rate requires an increase of the diameter of the cable and the corresponding increase in cost, weight, and rigidity.² These issues are significantly improved using fiber optical cables to transmit data with packets of light instead of electrons. Such fiber optical applications rely on 1530 nm to 1565 nm light as these wavelengths are transparent to transmission materials. As such, there is significant value in developing single-photon sources that generate such light. Single-walled carbon nanotubes (SWCNTs) are frequently considered for this application due to the introduction of infrared emission features as the result of functionalization. However, functionalization introduces a

range of emission features, the origin of which are not explained. In this dissertation, the electronic and optical changes induced by functionalization are computationally explored.

1.1. Single Walled Carbon Nanotube Structure & Properties

1.1.1. Forming a Tubule from a Graphene Sheet

A graphene sheet is a two-dimensional planar nanostructure composed of hexagonal rings of sp^2 hybridized carbon atoms bound by covalent bonds³. Each carbon atom in the lattice contains a single unhybridized pi orbital. Overlap of these orbitals enables electrons to readily pass between carbon atoms, resulting in an extended network of electron delocalization.³ A graphene sheet can be rolled into a cylindrical shape, thereby generating a pseudo one-dimensional structure known as a single-walled carbon nanotube (SWCNT).

1.1.2. SWCNT Chirality

Due to the presence of two distinct axes of symmetry, the layout of carbon atoms in the x and y directions of a graphene sheet are not equivalent. A path traversing the sheet in the x-direction follows carbon atoms in the “armchair” shape, while traversing the sheet in the y-direction follows a “zigzag” path. Rolling a planar structure in to a tubule form involves the superposition of two points on the plane. In the case of the formation of SWCNTs, those points can be located at any two carbon atoms. A large diversity of chemical structures can result from modifying which different points are connected to form the tube. A vector is drawn between the points to establish the “chiral vector”, which characterizes the resulting SWCNT structure. The “chirality” of the SWCNT is then defined as the number of basis vectors a_1 and a_2 that make up the chiral vector, where a_1 and a_2 are vectors forming an angle of $+30^\circ$ and -30° with the x-axis respectively (figure 1.1).⁴ These integer numbers are widely labeled as n and m, where the chiral vector is described as:

$$C_h = na_1 + ma_2 \quad (\text{Equation 1.1})$$

The chirality of the SWCNT is therefore described by two chiral indices, n and m , that completely describe a unique tubule geometry. Chiralities are generally denoted in the form (n,m) . The resulting structure is characterized as either “zigzag” for the case of $n>m=0$, “chiral” for $n\neq m\neq 0$, or “armchair” for $n=m$. In addition to distinct chiralities, SWCNTs have a property known as “handedness” which describes the direction in which the carbon atoms “spiral”. For the case in which $n>m$, the SWCNT is denoted as “left handed”. For the case in which $n<m$, the SWCNT is denoted as “right handed”.

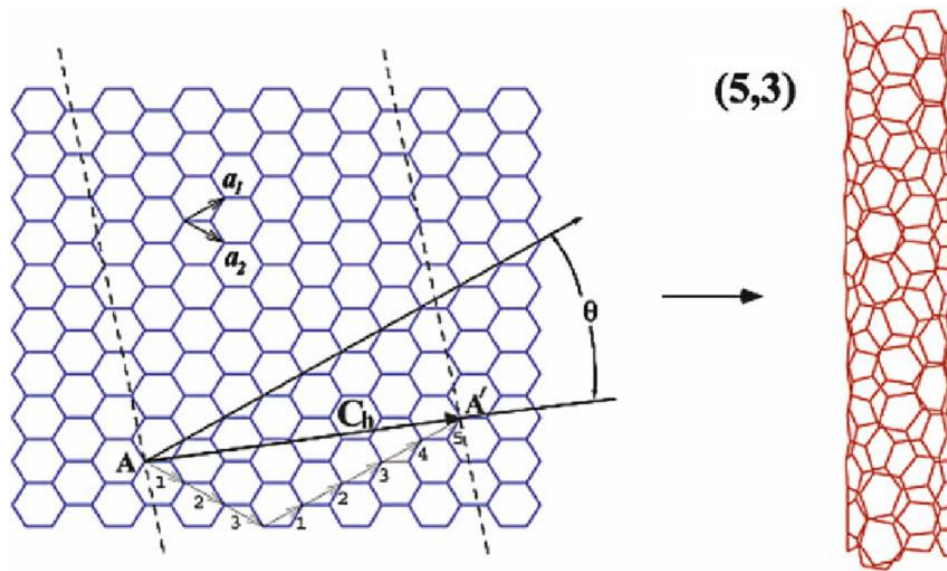


Figure 1.1. Schematic representing the orientation of rolling a graphene sheet to form a SWCNT. The “chiral vector” is labeled by C_h . Figure was adapted from reference 4.

1.1.3. Diameter Dependent Electronic & Optical Properties: Particle in a 1-D Box

As with the graphene sheet, the SWCNT preserves the properties of electron delocalization in the direction along the tube axis, while the electron confinement is enforced in the directions perpendicular to the axis. Due to this electron confinement, electronic and optical properties in SWCNTs follow the model of a particle in a box. In this model, the wave function is assumed to be confined to a box of length L with an infinite potential barrier at the edges. The result of these constraints are wave functions resembling standing waves with nodes at the edges of the box. The lowest energy solution has no additional nodes, while the number of nodes for higher energy solutions contain nodes proportional to the quantum number (# nodes from $0 < x < L = n-1$) In this model, the energy of the particle as well as energy spacing is therefore inversely proportional to the square of the length of the box. This simple model can be applied to nanomaterials to justify their electronic and optical properties, where smaller nanostructures have larger HOMO-LUMO gaps and therefore higher energy optical features (figure 1.2).^{5,6}

Therefore, a large degree can be said about the electronic and optical properties by simply

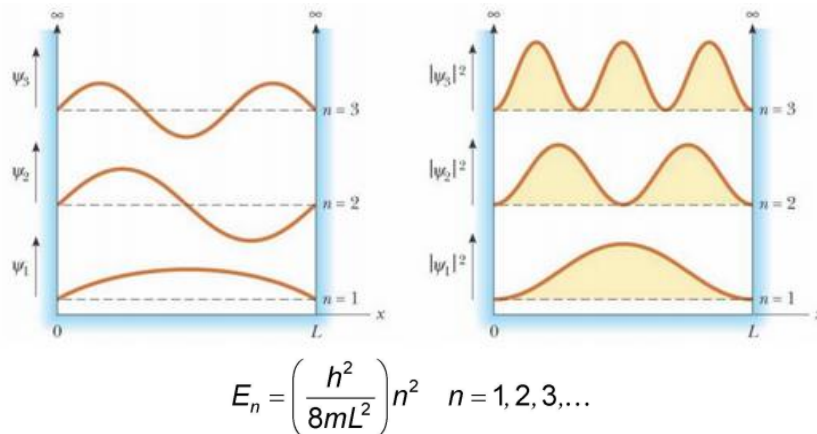


Figure 1.2. “Particle in a Box” model, where the wave function is considered to be confined in a one dimensional well with edges of an infinitely high potential. The energy of each level is described by the equation on the right, where h is Plank’s constant, m is the mass of the particle, L is the length of the box, and n is an integer corresponding to the quantum state. Figure was adapted from reference 5.

characterizing the tube diameter. Due to geometrical arguments, the diameter of a SWCNT is defined by its chiral indices as:

$$d = \left(\frac{a}{\pi}\right)\sqrt{n^2 + nm + m^2} \quad (\text{Equation 1.2})$$

where a is the length of the vectors a_1 and a_2 . While this gives us a lot of information pertaining to the electronic and optical properties of SWCNTs, it isn't the only structural parameter that influences their properties.

1.1.4. Chiral Angle

Another important characteristic of SWCNTs is the “chiral angle”. This is defined by:

$$\tan(\theta) = \frac{\sqrt{3}}{2n+m} \quad (\text{Equation 1.3})$$

When viewed from the side, the carbon atoms appear to “line up” along a vector that lies θ° from the SWCNT axis. As such, the chiral angle is a readily visible parameter.

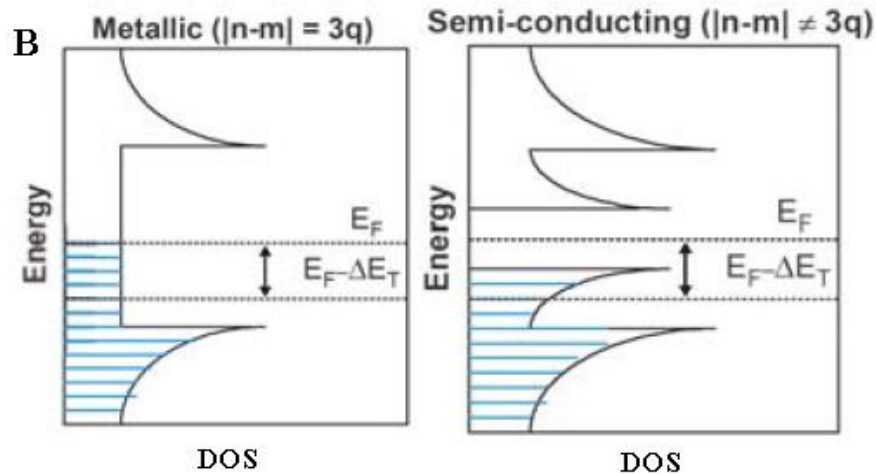


Figure 1.3. Density of States (DOS) in the 1-D confined SWCNT systems. Figure adapted from source 9.

1.1.5. Electronic Structure based on Chiral Indices

Due to the layout of carbon atoms in the SWCNT unit vector, they sometimes exhibit a conducting electronic structure similar to graphene. This is the case when the relationship

$n-m=3i$ holds, where i is any integer.^{7,8} These are “conducting” SWCNTs as this special relationship results in a shallow band of states between the valence and conduction bands and therefore a diminished HOMO-LUMO gap. For all other chiralities (ie. where $n-m\neq 3i$), the HOMO-LUMO gap of the SWCNT is on the order of a couple electronvolts (eV) and therefore they are semiconducting materials.^{9,10} Furthermore, the electronic structure of SWCNTs exhibits distinct bands with a significant density of states known as “Van Hove (VH) singularities” due to their one-dimensional confinement.^{3,11,12} These VH singularities are important in considering the optical properties of SWCNTs.

1.1.6. Optical Properties of SWCNTs

Since the structure of SWCNT consists of a lattice of sp^2 hybridized atoms with electron density delocalized across the entire system, there exists a number of optically allowed $\pi \rightarrow \pi^*$ transitions between Van Hove singularities exist. Angular momentum considerations dictate that the optically allowed transitions occur between VH singularities $-n$ to n , where 0 is the position of the Fermi level. When irradiated with the proper wavelength of light, excitation of the SWCNTs predominantly occurs between the second singularity below the edge of the valence band and the second singularity above the edge of the conduction band. This type of transition is labeled the 2-2 transition and has an energy E_{22} . Vibrational reorganization occurs after absorption, generating emission between the Van Hove singularities located at the edge of the gap. This is a 1-1 transition with energy E_{11} . Due to the previously mentioned chirality dependent electronic structure, the precise energies of excitation and emission are dependent on the chirality as well. Typical energies of absorption energies for readily synthesized SWCNTs are around 600 nm, while emission features range from 1000-1200 nm.^{13,14}

1.2. Practical Application & Limitations of SWCNTs

Due to their unique chirality dependent electronic and optical properties, combined with their remarkable thermal, mechanical, and chemical properties,¹⁵⁻¹⁷ SWCNTs have been the subject of intense investigation since the definition of their structure in 1991.¹⁸ Their nanoscale dimensions and optoelectronic properties enables them to be used in various industrial applications such as field emission display devices,¹⁹⁻²¹ electronics,^{16,22,23} and photovoltaic devices.²⁴⁻²⁷ Furthermore, the transparent nature and precise energy of their frontier molecular orbitals makes SWCNTs useful for utilization as hole-injection layers in light emitting diodes.²⁸⁻³² In addition to the applications that take advantage of their electronic properties, SWCNTs have been proposed as active layers in sensors³³⁻³⁸ partially due to their high surface-to-volume ratio and superior electron transport properties. However, there are a number of limitations that must be overcome for the full utilization of SWCNTs in this wide range of applications to be realized.

1.2.1. Challenges Generating Chirality Pure SWCNT Samples

SWCNTs to be used for the aforementioned applications require their properties and therefore chiralities be very carefully controlled. While recent advances have led to the production of samples of a few species,³⁹ chirality specific synthesis has thus far eluded experimental efforts. Due to the strong π - π interactions between individual SWCNTs, they tend to form strong bundles. As such, a potpourri of different methods have been utilized to post-synthetically break their bundles^{40,41} enabling their sorting into desired chiralities. The strategies for this frequently utilize density differentiation by centrifugation,^{42,43} size exclusion chromatography,⁴⁴⁻⁴⁶ electrophoresis,⁴⁷ and combinations of these methods. These methods rely on surfactants to selectively interact with, disperse, and dissolve SWCNTs of specific chiralities

or electronic types.⁴⁸ Deoxyribonucleic acid (DNA) is among the surfactants that have shown promise for use of SWCNTs, both in experiment^{49–52} and theory.⁵³

Another class of surfactants that receives a great deal of attention for selective dissolution and dispersion of SWCNTs is conjugated polymers. A vast body of literature characterizes specific conjugated polymer systems that are able to non-covalently interact with various types of SWCNTs.^{54–61} Because of this experimental success, a number of computational studies have been performed with the goal of describing both the energetic and morphological characteristics of such polymer – SWCNT systems.^{54,60,62–69} A common assumption in course grained computational studies of these systems^{62,67} is that the predominant interactions between the conjugated polymer and SWCNT involve π stacking between the polymer backbone and the extended π system of the sp^2 hybridized carbon network in the SWCNTs. As such, the large alkyl groups present in the polymer are frequently omitted from computational models. Such an approximation enables simplification of the models and therefore reduction of computational costs, but it results in the complete neglect of interactions between the sidechain alkyl groups and the SWCNT. While these interactions are expected to be weak, they will still contribute to the strength of interaction between the conjugated polymer and SWCNTs and therefore play a role in both the dispersion ability and selectivity of such conjugated polymers. Because the sidechains of conjugated polymers are expected to have some impact on their binding to various chiralities of SWCNT, Chapter 2 of this dissertation focusses on characterizing the effect of alkyl side groups of poly(9,9-di-n-octylfluorenyl-2,7-diyl) (PFO) on its adsorption energy and morphology in PFO-SWCNT composites. Such information is important to assess the viability of using sidechain length as a degree of freedom in experimental efforts to sort SWCNT chiralities as well as determine the validity of excluding such sidechains from computational models.

1.3. Tuning SWCNT Properties by Covalent Functionalization

While pristine SWCNTs exhibit a relatively wide range of properties, sometimes further tuning is required to optimize their performance for a given application. Covalent functionalization of SWCNTs is commonly implemented as a strategy for manipulating the intrinsic properties of SWCNTs, and the effects of such functionalization have been widely reported. There have recently been a number of experimental investigations exploring the use of functionalized SWCNTs for active layers light emitting and photovoltaic devices.^{25,70–72} Integrating a range of SWCNT species into such a device would facilitate the adsorption of light across the broad wavelengths of the solar spectrum due to the variety of band gaps in a normal SWCNT film. However, efficiency of such devices has generally been below that of existing technologies, partially because the lowest electronic transition in functionalized SWCNTs is generally optically dark. It has been suggested theoretically⁷³ that covalent functionalization should brighten the lowest optical transition, which should improve efficiency in photovoltaic devices.

Covalent functionalization with halides and alcohols changes the electronic properties of SWCNTs.^{74–76} Further studies have been performed functionalizing SWCNTs with carboxylic acids,^{77,78} amides,⁷⁹ and amines.^{79,80} Such functionalization not only results in a change to electronic and optical properties, but also provides reactive sites thereby providing the framework for further synthetic modification. Additionally, carboxylate and alcohol groups are known for their ability to form chemical bonds to other reagents, such as metal-organic complexes,⁸¹ porphyrins,^{82,83} polymer chains,^{84–86} proteins,²⁹ and DNA.^{87,88} This improves their promise for applications in sensor devices, antibiotics, and drug delivery systems.^{41,89–91} A significant number of studies detailing oxygen functionalization have also been performed.^{92–95}

Covalent functionalization occurs at the sidewalls and/or open ends or tips of the SWCNTs through chemical synthesis, oxidation, and acid treatments.^{96–101} Due to the large strain and weak reacting nature of sp^2 -hybridized carbons, SWCNTs are more susceptible of being functionalized on the tips or edges.^{102–104} Unfortunately, a precise control over positions and concentrations of functional groups at the nanotube surface is still a challenge^{99,105–107} and the mechanisms by which functionalization occurs and modifies the pristine SWCNT properties is largely unknown. First principle calculations are frequently utilized to gain detailed insights into interactions between the functional groups and SWCNTs and identify the resulting optoelectronic behaviors.¹⁰⁷

1.3.1. Chlorine Functionalization

In the quest to functionalize SWCNTs to generate new and useful properties, halogenation of SWCNTs has been performed.^{108–110} This is perhaps the easiest functionalization to accomplish due to the high reactivity of fluorine with the SWCNT surface.¹¹¹ Attempts of chlorination^{112–116} and bromination¹¹⁷ of SWCNTs with various techniques have also been successful. One source of recent interest has been the functionalization of SWCNTs with $AuCl_3$. Functionalization with $AuCl_3$ results in a p-type doped system.^{118,119} However, the mechanism of this functionalization is not exactly known. Some proposed mechanisms include the adsorption of individual chlorine atoms¹²⁰ or the adsorption of an entire gold chloride cluster.¹²¹ However, a more complete understanding of the mechanisms and regiochemistry of functionalization of these systems is imperative.

There has been a significant amount of research computationally characterizing the properties of chlorinated SWCNTs.^{114,121–124} Based on these previous efforts, it has been shown that the binding of a single Cl atom to the SWCNT sidewall creates a defect in the sp^2 lattice.

This substantially increases the favorability of binding a second Cl atom to a nearby site¹¹⁴ with certain sites being more favorable than others.¹²⁴ Chlorination has also been shown to shorten the band gap of semiconducting SWCNTs by introducing unoccupied midgap states: this is consistent with p-type doping.¹²² The exact changes to the electronic structure have been shown to be dependent on the precise sites of chlorine functionalization at the surface of the SWCNT.¹¹⁴ There is limited computational research regarding the effect of chlorination on the excited state properties of the SWCNT. To this end, Chapter 4 of this dissertation focusses on characterizing the effects on the electronic and optical properties of chlorine functionalization of both charged and neutral (6,2) SWCNTs.

1.3.2. Functionalization with Aryl Groups

Recent studies have focused on functionalization with aryl-based dopants.^{125,95,126-130} In these studies, absorption occurs along the pristine portion of the SWCNT at energy E_{11} . The exciton then undergoes vibrational reorganization and becomes trapped at the defect site, and the subsequent emission occurs at lower energy E_{11}^* .^{127,131} Such low energy emission features dramatically increases the plausibility of using SWCNTs in communications applications.⁹⁵ While limited computational exploration of the introduction of these low-energy optical features has been performed,¹³² a clear understanding explaining the presence of a number of emission features has not yet be achieved.

Due to the hexagonal lattice of SWCNTs, a number non-chemically equivalent positions for functionalization arise, allowing for the creation of multiple different functional configurations. Previous studies have successfully characterized the effect of functionalization along different bonds on the electronic structure local to the defect site.^{127,133} These studies have eluded to the position-dependence of functionalization on local electronic structure and therefore

optical properties of functionalized SWCNTs. However, to date a study exploring the effects of functionalization with aryl and hydrogen dopants in different positions with respect to the SWCNT axis and in the presence of solvent has not been performed. Additionally, the effects of such functionalization have previously been shown to be defect-based.¹²⁷ In this dissertation, Chapter 5 focuses on relating the energy of emission features of covalently functionalized SWCNTs to distinct positions of the functional groups. For the first time, the diverse emissive features of functionalized SWCNTs is attributed to the existence of multiple functionalization configurations that induce differing degrees of exciton localization around the defect site. This information is valuable for establishing structure-property relationships and formulating synthetic schemes that maximize desirable optical characteristics for specific applications.

1.4. The State of Computational Methodology for SWCNTs

A diverse set of existing computational methods can be applied to SWCNT systems. Perhaps the simplest methodology involves simply solving for the positions of the nuclei by treating them as classical points and considering the forces that govern their geometrical configurations. This is computationally inexpensive and can be done for systems of thousands of atoms, but only provides the geometries of the system and lacks information describing its electronic structure. Since interactions with light involve transitions between electronic levels, the full electronic structure of the systems must be obtained where optical features are of interest. This is much more computationally expensive and could historically be performed only on systems consisting of a few atoms. As the result of the advent of modern computers with thousands of processing cores, performing such calculations on systems with thousands of atoms (such as SWCNTs) is just now becoming feasible.

1.4.1. Classical Methods: Molecular Mechanics

The fundamentals of chemical bonding have been known for quite some time now. In the simplest terms, molecular geometry can be described by the valence shell electron pair repulsion model (VSEPR). In this model, it is assumed that the positive charges of the nuclei in a chemical system repel each other and are therefore distributed in a way to fill the maximum amount of space possible.¹³⁴ A slightly higher-level model known as hybridization attributes the shapes of molecules to the presence of electrons in orbitals with distinct shapes of their own. Each atom is assigned a certain hybridization depending on its electron configuration, and the hybridization in turn dictates the bond lengths, angles, and dihedral angles to adjacent atoms. By combining and filling orbitals in the way dictated by the number of electrons, the resulting system is laid out in a certain configuration.¹³⁴ Both of these models are elegantly simple and yet very powerful to describe the geometry of chemical systems.

In order to predict the geometries using classical molecular mechanics, a parameter set is first developed describing the geometry about each atom considering its identity and hybridization. The parameters describing bond lengths, angles, and dihedral angles are defined by considering the atoms as simple balls on a spring, and the parameter set contains all the force constants and equilibrium values for each type of atom. Additional terms are introduced to describe phenomenon such as hydrogen bonding, Vander Waals interactions, and the formation of cyclic structures of different sizes. The forces on all atoms in a computational system can then be calculated from simple equations of harmonic oscillators and the parameters in this set. The system is allowed to relax and the new forces are calculated. This procedure is repeated until a minimum energy is obtained within a certain threshold is obtained. Because it only requires a few algebraic operations per atom, determining geometries using this method is

computationally efficient for even large systems. As a result, it was the methodology of choice for optimizing SWCNTs in the presence of surfactants in Chapter 2 of this dissertation. In order to increase the accuracy of these calculations, the chosen parameter set was modified to provide geometries for the surfactant molecules that match ab-initio results.

1.4.2. Electronic Structure Calculations

1.4.2.1. Basic Introduction to Quantum Chemical Calculations

The fundamental physics governing the electronic structure of a chemical system and therefore its physical and bonding characteristics have been completely known for some time. The Schrödinger equation, developed by Erwin Schrödinger in 1925 and published in 1926,¹³⁵ completely describes the wave function of a system consisting of electrons spatially distributed about charged nuclei as an eigenfunction where the Hamiltonian is the total energy operator. The eigenvalue is in turn total energy, and the wave function uniquely describes all the observables of the system.⁶ Despite this, the wave functions of even the smallest real systems are far too complex to solve for explicitly. A significant challenge addressed by computational chemistry is how a system's wave function can be computationally approximated. Such procedures can subsequently be used to predict the properties of real chemical systems.

1.4.2.2. Hartree-Fock & Semiempirics

The Hartree-Fock method of quantum chemical calculations is frequently used to determine the properties of chemical systems. In this method, the number of terms in the Hamiltonian is first reduced using the Born-Oppenheimer approximation¹³⁶ in which the nuclei are assumed to be sufficiently massive and therefore fixed. The resulting “electronic Hamiltonian” only consists of terms describing electronic kinetic energy, electron-nuclear interactions, and electron-electron interactions. The wave function of the system is

approximated as a superposition of weighted one-electron orbitals (the so called “basis set”). Following the vibrational principle, the real energy of the system using this approximated wave function will be greater-than or equal-to the real wave function. A self-consistent approach is then utilized to solve for the coefficients to minimize the total energy of the wave function approximating the real system. While this approach is powerful and successfully used to predict the properties of a range of small systems, it is also expensive due to the relatively high computational cost of the two-electron integrals describing the electron-electron interactions in the system. As a result, the interactions are frequently parameterized from experimental or theoretical results. The resulting semi-empirical methodology can be implemented at a much smaller computational cost, resulting in its application to much larger system. However, is met with limitations in the diversity of systems that can be considered with a chosen methodology. Because electron-electron interactions must behave similarly in the system of interest as they do in the system from which the parameters were derived, a menagerie of different semi empirical methodologies exist. Of these, Austin Model 1 (AM1)¹³⁷ and intermediate neglect of differential overlap (INDO)¹³⁸ have been shown to accurately approximate the curvature and vibrational effects in SWCNTs.¹³⁹ As such, they have been used extensively for calculating the geometries of SWCNTs in this dissertation.

1.4.2.3. Density Functional Theory

A fundamental cornerstone of quantum mechanics is that square of the wave function is defined as the probability of finding an electron at that position. It is therefore natural to work with electron density (correlating to charge) in lieu of wave functions. In 1964, Hohenberg and Kohn published a seminal paper which established two significant theorems: 1) the external potential of an system, and therefore it’s total energy, is a unique functional of electron density,

and, 2) the ground state energy can be obtained variationally, and the density that results in a minimum total energy is the exact ground state density.¹⁴⁰ The following year, Kohn and Sham developed the formalism in which the exact ground state density is expressed as the ground state density of a fictitious system of non-interacting particles. This allows us to treat density in the same way as previously discussed for wave functions.¹⁴¹ This methodology, known as Density Functional Theory (DFT) is one of the most utilized techniques for determining electronic structure as the result of its improved chemical accuracy over Hartree-Fock without significant increases in computational cost. As such, it has become the most frequently used methodology in the field of computational chemistry. Due to the development of powerful supercomputers, DFT can now be implemented on large systems including SWCNTs.

Perhaps the most challenging part of applying DFT to real systems is properly describing the terms involving electron-electron interactions and electron kinetic energy in the Hamiltonian with a physically real density functional. A large number of approximate density functionals have been developed for this purpose with a wide range of constructs, the basis of all of which is the local density approximation (LDA). This model is constructed around the concept of a uniform electron gas in a positive background charge such that the entire system is neutral. This enables description of the energies resulting from electron density and is an appropriate approximation where electron density is evenly distributed in space. However, for systems where the electron density isn't uniformly distributed, consideration of gradients in density need to be taken into account. The generalized-gradient approximation (GGA) accomplishes this and provides functionals more suited for molecular systems than LDA.¹⁴² Further methodologies combine GGA and portions of density-dependent energy from Hartree Fock methods. By combining these components in different ratios for exchange and correlation, many so-called

“hybrid” functionals have been developed that can be accurately used for a wide range of chemical systems. The most commonly known and applied of these is the Becke, three-parameter, Lee-Yang-Parr (B3LYP) functional^{143,144} which has been shown to give accurate results for a wide range of chemical systems¹⁴⁵ including SWCNTs. As such, portions of this dissertation consider it as a “benchmark” including Chapter 3 where electronic structure for a number of systems is compared.

While B3LYP provides relatively good results, further modification of the functional has frequently been performed in order to improve the electronic structure. This involves changing the weights of each portion as the distance from the nucleus varies. One such functional that implements this is the coulomb-attenuating method (CAM-B3LYP)¹⁴⁶ which varies the percent of Hartree-Fock exchange from 19% near the nucleus to 65% at greater distances. It has been previously shown that using the CAM-B3LYP for calculations involving SWCNTs more properly describes electron density localization along the axial direction of the tube.¹²⁷ It is therefore the chosen functional for the majority of the DFT calculations in this dissertation.

Ground state density functional calculations have successfully been used to determine the unique properties introduced by functionalization. In these studies, periodic boundary conditions were used to study the stability and electronic structure of semiconducting zigzag and metallic armchair nanotubes functionalized at the side-wall with carboxylic acid, alcohol, amine, and alkyl functional groups.¹⁴⁷ It was found that these functional groups create sp^3 defects at the SWCNT surface resulting in trap states introduced into the band gap of a pristine nanotube, while methylene groups bound to metallic (9,0) SWCNT form pentagon/heptagon defects leading to opening of the band gap and a change in its metallic to semiconductor character.

Since DFT properly describes the uncorrelated gaps in nanomaterials with a range of dimensionalities including 1-D systems,¹⁴⁸ it is reasonable to apply it to SWCNTs for predicting optical properties. In order to accurately predict optical properties, methodology that accurately captures the effects from the presence of electron-hole pairs (“excitons”) needs to be implemented. One such DFT based methodology involves solving the Bethe-Salpeter equation (BSE). In this approach, a DFT calculations are first performed under the LDA. The resulting Kohn-Sham energies and wave functions are used as a starting point for further calculations describing the excitons. The BSE are then solved numerically using these two components. Such an approach has been used successfully to describe optical excitations, recently in the case of bi-exciton formation.^{149,150} However, it is met with significant computational cost and therefore the number of optical transitions that can be considered is limited. While only a few states are required for pristine systems with a high degree of symmetry, functionalization of SWCNTs breaks this symmetry. As such, many more excited states are required and the less-expensive linear-response time dependent DFT is preferred.

1.4.2.4. Time-Dependent Density Functional Theory

The first Hohenberg-Kohn theorem can be extended to the time dependent case, where a time dependent potential uniquely corresponds to a time-dependent density. This was shown by Runge and Gross.¹⁵¹ In linear-response time dependent DFT (TDDFT), the Hamiltonian is approximated as the sum of the Hamiltonian in the ground state plus some time-dependent perturbation. Consequentially, the total time-dependent density can be expressed as the sum of the ground state geometry and a time-dependent transition density. The transition density is constructed from a superposition of transitions between the ground state orbitals, and the Casida equation can be solved to provide proper coefficients. The resulting solutions provide a

description of the transitions, including their energies and dipoles. The relatively small expense of this method make it optimal for pristine SWCNT systems, and it has frequently been successfully applied to reproduce at least qualitative scaling behavior.^{107,139} In addition, it has been used to describe how SWCNT excitation energies are affected by functionalization.^{132,133} Calculations based on TDDFT have predicted that chemisorption of hydrogen and aryl groups at the sidewall of semiconducting SWCNTs significantly modifies the optical selection rules so that the lowest-energy transitions become optically active.^{132,133,152} However, such optical brightening of the lowest energy state is highly sensitive to the position of the adsorbent.¹³² These predictions agree well with the recent experimental findings of a satellite bright emission peak in SWCNTs with sp^3 defects introduced via controllable chemical functionalization.^{153,154} Similar results have been obtained both computationally and experimentally for oxygen-doped SWCNTs.⁹³

1.4.3. Approximation in the Models: Finite Computational Cells

While a number of software packages exist implementing the TDDFT formalism as previously described, none currently utilize periodic boundary conditions. As such, the computational cells need to be generated of finite size. TDDFT calculations of SWCNTs functionalized at the sidewalls^{93,132,133,152} have been mostly conducted on finite-size nanotubes of about 10 nm in length with tips capped by hydrogen atoms and CH_2 groups to eliminate dangling bonds at the tube edge. However, the appearance of mid-gap states associated with the edges is sensitive to the ratio between H and CH_2 capping groups, which, in turn, has been found to depend on the tube chirality. Unfortunately, a precise form of this dependence is still unclear and only empirical approaches have been reported in the literature.^{107,139} This is a major problem, as proper capping schemes that make the finite system mimic the electronic structure of the infinite

system are required for each capping scheme before the properties of the pristine or functionalized systems can be accurately computed. As such, Chapter 3 of this dissertation focusses on determining the effects of a wide range of capping groups on the electronic and optical properties of SWCNTs. Consideration of the impact of capping groups is essential in developing capping schemes and thereby enables accurate computations on functionalized systems.

1.4.4. Analytical Model for Correcting for Computational Error

Finite computational models have been used to perform TDDFT on covalently-functionalized SWCNTs throughout this dissertation. In reality, these systems are on the orders of micrometers in length, which is prohibitively expensive for DFT. While qualitative trends derived from these finite-length systems may be useful towards analyzing optical features due to chemical modifications, the value of quantitative data is compromised due to several approximations. These include artificial localization as the result of using a finite-length SWCNT system (“confinement error”) and the use of an incomplete basis set and self-interaction errors in the density functional, (collectively referred to as “methodology errors”). All these errors tend to blueshift computed optical features relative to experiment. Ideally, energies must be corrected to form direct comparisons between theory and experiment. One method to accomplish this would be to introduce a constant energy shift. While this method is simple, it does not consider the two sources of error independently. In the computed systems, methodology errors are similar across all species whereas confinement errors depend on electron localization. These are insignificant for species with excitons localized close to the defect site but become substantial for species where the exciton is delocalized across the whole tube. In latter systems, a single shift may overcorrect since it neglects species-dependent confinement

error; a subsequent subtraction of confinement error proportional to the degree to which the exciton is localized would be required. A proper scheme that corrects transition energies with different degrees of exciton localization must treat confinement and methodology errors independently. Development of such a scheme is the focus of Chapter 6. The novel scheme developed here provides the theoretical framework for shifting optical features for all calculations involving finite computational cells. In addition, Chapter 6 presents the properties resulting from functionalization along different functionalization configurations for different chiralities of SWCNT.

1.5. References

- (1) The Disadvantages of Copper Wire <http://sciencing.com/disadvantages-copper-wire-5973732.html> (accessed Sep 18, 2017).
- (2) Copper Cable Limitations - Silicon-Line <http://www.silicon-line.com/copper-cable-limitations.html> (accessed Sep 18, 2017).
- (3) Saito, R.; Dresselhaus, G.; Dresselhaus, M. S. *Physical Properties of Carbon Nanotubes*; Imperial College Press: London, 1998.
- (4) Tan, C. W.; Tan, K. H.; Ong, Y. T.; Mohamed, A. R.; Zein, S. H. S.; Tan, S. H. Carbon Nanotubes Applications: Solar and Fuel Cells, Hydrogen Storage, Lithium Batteries, Supercapacitors, Nanocomposites, Gas, Pathogens, Dyes, Heavy Metals and Pesticides. In *Environmental Chemistry for a Sustainable World*; Springer, Dordrecht, 2012; pp 3–46.
- (5) Quantum Mechanics http://www.unistudyguides.com/wiki/Quantum_Mechanics (accessed Oct 18, 2017).
- (6) Griffiths, D. J. *Introduction to Quantum Mechanics*, 2nd ed.; Pearson Prentice Hall: Upper Saddle River, NJ, 2005.

- (7) Saito, R.; Sato, K.; Oyama, Y.; Jiang, J.; Samsonidze, G. G.; Dresselhaus, G.; Dresselhaus, M. S. Cutting Lines near the Fermi Energy of Single-Wall Carbon Nanotubes. *Phys. Rev. B* **2005**, *72* (15).
- (8) Uzun, E. Calculation of Cutting Lines of Single-Walled Carbon Nanotubes. *Cumhur. Sci. J.* **2012**, *33* (1), 65–76.
- (9) Mintmire, J. W.; Dunlap, B. I.; White, C. T. Are Fullerene Tubules Metallic? *Phys. Rev. Lett.* **1992**, *68* (5), 631–634.
- (10) Dekker, C. Carbon Nanotubes as Molecular Quantum Wires. *Phys. Today* **1999**, *52* (5), 22.
- (11) Dass, D.; Prasher, R.; Vaid, R. Analytical Study Of Unit Cell And Molecular Structures Of Single Walled Carbon Nanotubes. *Int. J. Comput. Eng. Res.* *2* (6), 1447–1457.
- (12) Xin, X.; Xu, G.; Li, H. Dispersion and Property Manipulation of Carbon Nanotubes by Self-Assembles of Amphiphilic Molecules. In *Physical and Chemical Properties of Carbon Nanotubes*; Suzuki, S., Ed.; InTech, 2013.
- (13) Streit, J. K.; Bachilo, S. M.; Ghosh, S.; Lin, C.-W.; Weisman, R. B. Directly Measured Optical Absorption Cross Sections for Structure-Selected Single-Walled Carbon Nanotubes. *Nano Lett.* **2014**, *14* (3), 1530–1536.
- (14) O’Connell, M. J. Band Gap Fluorescence from Individual Single-Walled Carbon Nanotubes. *Science* **2002**, *297* (5581), 593–596.
- (15) Kong, J.; Franklin, N. R.; Zhou, C.; Chapline, M. G.; Peng, S.; Cho, K.; Dai, H. Nanotube Molecular Wires as Chemical Sensors. *Science* **2000**, *287*, 622–625.

- (16) Ravindran, S.; Chaudhary, S.; Colburn, B.; Ozkan, M.; Ozkan, C. S. Covalent Coupling of Quantum Dots to Multiwalled Carbon Nanotubes for Electronic Device Applications. *Nano Lett.* **2003**, *3*, 447–453.
- (17) Baughman, R. H.; Zakhidov, A. A.; de Heer, W. A. Carbon Nanotubes--the Route toward Applications. *Science* **2002**, *297*, 787–792.
- (18) Iijima, S. Helical Microtubules of Graphitic Carbon. *Nature* **1991**, *354* (6348), 56–58.
- (19) Postma, H. W. C.; Teepen, T.; Yao, Z.; Grifoni, M.; Dekker, C. Carbon Nanotube Single-Electron Transistors at Room Temperature. *Science* **2001**, *293*, 76–79.
- (20) Misewich, J. A.; Martel, R.; Avouris, P.; Tsang, J. C.; Heinze, S.; Tersoff, J. Electrically Induced Optical Emission from a Carbon Nanotube FET. *Science* **2003**, *300*, 783–786.
- (21) Martel, R. al; Schmidt, T.; Shea, H. R.; Hertel, T.; Avouris, P. Single-and Multi-Wall Carbon Nanotube Field-Effect Transistors. *Appl. Phys. Lett.* **1998**, *73*, 2447.
- (22) Mason, N.; Biercuk, M. J.; Marcus, C. M. Local Gate Control of a Carbon Nanotube Double Quantum Dot. *Science* **2004**, *303*, 655–658.
- (23) Li, J.; Papadopoulos, C.; Xu, J. M.; Moskovits, M. Highly-Ordered Carbon Nanotube Arrays for Electronics Applications. *Appl. Phys. Lett.* **1999**, *75*, 367.
- (24) Cataldo, S.; Salice, P.; Menna, E.; Pignataro, B. Carbon Nanotubes and Organic Solar Cells. *Energy Environ. Sci.* **2012**, *5* (3), 5919–5940.
- (25) Brown, P.; Takechi, K.; Kamat, P. V. Single-Walled Carbon Nanotube Scaffolds for Dye-Sensitized Solar Cells. *J. Phys. Chem. C* **2008**, *112* (12), 4776–4782.
- (26) Landi, B. J.; Raffaele, R. P.; Castro, S. L.; Bailey, S. G. Single-Wall Carbon Nanotube–polymer Solar Cells. *Prog. Photovolt. Res. Appl.* **2005**, *13* (2), 165–172.

- (27) Lee, J. U. Photovoltaic Effect in Ideal Carbon Nanotube Diodes. *Appl. Phys. Lett.* **2005**, *87* (7), 073101.
- (28) Zhang, D.; Ryu, K.; Liu, X.; Polikarpov, E.; Ly, J.; Tompson, M. E.; Zhou, C. Transparent, Conductive, and Flexible Carbon Nanotube Films and Their Application in Organic Light-Emitting Diodes. *Nano Lett.* **2006**, *6* (9), 1880–1886.
- (29) Bansal, M.; Srivastava, R.; Lal, C.; Kamalasanan, M. N.; Tanwar, L. S. Carbon Nanotube-Based Organic Light Emitting Diodes. *Nanoscale* **2009**, *1* (3), 317–330.
- (30) Mueller, T.; Kinoshita, M.; Steiner, M.; Perebeinos, V.; Bol, A. A.; Farmer, D. B.; Avouris, P. Efficient Narrow-Band Light Emission from a Single Carbon Nanotube P–n Diode. *Nat. Nanotechnol.* **2010**, *5* (1), 27–31.
- (31) Wang, S.; Zeng, Q.; Yang, L.; Zhang, Z.; Wang, Z.; Pei, T.; Ding, L.; Liang, X.; Gao, M.; Li, Y.; et al. High-Performance Carbon Nanotube Light-Emitting Diodes with Asymmetric Contacts. *Nano Lett.* **2011**, *11* (1), 23–29.
- (32) Bahena-Garrido, S.; Shimoi, N.; Abe, D.; Hojo, T.; Tanaka, Y.; Tohji, K. Planar Light Source Using a Phosphor Screen with Single-Walled Carbon Nanotubes as Field Emitters. *Rev. Sci. Instrum.* **2014**, *85* (10), 104704.
- (33) Chen, T.; Wei, L.; Zhou, Z.; Shi, D.; Wang, J.; Zhao, J.; Yu, Y.; Wang, Y.; Zhang, Y. Highly Enhanced Gas Sensing in Single-Walled Carbon Nanotube-Based Thin-Film Transistor Sensors by Ultraviolet Light Irradiation. *Nanoscale Res. Lett.* **2012**, *7* (1), 644.
- (34) Dhall, S.; Jaggi, N.; Nathawat, R. Functionalized Multiwalled Carbon Nanotubes Based Hydrogen Gas Sensor. *Sens. Actuators Phys.* **2013**, *201*, 321–327.

- (35) Zhang, T.; Nix, M. B.; Yoo, B.-Y.; Deshusses, M. A.; Myung, N. V. Electrochemically Functionalized Single-Walled Carbon Nanotube Gas Sensor. *Electroanalysis* **2006**, *18* (12), 1153–1158.
- (36) Li, J.; Lu, Y.; Ye, Q.; Cinke, M.; Han, J.; Meyyappan, M. Carbon Nanotube Sensors for Gas and Organic Vapor Detection. *Nano Lett.* **2003**, *3* (7), 929–933.
- (37) Zhang, W.-D.; Zhang, W.-H.; Zhang, W.-D.; Zhang, W.-H. Carbon Nanotubes as Active Components for Gas Sensors, Carbon Nanotubes as Active Components for Gas Sensors. *J. Sens. J. Sens.* **2009**, *2009*, *2009*, e160698.
- (38) Wang, Y.; Yeow, J. T. W.; Wang, Y.; Yeow, J. T. W. A Review of Carbon Nanotubes-Based Gas Sensors, A Review of Carbon Nanotubes-Based Gas Sensors. *J. Sens. J. Sens.* **2009**, *2009*.
- (39) Liu, J.; Wang, C.; Tu, X.; Liu, B.; Chen, L.; Zheng, M.; Zhou, C. Chirality-Controlled Synthesis of Single-Wall Carbon Nanotubes Using Vapour-Phase Epitaxy. *Nat. Commun.* **2012**, *3*, 1199.
- (40) Reich, S.; Thomsen, C.; Ordejon, P. Electronic Band Structure of Isolated and Bundled Carbon Nanotubes. *Phys. Rev. B* **2002**, *65*, 155411.
- (41) Tasis, D.; Tagmatarchis, N.; Bianco, A.; Prato, M. Chemistry of Carbon Nanotubes. *Chem. Rev.* **2006**, *106*, 1105–1136.
- (42) Arnold, M. S.; Green, A. A.; Hulvat, J. F.; Stupp, S. I.; Hersam, M. C. Sorting Carbon Nanotubes by Electronic Structure Using Density Differentiation. *Nat. Nanotechnol.* **2006**, *1* (1), 60–65.

- (43) Ghosh, S.; Bachilo, S. M.; Weisman, R. B. Advanced Sorting of Single-Walled Carbon Nanotubes by Nonlinear Density-Gradient Ultracentrifugation. *Nat. Nanotechnol.* **2010**, *5* (6), 443–450.
- (44) Flavel, B. S.; Kappes, M. M.; Krupke, R.; Hennrich, F. Separation of Single-Walled Carbon Nanotubes by 1-Dodecanol-Mediated Size-Exclusion Chromatography. *ACS Nano* **2013**, *7* (4), 3557–3564.
- (45) Liu, H.; Nishide, D.; Tanaka, T.; Kataura, H. Large-Scale Single-Chirality Separation of Single-Wall Carbon Nanotubes by Simple Gel Chromatography. *Nat. Commun.* **2011**, *2*, 309.
- (46) Liu, H.; Tanaka, T.; Urabe, Y.; Kataura, H. High-Efficiency Single-Chirality Separation of Carbon Nanotubes Using Temperature-Controlled Gel Chromatography. *Nano Lett.* **2013**, *13* (5), 1996–2003.
- (47) Tanaka, T.; Liu, H.; Fujii, S.; Kataura, H. From Metal/Semiconductor Separation to Single-Chirality Separation of Single-Wall Carbon Nanotubes Using Gel. *Phys. Status Solidi RRL – Rapid Res. Lett.* **2011**, *5* (9), 301–306.
- (48) Zhang, H.; Wu, B.; Hu, W.; Liu, Y. Separation and/or Selective Enrichment of Single-Walled Carbon Nanotubes Based on Their Electronic Properties. *Chem. Soc. Rev.* **2011**, *40* (3), 1324–1336.
- (49) Williams, R. M.; Nayeem, S.; Dolash, B. D.; Sooter, L. J. The Effect of DNA-Dispersed Single-Walled Carbon Nanotubes on the Polymerase Chain Reaction. *PLOS ONE* **2014**, *9* (4), e94117.
- (50) Liang, Z.; Lao, R.; Wang, J.; Liu, Y.; Wang, L.; Huang, Q.; Song, S.; Li, G.; Fan, C. Solubilization of Single-Walled Carbon Nanotubes with Single-Stranded DNA Generated from Asymmetric PCR. *Int. J. Mol. Sci.* **2007**, *8* (7), 705–713.

- (51) Zheng, M.; Jagota, A.; Semke, E. D.; Diner, B. A.; Mclean, R. S.; Lustig, S. R.; Richardson, R. E.; Tassi, N. G. DNA-Assisted Dispersion and Separation of Carbon Nanotubes. *Nat. Mater.* **2003**, *2* (5), 338–342.
- (52) Zheng, M.; Jagota, A.; Strano, M. S.; Santos, A. P.; Barone, P.; Chou, S. G.; Diner, B. A.; Dresselhaus, M. S.; Mclean, R. S.; Onoa, G. B. Structure-Based Carbon Nanotube Sorting by Sequence-Dependent DNA Assembly. *Science* **2003**, *302*, 1545–1548.
- (53) Mayo, M. L.; Chen, Z. Q.; Kilina, S. V. Computational Studies of Nucleotide Selectivity in DNA–Carbon Nanotube Hybrids. *J. Phys. Chem. Lett.* **2012**, *3* (19), 2790–2797.
- (54) Mayo, M. L.; Hogle, D.; Yilmaz, B.; Köse, M. E.; Kilina, S. Morphology and Dispersion of Polycarbazole Wrapped Carbon Nanotubes. *RSC Adv.* **2013**, *3* (43), 20492–20502.
- (55) Furmanchuk, A.; Leszczynski, J.; Tretiak, S.; Kilina, S. V. Morphology and Optical Response of Carbon Nanotubes Functionalized by Conjugated Polymers. *J. Phys. Chem. C* **2012**, *116* (12), 6831–6840.
- (56) Gomulya, W.; Costanzo, G. D.; de Carvalho, E. J. F.; Bisri, S. Z.; Derenskyi, V.; Fritsch, M.; Fröhlich, N.; Allard, S.; Gordiichuk, P.; Herrmann, A.; et al. Semiconducting Single-Walled Carbon Nanotubes on Demand by Polymer Wrapping. *Adv. Mater.* **2013**, *25* (21), 2948–2956.
- (57) Hwang, J.-Y.; Nish, A.; Doig, J.; Douven, S.; Chen, C.-W.; Chen, L.-C.; Nicholas, R. J. Polymer Structure and Solvent Effects on the Selective Dispersion of Single-Walled Carbon Nanotubes. *J. Am. Chem. Soc.* **2008**, *130* (11), 3543–3553.
- (58) Ozawa, H.; Ide, N.; Fujigaya, T.; Niidome, Y.; Nakashima, N. One-Pot Separation of Highly Enriched (6,5)-Single-Walled Carbon Nanotubes Using a Fluorene-Based Copolymer. *Chem. Lett.* **2011**, *40* (3), 239–241.

- (59) Mistry, K. S.; Larsen, B. A.; Blackburn, J. L. High-Yield Dispersions of Large-Diameter Semiconducting Single-Walled Carbon Nanotubes with Tunable Narrow Chirality Distributions. *ACS Nano* **2013**, *7* (3), 2231–2239.
- (60) Gomulya, W.; Gao, J.; Loi, M. A. Conjugated Polymer-Wrapped Carbon Nanotubes: Physical Properties and Device Applications. *Eur. Phys. J. B* **2013**, *86* (10).
- (61) Liu, C.-X.; Choi, J.-W. Improved Dispersion of Carbon Nanotubes in Polymers at High Concentrations. *Nanomaterials* **2012**, *2*, 329–347.
- (62) Berton, N.; Lemasson, F.; Poschlad, A.; Meded, V.; Tristram, F.; Wenzel, W.; Hennrich, F.; Kappes, M. M.; Mayor, M. Selective Dispersion of Large-Diameter Semiconducting Single-Walled Carbon Nanotubes with Pyridine-Containing Copolymers. *Small* **2014**, *10* (2), 360–367.
- (63) Minoia, A.; Chen, L.; Beljonne, D.; Lazzaroni, R. Molecular Modeling Study of the Structure and Stability of Polymer/Carbon Nanotube Interfaces. *Polymer* **2012**, *53* (24), 5480–5490.
- (64) Haghghatpanah, S.; Bolton, K. Molecular-Level Computational Studies of Single Wall Carbon Nanotube–polyethylene Composites. *Comput. Mater. Sci.* **2013**, *69*, 443–454.
- (65) Bohlén, M.; Bolton, K. Molecular Dynamics Studies of the Influence of Single Wall Carbon Nanotubes on the Mechanical Properties of Poly(Vinylidene Fluoride). *Comput. Mater. Sci.* **2013**, *68*, 73–80.
- (66) Zheng, Q.; Xue, Q.; Yan, K.; Hao, L.; Li, Q.; Gao, X. Investigation of Molecular Interactions between SWNT and Polyethylene/Polypropylene/Polystyrene/Polyaniline Molecules. *J. Phys. Chem. C* **2007**, *111* (12), 4628–4635.
- (67) Gerstel, P.; Klumpp, S.; Hennrich, F.; Poschlad, A.; Meded, V.; Blasco, E.; Wenzel, W.; Kappes, M. M.; Barner-Kowollik, C. Highly Selective Dispersion of Single-Walled Carbon

Nanotubes via Polymer Wrapping: A Combinatorial Study via Modular Conjugation. *ACS Macro Lett.* **2014**, *3* (1), 10–15.

(68) Gurevitch, I.; Srebnik, S. Monte Carlo Simulation of Polymer Wrapping of Nanotubes. *Chem. Phys. Lett.* **2007**, *444* (1–3), 96–100.

(69) Yang, H.; Bezugly, V.; Kunstmann, J.; Filoramo, A.; Cuniberti, G. Diameter-Selective Dispersion of Carbon Nanotubes via Polymers: A Competition between Adsorption and Bundling. *ACS Nano* **2015**, *9* (9), 9012–9019.

(70) Kongkanand, A.; Martínez Domínguez, R.; Kamat, P. V. Single Wall Carbon Nanotube Scaffolds for Photoelectrochemical Solar Cells. Capture and Transport of Photogenerated Electrons. *Nano Lett.* **2007**, *7* (3), 676–680.

(71) Dang, X.; Yi, H.; Ham, M.-H.; Qi, J.; Yun, D. S.; Ladewski, R.; Strano, M. S.; Hammond, P. T.; Belcher, A. M. Virus-Templated Self-Assembled Single-Walled Carbon Nanotubes for Highly Efficient Electron Collection in Photovoltaic Devices. *Nat. Nanotechnol.* **2011**, *6* (6), 377–384.

(72) Kaur, R.; Priya, N.; Deep, A. Improved Performance of Carbon Nanotubes—manganese Doped Cadmium Sulfide Quantum Dot Nanocomposite Based Solar Cell. *Mater. Res. Express* **2016**, *3* (1), 015501.

(73) Kilina, S.; Ramirez, J.; Tretiak, S. Brightening of the Lowest Exciton in Carbon Nanotubes via Chemical Functionalization. *Nano Lett.* **2012**, *12* (5), 2306–2312.

(74) Aurore Denneulin and Julien Bras and Anne Blayo and Bertine Khelifi and Francine Roussel-Dherbey and Charles, N. The Influence of Carbon Nanotubes in Inkjet Printing of Conductive Polymer Suspensions. *Nanotechnology* **2009**, *20*, 385701.

- (75) Kourkouli, S. N.; Siokou, A.; Stefopoulos, A. A.; Ravani, F.; Plocke, T.; Müller, M.; Maultzsch, J.; Thomsen, C.; Papagelis, K.; Kallitsis, J. K. Electronic Properties of Semiconducting Polymer-Functionalized Single Wall Carbon Nanotubes. *Macromolecules* **2013**, *46*, 2590–2598.
- (76) Yoon, S.-M.; Kim, U. J.; Benayad, A.; Lee, I. H.; Son, H.; Shin, H.-J.; Choi, W. M.; Lee, Y. H.; Jin, Y. W.; Lee, E.-H. Thermal Conversion of Electronic and Electrical Properties of AuCl₃-Doped Single-Walled Carbon Nanotubes. *Acs Nano* **2011**, *5*, 1353–1359.
- (77) Stylianakis, M. M.; Mikroyannidis, J. A.; Kymakis, E. A Facile, Covalent Modification of Single-Wall Carbon Nanotubes by Thiophene for Use in Organic Photovoltaic Cells. *Sol. Energy Mater. Sol. Cells* **2010**, *94* (2), 267–274.
- (78) Lafuente, E.; Callejas, M. A.; Sainz, R.; Benito, A. M.; Maser, W. K.; Sanjuán, M. L.; Saurel, D.; de Teresa, J. M.; Martínez, M. T. The Influence of Single-Walled Carbon Nanotube Functionalization on the Electronic Properties of Their Polyaniline Composites. *Carbon* **2008**, *46* (14), 1909–1917.
- (79) Ramanathan, T.; Fisher, F. T.; Ruoff, R. S.; Brinson, L. C. Amino-Functionalized Carbon Nanotubes for Binding to Polymers and Biological Systems. *Chem. Mater.* **2005**, *17* (6), 1290–1295.
- (80) Zeng, L.; Alemany, L. B.; Edwards, C. L.; Barron, A. R. Demonstration of Covalent Sidewall Functionalization of Single Wall Carbon Nanotubes by NMR Spectroscopy: Side Chain Length Dependence on the Observation of the Sidewall Sp³. *Nano Res.* **2008**, *1* (1), 72–88.
- (81) Moradi, O.; Zare, K.; Monajjemi, M.; Yari, M.; Aghaie, H. The Studies of Equilibrium and Thermodynamic Adsorption of Pb (II), Cd (II) and Cu (II) Ions from Aqueous Solution onto

SWCNTs and SWCNT–COOH Surfaces. *Fuller. Nanotub. Carbon Nanostructures* **2010**, *18*, 285–302.

(82) Shirsat, M. D.; Sarkar, T.; Kakoullis Jr, J.; Myung, N. V.; Konnanath, B.; Spanias, A.; Mulchandani, A. Porphyrin-Functionalized Single-Walled Carbon Nanotube Chemiresistive Sensor Arrays for VOCs. *J. Phys. Chem. C* **2012**, *116*, 3845–3850.

(83) Zhao, H.; Zhu, Y.; Chen, C.; He, L.; Zheng, J. Synthesis, Characterization, and Photophysical Properties of Covalent-Linked Ferrocene–porphyrin–single-Walled Carbon Nanotube Triad Hybrid. *Carbon* **2012**, *50*, 4894–4902.

(84) Kong, H.; Gao, C.; Yan, D. Controlled Functionalization of Multiwalled Carbon Nanotubes by in Situ Atom Transfer Radical Polymerization. *J. Am. Chem. Soc.* **2004**, *126*, 412–413.

(85) Gao, J.; Zhao, B.; Itkis, M. E.; Bekyarova, E.; Hu, H.; Kranak, V.; Yu, A.; Haddon, R. C. Chemical Engineering of the Single-Walled Carbon Nanotube–Nylon 6 Interface. *J. Am. Chem. Soc.* **2006**, *128*, 7492–7496.

(86) Koromilas, N. D.; Lainioti, G. C.; Gialeli, C.; Barbouri, D.; Kouravelou, K. B.; Karamanos, N. K.; Voyiatzis, G. A.; Kallitsis, J. K. Preparation and Toxicological Assessment of Functionalized Carbon Nanotube-Polymer Hybrids. *PloS One* **2014**, *9*, e107029.

(87) Dwyer, C.; Guthold, M.; Falvo, M.; Washburn, S.; Superfine, R.; Erie, D. DNA-Functionalized Single-Walled Carbon Nanotubes. *Nanotechnology* **2002**, *13*, 601.

(88) Katti, D. R.; Sharma, A.; Pradhan, S. M.; Katti, K. S. Carbon Nanotube Proximity Influences Rice DNA. *Chem. Phys.* **2015**, *455*, 17–22.

- (89) Kum, M. C.; Joshi, K. A.; Chen, W.; Myung, N. V.; Mulchandani, A. Biomolecules-Carbon Nanotubes Doped Conducting Polymer Nanocomposites and Their Sensor Application. *Talanta* **2007**, *74*, 370–375.
- (90) He, H.; Pham-Huy, L. A.; Dramou, P.; Xiao, D.; Zuo, P.; Pham-Huy, C. Carbon Nanotubes: Applications in Pharmacy and Medicine. *BioMed Res. Int.* **2013**, *2013*.
- (91) Lvova, L.; Mastroianni, M.; Pomarico, G.; Santonico, M.; Pennazza, G.; Di Natale, C.; Paolesse, R.; D'Amico, A. Carbon Nanotubes Modified with Porphyrin Units for Gaseous Phase Chemical Sensing. *Sens. Actuators B Chem.* **2012**, *170*, 163–171.
- (92) Ghosh, S.; Bachilo, S. M.; Simonette, R. A.; Beckingham, K. M.; Weisman, R. B. Oxygen Doping Modifies Near-Infrared Band Gaps in Fluorescent Single-Walled Carbon Nanotubes. *Science* **2010**, *330* (6011), 1656–1659.
- (93) Ma, X.; Adamska, L.; Yamaguchi, H.; Yalcin, S. E.; Tretiak, S.; Doorn, S. K.; Htoon, H. Electronic Structure and Chemical Nature of Oxygen Dopant States in Carbon Nanotubes. *ACS Nano* **2014**, *8* (10), 10782–10789.
- (94) Miyauchi, Y.; Iwamura, M.; Mouri, S.; Kawazoe, T.; Ohtsu, M.; Matsuda, K. Brightening of Excitons in Carbon Nanotubes on Dimensionality Modification. *Nat. Photonics* **2013**, *7* (9), 715–719.
- (95) Hartmann, N. F.; Yalcin, S. E.; Adamska, L.; H  roz, E. H.; Ma, X.; Tretiak, S.; Htoon, H.; Doorn, S. K. Photoluminescence Imaging of Solitary Dopant Sites in Covalently Doped Single-Wall Carbon Nanotubes. *Nanoscale* **2015**, *7* (48), 20521–20530.
- (96) Kuzmany, H.; Kukovecz, A.; Simon, F.; Holzweber, M.; Kramberger, C.; Pichler, T. Functionalization of Carbon Nanotubes. *Synth. Met.* **2004**, *141*, 113–122.

- (97) Kar, T.; Scheiner, S.; Roy, A. K. The Effect on Acidity of Size and Shape of Carboxylated Single-Wall Carbon Nanotubes. A DFT-SLDB Study. *Chem. Phys. Lett.* **2008**, *460*, 225–229.
- (98) Wongchoosuk, C.; Udomvech, A.; Kerdcharoen, T. The Geometrical and Electronic Structures of Open-End Fully Functionalized Single-Walled Carbon Nanotubes. *Curr. Appl. Phys.* **2009**, *9*, 352–358.
- (99) Kar, T.; Scheiner, S.; Patnaik, S. S.; Bettinger, H. F.; Roy, A. K. IR Characterization of Tip-Functionalized Single-Wall Carbon Nanotubes. *J. Phys. Chem. C* **2010**, *114*, 20955–20961.
- (100) Kar, T.; Akdim, B.; Duan, X.; Pachter, R. Open-Ended Modified Single-Wall Carbon Nanotubes: A Theoretical Study of the Effects of Purification. *Chem. Phys. Lett.* **2006**, *423*, 126–130.
- (101) Salzmann, C. G.; Llewellyn, S. A.; Tobias, G.; Ward, M. A.; Huh, Y.; Green, M. L. The Role of Carboxylated Carbonaceous Fragments in the Functionalization and Spectroscopy of a Single-Walled Carbon-Nanotube Material. *Adv. Mater.* **2007**, *19*, 883–887.
- (102) Mawhinney, D. B.; Naumenko, V.; Kuznetsova, A.; Yates, J. T.; Liu, J.; Smalley, R. E. Infrared Spectral Evidence for the Etching of Carbon Nanotubes: Ozone Oxidation at 298 K. *J. Am. Chem. Soc.* **2000**, *122*, 2383–2384.
- (103) Mazzoni, M. S. C.; Chacham, H.; Ordejón, P.; Sánchez-Portal, D.; Soler, J. M.; Artacho, E. Energetics of the Oxidation and Opening of a Carbon Nanotube. *Phys. Rev. B* **1999**, *60*, R2208–R2211.
- (104) Chelmecka, E.; Pasterny, K.; Kupka, T.; Stobinski, L. DFT Studies of OH-Functionalized Open-Ended Zigzag, Armchair, and Chiral Single Wall Carbon Nanotubes. *Phys. Status Solidi - Appl. Mater. Sci.* **2011**, *208*, 1774–1777.

- (105) Balasubramanian, K.; Burghard, M. Chemically Functionalized Carbon Nanotubes. *Small* **2005**, *1*, 180–192.
- (106) Hirsch, A.; Vostrowsky, O. Functionalization of Carbon Nanotubes. In *Functional molecular nanostructures*; Springer, 2005; pp 193–237.
- (107) Kilina, S.; Kilin, D.; Tretiak, S. Light-Driven and Phonon-Assisted Dynamics in Organic and Semiconductor Nanostructures. *Chem. Rev.* **2015**, *115*, 5929–5978.
- (108) Mickelson, E. T.; Huffman, C. B.; Rinzler, A. G.; Smalley, R. E.; Hauge, R. H.; Margrave, J. L. Fluorination of Single-Wall Carbon Nanotubes. *Chem. Phys. Lett.* **1998**, *296* (1–2), 188–194.
- (109) Khabashesku, V. N.; Billups, W. E.; Margrave, J. L. Fluorination of Single-Wall Carbon Nanotubes and Subsequent Derivatization Reactions. *Acc. Chem. Res.* **2002**, *35* (12), 1087–1095.
- (110) Alemany, L. B.; Zhang, L.; Zeng, L.; Edwards, C. L.; Barron, A. R. Solid-State NMR Analysis of Fluorinated Single-Walled Carbon Nanotubes: Assessing the Extent of Fluorination. *Chem. Mater.* **2007**, *19* (4), 735–744.
- (111) Hirsch, A. Functionalization of Single-Walled Carbon Nanotubes. *Angew. Chem. Int. Ed.* **2002**, *41* (11), 1853.
- (112) Abdelkader, V. K.; Scelfo, S.; García-Gallarín, C.; Godino-Salido, M. L.; Domingo-García, M.; López-Garzón, F. J.; Pérez-Mendoza, M. Carbon Tetrachloride Cold Plasma for Extensive Chlorination of Carbon Nanotubes. *J. Phys. Chem. C* **2013**, *117* (32), 16677–16685.
- (113) Abdelkader, V. K.; Domingo-García, M.; Gutiérrez-Valero, M. D.; López-Garzón, R.; Melguizo, M.; García-Gallarín, C.; Lopez-Garzon, F. J.; Pérez-Mendoza, M. J. Sidewall Chlorination of Carbon Nanotubes by Iodine Trichloride. *J. Phys. Chem. C* **2014**, *118* (5), 2641–2649.

- (114) Erbahar, D.; Berber, S. Chlorination of Carbon Nanotubes. *Phys. Rev. B* **2012**, *85* (8), 085426.
- (115) Pełech, I.; Pelech, R.; Narkiewicz, U.; Moszyński, D.; Jędrzejewska, A.; Witkowski, B. Chlorination of Carbon Nanotubes Obtained on the Different Metal Catalysts. *J. Nanomater.* **2013**, *2013*, 1–9.
- (116) Osikoya, A. O.; Dikio, C. W.; Ayawei, N.; Wankasi, D.; Afolabi, A. S.; Dikio, E. D. Synthesis, Characterization and Adsorption Studies of Chlorine-doped Carbon Nanotubes. *Adv. Mater. Sci. Appl.* **2015**, *4* (2), 53–62.
- (117) Oliveira, L.; Lu, F.; Andrews, L.; Takacs, G. A.; Mehan, M.; Debies, T. UV Photo-Chlorination and -Bromination of Single-Walled Carbon Nanotubes. *J. Mater. Res.* **2014**, *29* (02), 239–246.
- (118) Lee, I. H.; Kim, U. J.; Son, H. B.; Yoon, S.-M.; Yao, F.; Yu, W. J.; Duong, D. L.; Choi, J.-Y.; Kim, J. M.; Lee, E. H.; et al. Hygroscopic Effects on AuCl₃-Doped Carbon Nanotubes. *J. Phys. Chem. C* **2010**, *114* (26), 11618–11622.
- (119) Yoon, S.-M.; Kim, U. J.; Benayad, A.; Lee, I. H.; Son, H.; Shin, H.-J.; Choi, W. M.; Lee, Y. H.; Jin, Y. W.; Lee, E.-H.; et al. Thermal Conversion of Electronic and Electrical Properties of AuCl₃-Doped Single-Walled Carbon Nanotubes. *ACS Nano* **2011**, *5* (2), 1353–1359.
- (120) Kim, S. M.; Kim, K. K.; Jo, Y. W.; Park, M. H.; Chae, S. J.; Duong, D. L.; Yang, C. W.; Kong, J.; Lee, Y. H. Role of Anions in the AuCl₃-Doping of Carbon Nanotubes. *ACS Nano* **2011**, *5* (2), 1236–1242.
- (121) Murat, A.; Rungger, I.; Jin, C.; Sanvito, S.; Schwingenschlögl, U. Origin of the P-Type Character of AuCl₃ Functionalized Carbon Nanotubes. *J. Phys. Chem. C* **2014**, *118* (6), 3319–3323.

- (122) Pan, H.; Feng, Y. P.; Lin, J. Y. Ab Initio Study of F- and Cl-Functionalized Single Wall Carbon Nanotubes. *J. Phys. Condens. Matter* **18**.
- (123) Duong, D. L.; Lee, I. H.; Kim, K. K.; Kong, J.; Lee, S. M.; Lee, Y. H. Carbon Nanotube Doping Mechanism in a Salt Solution and Hygroscopic Effect: Density Functional Theory. *ACS Nano* **2010**, *4* (9), 5430–5436.
- (124) Saha, S.; Dinadayalane, T. C.; Murray, J. S.; Leszczynska, D.; Leszczynski, J. Surface Reactivity for Chlorination on Chlorinated (5,5) Armchair SWCNT: A Computational Approach. *J. Phys. Chem. C* **2012**, *116* (42), 22399–22410.
- (125) Piao, Y.; Meany, B.; Powell, L. R.; Valley, N.; Kwon, H.; Schatz, G. C.; Wang, Y. Brightening of Carbon Nanotube Photoluminescence through the Incorporation of Sp³ Defects. *Nat. Chem.* **2013**, *5* (10), 840–845.
- (126) Shiraki, T.; Shiraishi, T.; Juhász, G.; Nakashima, N. Emergence of New Red-Shifted Carbon Nanotube Photoluminescence Based on Proximal Doped-Site Design. *Sci. Rep.* **2016**, *6*, 28393.
- (127) Kim, M.; Adamska, L.; Hartmann, N. F.; Kwon, H.; Liu, J.; Velizhanin, K. A.; Piao, Y.; Powell, L. R.; Meany, B.; Doorn, S. K.; et al. Fluorescent Carbon Nanotube Defects Manifest Substantial Vibrational Reorganization. *J. Phys. Chem. C* **2016**, *120* (20), 11268–11276.
- (128) Hartmann, N. F.; Velizhanin, K. A.; Haroz, E. H.; Kim, M.; Ma, X.; Wang, Y.; Htoon, H.; Doorn, S. K. Photoluminescence Dynamics of Aryl Sp³ Defect States in Single-Walled Carbon Nanotubes. *ACS Nano* **2016**, *10* (9), 8355–8365.
- (129) He, X.; Hartmann, N. F.; Ma, X.; Kim, Y.; Ihly, R.; Blackburn, J. L.; Gao, W.; Kono, J.; Yomogida, Y.; Hirano, A. Tunable Room-Temperature Single-Photon Emission at Telecom Wavelengths from Sp³ Defects in Carbon Nanotubes. *Nat. Photonics* **2017**, nphoton. 2017.119.

- (130) He, X.; Gifford, B. J.; Hartmann, N. F.; Ihly, R.; Ma, X.; Kilina, S. V.; Luo, Y.; Shayan, K.; Strauf, S.; Blackburn, J. L.; et al. Low-Temperature Single Carbon Nanotube Spectroscopy of Sp^3 Quantum Defects. *ACS Nano* **2017**.
- (131) Adamska, L.; Nayyar, I.; Chen, H.; Swan, A. K.; Oldani, N.; Fernandez-Alberti, S.; Golder, M. R.; Jasti, R.; Doorn, S. K.; Tretiak, S. Self-Trapping of Excitons, Violation of Condon Approximation, and Efficient Fluorescence in Conjugated Cycloparaphenylenes. *Nano Lett.* **2014**, *14* (11), 6539–6546.
- (132) Ramirez, J.; Mayo, M. L.; Kilina, S.; Tretiak, S. Electronic Structure and Optical Spectra of Semiconducting Carbon Nanotubes Functionalized by Diazonium Salts. *Chem. Phys.* **2013**, *413*, 89–101.
- (133) Kilina, S.; Ramirez, J.; Tretiak, S. Brightening of the Lowest Exciton in Carbon Nanotubes via Chemical Functionalization. *Nano Lett.* **2012**, *12* (5), 2306–2312.
- (134) Chang, R. *Chemistry*, 10th ed.; McGraw-Hill: Boston, 2010.
- (135) Phys. Rev. 28, 1049 (1926) - An Undulatory Theory of the Mechanics of Atoms and Molecules <https://journals.aps.org/pr/abstract/10.1103/PhysRev.28.1049> (accessed Nov 12, 2017).
- (136) Zur Quantentheorie der Molekeln - Born - 1927 - Annalen der Physik - Wiley Online Library <http://onlinelibrary.wiley.com/doi/10.1002/andp.19273892002/abstract;jsessionid=0A55C3B24223E8DC78BDF4DD42F8D9D0.f04t02> (accessed Nov 12, 2017).
- (137) Dewar, M. J.; Zoebisch, E. G.; Healy, E. F.; Stewart, J. J. Development and Use of Quantum Mechanical Molecular Models. 76. AM1: A New General Purpose Quantum Mechanical Molecular Model. *J. Am. Chem. Soc.* **1985**, *107*, 3902–3909.

- (138) Ridley, J.; Zerner, M. An Intermediate Neglect of Differential Overlap Technique for Spectroscopy: Pyrrole and the Azines. *Theor. Chim. Acta* **1973**, *32* (2), 111–134.
- (139) Kilina, S.; Tretiak, S. Excitonic and Vibrational Properties of Single-Walled Semiconducting Carbon Nanotubes. *Adv. Funct. Mater.* **2007**, *17* (17), 3405–3420.
- (140) Hohenberg, P.; Kohn, W. Inhomogeneous Electron Gas. *Phys. Rev.* **1964**, *136* (3B), B864–B871.
- (141) Kohn, W.; Sham, L. J. Self-Consistent Equations Including Exchange and Correlation Effects. *Phys. Rev.* **1965**, *140* (4A), A1133–A1138.
- (142) Cramer, C. J. *Essentials of Computational Chemistry: Theories and Models*, 2nd ed.; Wiley: Chichester, West Sussex, England ; Hoboken, NJ, 2004.
- (143) Becke, A. D. Density-functional Thermochemistry. III. The Role of Exact Exchange. *J. Chem. Phys.* **1993**, *98* (7), 5648–5652.
- (144) Vosko, S. H.; Wilk, L.; Nusair, M. Accurate Spin-Dependent Electron Liquid Correlation Energies for Local Spin Density Calculations: A Critical Analysis. *Can. J. Phys.* **1980**, *58*, 1200–1211.
- (145) Stephens, P. J.; Devlin, F. J.; Chabalowski, C. F.; Frisch, M. J. Ab Initio Calculation of Vibrational Absorption and Circular Dichroism Spectra Using Density Functional Force Fields. *J. Phys. Chem.* **1994**, *98*, 11623–11627.
- (146) Yanai, T.; Tew, D. P.; Handy, N. C. A New Hybrid Exchange–correlation Functional Using the Coulomb-Attenuating Method (CAM-B3LYP). *Chem. Phys. Lett.* **2004**, *393* (1–3), 51–57.
- (147) Milowska, K. Z.; Majewski, J. A. Functionalization of Carbon Nanotubes With-CH,-NH Fragments,-COOH and-OH Groups. *ArXiv Prepr. ArXiv12091535* **2012**.

- (148) Brothers, E. N.; Izmaylov, A. F.; Normand, J. O.; Barone, V.; Scuseria, G. E. Accurate Solid-State Band Gaps via Screened Hybrid Electronic Structure Calculations. *J. Chem. Phys.* **2008**, *129* (1), 011102.
- (149) Kryjevski, A.; Gifford, B.; Kilina, S.; Kilin, D. Theoretical Predictions on Efficiency of Bi-Exciton Formation and Dissociation in Chiral Carbon Nanotubes. *J. Chem. Phys.* **2016**, *145* (15), 154112.
- (150) Kryjevski, A.; Mihaylov, D.; Gifford, B.; Kilin, D. Singlet Fission in Chiral Carbon Nanotubes: Density Functional Theory Based Computation. *J. Chem. Phys.* **2017**, *147* (3), 034106.
- (151) Runge, E.; Gross, E. K. Density-Functional Theory for Time-Dependent Systems. *Phys. Rev. Lett.* **1984**, *52*, 997.
- (152) Wang, H.; Wang, H.; Chen, Y.; Liu, Y.; Zhao, J.; Cai, Q.; Wang, X. Phosphorus-Doped Graphene and (8, 0) Carbon Nanotube: Structural, Electronic, Magnetic Properties, and Chemical Reactivity. *Appl. Surf. Sci.* **2013**, *273*, 302–309.
- (153) Kumar, D.; Singh, K.; Verma, V.; Bhatti, H. S. Investigation of Optical Properties of Pristine and Functionalized Single-Walled Carbon Nanotubes. *J. Mater. Sci. Mater. Electron.* 1–10.
- (154) Piao, Y.; Meany, B.; Powell, L. R.; Valley, N.; Kwon, H.; Schatz, G. C.; Wang, Y. Brightening of Carbon Nanotube Photoluminescence through the Incorporation of Sp³ Defects. *Nat. Chem.* **2013**, *5* (10), 840–845.

2. SINGLE WALLED CARBON NANOTUBE – POLYMER SIDECHAIN INTERACTIONS AND MORPHOLOGY

2.1. Motivation

In the quest for new materials for use in modern electronic applications, single walled carbon nanotubes (SWCNTs) stand out due to their chirality dependent electronic and optical properties. However, current synthetic methods are unable to produce SWCNTs of a specific geometry. As a result, post-synthetic separation methods are relied upon to generate samples suitable for use in such applications. This involves covering the surface with a surfactant with multiple structural components, one of which interacts well with the SWCNT and another that interacts well with the solvent. One such surfactant is poly(9,9-di-n-octylfluorenyl-2,7-diyl) (PFO) yielding octyl alkyl chains, which selectively dissolves and disperses SWCNTs of certain chiralities. As such, it is imperative to understand the mechanism of binding of these polymers to SWCNTs. Additionally, the electronic structure of such composites is of computational interest for evaluation of their performance in devices. It is commonly thought that the predominant interaction between the SWCNT and polymer chain is the π - π stacking, while the weaker van der Waals interactions are frequently neglected. While the sidechains are not expected to contribute much to the electronic structure of SWCNT-polymer composites, the current study demonstrates that their effect on the morphology of such systems is significant. Short sidechains introduce additional van der Waals interactions to the system, while moderate length sidechains distort the geometry of the polymer backbone resulting in destruction of π - π stacking and therefore decrease the overall interaction. Sidechains longer than octyl induce a shift in angle about which the polymer wraps the SWCNT and therefore decreases the binding energy further. This new information suggests that using polymers modified to possess different

length sidechains may be an effective strategy for introducing diameter-specific interactions and selectivity. In this chapter, the precise morphology of the polymer with varying length sidechains in composite systems with SWCNTs is explored and found to be dependent on a complex interplay between Vander Waals and π - π interactions.

2.2. Computational Methodology

2.2.1. Reparametrizing the Force Field

In order to accurately model the morphologies of SWCNT-PFO systems using molecular mechanics, the interactions in the model must first sufficiently mimic those interactions in the real system. This is generally accomplished by substituting parameters in an existing force field with new values that result in agreement between the molecular mechanics calculations that utilize them and higher level theory or experiment. In this case, reparameterization was accomplished by optimizing the geometry of an oligomer containing five unit cells of PFO monomer with alkyl side chains substituted by methyl groups ($m=5$, total length 41.4 Å, figure 2.1a) in vacuum using density functional theory (DFT) and parameterizing based on the geometry of the most central unit. This unit is sufficiently distant from the ends of the oligomer chain that end effects shouldn't significantly perturb the geometry. These calculations were performed using Gaussian09 software¹ and the B3LYP functional²⁻⁴ with a 6-31G* basis set.⁵⁻⁷ Alkyl chains were replaced with methyl ($n=1$) for DFT calculations because it is assumed that this substitution won't change the electronic structure by a significant degree and that sidechains don't play a significant role in perturbing the geometry of the backbone in the pristine polymer since π - π interactions dominate. This assumption is particularly valid when the side groups are spaced as distantly as possible to minimize steric effects and torsional strain. As such, the initial configuration was assembled in a head-to-tail manner to place the side chains on adjacent

monomer units on alternating sides of the polymer backbone. Once the geometry of this system was determined using DFT, the MM3 force field⁸⁻¹¹ was reparametrized to match the geometry of this ab-initio computed system. The Tinker software package¹² was utilized for all molecular mechanics calculations. While the default MM3 force field accurately predicted the geometry for the majority of the system, necessary adjustment of the parameters controlling the dihedral angle between monomer units to match the 37.5° predicted by DFT (figure 2.1c) as well as the bond length between two sp² hybridized carbon atoms in five membered rings was performed.

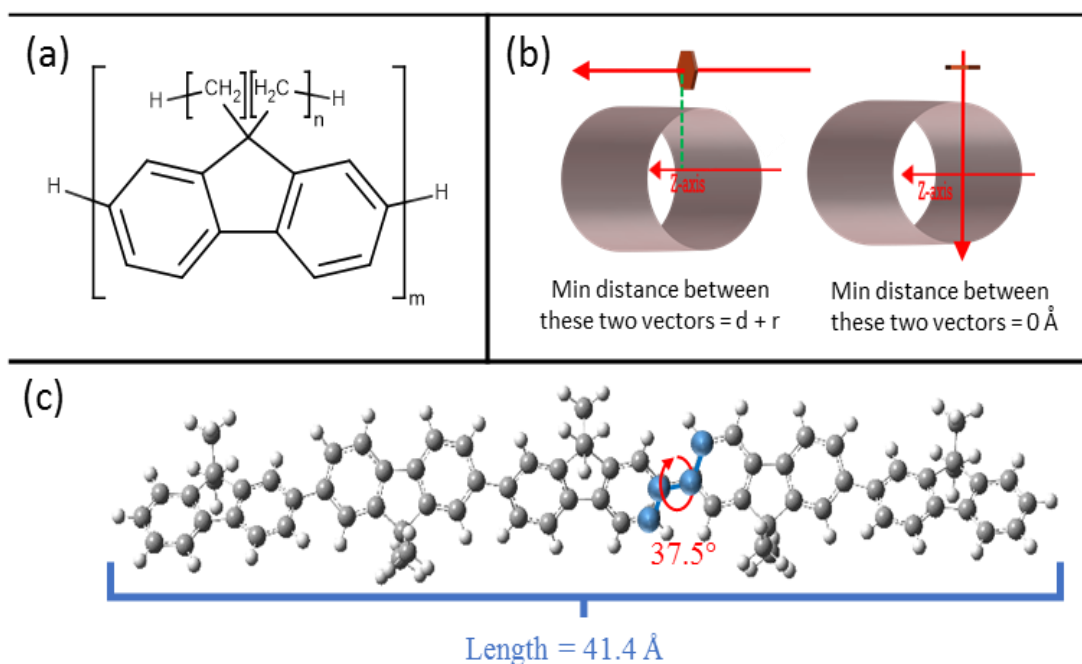


Figure 2.1. (a) A single unit of monomer for poly(9,9-di-*n*-octylfluorenyl-2,7-diyl) (PFO) where n represents the number of methylene groups in the alkyl side chain and m represents the degree of polymerization, (b) the parameter used to quantify “twisting” of the polymer backbone in the SWCNT-PFO systems. A value of zero indicates that the normal vector to the polymer unit intersects with the axis of the SWCNT, thereby maximizing π - π overlap. A value of one indicates that the polymer unit is perpendicular to the surface of the SWCNT, and therefore the minimum distance between the vector normal to the unit and the SWCNT axis is equal to the radius of the SWCNT + the distance between the SWCNT and the center of mass of the polymer unit, and (c) the pentamer ($m=5$) optimized with DFT using the B3LYP functional and the 6-31G* basis set from which the force field was reparametrized. The torsion angle at the central unit of this oligomer is 37.5°.

2.2.2. Optimization of the SWCNT-PFO Composites w/ Different Length Sidechains

With accurate parameters that adequately match DFT calculations achieved, the systems of SWCNT-PFO composites were constructed and their geometry optimized. The SWCNTs were generated using Tubegen software.¹³ A single monomer was then placed on the SWCNT 2.5 Å from and parallel to the surface. This monomer was replicated and positioned to produce a polymer chain 40 units long with nine distinct wrapping configurations about the SWCNT at angles of 0 degrees to 80 degrees with respect to the SWCNT axis in 10 degree increments. This relatively large number of initial configurations was generated for each SWCNT-PFO derivative pair in order to replicate the random geometries that would be likely be produced along a lengthy and more computationally expensive molecular dynamics simulation, an approximation that was successfully implemented in numerous previous studies^{14–17}. The wrapped SWCNT geometries were optimized using molecular mechanics with the new parameter set. This was accomplished in two steps: first by freezing the SWCNT and relaxing the geometry of the polymer about the tube, and then relaxing both the SWCNT and polymer and allowing the system to relax to its final geometry. This two-step process was required to first minimize the interactions deforming the SWCNT from a “straight” geometry and thereby minimize bending of the tubes.

2.2.3. Analysis of the Binding Strengths of Polymer to SWCNT

Once the optimized geometry of the entire system was determined, the adsorption energy (E_{ads}) of the polymer to the SWCNT was determined for all geometries using the following equation:

$$E_{ads} = E_{SWCNT-PFO} - (E_{SWCNT} - E_{PFO}) \quad (\text{Equation 2.1})$$

where $E_{SWCNT-PFO}$ is the total energy of the SWCNT-PFO system, E_{SWCNT} is the energy of the optimized pristine SWCNT, and E_{PFO} is the energy of the isolated 40 unit long PFO chain

optimized from the 0-degree wrapping configuration. The morphology of only the strongest binding configuration of the SWCNT-PFO system was then characterized since these species are expected to be most predominant in real samples and will therefore play the greatest role in dissolving and dispersing the SWCNTs.

2.2.4. Analysis of the Morphologies of the Systems

A number of structural characteristics are of interest in evaluating the factors contributing to adsorption of PFO of different lengths side chains to the SWCNT surface. These include the average distance between the SWCNT and the carbon atoms of the sp^2 hybridized PFO backbone, the average distance between the SWCNT and the sp^3 hybridized atoms of the PFO sidechain, the final wrapping angle of the PFO chain about the SWCNT, and the torsion angle between PFO units in the polymer. From this data, the fraction of carbon atoms in the sidechain interacting with the SWCNT via van der Waals interactions was defined as the number of sidechain carbon atoms that were within a 5\AA distance from the surface of the SWCNT. Additionally, a further morphological parameter of the systems was defined to characterize the degree of “twisting” of the backbone along the SWCNT surface. This is necessary since optimum interaction between the polymer sidechains and the SWCNT occurs when the two are in close proximity. However, this twists the backbone away from planarity with the SWCNT surface and therefore occurs at the cost of π stacking. To define the twisting parameter, a vector normal to each monomer unit within the polymer was defined. The minimum distance between this vector and the axis of the SWCNT was then determined and divided by the distance between the center of mass of the monomer unit and the axis of the SWCNT. As such, the value of the twisting parameter ranges from zero to one where a value of zero implies the unit is aligned perfectly parallel on the surface of the SWCNT and thereby maximizes $\pi - \pi$ overlap and a value

of one implies the monomer unit is aligned completely perpendicular to the surface of the SWCNT and thereby minimizes $\pi - \pi$ overlap (see figure 2.1b for a schematic representation of this parameter). Since $\pi - \pi$ stacking requires both planar overlap *and* close proximity between the π systems, both of these criteria were evaluated to determine which units interact via this mechanism. Utilizing the measure of distance between the sp^2 hybridized backbone atoms and the SWCNT as well as the twisting on the surface, the number in monomer units of the polymer that would be expected to interact via $\pi - \pi$ interactions was determined. For this, it was assumed that a unit interacts via $\pi - \pi$ interactions if the distance between every atom in the monomer unit and the SWCNT surface is less than 4 Å *and* the twisting parameter was determined to be less than 0.4. As such, the number of polymer units that are both perpendicular to the surface of the SWCNT surface and within the distance expected for $\pi - \pi$ stacking are counted.

2.3. Evaluation of the Role of Sidechains in PFO-SWCNT Binding

The profile for the adsorption energy of the PFO with varying length alkyl chains to SWCNTs of different chiralities is complex and exhibits local maxima for binding energy with methyl side groups and octyl side groups (figure 2.2a). For the purpose of analyzing the role of sidechains, the discussion will focus on interactions in three distinct regimes: $n < 3$ (short side chains), $3 < n < 8$ (intermediate length side chains), and $n > 8$ (long side chains).

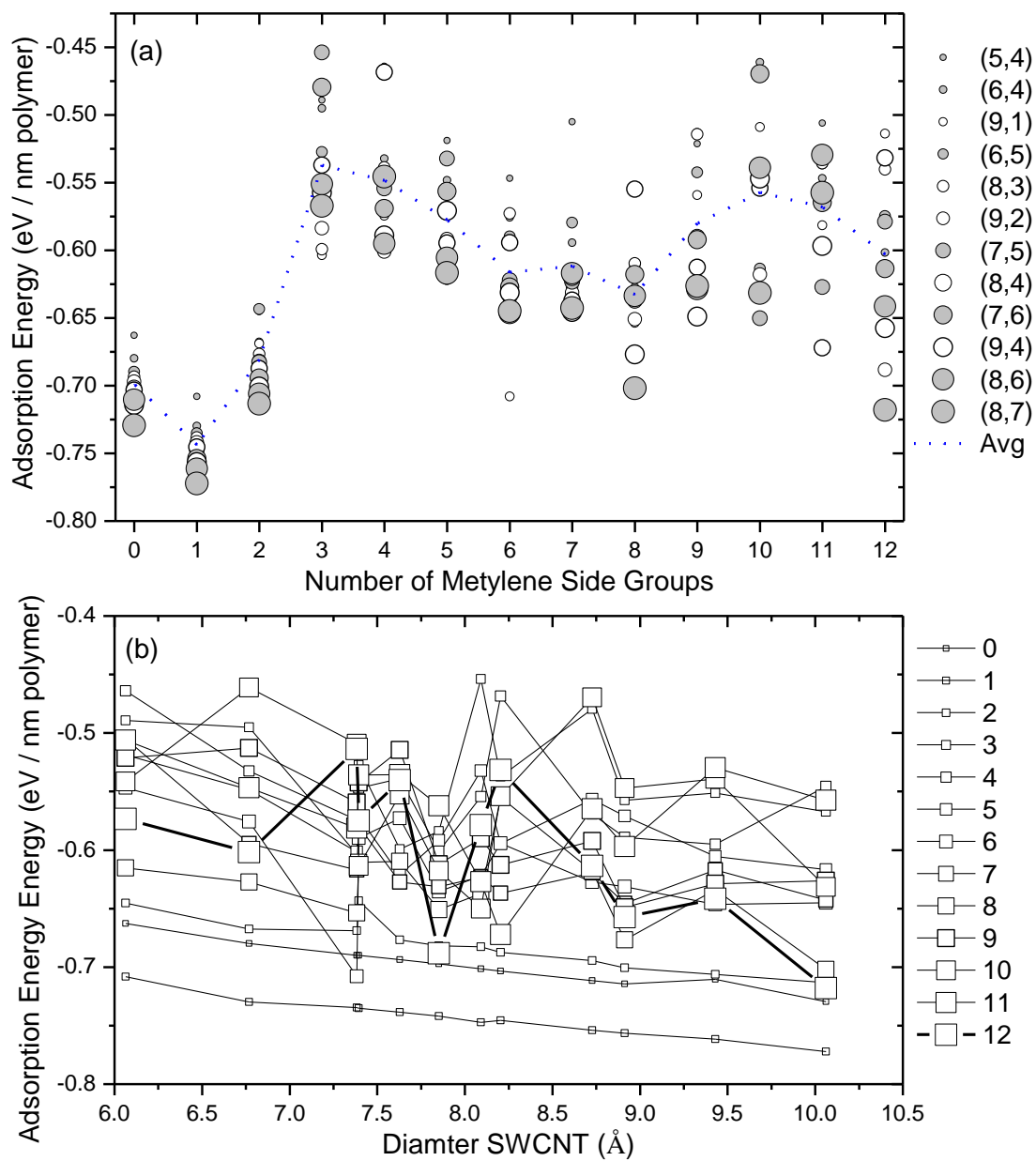


Figure 2.2. Adsorption energies per unit length of PFO to the SWCNT as a function of (a) number of methylene groups in the alkyl chain, and (b) diameter of the SWCNT. For panel a, larger circles indicate larger diameter SWCNTs, filled circles indicate a chiral angle $\theta > 20^\circ$, and empty circles indicate a chiral angle $\theta < 20^\circ$. For panel b, the size of the data point correlates to the length of the alkyl sidechain on PFO.

2.3.1. Short Alkyl Sidechains

2.3.1.1. $n=0 \rightarrow n=1$ Increased Vander Waals Interactions without a Cost

In the case of very short side chains ($n=0$ to $n=3$), the adsorption energy shows a very distinct trend where binding is more favorable for larger SWCNTs. In these cases, trends between binding and SWCNT chiral angle/electronic type are absent. This diameter dependence is the result of the ability of the polymer to adopt its most favorable conformation. In the case of small tubes, wrapping requires significant “warping” and the planar configuration of the polymer units is disrupted. In larger SWCNTs, this effect is much smaller and therefore the energy is more stable due to decreased deformation from the optimal polymer configuration. Additionally, these species with very short side chains have the smallest wrapping angles. As such, deformation from the pristine polymer geometry is minimal and the binding is the strongest.

This same effect allows composites with very short side-chains to exhibit increased stability over systems with long sidechains. For hydrogen side groups, the torsion angle within the polymer is much smaller than either in the pristine polymer or any of the other SWCNT-PFO systems, consistently taking on a value of about 24° due to the absence of steric hindrance when the PFO doesn't yield alkyl side chains. An increase of adsorption strength is observed going from $n=0$ with only a hydrogen side group to $n=1$ with the methyl side group; this effect is accompanied by a significant increase in torsion angle between the polymer units to the more favorable 32° (figure 2.3b). This change in geometry stabilizes the polymer. Additionally, the presence of a methyl group in this system allows for interaction via van der Waals interactions with the SWCNTs. Because of this interaction between the SWCNT and the methyl groups on opposite sides of the polymer backbone, the polymer chain is morphed to a less planar

configuration. Despite this, the normal vector to the monomer units alternates from one side of the SWCNT axis to the other going down the polymer chain (figure 2.4), resulting in a retention of the relatively planar geometry with respect to the SWCNT surface and strong π - π interactions. Because of this configuration, half of the methyl groups are located directionally toward the SWCNT and therefore fall within the van der Waals interaction distance (figure 2.5b) while the other half remain on the opposite side of the polymer backbone. As a result, the cumulative effect of the additional van der Waals interactions simply contributes about 0.05 eV/nm polymer to the adsorption energy. This is also the only circumstance under which a significant change in torsion angle in the polymer is observed, and for all other side chains this effect is constant as the

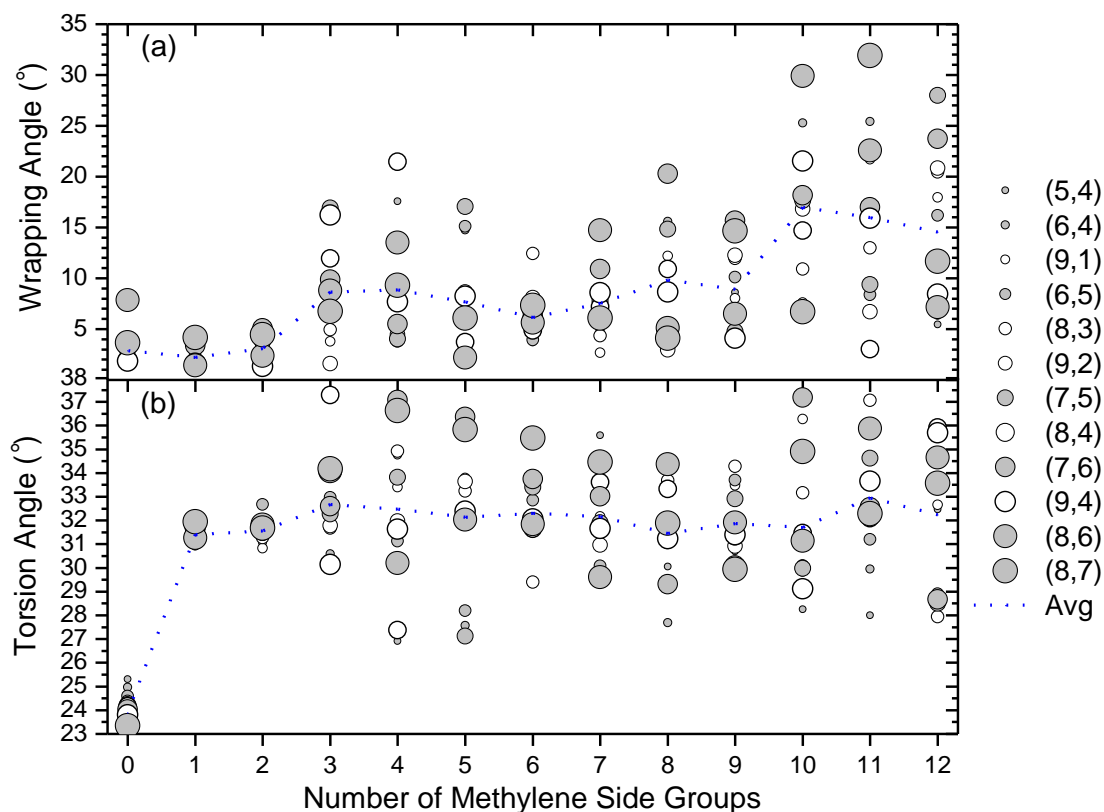


Figure 2.3. Characterization of the geometry of the PFO polymer optimized in the presence of the SWCNT, including (a) the average wrapping angle of the PFO units and (b) the average torsion angle between polymer units. Larger circles indicate larger diameter SWCNTs, filled circles indicate a chiral angle $\theta > 20^\circ$, and empty circles indicate a chiral angle $\theta < 20^\circ$

torsion angle remains approximately 32° in the presence of the SWCNT. As such, further changes to the adsorption energy profile cannot be attributed to further changes in dihedral angle of the polymer.

2.3.1.2. $n=1 \rightarrow n=3$ Vander Waals Interactions Induce Twisting & Instability

Due to their increased number, more atoms in the alkyl sidechain would be expected to interact with the SWCNT as the length of the alkyl group increases. However, the portion of sidechain atoms interacting is actually reduced as the sidechain lengthens beyond $n=1$ (figure 2.5b). This is due to simple geometrical constraints: the additional atoms in the sidechain can not interact with the SWCNT simultaneously with the atoms in the backbone. (figure 2.4). The

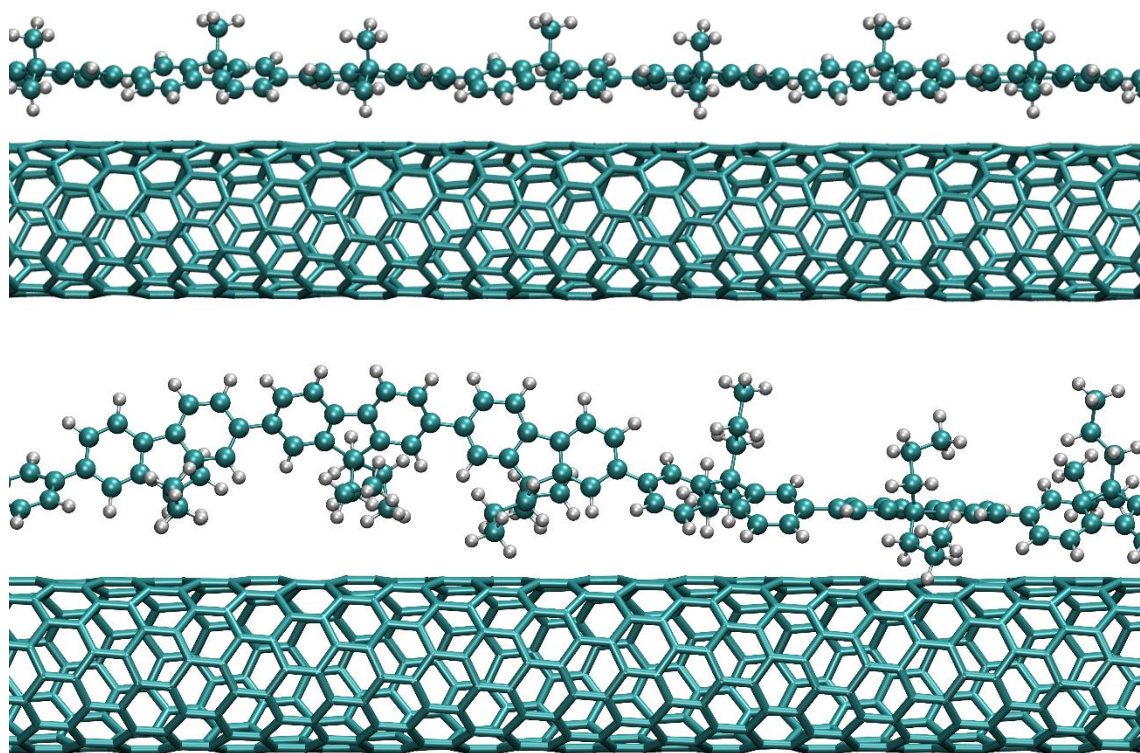


Figure 2.4. Top: (8,6) SWCNT with PFO where side chains are replaced with methyl groups. Due to the lack of steric hindrance between side groups and the SWCNT, polymer backbone interacts with the SWCNT via π - π stacking. Bottom: SWCNT with PFO where side chains are replaced with propyl groups. The introduction of the relatively bulkier side groups results in twisting in the backbone and reduced π - π stacking.

atoms introduced by elongating the chain will be more distant to the SWCNT and (figure 2.5a) and will therefore not be able to interact via Vander Waals interactions. Additionally, extending the sidechain results in an additional morphological change: significant twisting in the polymer backbone is observed as the length of the sidechain increases going from $n=2$ to $n=3$ (figure 2.6b), and as a result π - π stacking is significantly disrupted (figure 2.6c). Furthermore, the

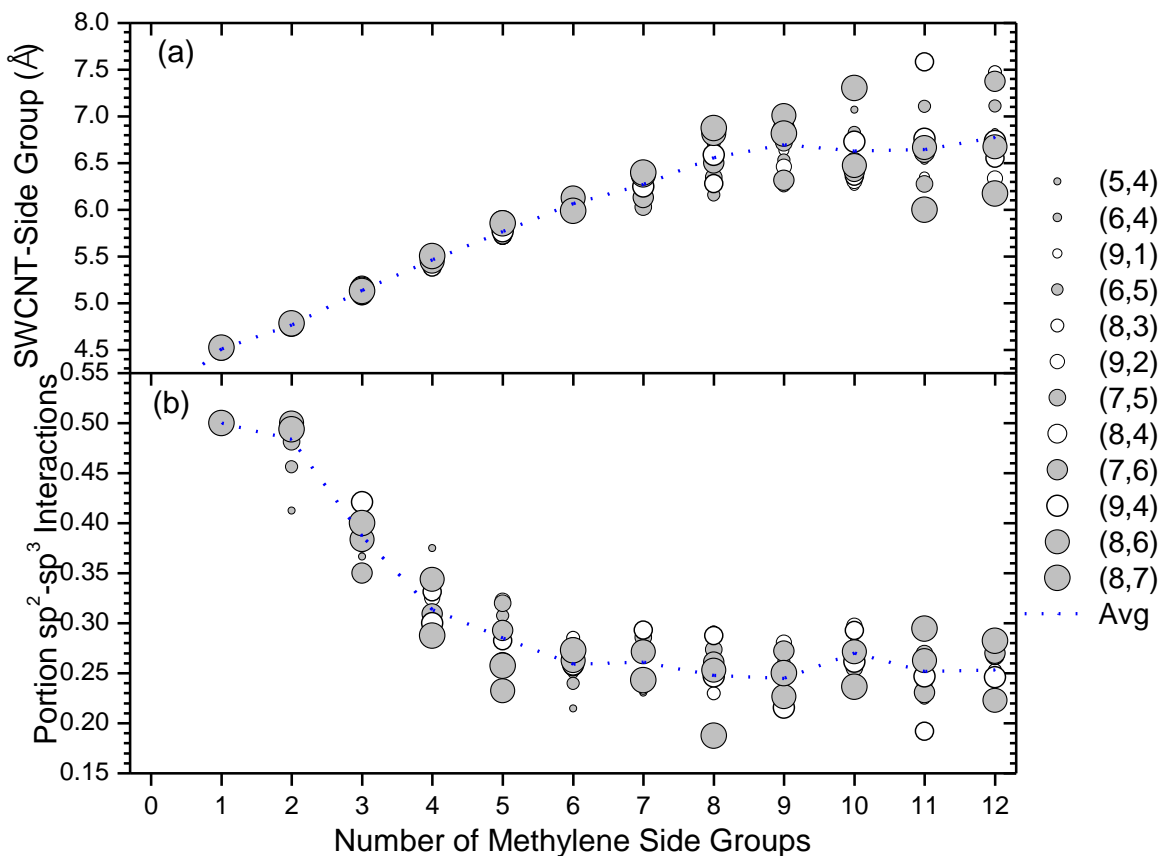


Figure 2.5. Characterization of the interaction of the PFO side chains with the SWCNT, including (a) average distance between the SWCNT surface and the atoms of the PFO alkyl group, and (b) the fraction of carbon atoms in the alkyl group that are within range to interact with the SWCNT surface via van der Waals interactions. Larger circles indicate larger diameter SWCNTs, filled circles indicate a chiral angle $\theta > 20^\circ$, and empty circles indicate a chiral angle $\theta < 20^\circ$.

adsorption strength in these systems is significantly reduced by about 0.2 eV/nm polymer. This interaction also induces a slight increase in the wrapping angle from about 3° to 8° (figure 2.3a).

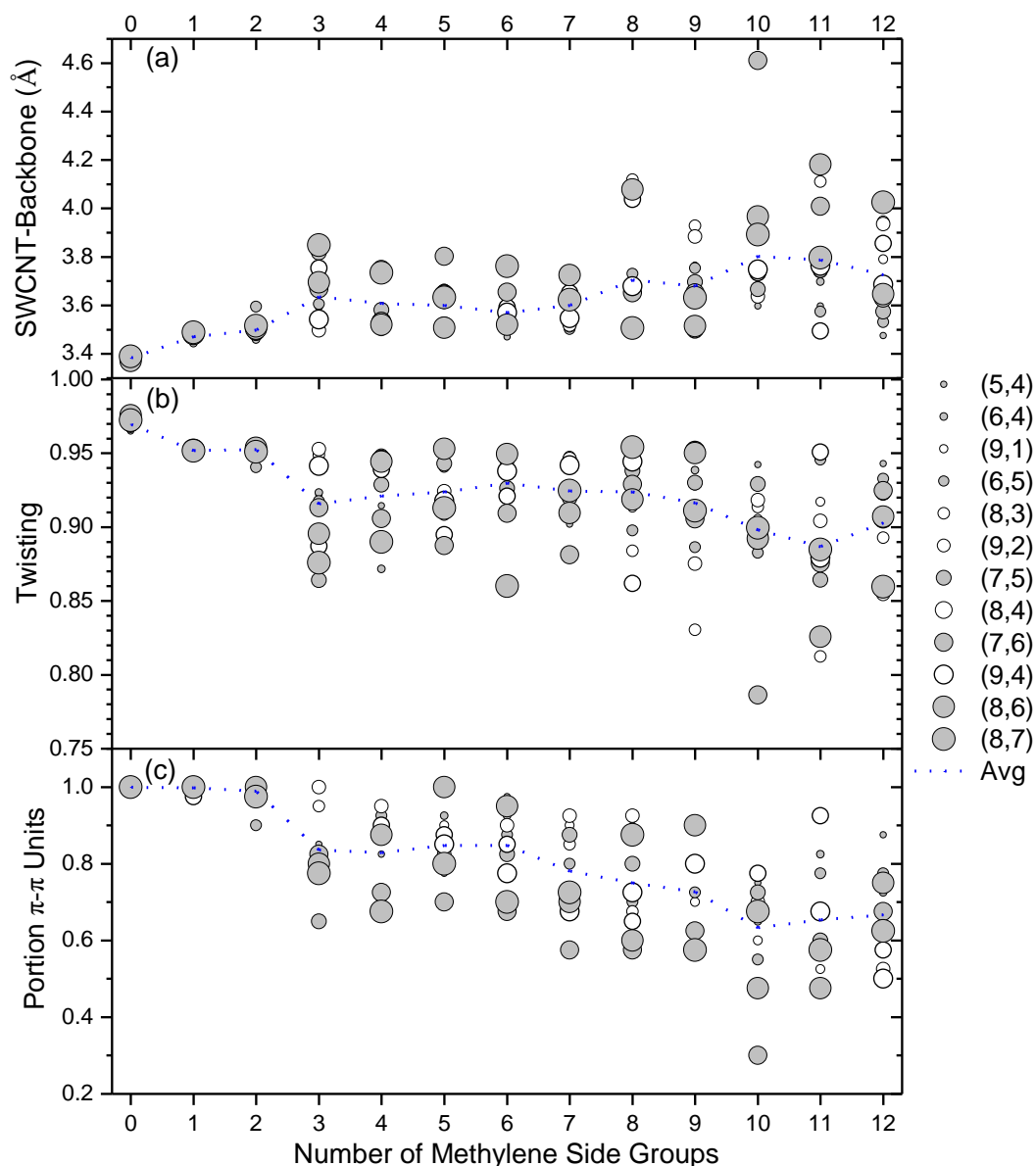


Figure 2.6. Characterization of the interaction of the PFO backbone with the SWCNT, including (a) average distance between the SWCNT surface and the PFO backbone, (b) average closest approach distance between a vector normal to each polymer unit and the axis of the SWCNT, and (c) the number of PFO units that are both planar to the surface and have all backbone C atoms within pi-pi stacking range. Larger circles indicate larger diameter SWCNTs, filled circles indicate a chiral angle $\theta > 20^\circ$, and empty circles indicate a chiral angle $\theta < 20^\circ$.

The interaction between the side chains and the SWCNT for these geometries is much less ordered than for shorter side chains: some of the units exhibit the alkyl chain on one side of the polymer backbone interacting with the SWCNT while the other does not. However, many units show the side chains on both sides of the polymer backbone interacting with the SWCNT, maximizing van der Waals interactions while inducing complete disruption of π - π stacking (figure 2.4). For these systems, the increase in van der Waals interactions as a result of the additional atoms in the alkyl side chain is insufficient to offset the corresponding decrease in the portion of π - π interacting units as a result of twisting, and the net effect is an observed decrease in the strength of adsorption.

2.3.2. Intermediate Length Sidechains

2.3.2.1. $n=3 \rightarrow n=8$ Little Impact on Morphology for Longer Sidechains

The twisting of the polymer backbone reaches a maximum for $n=3$, and further twisting in the backbone is not observed as the length of the side chain increases (figure 2.6b). Additionally, the distance between the SWCNT and the polymer backbone in this region is stable (figure 2.6a), and as such the fraction of polymer units that interact via π - π interactions doesn't change (figure 2.6c). Due to the consistency in morphology across this range of intermediate length sidechains, additional destabilization from lengthening the sidechain is absent. The only effect in this region is an increase in number of Vander Waals Interactions.

2.3.2.2. Increased number of Vander Waals Interactions Increases Adsorption

While the fraction of atoms interacting via van der Waals interactions decreases slightly going from $n=3$ to $n=5$, the net result of adding more atoms to the side chain is an increase in the number of atoms undergoing adsorption through that interaction. For $n=6$, there is a slight decrease in distance between the SWCNT and polymer backbone that is accompanied by an

increase in the fraction of π - π interacting units (figure 2.6, a & c), resulting in a local maximum in adsorption energy (figure 2.2a). Additionally, going from $n=5$ to $n=8$ results in both an increase in the fraction and absolute number of atoms within the van der Waals interaction range. As such, this increased interaction coupled with the fact that additional twisting in the backbone is absent and therefore the constant number of π - π interacting units results in an increase in adsorption strength to a local maximum at $n=8$. Since sidechains are required for processing conjugated polymers due to their impact on solubility as well as this locally high interaction strength with SWCNT, $n=8$ is likely the best candidates for using in the sorting of SWCNTs. It is no surprise that this length sidechain is the species that is most frequently used in experiment.

2.3.3. Long Sidechains

2.3.3.1. $n=8 \rightarrow n=12$: Decreased Stability Due to Increased Wrapping Angle

The changes in morphology in the region from $n=3$ to $n=8$ are minimal, and therefore the predominant effect contributing to binding energy is the number of side chain atoms interacting via van der Waals interactions. This marginal change in morphology throughout this region includes only slight deviations to the wrapping angle of the polymer. However, this is not the case when the length of the polymer sidechains are lengthened beyond octyl groups, where a significant change in wrapping angle is observed. The further lengthening of the side chains increases the steric interactions between adjacent units. While this steric hindrance is minimized for the head-to-tail conformation, it still is a factor when it comes to very long sidechains. Increasing the slope with which the polymer wraps around the SWCNT relieves this steric hindrance: translating the monomer units circumferentially around the SWCNT allows for retention of the torsion angle within the polymer while affording a greater volume in space for

the alkyl groups to occupy. This morphological change results in an increase in the wrapping angle (figure 2.3a), thereby increasing binding energies.

2.3.3.2. Binding Energy Dependence on Wrapping Angle

To corroborate the effect of increasing wrapping angle on binding energies, a trend is generated between these two variables for the optimized geometries from different starting configurations given a single SWCNT and polymer. These trends indicate that higher wrapping angles result in weaker binding (positive correlation in figure 2.7). The slope indicates the degree to which increasing the wrapping angle decreases adsorption strength, and as such the correlation was formed for all permutations in the SWCNT/polymer series (figure 2.8). For short side chains, changing the wrapping angle plays a less significant role in the adsorption strength because of the lack of sidechains to destabilize the system from steric effects. However, as the sidechains increase in length the increase in wrapping angle is accompanied by a decrease in

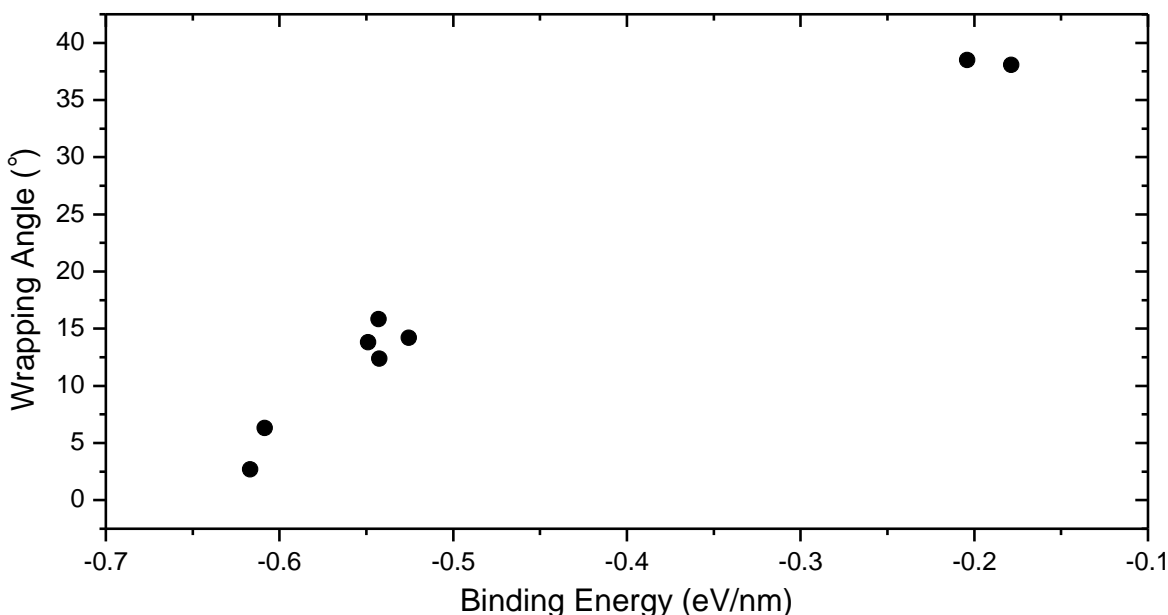


Figure 2.7. Binding energy vs final wrapping angle for all optimized geometries of (9,1) SWCNT with n=7 PFO. All geometries with stronger binding exhibit a steeper final wrapping angle.

binding strength. From this data, it is evident that increasing the wrapping angle results in a decrease in binding strength, accounting for the destabilized species with long side chains and increased wrapping angles.

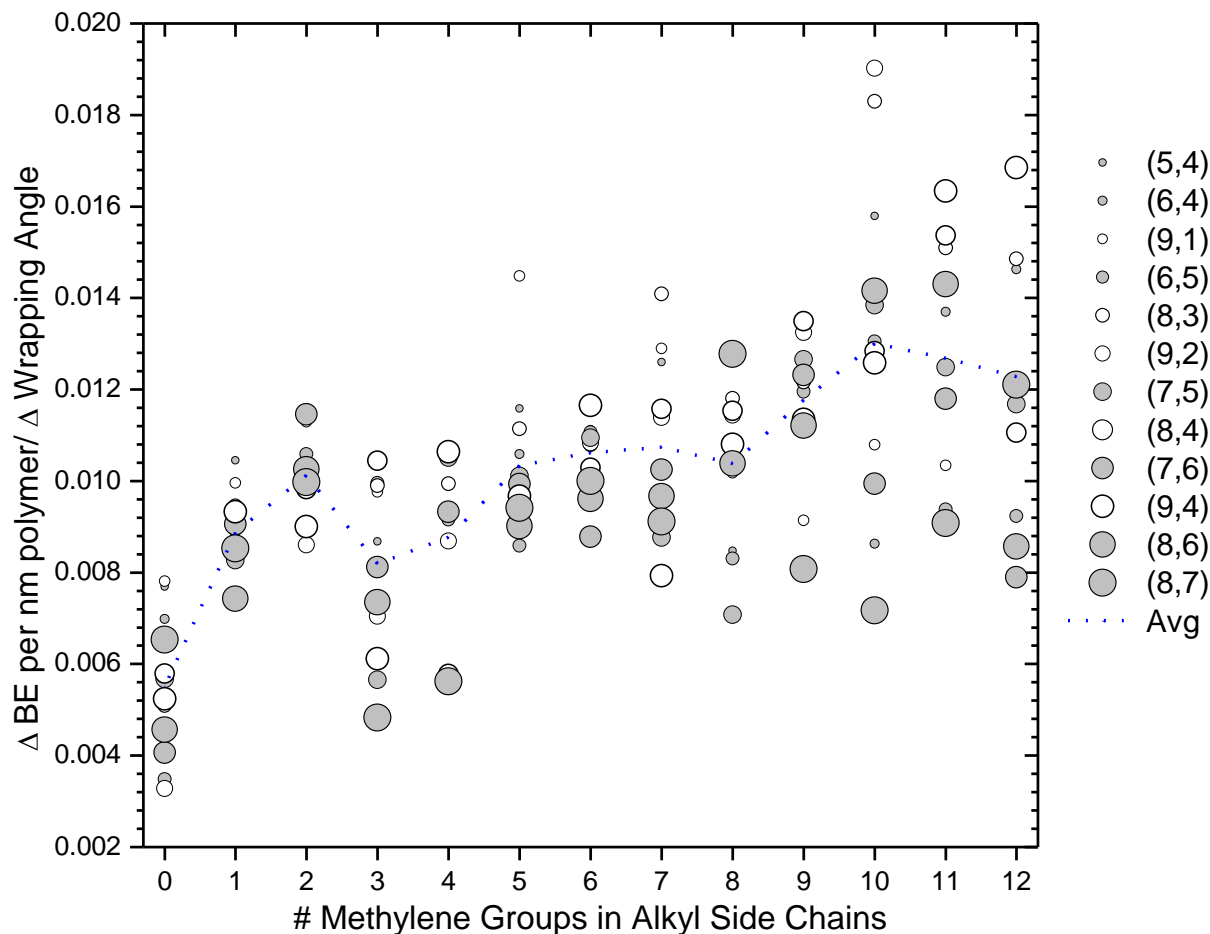


Figure 2.8. The slope of binding energy vs final wrapping angle for all geometries with different number of side groups. For very short side groups, little dependence of wrapping angle on binding energy is observed. For longer side chains, from $n=10$ to $n=12$, a strong dependence of wrapping angle on binding energy is observed.

2.4. Conclusions

The adsorption strength of PFO is highly dependent on the length of their alkyl sidechains, and while π - π interactions provide the predominant force holding the polymer-SWCNT complex together, the weaker van der Waals interactions between the sidechains and

SWCNT cannot be neglected. Understanding the net effect of lengthening the sidechain on adsorption energy requires evaluation of the complex interplay between Vander Waals interactions and π - π stacking with the SWCNT. The former forms relatively weak interactions but can still lead to increased binding between the polymer and SWCNT provided its contribution is not at the expense of the latter. For very short sidechains, the π -interactions dominate and the van der Waals interactions between the sidechain and SWCNT serve to slightly increase the adsorption energy. However, for longer chains steric hindrance between the SWCNT and sidechains as well as the chains themselves begins to dominate resulting in the twisting of the polymer backbone and therefore destruction of the π - π overlap. The result is weaker binding despite the additional van der Waals interactions between the sidechain and the SWCNT. Maximal twisting in the polymer backbone is observed for the propyl sidechain ($n=3$), and further elongation results in stabilization of the binding energy due to the additional van der Waals interactions without the expense of further destruction of π overlap. For sidechains longer than octyl ($n=8$), the steric hindrance between sidechains in the polymer forces it into a configuration that increases the angle about which the polymer wraps the SWCNT. As a result, binding strength again decreases. The most preferential binding is observed for very short sidechains, but due to synthetic considerations these may not be realistic. A local maximum in binding strength is observed for the PFO with octyl chains, the most commonly used species. While the effect of sidechains on electronic structure is minimal, the results in this chapter show that the morphology of the polymer chain about the SWCNT is heavily dependent on the sidechains, and therefore geometry sensitive computational models must take these effects into account.

2.5. References

- (1) Frisch, M. J.; Trucks, G. W.; Schlegel, H. B.; Scuseria, G. E.; Robb, M. A.; Cheeseman, J. R.; Scalmani, G.; Barone, V.; Mennucci, B.; Petersson, G. A.; et al. *Gaussian 09*; Gaussian, Inc.: Wallingford, CT, USA, 2009.
- (2) Lee, C.; Yang, W.; Parr, R. G. Development of the Colle-Salvetti Correlation-Energy Formula into a Functional of the Electron Density. *Phys. Rev. B* **1988**, *37* (2), 785–789.
- (3) Becke, A. D. Density-functional Thermochemistry. III. The Role of Exact Exchange. *J. Chem. Phys.* **1993**, *98* (7), 5648–5652.
- (4) Vosko, S. H.; Wilk, L.; Nusair, M. Accurate Spin-Dependent Electron Liquid Correlation Energies for Local Spin Density Calculations: A Critical Analysis. *Can. J. Phys.* **1980**, *58* (8), 1200–1211.
- (5) Hariharan, P. C.; Pople, J. A. The Influence of Polarization Functions on Molecular Orbital Hydrogenation Energies. *Theor. Chim. Acta* **1973**, *28* (3), 213–222.
- (6) Ditchfield, R.; Hehre, W. J.; Pople, J. A. Self-Consistent Molecular-Orbital Methods. IX. An Extended Gaussian-Type Basis for Molecular-Orbital Studies of Organic Molecules. *J. Chem. Phys.* **1971**, *54*, 724–728.
- (7) Collins, J. B.; von R. Schleyer, P.; Binkley, J. S.; Pople, J. A. Self-Consistent Molecular Orbital Methods. XVII. Geometries and Binding Energies of Second-Row Molecules. A Comparison of Three Basis Sets. *J. Chem. Phys.* **1976**, *64*, 5142–5151.
- (8) Allinger, N. L.; Yuh, Y. H.; Lii, J. H. Molecular Mechanics. The MM3 Force Field for Hydrocarbons. 1. *J. Am. Chem. Soc.* **1989**, *111* (23), 8551–8566.
- (9) Lii, J. H.; Allinger, N. L. Molecular Mechanics. The MM3 Force Field for Hydrocarbons. 2. Vibrational Frequencies and Thermodynamics. *J. Am. Chem. Soc.* **1989**, *111* (23), 8566–8575.

- (10) Lii, J. H.; Allinger, N. L. Molecular Mechanics. The MM3 Force Field for Hydrocarbons. 2. The van Der Waals' Potentials and Crystal Data for Aliphatic and Aromatic Hydrocarbons. *J. Am. Chem. Soc.* **1989**, *111* (23), 8576–8582.
- (11) Allinger, M. L.; Li, F.; Yan, L. Molecular Mechanics. The MM3 Force Field for Alkenes. *J Comput Chem* **1990**, *11* (7), 848–867.
- (12) Ponder, J. W. *Tinker*; 2010.
- (13) Frey, J. T.; Doren, D. J. *TubeGen 2.4*; University of Delaware: Newark DE, 2011.
- (14) Mayo, M. L.; Chen, Z. Q.; Kilina, S. V. Computational Studies of Nucleotide Selectivity in DNA–Carbon Nanotube Hybrids. *J. Phys. Chem. Lett.* **2012**, *3* (19), 2790–2797.
- (15) Mayo, M. L.; Hogle, D.; Yilmaz, B.; Köse, M. E.; Kilina, S. Morphology and Dispersion of Polycarbazole Wrapped Carbon Nanotubes. *RSC Adv.* **2013**, *3* (43), 20492–20502.
- (16) Furmanchuk, A.; Leszczynski, J.; Tretiak, S.; Kilina, S. V. Morphology and Optical Response of Carbon Nanotubes Functionalized by Conjugated Polymers. *J. Phys. Chem. C* **2012**, *116* (12), 6831–6840.
- (17) Kilina, S.; Yarotski, D. A.; Talin, A. A.; Tretiak, S.; Taylor, A. J.; Balatsky, A. V. Unveiling Stability Criteria of DNA-Carbon Nanotubes Constructs by Scanning Tunneling Microscopy and Computational Modeling. *J. Drug Deliv.* **2011**, 2011.

3. CAPPING OF FINITE SWCNT SYSTEMS FOR ELECTRONIC STRUCTURE CALCULATIONS

3.1. Motivation

Computational simulations involving density functional theory (DFT) and linear response time-dependent density functional theory (TDDFT) prove invaluable for determining the electronic structure and optical properties of single walled carbon nanotubes (SWCNTs). While advances in technology have enabled the application of these techniques to larger and larger systems over the past decades, the current state still limits the computations to sizes of approximately 1000 atoms. Because of this, finite SWCNT systems must be constructed before further calculations can be performed. The dangling bonds at the ends of these systems must be “capped” with some chemical species in a systematic way to eliminate superfluous trap states localized on the edges of the SWCNT system and produce electronic structure for the finite system resembling that of its infinite counterparts. This has been historically accomplished in an empirical manner by testing a number of capping schemes involving methylene groups and hydrogen atoms. However, a full understanding of the effects of capping groups and more analytic approach to developing finite SWCNT models has yet to be achieved. Toward this end, this chapter focusses on characterizing the effects of various capping groups with different bond character and electron withdrawing properties on the bond length, charge distribution and electronic structure of single-walled (10,5) carbon nanotubes (SWCNTs) using semi empirical and DFT methods. The absorption characteristics of these systems was also investigated using linear-response time-dependent density functional theory (TDDFT). Through characterization of the natural bond orbitals (NBOs), it is shown that the charge distributions and bond lengths along the edges of the finite SWCNT systems depend on the functional group. However, the precise

electron withdrawing characteristics of the functional groups play an insignificant role in the electronic structure: of significant greater importance is the positions and number of groups with sp^2 hybridized connectivity. The number of such functional groups required displays some chirality-dependent trends. This information is of utmost value in setting up computational models for further acquisition of meaningful results.

3.2. The Menagerie of Capping Schemes

For a complete analysis of the role of capping groups on the electronic structure and optical features of SWCNTs, all possible configurations must be considered. These configurations are described in this section.

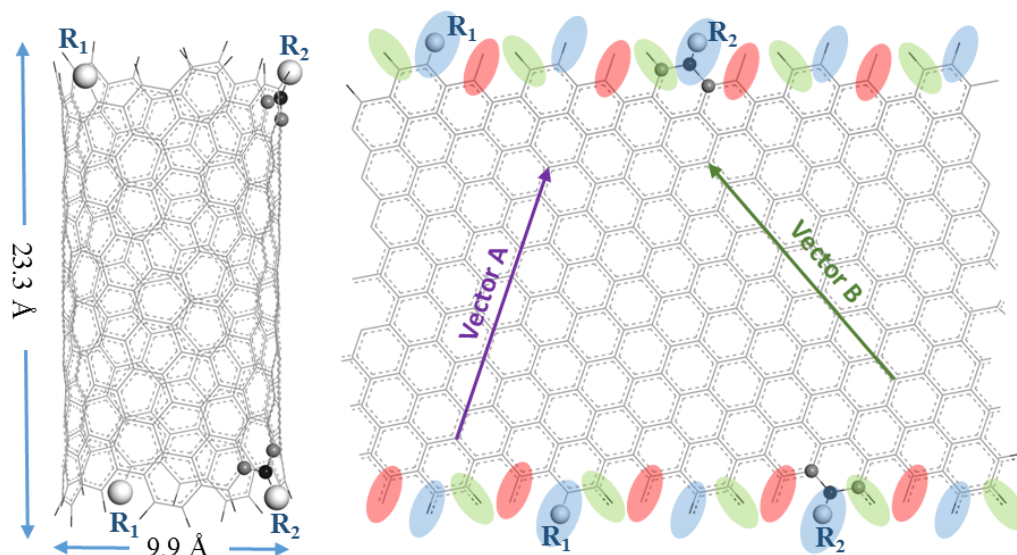


Figure 3.1. Structural parameters for the edge-functionalized (10,5) SWCNT and different capping schemes possible for this nanotube. Positions labeled by R_1 and R_2 are those that are used for calculations of 14 different functional schemes shown in Figure 2. Bonds highlighted in the same color represent the same symmetry position at the tube's edge referred to as A_1 (blue), A_2 (green), and B (red).

3.2.1. Bonds at the SWCNT Terminus

3.2.1.1. Three Distinct types of Bonds in SWCNTs

Due to the lack of symmetry, all chiral SWCNTs ($0 < n \neq m$) have bonds that lie along three distinct vectors with respect to the tube axis. The first vector (labelled “Vector A” here) is the chiral vector and represents the direction with which the graphene sheet would be rolled to form the SWCNT. The other two vectors lie at $\pm 30^\circ$ from the chiral vector. Following one of these results in a path near the circumference of the tube (herein referred to as “circumferential vector”), and the other lies in the third direction, appearing “across” the chiral vector in the formed tube (labelled “Vector B”). Figure 3.1 contains a graphical representation the two relevant types of bonds for capping purposes.

3.2.1.2. Possible Capping Positions

Of the three distinct types of bonds of SWCNTs, only two are present as dangling bonds on the cap. While bonds laying along the circumferential vector are present near the caps of the SWCNT, valances of atoms cannot be completed by functionalizing along this direction. Bonds laying along the chiral vector can be further divided into two distinct types. The first type (labelled A_1 , highlighted blue in figure 3.1) originate from carbon atoms vicinal to functionality along vector B. The second type of type of bond lies along the chiral vector but is separated from other carbons containing cap functionalization by at least two atoms (labelled A_2 , highlighted green in figure 3.1). The third type of bond lies along vector B and is always accompanied by an adjacent A_1 (labelled B, highlighted red in figure 3.1). Because the three of these capping positions are chemically distinct, the electronic structure resulting from capping at all three must be considered independently.

3.2.1.3. Distance Between Capping Groups

The number of capping positions of each type that exist in a SWCNT depends on its chirality. For all tubes of (n,m) chirality, the following relationships are used to quantify capping positions with each distinct type:

$$\#A_1 = m \quad (\text{Equation 3.1})$$

$$\#A_2 = n-m \quad (\text{Equation 3.2})$$

$$\#B = m \quad (\text{Equation 3.3})$$

Due to the presence of multiple bonds of each type, the distance between capping groups needs to be considered. For a capping scheme using a single functional group at all positions (in this case hydrogen atoms), this consideration is irrelevant as there is only a single capping scheme. However, capping different positions of the same type generates chemically distinct systems when non-equivalent groups are introduced. Capping groups can be placed on a single type of bond in close proximity (ie two A_1 positions adjacent to each other) or distant from each other (ie two A_1 positions with radially opposing placement). These effects need to be independently considered due to the possibility of distance-dependent interactions between capping groups.

3.2.2. Atoms at the SWCNT Terminus

3.2.2.1. Different Capping Functionalities

Fourteen combinations of functional groups were chosen to explore the dependence of capping with species of different electron withdrawing characteristics and bond orders (figure 2). In order to investigate the impact of bond order, electronegativity, and inductive effects on the electronic structure of capped tubes, the functional groups were chosen to include methylene and hydrogen as well several alcohol, ester, carboxylic acid, and ether derivatives. The capping schemes can be further divided into three distinct classes based on the bond order of the

connectivity between the (10,5) SWCNT and the functional group, as illustrated in figure 3.2.

The first class of compounds consists of two functional groups, R_1 and R_2 , attached to the nanotube edges via the double bond (compounds 1 thru 4 in figure 3.2). In Class I, the atom bonded vicinal to the SWCNT on both functional groups is sp^2 -hybridized (bond order 2). In the second class of compounds (Class II), one functional group is attached to the nanotube edge via a single bond and the other via a double bond (bond order 1 and 2 respectively, compounds 5 thru 7 in figure 3.2). The third class (Class III) contains both functional groups interacting with the nanotube edge via only single bonds (bond order 1, compounds 7 thru 14 in figure 3.2). For all cases, all remaining dangling bonds at the nanotube's edges are capped by hydrogen atoms as shown in figure 3.1.

		Class I				Class II		
		1	2	3	4	5	6	7
R_1								
R_2								
		Class III						
		8	9	10	11	12	13	14
R_1								
R_2								

Figure 3.2. Functional groups attached to the edge of the (10,5) SWCNT. Class I compounds are those where both functional groups, R_1 and R_2 , have connectivity to the SWCNT via double bonds (sp^2 -connectivity), Class II compounds have one connectivity via a double bond and the other via a single bond (mixed sp^2 - and sp^3 -connectivity), and Class III compounds have connectivity exclusively through single bonds (sp^3 -connectivity).

3.2.2.2. Prevalence of sp^2 Hybridized Capping Groups

In a previous studies on the electronic and optical properties of the (10,5) SWCNT, the proper capping scheme was found to involve all hydrogen atoms with two methylene groups¹. While most capping schemes in the research presented in this chapter include up to two non-hydrogen functional groups, further modification to the electronic structure can be accomplished by substituting in more than two positions. This procedure produces analogues of the Class II functionalization scheme 7 that need to be considered in order to ensure that the optimal capping for elimination of superfluous cap-localized trap states is captured by the fourteen schemes previously discussed.

3.2.2.3. Differentiation Between Carbon Atoms Vicinal to Capping

For the purpose of characterization of the bond lengths and charge distributions in systems studied here, it is necessary to differentiate the different carbon atoms in the SWCNT vicinal to functionalization. The notation that has been adopted for this purpose is presented in figure 3.1. The carbon atom in the SWCNT to which the functional group is directly attached is labelled “C”. The two adjacent carbon atoms are then labelled “C₁” and “C₂”. These two carbon atoms are non-equivalent for any non-zigzag SWCNT due to the presence of the distinct axis of chirality previously discussed.

3.3. Computational Methodology

3.3.1. Generation of the Systems

Pristine SWCNTs of diameter 9.93 Å and length 23.3 Å (two fundamental unit cells long, figure 3.1) were generated using Tubegen 3.4 software.² The systems were then capped using the fourteen different functionalization schemes previously discussed (figure 3.2). For this, all fourteen structures were capped with functional groups R₁ and R₂ on opposing radial positions,

as illustrated in the left panel of figure 3.1. Additionally, five geometries for capping scheme 7 are generated with the methylene group as one functional group (R_1) and hydrogen as the other (R_2). The position of functionalization in these compounds is varied such that the methylene groups is located either on opposing sides or the same side radially. Additionally, the position of the connectivity is varied to cover the A_1 , A_2 , and B positions previously described (figure 3.2, right panel). Additional calculations utilize increasing numbers of methylene groups (from two to eight) on the edges of the SWCNT in the A_1 and A_2 positions.

3.3.2. Optimization of the Geometries of the Systems

Geometry optimization was performed using the semi-empirical Austin Model 1 (AM1)^{3,4} using Gaussian software package,⁵ generating the lowest energy ground state structures of all the capped SWNTs. Semi empirical methods are a natural choice here due to their lower computational expense compared than DFT, while giving comparative results.⁶ Previous studies have shown that the AM1 semi empirical method provides fairly accurate optimized geometries for π -conjugated systems such as SWCNTs.^{1,7,8} Additionally, AM1 calculations of pristine (7,6) SWCNTs of ~10 nm in length capped by hydrogens have shown to reproduce the subtle structure and the relevant vibrational effect in the ground and excited state dynamics of SWNTs that were observed in experimental findings.⁹⁻¹¹

3.3.3. Calculation of the Electronic Structure

3.3.3.1. Justification of Chosen Basis Sets

With suitable AM1 optimized geometries obtained, single-point electronic structure calculations were performed utilizing a minimal STO-3G^{12,13} basis as well as the larger 3-21G¹⁴⁻¹⁶ basis using multiple density functionals including the hybrid Becke, three-parameter, Lee-Yang-Parr (B3LYP)^{17,18} and coulomb-attenuating method B3LYP (CAM-B3LYP)¹⁹ as

incorporated into Gaussian Software package.⁵ Significant differences in the electronic structures obtained using STO-3G versus 3-21G basis sets are not observed, a result corroborated by previous studies that have shown that an increase in size of the basis set beyond STO-3G is not accompanied by significant changes in qualitative behavior of either the density of states (DOS) or absorption spectra of various SWCNTs. As such, all further results discussed in this chapter are obtained using the STO-3G basis set unless otherwise specified.

3.3.3.2. Justification of Chosen Density Functionals

Previous studies of pristine SWNTs have shown that excitons are overbound in conjugated organic materials when pure HF exchange is used, while no excitonic effect is observed when pure GGA density functionals are used²⁰. Therefore, the results presented here are obtained using B3LYP^{17,18,21–23} which uses 20% Hartree Fock (HF) exchange and the long-range corrected CAM-B3LYP¹⁹ that varies the HF exchange from 19% for short range interactions and up to 65% HF exchange for long range interactions in an attempt to better reproduce dispersion effects. For charge distribution analysis, the natural bond orbitals (NBO) are calculated subsequent to single point energy calculation using NBO3²⁴ as implemented by the Gaussian software package.

3.3.4. Calculation of Excited State Properties

Time dependent DFT (TDDFT)²⁵ was used to analyze the excited state transitions in SWCNTs capped with the aforementioned schemes. Fifty singlet excited state transitions were generated for the two unit-cell length systems. In order to explore length dependence on optical properties, 25 excited state transitions were calculated for several capping structures of Class-I for longer nanotubes of seven and nine unit cells, generating systems with the total length of 8.2 nm and 10.5 nm respectively. All excited state transitions were broadened with a Gaussian

function of linewidth 0.05 eV to reproduce thermal broadening that occur under experimental conditions. Finally, natural transition orbitals (NTOs)²⁶ were generated using Gaussian-09 software⁵ to visualize the nature of the optical transitions.

3.4. The Role of Functionalization Position

3.4.1. Electronic Structure

The (10,5) SWCNT with an all-hydrogen capping scheme (structure 14) calculated with CAM-B3LYP has a highest occupied molecular orbital (HOMO) to lowest unoccupied molecular orbital (LUMO) gap of 1.52 eV and will be used as a baseline for comparisons of electronic structure throughout this section. To elucidate the dependence of the position of a single sp^2 hybridized functional group, one hydrogen from scheme 14 has been replaced with methylene forming functionalization scheme 7. This choice is dictated by both the desired bond order (generating a Class II capping scheme) as well as the relatively weak electron withdrawing character of the methylene as opposed to oxygen-containing groups. Since both tube's edges have to be functionalized, it is natural to place the methylene on either the radially opposing sides or the same across sides of the SWCNT, while also varying its connectivity along vectors A or B (A_1 , A_2 , and B positions shown in figure 3.1, labelled O- A_1 and S- A_1 for functionalization along the A_1 vector on opposite sides and same sides respectively, with similar notation for A_2 and B vectors). Little effect on the electronic structure is observed as a result of placement of the methylene groups on type A_1 or A_2 bonds or placing them on the caps at either radially same or opposing positions (figure 3.3a). Since radially same or opposing positions are the extremes as far as the distance between capping groups, it can be assumed that as any functionalization with a single methylene group on either A_1 or A_2 positions anywhere on the cap will give similar results as far as electronics is concerned. In addition, the energy gap of these

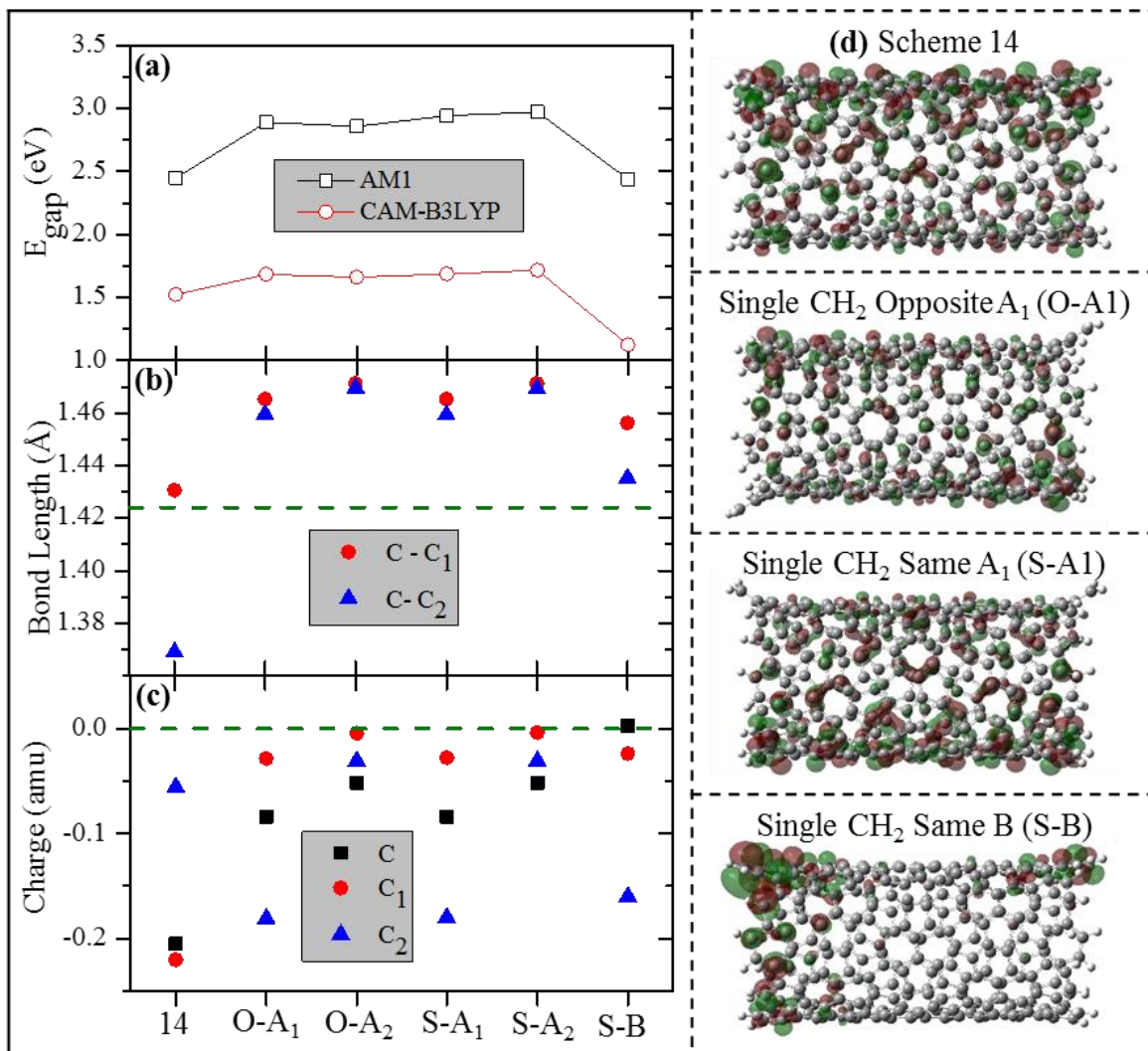


Figure 3.3. Comparison of the electronic and geometrical parameters of the (10,5) SWCNT capped only by hydrogens (compound **14**), as a reference point, and by hydrogens and one CH₂ group (compound **7**) with the CH₂ group attached at various positions (A₁, A₂, and B) along the nanotube edge, according to Figure 1. Position of the group at the other tube's edge is identified either by O or S, when the CH₂ groups are either at the opposite or the same sides with respect to the nanotube axis. The geometries are optimized by AM1 for all structures. **(a)** The energy gaps computed by AM1 and DFT using the CAM-B3LYP functional. **(b)** The bond lengths between the carbon atom of the SWCNT to that the CH₂ group is attached (C) and the adjacent carbon atom (C₁ or C₂). **(c)** The NBO charge on C, C₁, and C₂ atoms of SWCNT calculated by the CAM-B3LYP. **(d)** Highest Occupied Molecular Orbital (HOMO) for each capping case calculated by the CAM-B3LYP. The dashed green line indicates the average bond length and charge for the central portion of the SWCNT where perturbation by capping groups is absent. There is insignificant difference between energies and orbital delocalization for either the same or opposite A-positions, while B-position results in localization of HOMO at the edges and noticeable decreasing in the energy gap.

structures is similar to those of structure **14** (Class III) with the hydrogen passivation, especially when calculated using DFT instead of semi empirics. In contrast, placing the CH₂ group at the B-position leads to a noticeable decrease in the HOMO-LUMO gap (by about 0.5 eV). This trend in energies is well reproduced either by AM1 or DFT approaches, with AM1 resulting in a constantly larger energy gaps (~ 2.9 eV vs. ~1.5 eV). Such an overestimation of the energy gaps by semiempirical methods as well as the fact that the energy gap of SWCNTs increases with a portion of the HF exchange when DFT is used is well known⁸, while qualitative behaviour is not sensitive to the method²⁷. In addition to just the HOMO-LUMO gap, the position of several orbitals below the HOMO and above the HOMO is unchanged as a result of functionalizing with a single methylene group along either A₁ or A₂ vectors. However, a number of states are located within the gap for functionalization along vector B independent of methodology (figure 3.4).

3.4.2. Molecular Orbitals

The similarities in energy gaps between structures **7**, with CH₂ being at either A₁ or A₂ positions, correlate to nearly identical shapes of HOMOs for these species. Electronic density is delocalized across the entire system except the region on the SWCNT cap where the methylene groups are located (figure 3.3d). For methylene groups on opposing sides of the tube radially, the HOMO predominantly has as a “spiral” type shape wherein the electron density is located on central part of the nanotube but avoids the CH₂ group near the ends. Where the methylene groups are on the same side radially, the electron density is found predominantly on the opposing side of the tube. However, functionalization with a methylene group at B-position leads to localization of the electronic density at the tube’s edges, thus resulting in HOMO being a trap mid-gap state and thereby decreasing HOMO-LUMO gap of the system. This trend is followed by the LUMO and it is consistent with both DFT and AM1 calculations, shown in figure 3.3.

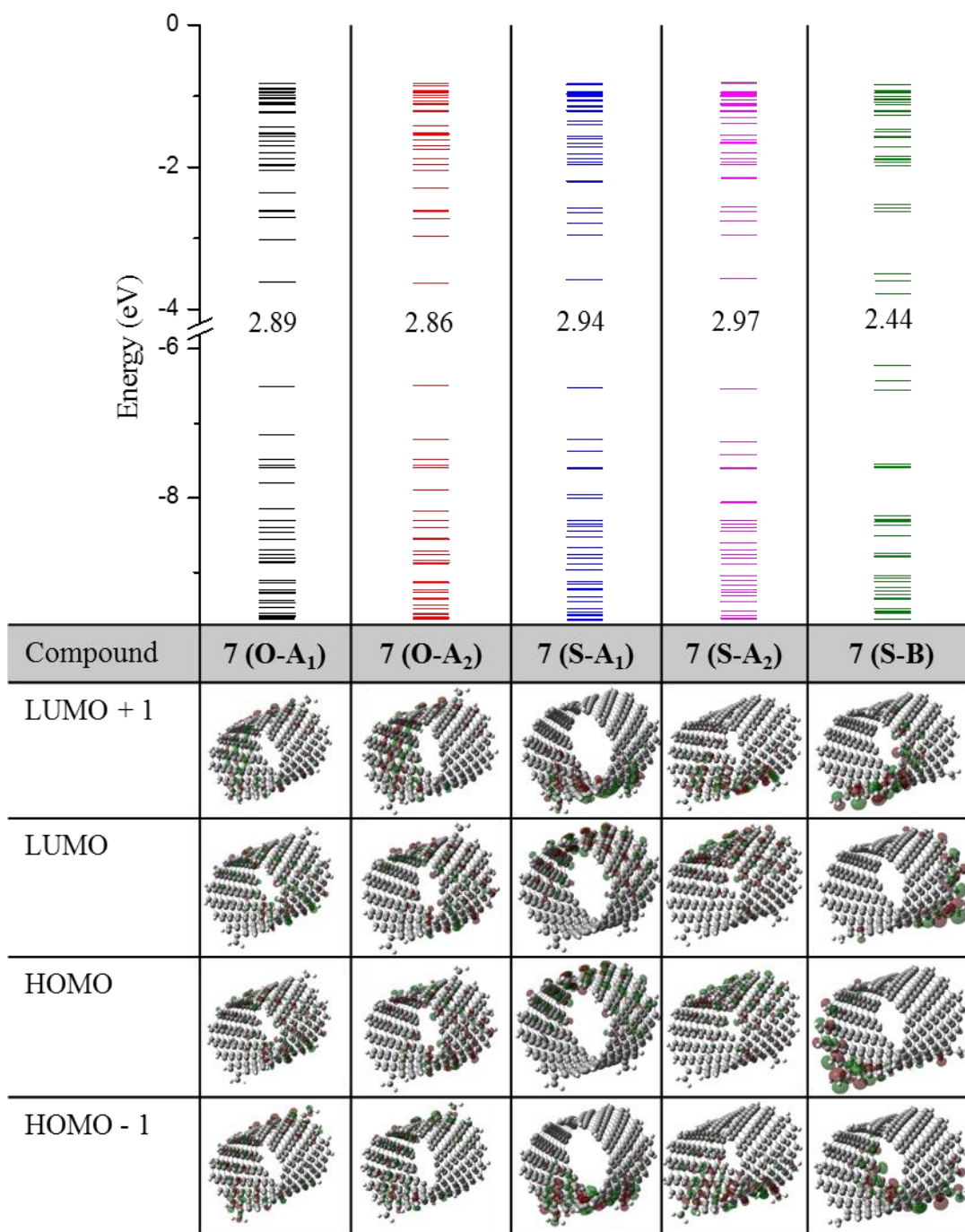


Figure 3.4. Molecular orbital diagrams and ground state molecular orbitals for two units of (10,5) SWCNT functionalized by a single sp^2 -hybridized CH_2 group (compound **7**) on different positions of the tube edge using AM1 methodology. The number listed in the HOMO-LUMO gap of the MO diagram (the top panel) is the energy of the gap in eV.

3.4.3. Bond Lengths at the SWCNT Edges Adjacent to Methylene Functionalization

Analysis of adjacent bond lengths near the edges quantifies double-bond like character, bond-length alternation, and provides a solid measure of delocalization of electrons from the functional group to the SWCNT. Due to resonance in the electron density contributed to the SWCNT through the double bond with the methylene group, the C-C₁ and C-C₂ bonds at the nanotube edge exhibit similar lengths of ~1.46-1.47 Å for functionalization at all A₁ and A₂-positions, figure 3.3b. This is in agreement with the delocalized character of molecular orbitals in these cases. In contrast, the structure with the B-position shows more single-like (~1.46 Å) and double-like (~1.44 Å) character of adjacent C-C bonds, which correlates with the edge-localized character of HOMO and LUMO.

3.4.4. Charges on Carbon Atoms Adjacent to Methylene Functionalization

For all structures functionalized along an A vector, the charge on the carbon adjacent the functional group is slightly negative (-0.1/-0.05 a. u.). However, this charge is less negative than for a capping scheme utilizing all hydrogen atoms due to the higher electronegativity of methylene compared to hydrogen. C₁ and C₂ (those atoms separated from the functional group by C) contain charges that are very similar when the methylene group is bonded along the A₂ vector but very different when methylene is bonded along A₁. In the A₁ case, C₁ is bonded to all sp² hybridized carbon atoms and therefore more positively charged due to their electron withdrawing nature. However, C₂ shares a bond with the less electronegative hydrogen atom and therefore is more negatively charged (figure 3.3c). Functionalization along a B-position results on completely neutral carbon with the methylene attached, while adjacent carbons hold similar slightly negative charge as those in A₁-position. Except for this slight difference in charge on C atom with attached sp²-functional group, correlations between charge distributions on carbons at

nanotube edges and the trends in energy gaps are absent. This is due to the fact that charge results from averaged character of the total charge density distribution that is integrated over all electronic states, while the energy gap is controlled only by electron density in two specific states (HOMO and LUMO). None-the-less, these results readily demonstrate that all charges on carbon atoms near the SWCNT can be justified by inductive arguments, and resonance contribution of electrons from the methylene to the SWCNT is absent.

3.4.5. Summary the Role of Functionalization Position

Functionalizing SWCNTs at the cap with a single methylene group demonstrates an independence of position as long as it is placed on a dangling bond along the chiral vector. Such functionalization at either A_1 or A_2 positions results in only marginal differences in electronic structure due to insignificant differences in the electron localization in the frontier molecular orbitals. In addition, the bond lengths adjacent to functionalization become nearly equal due to resonance. Any observed electron redistribution is the result of substitution of hydrogen with the more electronegative methylene, and contribution of electrons through the methylene-SWCNT bond is absent.

3.5. The Role of Prevalence of sp^2 -hybridized Functionality

3.5.1. Electronic Structure & Electron Density

To study the effect of increasing the number of sp^2 -hybridized groups capping at the edges of the SWCNT, additional hydrogen groups were substituted with methylene. This functionalization was performed for only A_1 and A_2 type capping locations due to the previously demonstrated invariance in electronic structure resulting from capping at those positions. Up to five hydrogen atoms can be replaced with methylene only on A_1 or A_2 bonds. For the (10,5) SWCNT, there are only five A_1 bonds. Therefore, functionalization of more than five positions

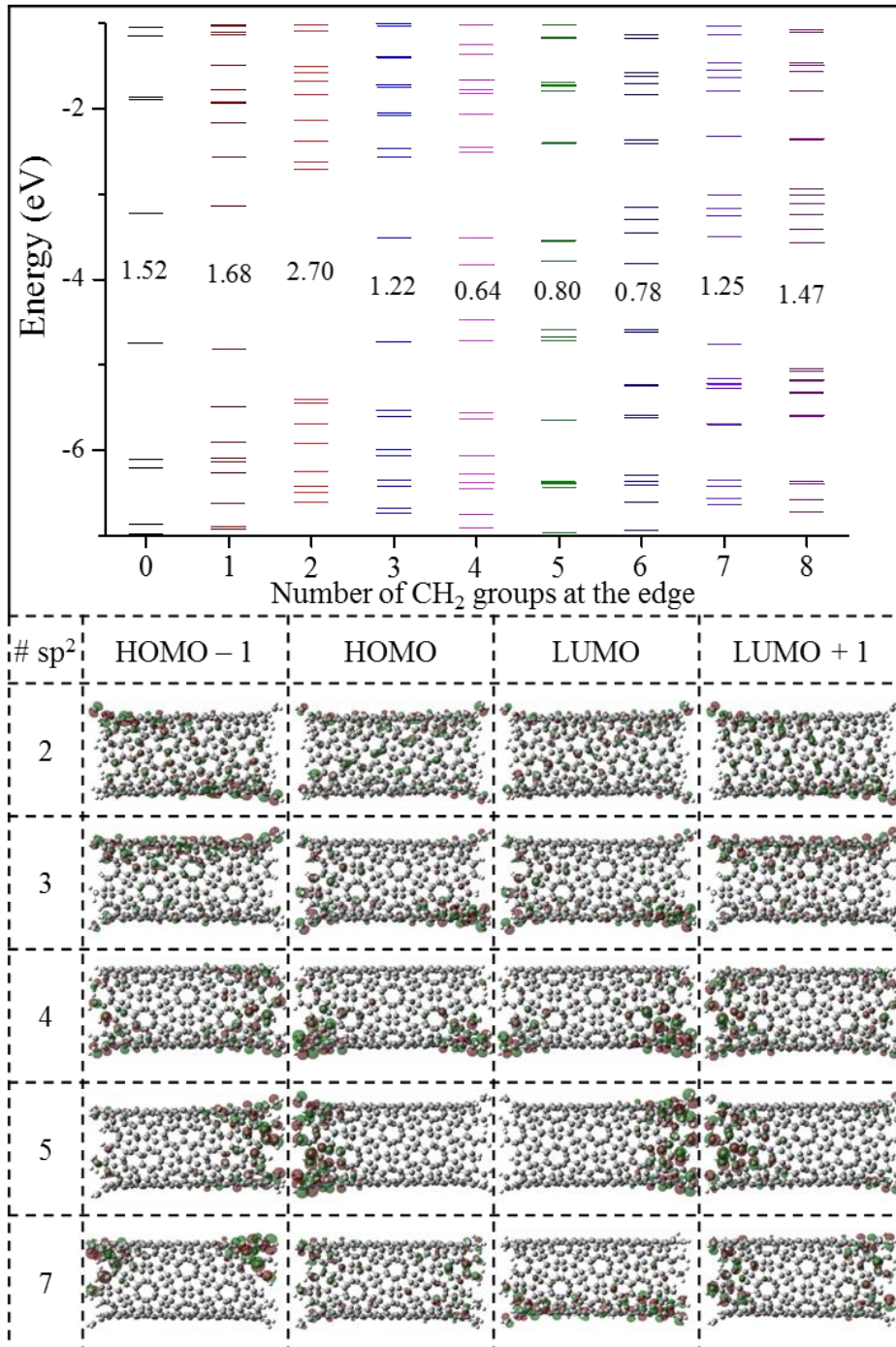


Figure 3.5. The electronic structure of (10,5) SWNT capped by different numbers of CH₂ groups along A-direction and calculated by DFT within the CAM-B3LYP functional. The number listed in the HOMO-LUMO gap of the energy diagram is the energy gap in eV. For the compound 14 with no CH₂ groups at the edge (0), the HOMO and HOMO-1, as well as the LUMO and LUMO+1, are two-fold degenerate. Addition of the CH₂ groups breaks this degeneracy.

along vector A requires some A₂ bonds to be utilized. The largest HOMO-LUMO gap of all the functionalization schemes studied was observed for functionalization with two methylene groups placed along the A vector (figure 3.7a). This particular functionalization scheme generates compound 1 (in Class I). Functionalization the cap of the SWCNT with more than two methylene groups introduces mid-gap states that result in a significantly closed HOMO-LUMO

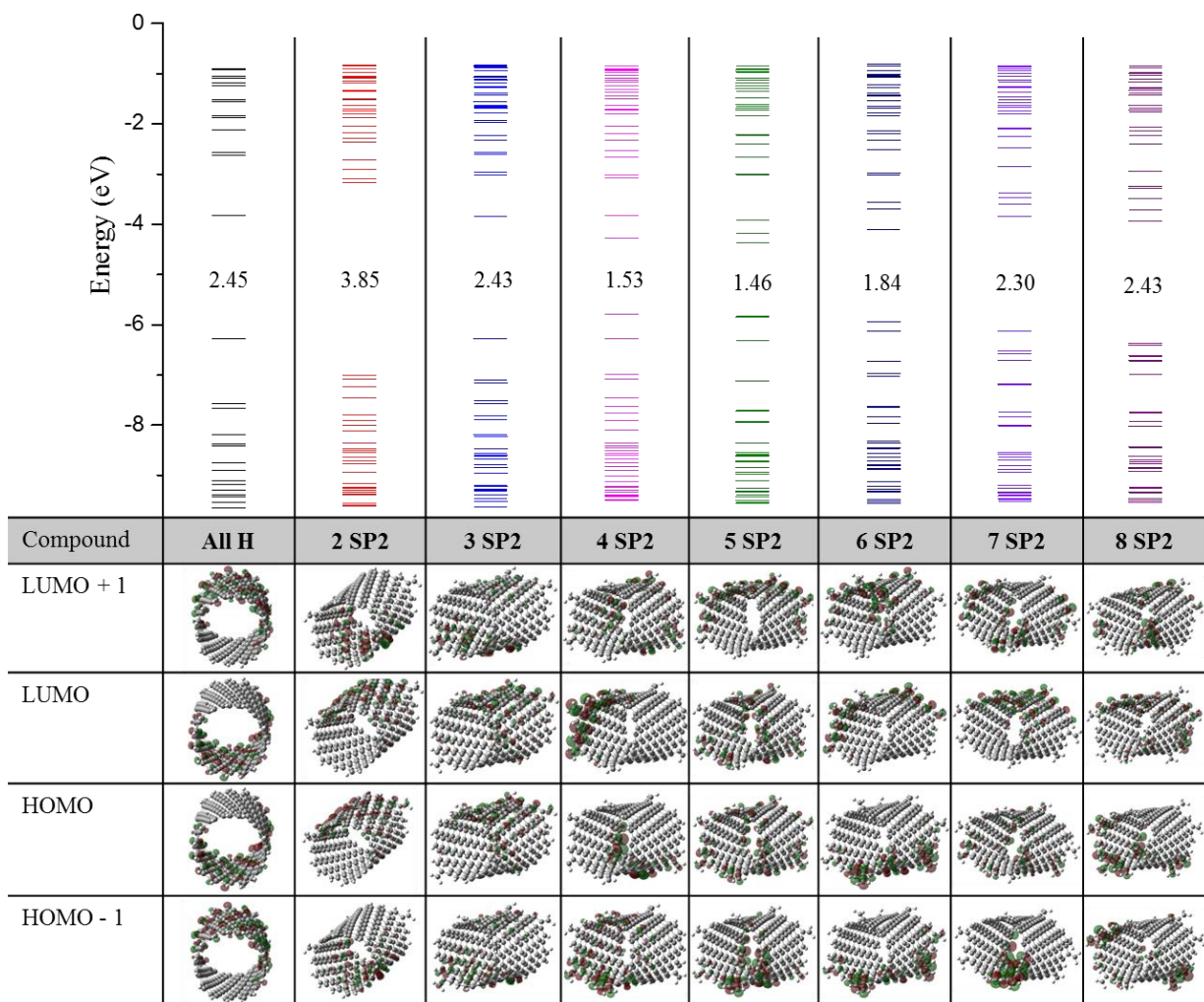


Figure 3.6. Molecular orbital diagrams and ground state molecular orbitals for two units of (10,5) SWCNT functionalized by different numbers of sp²-hybridized CH₂ groups on the caps using AM1 methodology. The number listed in the HOMO-LUMO gap of the MO diagram is the energy gap in eV.

gap. The electron density in these states is predominantly located near the caps of the SWCNT, resulting in mid-gap states in the electronic structure. Further increasing functionalization to four and five methylene groups introduces another one and two states into the gap respectively. Once all A_1 type positions are passivated, further functionalizing with six, seven, and eight sp^2 groups by placing methylene on A_2 groups then begins to remove these states from the gap. The states with less electron density held near the edges disappear and the gap reopens (figure 3.5a). These trends hold regardless of the methodology used (figure 3.5a vs 3.6a) due to similar trends in reorganization of electron density (figure 3.5b vs 3.6b).

3.5.2. Bond Lengths & Charges on Carbon Atoms Adjacent to the Edge

As with a functionalization along the edges with a single methylene group, the $C-C_1$ and $C-C_2$ bonds for each added methylene groups are very similar in length. There is nearly no dependence on the number of groups at the edge. However, there is a notable difference in the bond lengths for $C-C_1$ and $C-C_2$ between functionalization along A_1 versus A_2 bonds (figure 3.6b). The bond lengths are most similar when functionalization occurs along A_2 . All connectivity to carbon atoms involved in A_2 functionalization involves other sp^2 hybridized carbons. Due to resonance, these bonds are nearly equivalent. However, when functionalization is performed along A_1 , C_1 and C_2 are non-equivalent and therefore the bond lengths they are involved in deviate slightly. In this case, $C-C_2$ is the bond along the circumference of the SWCNT cap is slightly shorter than the internal $C-C_1$ bond. This effect becomes accentuated when the cap functionalization utilizes both A_1 and A_2 type bonds (figure 3.7). Strong electron localization is observed at the SWCNT edges (figure 3.7), contributing extra electron density along the circumferential bonds and therefore decreasing their length. This is accompanied by a slight increase in negative charge on these carbon atoms. Charges for functionalization along

only A_2 bonds are less negative due to the adjacent more electronegative sp^2 hybridized carbon atoms. Additionally, changing the number of sp^2 hybridized groups functionalizing along the A_2 vector results in no change in localized charges due to their separation from any other dangling bonds.

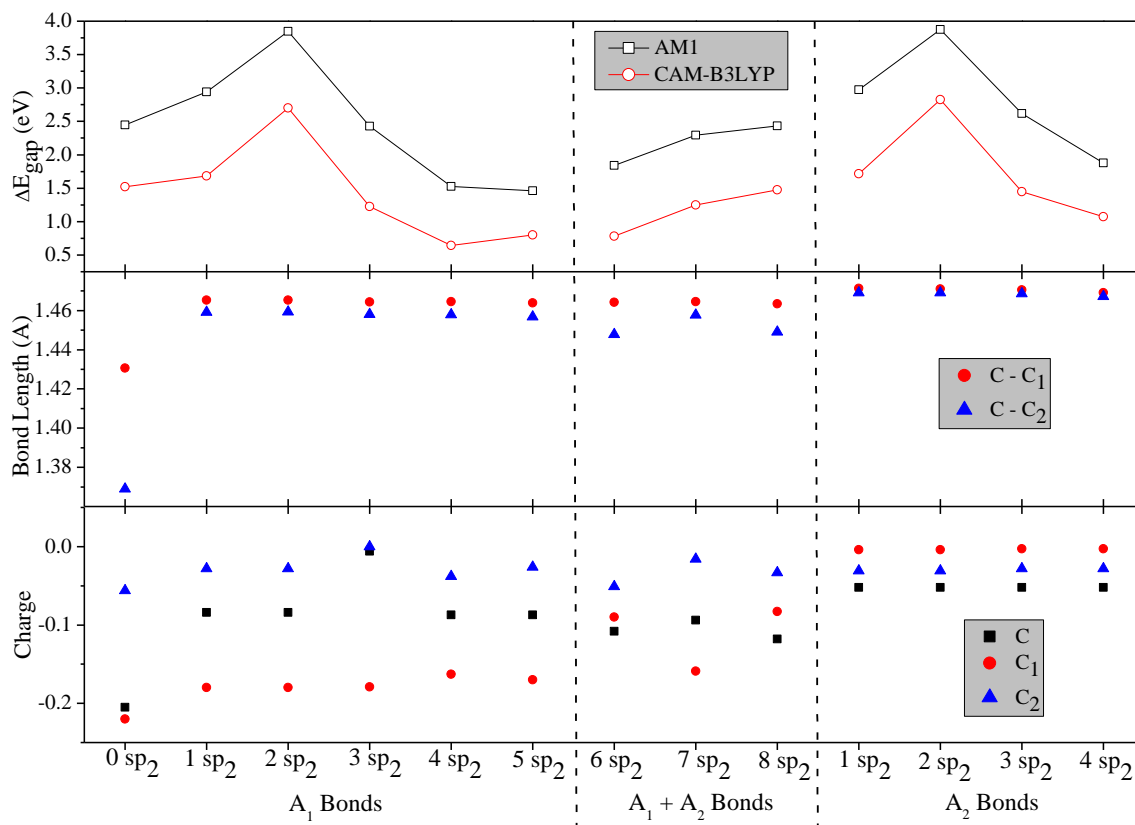


Figure 3.7. The electronic and geometrical characteristics of (10,5) SWCNT capped by different numbers of CH_2 groups. Top panel: The HOMO-LUMO gaps computed by AM1 and DFT within the CAM-B3LYP functional. Middle panel: The averaged bond lengths between the carbon atom of the SWCNT to that the CH_2 group is attached (C) and the adjacent carbon atom (C_1 or C_2). Bottom panel: The averaged charge on C, C_1 , and C_2 atoms of SWCNT using NBO calculated by the CAM-B3LYP functional.

3.5.3. Summary of the Role of Prevalence of sp^2 -hybridized Functionality

Functionalization of the caps of the SWCNT along vector A reveals optimal capping for functionalization with two methylene groups, where mid-gap states with electron density

localized on the cap are completely eliminated. Further functionalization results in reintroduction of trap states for up to five methylene groups, until a combination of A_1 and A_2 groups are used. This reduces the number of mid-gap states, but never to the same degree as for two methylene groups. Functionalization with up to four methylene groups exclusively along A_1 or A_2 bonds further demonstrates the invariance in electronic structure for these two vectors. Bond lengths and partial charges are marginally affected for all functionalization along vector A regardless of the number of sp^2 hybridized groups at the cap, indicating the local effect of each individual group is very similar. Only when taken as a whole are the differences in electronic structure and electron delocalization significant.

3.6. The Role of the Electron Donating/Withdrawing Groups at the SWCNT Cap

To determine the degree of influence of electron donating/withdrawing groups on the electronic structure and properties of (10,5) SWCNTs, fourteen schemes with different combinations of such groups were formed.

3.6.1. Class-Dependent Electronic Structure & Electron Localization in Frontier MOs

Class I structures (1-4), with two sp^2 functional groups at each tube edge, have the largest energy gap among the fourteen structures. Changing the nature of the groups within the class results in negligible changes in electronic structure. Other than the aforementioned differences in HOMO-LUMO gap due to the differences in methodology, all three methods exhibit qualitatively similar behavior with respect to the capping classes (figure 3.8a). This is true of the full electronic structure including the frontier molecular orbitals as well as those more energetically distant from the gap: the molecular orbital energies within each of the of classes are similar irrespective of the precise functionality for all three levels of theory (figure 3.8d). Electron localization in the orbitals is consistent with previously shown results as well, even in

the case of compound 2 with a slightly electron withdrawing nature. The presence of the oxygen in compound two doesn't result in electron density being withdrawn from the ring to the functional group on the cap, and CAM-B3LYP calculations show a slightly greater degree of delocalization than AM1 (figure 3.9). In addition, class II compounds exhibit the same behavior as previously demonstrated for a single methylene group at the cap. For all compounds in class II, where a single functional group are connected to the SWCNT through a second order bond, the HOMO-LUMO gap is similar. The same is true for class III compounds where no connectivity occurs through second order bonds.

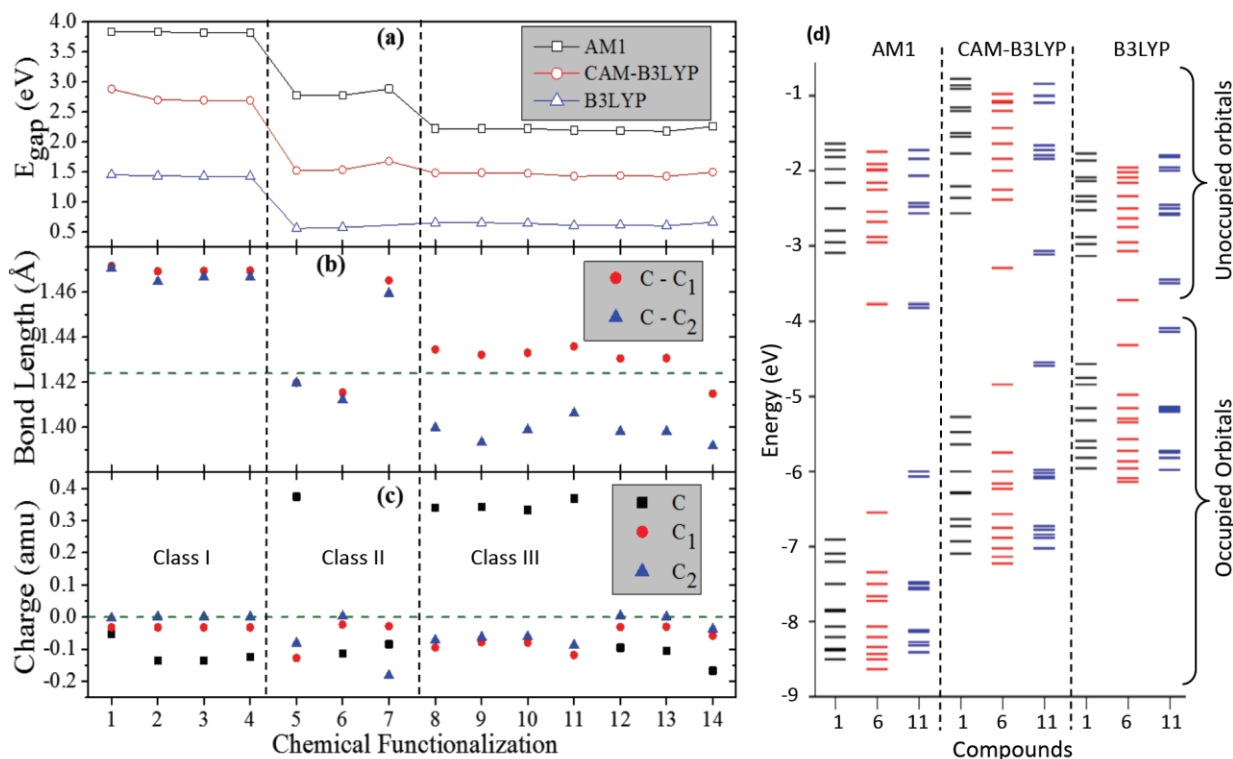


Figure 3.8. The electronic structure and geometrical parameters for the edge-functionalized (10,5) SWCNT optimized by AM1 method. (a) The HOMO-LUMO gap and (d) electronic levels calculated by semiempirical AM1 and DFT using CAM-B3LYP and BLYP functionals and 3-21G basis set. (b) Bond lengths for the AM1 optimized ground state geometry. (c) The charge on C, C₁, and C₂ carbons at the nanotube's edge using NBO analysis calculated by the CAM-B3LYP functional and 3-21G basis set. The dashed green line indicates the average C-C bond length and charge for the central portion of the SWCNT where perturbation by capping groups is absent.

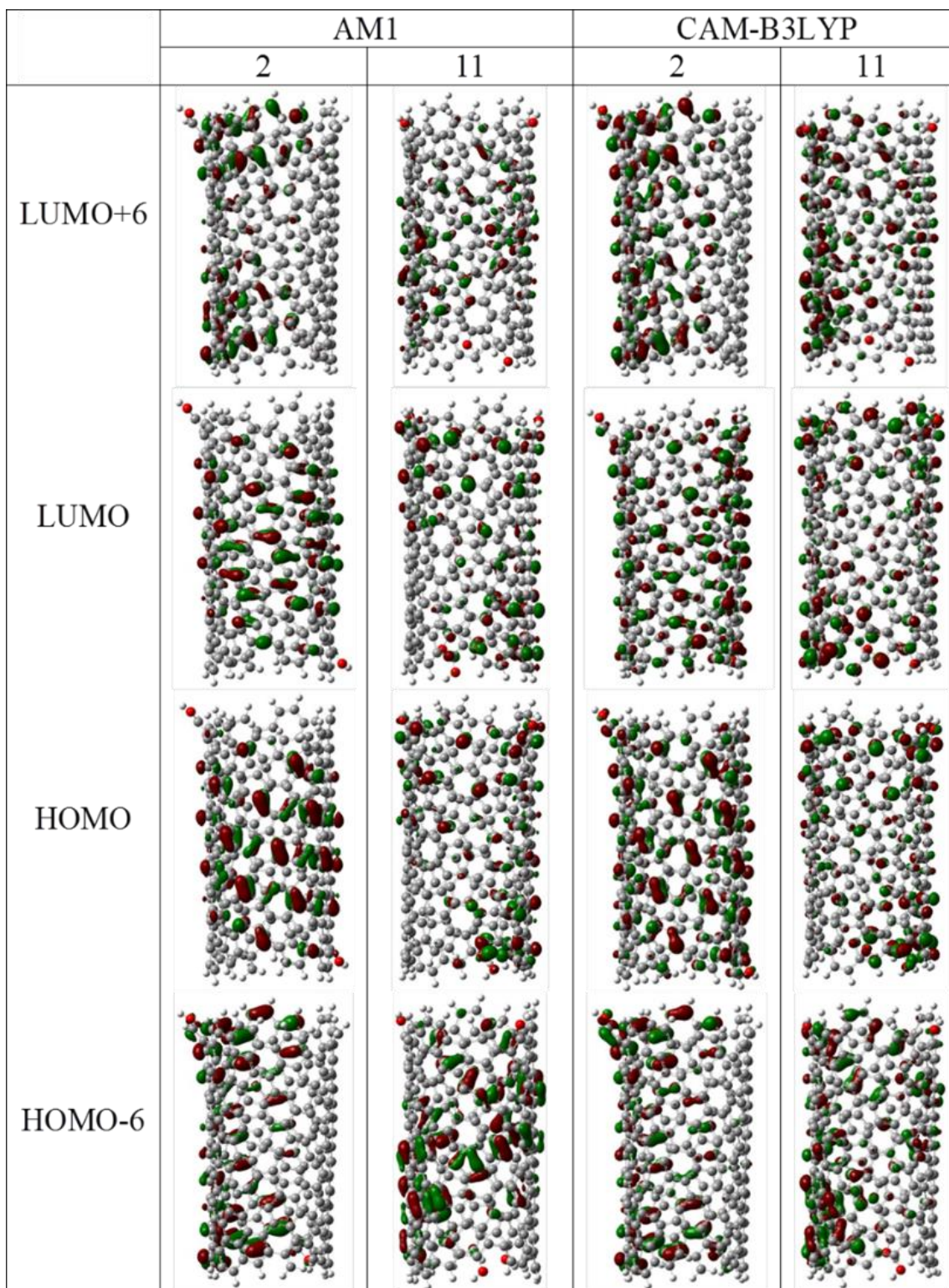


Figure 3.9. Plots of LUMO and HOMO for the (10,5) SWCNTs with functional groups 2 (Class I, sp^2 -capping) and 11 (Class III, sp^3 -capping) calculated by different methods (AM1 and CAM-B3LYP), while geometries are obtained by AM1.

3.6.2. Interclass Trends of Electronic Structure

These trends are justifiable given the molecular orbitals of the systems (figure 3.11). For all Class I compounds, the HOMO and LUMO each consist of two degenerate MOs. Changing one of the methylene groups by adding the electronegative alcohol while retaining the second order connectivity results in the formation of another other Class I compound (compound 2). This compound exhibits a slightly destabilized HOMO, while the LUMO is destabilized by the same degree. The net result is that no change in the HOMO-LUMO gap. This same effect is further observed when the second methylene group is substituted by the an alcohol forming compound 3, resulting in a further destabilized HOMO and LUMO and little net change in the HOMO-LUMO gap.

When alcohol is substituted with methoxy in both of the functional groups with sp^2 connectivity, further destabilization of the HOMO and LUMO are observed with no change in the net gap. However, substituting either of the sp^2 hybridized groups with functionality of bond order one generates a Class II compound and results in introducing states into the gap. The effect of changing the group is similarly insignificant, with stabilization of only the frontier molecular orbitals. For all cases across the series, more electron withdrawing groups result in destabilization of the HOMO and an asymmetric shift in the LUMO, resulting in unchanged gaps (figure 3.10). Using AM1 or B3LYP, the trends in HOMO-LUMO gap with respect to compound class are Class I > Class II > Class III for all compounds. However, for CAM-B3LYP, the trends are Class I > Class II \approx Class III. This discrepancy between methodologies is due to differences in electron density calculated with the different methodologies (figure 3.10). Using AM1, class II compounds with only a single sp^2 hybridized group functionalizing the cap has a greater degree of electron localization on the cap than when calculated using CAM-

B3LYP. This effect is vastly diminished for Class III compounds. As a result, the AM1 results show a significant decrease in HOMO-LUMO gap when calculated with AM1 that is absent for CAM-B3LYP. This trend likely further applies for B3LYP, resulting in no drop in gap for B3LYP going from Class II to Class III structures.

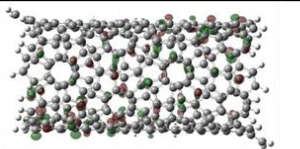
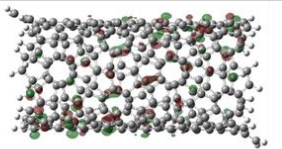
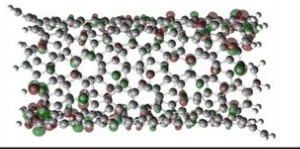
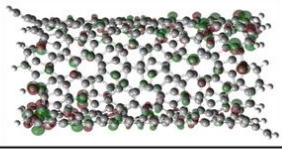
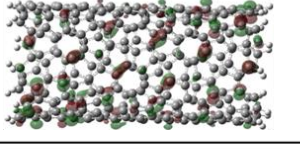
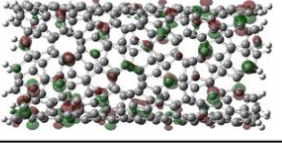
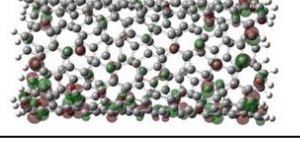
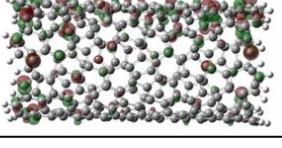
	Method	HOMO	LUMO
Compound 7 (Class II)	AM1		
	CAM-B3LYP		
Compound 14 (Class III)	AM1		
	CAM-B3LYP		

Figure 3.10. Molecular orbitals for compounds 7 (Class II) and 14 (class III) using AM1 and CAM-B3LYP methods. For class II compounds, more electron density is located near the SWCNT edges for CAM-B3LYP than for AM1, resulting in a reduced gap. This effect is not as significant for Class III compounds.

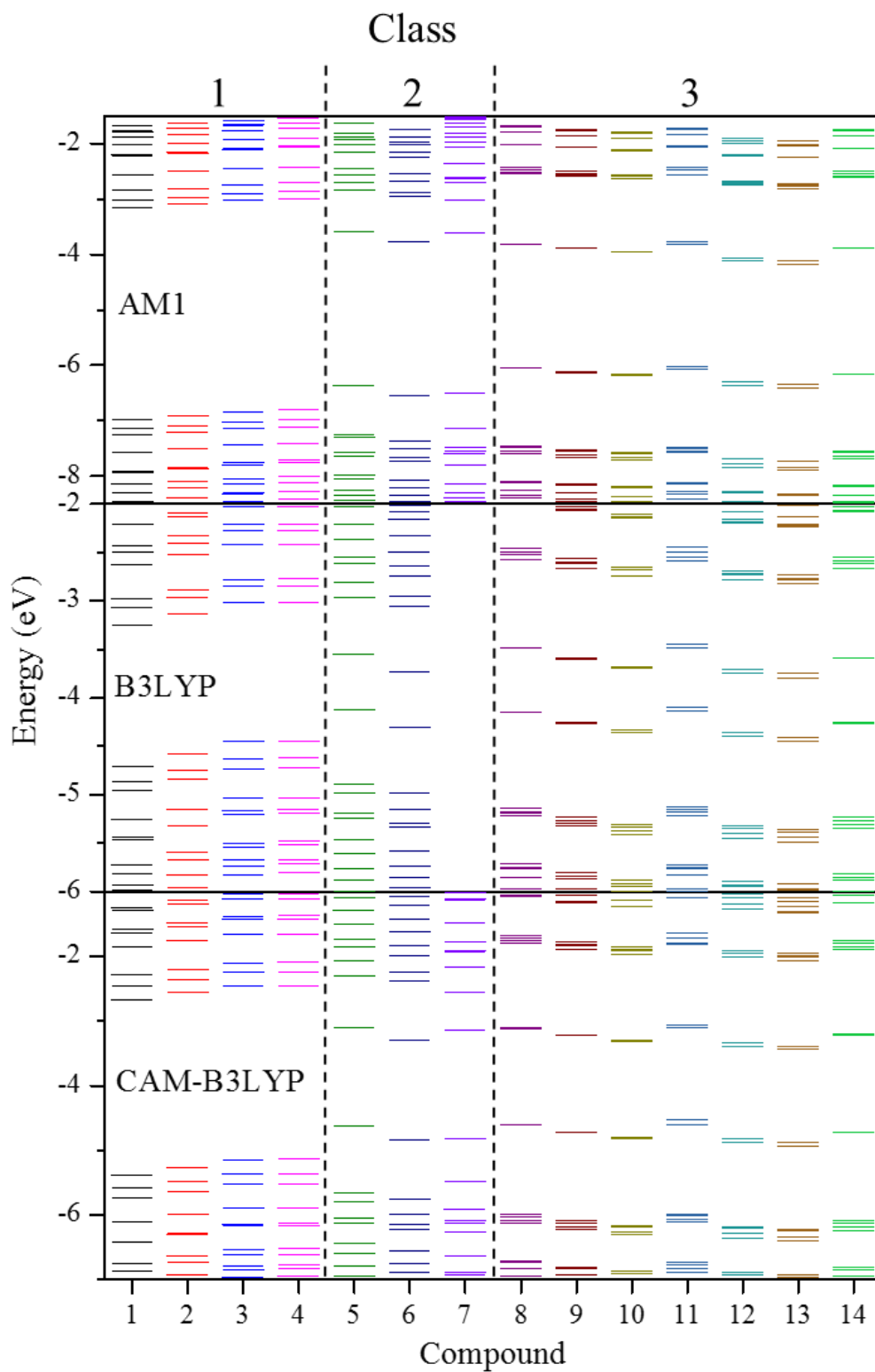


Figure 3.11. The electronic structure of (10,5) SWCNTs capped with fourteen different capping groups and calculated with different methods. All different methods represent single point energy calculations after the geometry is obtained using AM1.

3.6.3. Bond Lengths & Local Charges: Justification of the Electronic Structure

A significant correlation between the bond order of functionalization at C and the length of C-C₁ and C-C₂ bonds at the edge of SWCNT is depicted in Figure 3.8(b). For compounds in Class I, independent on the capping group, both of these bonds exhibit a noticeable single bond like character, resulting in their lengthening. The C-C₁ and C-C₂ bond lengths for compounds 1-4 are similar and around 1.47 Å, with a slight deviation from each other for non-equivalent R₁ and R₂ groups (compounds 2-4), figure 3.8(b). This bond elongation and more single-bond like character of C-C₁ and C-C₂, as compared to the C-C bond in the central unperturbed part of the SWCNT (varying from 1.41 Å to 1.44 Å), originates from the charge distribution induced by resonance at the sp² hybridized capping groups, as illustrated in Figure 3.12(a). Thus, in Class I compounds the carbon atom directly adjacent to the SWCNT (C) is sp² hybridized resulting in extended conjugation from the functional group into the six-membered ring to which it is bonded. Electron density can be contributed through this double-like bond to the bonded “C” atom resulting in a slightly negative charge on this atom, figure 3.8(c). The lone pair on the adjacent oxygen in the functional groups is able to intensify this contribution through resonance and causes a greater negative charge on “C” in compounds 2-4, while C₁ and C₂ atoms stay nearly neutral.

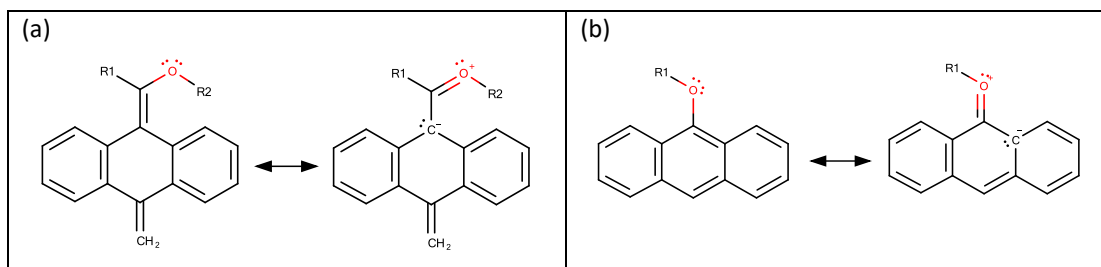


Figure 3.12. Schematic representation of hybrid resonance structures for the different types of capping groups used as a model for the (10,5) SWCNT with various side-groups attached at the tube's edges.

Similar results are observed for compounds 5-7 from Class II, where the measurements are taken at the carbon with the sp^2 hybridized functionalization. However, the carbon atoms with the sp^3 hybridized groups demonstrate more double-bond-like character for both C-C₁ and C-C₂ bonds in compounds 5 and 6, figure 3.8(b). In contrast, For Class III compounds 8-14, a large difference in bond length between C-C₁ and C-C₂ is observed indicating their non-equivalence induced by the sp^3 capping groups. For these cases where the bond order between the SWCNT and the functional group is a single bond, the adjacent C-C₂ bond is significantly shortened, while C-C₁ is close to the average resonance C-C bond in the central portion of the SWCNT, where perturbations by capping groups are negligible. A significant difference between C-C₁ and C-C₂ bond lengths induced by the sp^3 capping groups correlates with appearance of the mid-gap states that decrease HOMO-LUMO gaps in class III compounds.

Increased double-bond-like character and the difference between C-C₁ and C-C₂ bond lengths in compounds where an oxygen atom is bonded directly to the nanotube C atom (compounds 5, 8-11) are also associated with a significant positive charge on C shown in figure 3.8(c). This is because the electronegative oxygen in the capping groups is withdrawing electron density from this carbon. A slightly negative charge is observed on both C₁ and C₂ in these cases, likely the result of the ability of the bonded oxygen to donate electrons to portions of this conjugated ring through resonance, as illustrated in figure 3.12(b). As such, these compounds exhibit a strong redistribution of charges between the positively charged terminal C and the negatively charged C₁ and C₂, resulting in a higher dipole moment on the nanotube edge with these capping schemes. This strong dipole moment leads to stronger destabilization of both HOMO and LUMO in these compounds compared to those in oxygen free capping groups 6, 12, and 13, as can be seen in figure 3.11. However, this insignificantly affects the values of the

energy gap between compounds 8-11 and 12-13, because both HOMOs and LUMOs are shifted by nearly the same energy. Overall, there is a clear correlation between the values of the energy gap, the bond-order of the capping group and the bond length difference between the carbon involved in the functionalization and its adjacent carbons at the edge of SWCNT.

In addition to bond length, it is noted that for non-sp² hybridized side groups there is little tendency of the groups to “bend” outside the plane of the SWCNT surface as was observed with sp² functionalized groups. This is due to the absence of an unhybridized p orbital to overlap with the pi system of the SWCNT. Additionally, very little conformational change in the structure of SWCNT was observed after further functionalization.

3.6.4. Electronic Structure: Expanding beyond the Frontier MOs

To better understand the effect of capping groups on electron charge density, those states at lower and higher energy than the frontier molecular orbitals are analysed for the species with the extreme HOMO-LUMO gaps (structures 2 vs 11, differing by class and the inclusion of methylene groups instead of the electronegative hydroxyl groups). The HOMO and LUMO levels in compound 2 are delocalized in the middle of nanotube (figure 3.9). The 2p orbitals of hydrogen-containing carbon atoms at the edges of SWCNT significantly contributed to the electron density delocalization. At LUMO energy state π - π^* bonding are radially elongated whereas at HOMO the π - π^* bonding are elongated along the length of carbon nanotube. The π - π^* bonding in the HOMO seem to have larger contribution compared to LUMO. Compound 2 optimized using CAM-B3LYP method has showed more delocalization of electron density compared to optimized using AM1 method. The electron density in the nanotube has shifted towards the localized states near the capping edges with the blue shift in the LUMO and corresponding red shift in the HOMO. In the case of this Class t structure, the charge transfer

occurs from the HOMO to the LUMO, first at the helix of the nanotube (delocalized state at LUMO+3 and LUMO+4) and then shifted to the localized state at the capping edge of nanotube (LUMO+6).

In compound 6 of class III, the delocalized states the HOMO and LUMO have similar behaviours and they are localized around the edges of the nanotube with small contribution from the C atom attached to the carboxylic groups. The charge transfer shifts the state delocalized throughout walls of the SWCNT to the delocalized states away from the gap, and the states that resemble the frontier MOs in the Class I compound now become LUMO+6, HOMO-6. This is more pronounced for CAM-B3LYP, likely due to the lack of HF exchange and increase of electron exchange correlation in the functional. This shows that the electron density near the HOMO-LUMO gap corresponds to delocalized states, while states localized on the edges for compound two are found far into the gap. Completely localized states are not observed due to the high contribution from the hybridized states coming from the SWCNTs. From this, it is concluded that changing the functionalization to generate compounds of a different class results doesn't only change the position of the frontier molecular orbitals but instead results in significant modification to the electronic structure as a whole.

3.6.5. Summary of the Role of Electron Donating/Withdrawing Groups

Inclusion of different types of groups at the SWCNT caps changes the electronic structure of the system as well as the geometries and charges near the caps. However, the electronic structure changes only minimally if the bond order between the SWCNT and functional group is preserved. Electrons can be donated or withdrawn due to inductive and resonance effects respectively, but these effects only result in subtle difference in bond length and charges at the SWCNT cap. Any changes to the electronic structure as a result of this are

symmetrical in the HOMO and LUMO, and therefore the gap remains unchanged. The trend for gap is Class I > Class II > Class III regardless of the methodology used. As such, the predominant variable that must be regulated in the quest to generate finite SWCNT systems that don't have superfluous mid-gap trap states involves bond order and not precise electron withdrawing/donating nature of capping groups.

3.7. Optical Properties

3.7.1. Dependence on Methodology

Absorption spectra and oscillator strengths of compounds 1, 2, 6 and 11 are presented in figure 3.13. The performance of B3LYP and CAM-B3LYP functionals has been compared for these compounds. Overall, both methods coincide in main spectral features and provide qualitatively similar optical spectra. However, B3LYP results in red-shifted transitions as compared to CAM-B3LYP, while these shifts depend on the capping type: 0.61 eV, 0.32 eV and 0.12 eV for compounds 2, 6 and 11, respectively. This is the expected trend correlated with the decreased portion of the HF exchange in the density functional.^{1,27} The variance in the redshift of each compound for B3LYP vs. CAM-B3LYP calculations follows the trend of the energy gaps in these compounds with the largest gap for class I and the smallest gap for class III, as shown in figure 3.8(a).

3.7.2. Class Dependence of Optical Properties

In all cases, a few lowest transitions have a small oscillator strength followed by the brightest transition (S_B) that we associate to the main E_{11} band. For class II and III compounds this transition is red-shifted and less intense as compared to those of compounds 1 and 2 from the

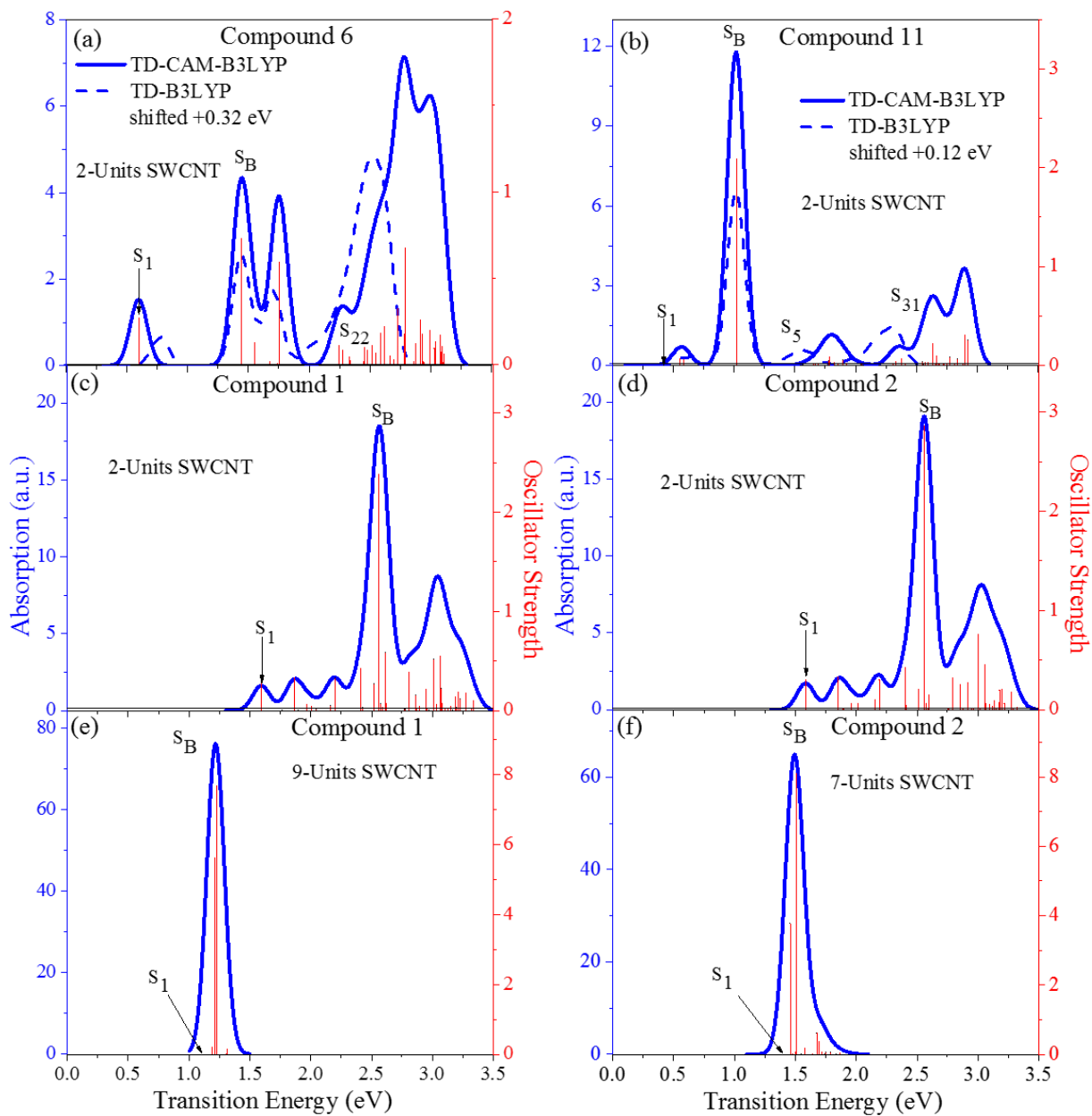


Figure 3.13. Absorption spectra (in arbitrary units) of the edge-functionalized (10,5) SWCNT of several lengths. Absorption spectra of the compound 6 of class II (a), 11 of class III (b), and 1 (c) and 2 (d) of class I computed with the TDDFT/B3LYP (dotted blue lines) and TDDFT/CAM-B3LYP (solid blue lines). TDDFT/B3LYP spectra are blue shifted to align the most intensive peak (S_B) for both methods. Vertical red lines denote each optical transition calculated by CAM-B3LYP functional with the oscillator strength shown at the right Y-axis (red), with the black arrows depicting the lowest-energy transition (S_1). In four top panels (a)-(d), the nanotube is of 2 lattice units in length. In bottom panels, the nanotube is of 9 units (e) and 7 units (f) in length. S_B defines the brightest transition associated with the E_{11} main band.

class I. The absorption spectra of compounds 1 and 2 exhibit very similar features (figures 3.13(c) and (d)), elucidating negligible effect of electron donating/withdrawing groups on the optical properties of SWNTs due to the similar character of the molecular orbitals for all compounds within Class I. In contrast, the change in the bond order of the capping groups has more dramatic effects on the energy alignment and oscillator strength of optical transitions, resulting in more red-shifted and less intensive E_{11} band with more complicated spectral shapes when sp^2 groups are changed by sp^3 capping. In all species, optically active transitions with noticeable oscillator strengths have $\pi-\pi^*$ character, while optically inactive transitions with a very low or zero oscillator strength have edge-localized nature, as illustrated in NTOs shown in figure 3.13.

3.7.3. Length Dependence on Optical Properties

The absorption spectra for longer nanotubes of ~8 nm (compound 1) and ~10 nm (compound 2) in length are calculated for several capping structures of class I (the highest energy transition species). In these cases, the length of the tube is significantly larger than the coherent size of an exciton (1.5-2 nm),²⁷ which allows for eliminating the edge effects, as compared to shorter models. Unfortunately, calculations of longer structures from Class II and III are computationally inviable because their energy gaps are nearly closed due to the edge-localized mid-gap states, interrupting convergence of the TDDFT computations. Therefore, only structures from Class-I with an open HOMO-LUMO gap converge in TDDFT calculations. In both long structures 1 and 2, the absorption spectra are red shifted compared to their shorter counterparts, figure 3.13 (e) and (f). This is a common trend according to the increased π -conjugated length of systems.¹ Additionally, the energy splitting between transitions is also decreases with the tube length resulting in a narrow and featureless E_{11} band. Similar to shorter

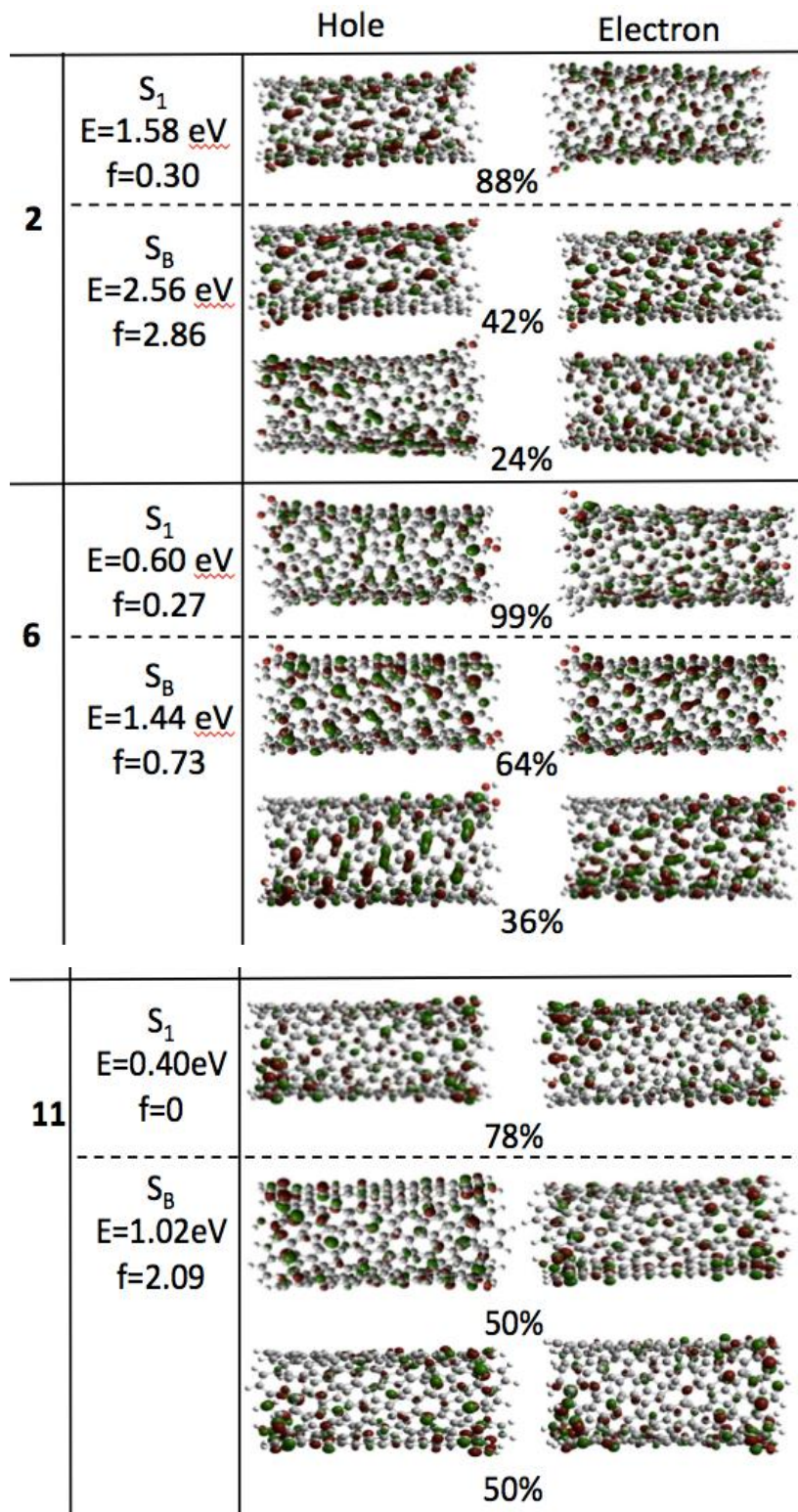


Figure 3.14. Natural transition orbitals (NTOs) contributing to the lowest energy (S_1) and the most bright (S_B) optical transitions for the capped SWCNTs (10,5) calculated using the CAM-B3LYP functional and 3-21G basis set for capping structures 2, 6, and 11. Geometries are optimized by AM1 semiempirical approach.

tubes, a few lowest energy states are optically dark or semi-dark having negligibly small oscillator strength. However, these lowest states are much less intense than in their short counterparts. This is because interactions and mixing between different excitons (optically dark and bright ones) are less pronounced in long tubes since excitons are more localized at the central part of the tube (see figure 3.15) and much less affected by the tube ends as in short structures. Nonetheless, the quantitative character of spectra of short tubes correlates well with the longer ones, pointing to the validity of the models used in these studies.

3.7.4. Summary of Optical Properties

The calculated optical properties show the presence of multiple dark states at the lowest energies, followed by a bright transition with π - π^* character. The energetics of these species are consistent with expectations from the ground-state molecular orbitals, where the bright transition is at higher energies for CAM-B3LYP than B3LYP. This bright state has the highest energies for Class I compounds. Additionally, changing the electron withdrawing nature of the group within Class I doesn't have much impact. Elongating the system results in slightly lower transition energies, but qualitative trends are preserved.

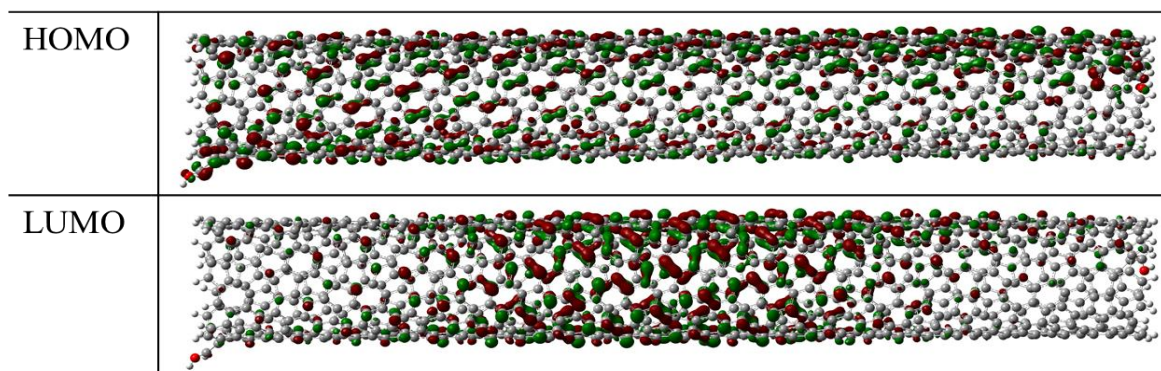


Figure 3.15. Molecular orbitals for compound 2 constructed with 7 unit cells of SWCNT. A transition from HOMO to LUMO is $\pi \rightarrow \pi^*$ in nature, with LUMO density having more localization at the central portion of the SWCNT with negligible involvement of capping groups.

3.8. Conclusions

Using semi empirics and density functional theory, the relationships between capping schemes involving various combinations of methylene, hydroxyl, and carboxylic groups attached to the edges of (10,5) SWCNT and the resulting electronic structure has been demonstrated. The schemes have been naturally divided into three classes differing by the bond order of the connectivity between the nanotube and the functional group, e.g., the sp^2 and sp^3 hybridized bonding, while having different electron withdrawing properties of ligands. It has thereby been shown that the hybridization of the bonding atom of the capping groups, as well as the number of functional groups bonded through an sp^2 -carbon, plays the predominant role in eliminating dangling bonds responsible for the optically forbidden edge-localized mid-gap states. These calculations reveal that for the (10,5) SWCNT, two sp^2 hybridized groups (methylene derivatives) are required on the caps to completely open up the energy gap. In this case, the HOMO and HOMO-1 (and LUMO and LUMO+1) are nearly degenerate states because of high symmetry of the edges, while the position of the sp^2 groups is such that they lie along the direction along which the orbitals are delocalized. Using only a single sp^2 group decreases the energy gap, due to a significant splitting between HOMO and HOMO-1 (LUMO and LUMO-1) states as a result of symmetry breaking. Addition of more than two sp^2 groups makes their position being at odds with the tube chiral vector bringing edge-localization of frontier orbitals and decreasing the energy gap. It has also been shown that the sp^2 hybridized carbon atom directly adjacent to the SWCNT has a slightly negative charge due to redistribution of electron density between the functional group and the six-membered nanotube's ring to which it is bonded. More negative charge on the sp^2 hybridized carbon requires a sparse distribution of sp^2 capping groups along the nanotube edge to avoid generation of a strong dipole moment, which

leads to edge-localized mid-gap states. This explains why two sp^2 groups is an optimal number of the capping groups for (10,5) SWCNT to provide the most opened energy gap, since they can be placed relatively far from each other while preserving conjugation structure of the tube's edge.

Variations in electron withdrawing/donating properties of the capping groups play very little role in changing the HOMO-LUMO gaps. The strongest electron withdrawing groups (ethers) destabilizes both the HOMO and LUMO, while relatively strong donating groups (carboxyl groups) stabilize the frontier orbitals. In all cases, however, the HOMO and LUMO are shifted symmetrically, so that the energy of the HOMO-LUMO gap is insignificantly affected by the electron withdrawing or donating properties of the capping groups inside the class. In contrast, the bond order of functionalization at the nanotube carbon governs the energy gap, where the gap reduces and edge-localized midgap states appear in structures capped only by sp^3 hybridized groups. Similarly, the optical spectra demonstrate negligible effects of electron donating/withdrawing groups on the lowest optical E_{11} band, while the change in the bond order of the capping groups significantly changes the energy alignment and oscillator strength of optical transitions, resulting in red-shifted and less intensive E_{11} band when two sp^2 groups are changed by sp^3 capping.

Consideration of these findings is absolutely essential in choosing the functional groups for tuning the optoelectronic properties of SWCNTs. In addition, these results provide a guideline in computations of finite size nanotubes: one can use such a capping scheme that completely eliminate all trap states at the edges, so that the finite SWCNT has the electronic structure comparable to its infinite counterparts, particularly near the energy gap where optical properties originate. Such a finite tube approach allows for calculations of optical spectra of

SWCNTs using TDDFT, which is a reasonably accurate and computationally efficient method compared to other available approaches. Overall, these results constitute a very significant contribution in the area SWCNT modelling, because a complete understanding of the role of tube's capping will allow for using smaller computational models and, therefore, make computations of a wide range of phenomena in SWNTs practical.

3.9. References

- (1) Kilina, S.; Tretiak, S. Excitonic and Vibrational Properties of Single-Walled Semiconducting Carbon Nanotubes. *Adv. Funct. Mater.* **2007**, *17* (17), 3405–3420.
- (2) Frey, J. T.; Doren, D. J. TubeGen 3.4; University of Delaware: Newark DE. 2011.
- (3) Dewar, M. J.; Zoebisch, E. G.; Healy, E. F.; Stewart, J. J. Development and Use of Quantum Mechanical Molecular Models. 76. AM1: A New General Purpose Quantum Mechanical Molecular Model. *J. Am. Chem. Soc.* **1985**, *107*, 3902–3909.
- (4) Dewar, M. J. S.; Zoebisch, E. G.; Healy, E. F.; Stewart, J. J. P. AM1: A New General Purpose Quantum Mechanical Molecular Model. *J. Am. Chem. Soc.* **1985**, *107* (13), 3902–3909.
- (5) Frisch, M. J.; Trucks, G. W.; Schlegel, H. B.; Scuseria, G. E.; Robb, M. A.; Cheeseman, J. R.; Scalmani, G.; Barone, V.; Mennucci, B.; Petersson, G. A.; et al. *Gaussian 09*; Gaussian, Inc.: Wallingford, CT, USA, 2009.
- (6) Stobinski, L.; Peszke, J.; Lin, H.-M. Computational Studies of SWCNTs Capped by Hemispheres of C₆₀ Fullerene, Based on Semi-Empirical Methods. *Rev Adv Mater Sci* **2003**, *5*, 363–370.
- (7) Wongchoosuk, C.; Udomvech, A.; Kerdcharoen, T. The Geometrical and Electronic Structures of Open-End Fully Functionalized Single-Walled Carbon Nanotubes. *Curr. Appl. Phys.* **2009**, *9*, 352–358.

- (8) Kilina, S.; Badaeva, E.; Piryatinski, A.; Tretiak, S.; Saxena, A.; Bishop, A. R. Bright and Dark Excitons in Semiconductor Carbon Nanotubes: Insights from Electronic Structure Calculations. *Phys. Chem. Chem. Phys.* **2009**, *11* (21), 4113–4123.
- (9) Gambetta, A.; Manzoni, C.; Menna, E.; Meneghetti, M.; Cerullo, G.; Lanzani, G.; Tretiak, S.; Piryatinski, A.; Saxena, A.; Martin, R. L. Real-Time Observation of Nonlinear Coherent Phonon Dynamics in Single-Walled Carbon Nanotubes. *Nat. Phys.* **2006**, *2*, 515–520.
- (10) Araujo, P. T.; Doorn, S. K.; Kilina, S.; Tretiak, S.; Einarsson, E.; Maruyama, S.; Chacham, H.; Pimenta, M. A.; Jorio, A. Third and Fourth Optical Transitions in Semiconducting Carbon Nanotubes. *Phys. Rev. Lett.* **2007**, *98* (6), 067401.
- (11) Shreve, A. P.; Haroz, E. H.; Bachilo, S. M.; Weisman, R. B.; Tretiak, S.; Kilina, S.; Doorn, S. K. Determination of Exciton-Phonon Coupling Elements in Single-Walled Carbon Nanotubes by Raman Overtone Analysis. *Phys. Rev. Lett.* **2007**, *98* (3), 037405.
- (12) Hehre, W. J.; Stewart, R. F.; Pople, J. A. Self-Consistent Molecular-Orbital Methods. I. Use of Gaussian Expansions of Slater-Type Atomic Orbitals. *J. Chem. Phys.* **1969**, *51* (6), 2657–2663.
- (13) Collins, J. B.; von R. Schleyer, P.; Binkley, J. S.; Pople, J. A. Self-Consistent Molecular Orbital Methods. XVII. Geometries and Binding Energies of Second-Row Molecules. A Comparison of Three Basis Sets. *J. Chem. Phys.* **1976**, *64*, 5142–5151.
- (14) Binkley, J. S.; Pople, J. A.; Hehre, W. J. Self-Consistent Molecular Orbital Methods. 21. Small Split-Valence Basis Sets for First-Row Elements. *J. Am. Chem. Soc.* **1980**, *102* (3), 939–947.

- (15) Gordon, M. S.; Binkley, J. S.; Pople, J. A.; Pietro, W. J.; Hehre, W. J. Self-Consistent Molecular-Orbital Methods. 22. Small Split-Valence Basis Sets for Second-Row Elements. *J. Am. Chem. Soc.* **1982**, *104* (10), 2797–2803.
- (16) Pietro, W. J.; Francl, M. M.; Hehre, W. J.; DeFrees, D. J.; Pople, J. A.; Binkley, J. S. Self-Consistent Molecular Orbital Methods. 23. Supplemented Small Split-Valence Basis Sets for Second-Row Elements. *J. Am. Chem. Soc.* **1982**, *104* (19), 5039–5048.
- (17) Vosko, S. H.; Wilk, L.; Nusair, M. Accurate Spin-Dependent Electron Liquid Correlation Energies for Local Spin Density Calculations: A Critical Analysis. *Can. J. Phys.* **1980**, *58*, 1200–1211.
- (18) Lee, C.; Yang, W.; Parr, R. G. Development of the Colle-Salvetti Correlation-Energy Formula into a Functional of the Electron Density. *Phys. Rev. B* **1988**, *37* (2), 785–789.
- (19) Yanai, T.; Tew, D. P.; Handy, N. C. A New Hybrid Exchange–correlation Functional Using the Coulomb-Attenuating Method (CAM-B3LYP). *Chem. Phys. Lett.* **2004**, *393* (1–3), 51–57.
- (20) Tretiak, S.; Igumenshchev, K.; Chernyak, V. Exciton Sizes of Conducting Polymers Predicted by Time-Dependent Density Functional Theory. *Phys. Rev. B* **2005**, *71*, 033201.
- (21) Kim, K.; Jordan, K. D. Comparison of Density Functional and MP2 Calculations on the Water Monomer and Dimer. *J. Phys. Chem.* **1994**, *98* (40), 10089–10093.
- (22) Stephens, P. J.; Devlin, F. J.; Chabalowski, C. F.; Frisch, M. J. Ab Initio Calculation of Vibrational Absorption and Circular Dichroism Spectra Using Density Functional Force Fields. *J. Phys. Chem.* **1994**, *98*, 11623–11627.
- (23) Becke, A. D. Density-Functional Exchange-Energy Approximation with Correct Asymptotic Behavior. *Phys. Rev. A* **1988**, *38* (6), 3098–3100.

- (24) Foster, J. P.; Weinhold, F. Natural Hybrid Orbitals. *J. Am. Chem. Soc.* **1980**, *102* (24), 7211–7218.
- (25) Runge, E.; Gross, E. K. Density-Functional Theory for Time-Dependent Systems. *Phys. Rev. Lett.* **1984**, *52*, 997.
- (26) Martin, R. L. Natural Transition Orbitals. *J. Chem. Phys.* **2003**, *118*, 4775–4777.
- (27) Kilina, S.; Kilin, D.; Tretiak, S. Light-Driven and Phonon-Assisted Dynamics in Organic and Semiconductor Nanostructures. *Chem. Rev.* **2015**, *115*, 5929–5978.

4. DOPING CHARACTER OF SINGLE-WALLED CARBON NANOTUBES FUNCTIONALIZED WITH CHLORINE

4.1. Motivation

Single walled carbon nanotubes (SWCNTs) are the focus of intense investigation as nanomaterial with a wide range of applications due to their chirality-dependent properties. Despite this, the range of properties exhibited by pristine SWCNTs is somewhat limited. Because of this, further structural modification is required to fine-tune characteristics such as electronic levels for use as advanced doping materials or optical transition energies for use as active layers in telecommunications devices. A widely used strategy for accomplishing such modifications involves sidewall chemical functionalization. Various recent experimental studies have reported success in modifying SWCNT properties via chemical functionalization, including functionalizing (6,2) SWCNTs with chlorine in order to introduce doped electronic character and (6,5) SWCNTs with aryl derivatives to introduce red-shifted emission features. Such modifications greatly increase their utility in practical applications and generates many open research questions. The nature of the mechanism that results in doped (6,2) SWCNTs is unknown. For (6,5) SWCNTs, a number of low-energy emission features are introduced by aryl functionalization, the origin of which is unknown. To optimize these new materials for their respective applications requires insights into these phenomena. Providing such insights is the goal of the computational studies presented in this and the next chapter.

This chapter focuses on evaluating the binding strength, electronic, and optical properties of (6,2) SWCNTs functionalized with chlorine using density functional theory (DFT) and linear-response time-dependent density functional theory (TDDFT) for both infinite length and finite-cell sizes with specific interest in the electronic structure that leads to p-doping. These studies

are performed for both neutral and charged systems and demonstrate that neutral chlorine atoms bind most favorably as pairs on the same chlorine ring producing an unoccupied midgap state consistent with p-type doping. SWCNTs functionalized with charged chlorine ions favor addition of a single chlorine to minimize charge localization, and the midgap state introduced in neutral chlorination becomes occupied with the introduction of a charge resulting in the production of an n-doped system. This information is invaluable for assessing the viability of these materials for use in applications where doping character is required. In addition to this work with chlorine functionalized (6,2) SWCNTs, the next chapter focuses on exploring how the role of configuration of chemical functionalization of (6,5) SWCNTs with aryl derivatives using similar techniques.

4.2. Computational Methodology

4.2.1. Generation of the Computational Cells

Pristine (6,2) SWCNTs were generated using Tubegen¹ software. The computational super cell for the calculations with periodic boundary conditions was generated to be three unit cells of SWCNT long with the introduction of 1 nm of vacuum in all dimensions perpendicular to the tube axis to minimize interactions between individual tubes. This computational cell was then sampled with a 1x1x1 Monkhorst-Pack k-point grid using the PBE functional^{2,3} and PAWS basis set.^{4,5} Finite systems of two unit cells (220 atoms, ~3 nm) and five unit cells (532 atoms, ~7.5 nm) in length were also generated. The cap of the finite systems was functionalized with one methylene group bonded along the direction of the chiral vector while the rest of the capping positions were functionalized with hydrogen atoms, a capping scheme that has previously been shown to eliminate edge-localized trap states.⁶ The pristine finite SWCNTs were then optimized using MOPAC⁷ software with AM1⁸ methodology and a minimal basis set as previously

described.⁹ The resulting optimized SWCNTs were functionalized with either one or two chlorine atoms initially placed about 1.5 Å from the carbon atom in a perpendicular direction from the SWCNT surface. To simulate the effect of functionalization with chlorine atoms as well as chloride ion, each system was optimized with both a zero and a negative one charge per

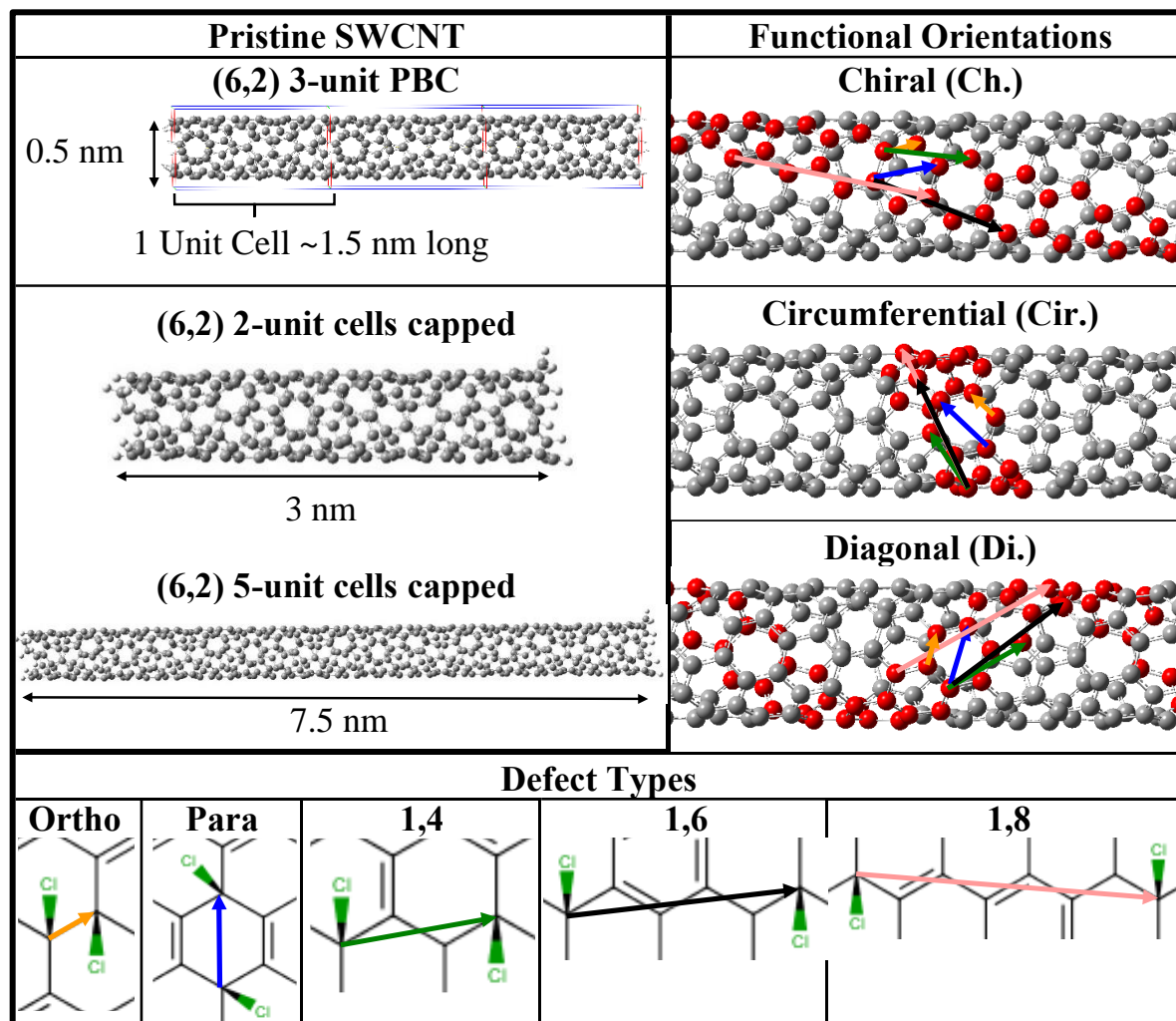


Figure 4.1. Overview of tube properties and defect arrangements. The upper left shows the characteristics of the pristine SWCNTs used. The bottom shows the different arrangements of Cl pairs with respect to each other. Ortho and para arrangements have two Cl atoms bound to the same ring, and 1,4, 1,6, and 1,8 arrangements have two Cl atoms bound to different rings. The upper right shows the different directions of the defects on the tube: along the tube's chiral axis, around the circumference of the tube, or diagonally wrapped around the tube.

chlorine adsorbed to the SWCNT surface. Geometry optimizations were performed for each arrangement. However, energetically favorable geometries for many systems were found to consist of isolated SWCNTs and chlorine species. This is most common for charged tubes, and data for these arrangements was not included in this chapter. All geometry optimizations and electronic structure calculations were performed using Gaussian09¹⁰ for finite length systems and the Vienna Ab-initio Simulation Package (VASP) 4.2¹¹⁻¹⁴ for calculations with PBC.

4.2.2. Consideration of Multiple Binding Configurations

As mentioned in chapter 3, chiral SWCNTs have several distinct bond-types depending on the axis of the bond with respect to the SWCNT axis. For the purposes of this chapter, the properties need to be characterized for functionalization with respect to different orientations to determine which are most stable. When functionalizing the SWCNT, two chlorine atoms can be added in three distinct orientations with respect to the SWCNT axis (figure 4.1). For each orientation, both ortho and para arrangements are generated where both chlorine atoms are bonded to carbon atoms that are located within the same hexagonal ring. Meta arrangements were not examined because they are not expected to be stable.^{15,16} Additionally, structures where the two chlorine atoms are placed at carbon sites on different rings were considered, including (1,4), (1,6), and (1,8) functionalization (resulting in functionalized carbon atoms being on adjacent rings, two rings apart, and three rings apart, respectively).

4.2.3. Methodologies Used

In order to facilitate the selection of methodology, the results for finite SWCNTs were compared using a number of different functionals and basis sets. Functionals that were tested include PBE,^{2,3} PBE1,^{2,3,17} B3LYP,¹⁸⁻²⁰ and wB97XD,^{21,22} all as implemented by the Gaussian09 software package with the 6-31G basis set. To characterize the effect of basis set size on the

results, STO-3G,^{23,24} 6-31G,²⁵⁻²⁹ and 6-31G*³⁰ basis sets were compared with the constant PBE1 functional.

4.2.4. Characterization of the Systems

4.2.4.1. Binding Energies

The binding energy of chlorine to the tube was determined by the following formula:

$$\Delta E_{\text{binding}} = [E_{\text{chlorinated CNT}} - (E_{\text{pristine CNT}} + n E_{\text{Cl}})] / n \quad (\text{Equation 4.1})$$

where $E_{\text{chlorinated CNT}}$ is the energy of the optimized chlorinated system, $E_{\text{pristine CNT}}$ is the energy of the optimized pristine SWCNT, E_{Cl} is the energy of the energy chlorine atom, and n is the number of chlorine atoms in the system. For cases with higher concentrations, the binding energy was determined using two equations. Equation 1 determines the binding energy of n chlorine atoms to the pristine SWCNT. Equation 2 determines the binding energy of m chlorine atoms to a tube with $(n - m)$ Cl atoms already bound:

$$\Delta E_{\text{b}} = (E_{\text{CNT \& } n \text{ Cl}} - (E_{\text{CNT}} + n E_{\text{Cl}})) / n \quad (\text{Equation 4.2})$$

$$\Delta E_{\text{b}} = (E_{\text{CNT \& } n \text{ Cl}} - (E_{\text{CNT} + (n - m) \text{ Cl}} + m E_{\text{Cl}})) / m \quad (\text{Equation 4.3})$$

4.2.4.2. Geometries

In order to determine the degree to which the optimized geometry of the pristine SWCNT changes in the presence of chlorine, the bond length alternation (BLA) was defined as the difference between the average bond lengths geminal to the functionalized carbon atom and the average of those bond lengths vicinal to the functionalized carbon atom in the SWCNT. For ortho configurations where a single bond is geminal to two functionalized carbon atoms, this shared bond was significantly lengthened over all other bonds and was therefore excluded from the average.

4.2.4.3. Electronic Structures & Optical Features

Density of states (DOS) were generated by broadening about the molecular orbitals using a Gaussian function with linewidth of 0.001 eV. TDDFT^{31,32} calculations were performed for finite tubes optimized with PBE1 functional and 6-31G* basis set, with 40 states calculated for 2-unit tubes and 20 states calculated for 5-unit tubes. Simulated optical spectra were generated by broadening about the TDDFT transitions using a Gaussian function with linewidth of 0.001 eV. The visualize the change in electron density from an optical transition, natural transition orbitals (NTOs)³³ were generated for the lowest energy and most intense TDDFT transitions.

4.3. Evaluation of the Methodologies

4.3.1. Benchmarking of Basis Set and Functional

It was found that the general trend of both binding energies as well as BLA of those chlorinated SWCNTs calculated with PBC and those finite tubes calculated with PBE1 and 6-31G* was in complete agreement (figures 4.2 and 4.3). Additionally, trends in binding energies and bond lengths between different methodologies for finite tubes were generally consistent. Significant differences in binding character is observed between methodologies, especially with regards to the C-Cl bond lengths. PBE1 and wB97XD functionals result in substantially shorter C-Cl bond lengths than PBE and B3LYP functionals. The 6-31G* basis set also shows substantially shorter bond lengths than 6-31G. As such, all further calculations and analysis was performed with finite SWCNT systems using the PBE1 functional and 6-31G* basis set. Finite systems were used over PBC due to the lack of substantial differences between the two types of systems and the relative ease of calculating finite systems over PBC systems, and the PBE1

functional was chosen over wB97XD due to the unreasonably large band gaps in wB97XD optimized systems.

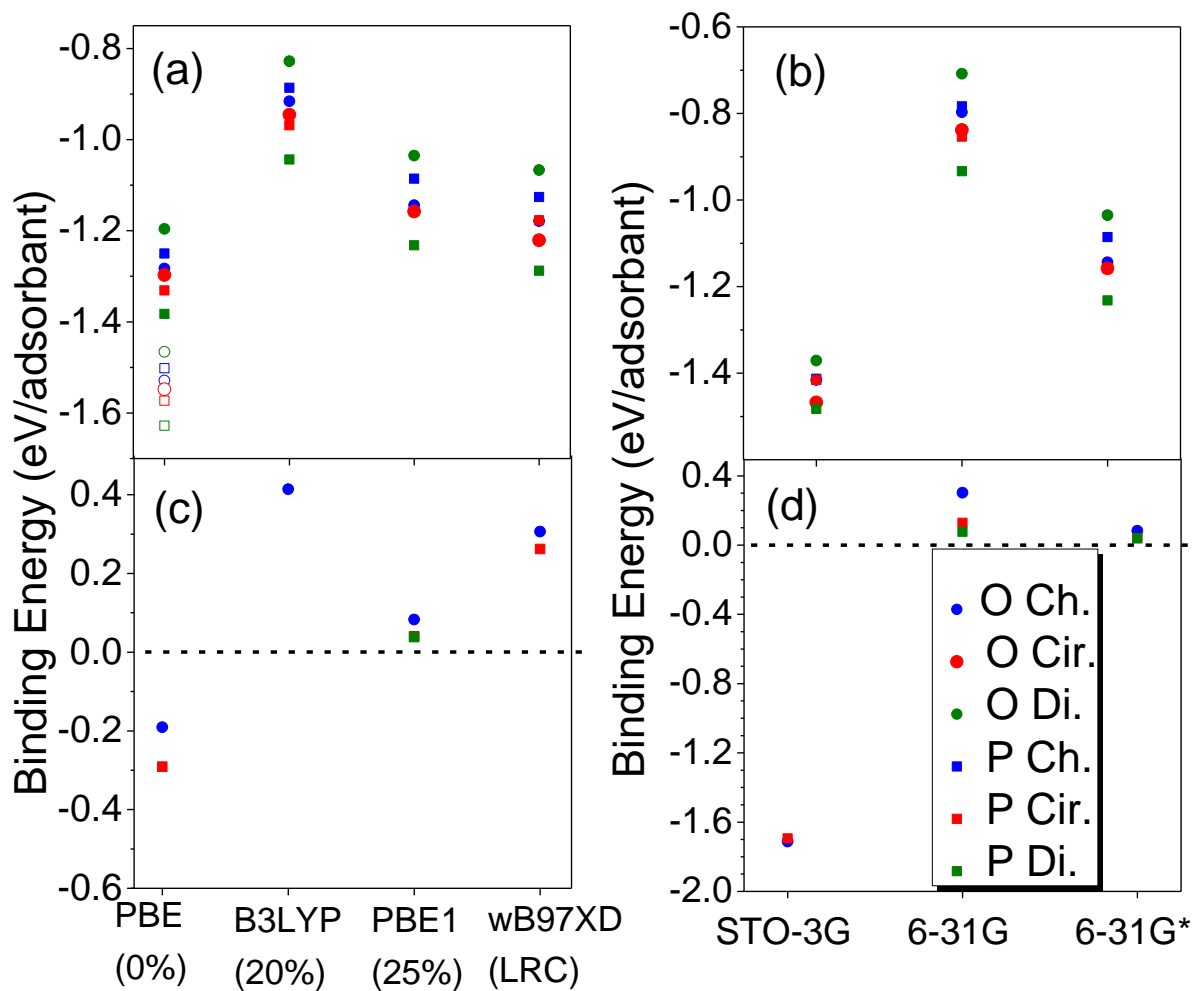


Figure 4.2. Comparison of binding energies for different methodologies. The data for the comparison between different functional (a,c) was computed with a consistent basis set of 6-31G*. The data for comparison between different basis sets (b,d) was computed with PBE1 consistently. Solid points indicate that the data was for finite tubes, whereas hollow points indicate are used for the data from calculations with PBC. Panels (a) and (b) are for neutral systems, and panels (c) and (d) are present data from systems with a negative charge.

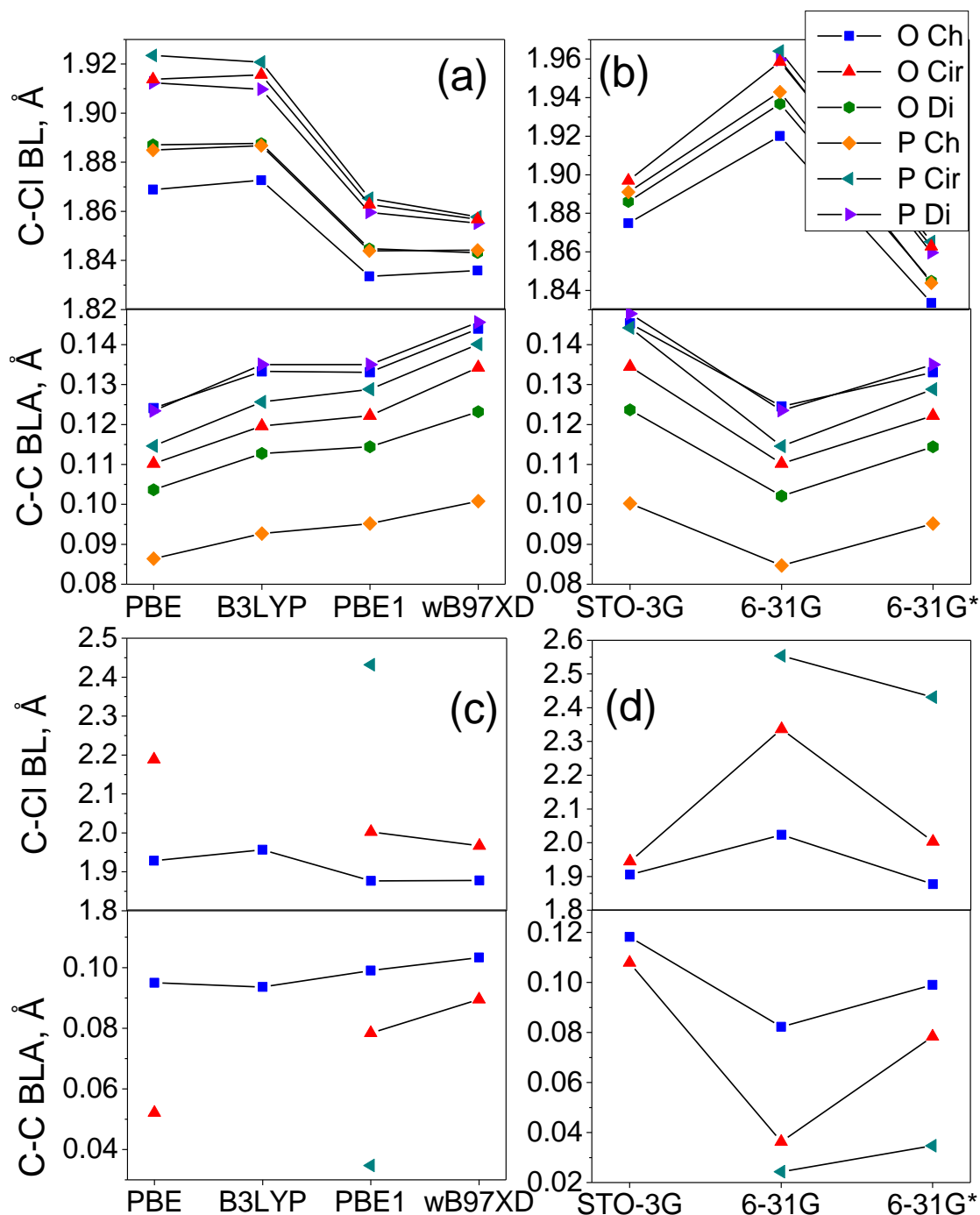


Figure 4.3. Bond character of chlorinated tubes at the chlorination site with respect to methodology. The upper part of each panel shows the average C-Cl bond length, and the lower part shows the C-C bond length alternation. Bond length alternation is the average difference between the C-C bonds adjacent to the chlorine defect, which are expected to be elongated, and C-C bonds two bonds away from the chlorine defect, which are expected to be shortened. Panels a and b describe neutral tubes, while panels c and d describe charged tubes. Panels a and c show how the bond character changes with different functionals, all optimized with a 6-31G* basis set. Panels b and d show the bond character changes with different basis sets, all optimized with the PBE1 functional.

The qualitative differences between trends of binding energies calculated with different functionals is marginal. However, going from 20% Hartree-Fock exchange in B3LYP to 25% Hartree-Fock exchange in PBE1 results in significantly shortened C-Cl bond lengths (figure 4.3(a)) and the corresponding stronger binding (figure 4.2(a)). As such, further calculations were performed with PBE1. It is worth noting that while the SWCNT systems calculated with PBC exhibited stronger SWCNT-Cl binding, the binding energies were qualitatively the same as the systems calculated with the capped SWCNTs (figure 4.2(a)). As such, further calculations were performed with the capped SWCNT. When comparing the basis sets, the qualitative trends for binding energy of different connectivity are very similar (figure 4.2(b)) with the exception of the circumferential arrangement for the smallest basis. However, the difference in binding energies between SWCNT-dichloride systems of different conformations is greatest for the larger basis set 6-31G, and trends between 6-31G and 6-31G* are entirely consistent. Adding the polarization to the basis set resulted in stronger binding energies as well as a greater transition from sp^2 to sp^3 character for the carbon atoms bonded to the chlorine in the system, as is evidenced by the decreasing C-Cl bond lengths and increasing C-C bond length within the hexagonal lattice. Based on this, and since this study is focusing on the covalent functionalization of SWCNTs with chlorine, the larger polarized basis set was chosen, and all further computations utilize the 6-31G* basis set.

4.4. Correlation between Binding Energies and Geometries

4.4.1. Neutral Systems: Favorable Binding Interactions on a Single Hexagonal Ring

All the neutral systems explored showed a favorable interaction between the SWCNT and chlorine atom (figure 4.4). Binding of a single neutral chlorine atom to the sidewall of the 2-unit (6,2) SWCNT is energetically favorable, with a binding energy of -0.81 eV. The C-Cl bond

length is 1.91 Å, and the length of C-C bonds adjacent to the carbon atom bonded to chlorine were shown to increase by about 0.06 Å due to disruption of sp^2 hybridization in the functionalized species (figure 4.5(b)). When a second chlorine atom is bonded to the same hexagonal ring of the SWCNT, the binding energy becomes substantially more favorable, with

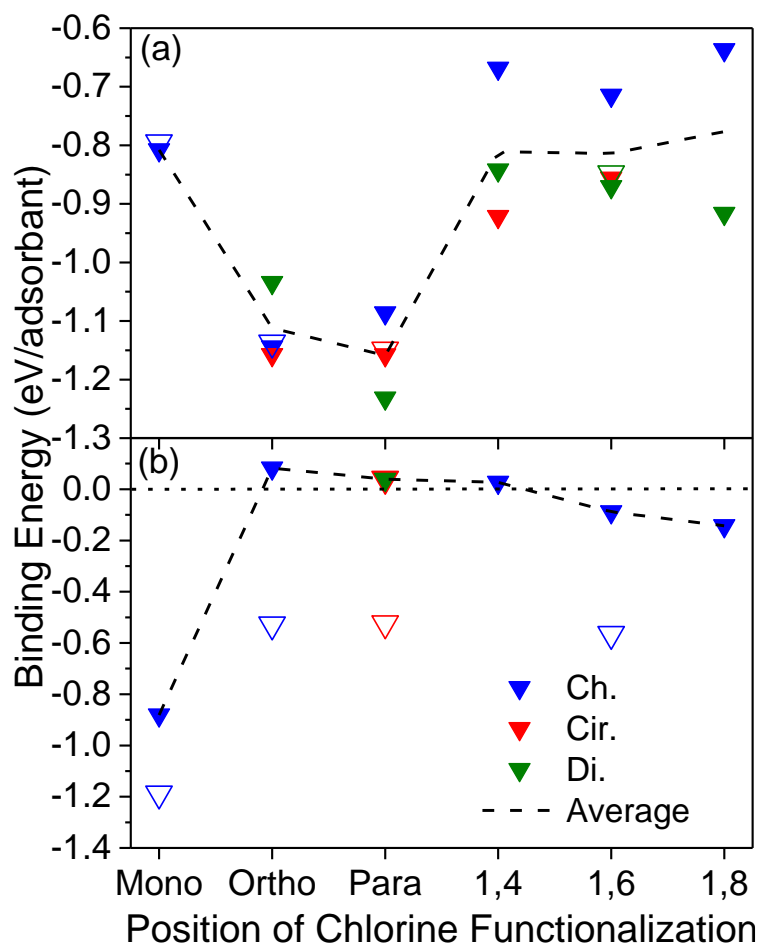


Figure 4.4. Binding energy of different configurations with varying distance between the two chlorine atoms for (a) neutral chlorinated SWCNTs and (b) charged chlorinated SWCNTs. Binding energy determined for finite tubes functionalized with the PBE1 functional and 6-31G* basis set. Hollow data points are for functionalized SWCNTs of length 5 units, and filled data points are for functionalized SWCNTs of length 2 units. For neutral cases, the most favorable binding occurs when two Cl atoms are bound on the same ring. For charged cases, monochlorination is most favorable, with dichlorination only becoming favorable as the distance between Cl atoms increases.

binding energies between -1.0 eV and -1.3 eV per chlorine atom depending on the arrangement, as shown in figure 4.4(a). Additionally, the C-Cl bonds become shorter, ranging from 1.83 to 1.87 Å. Covalent functionalization with a single chlorine atom in a ring results in the generation of a radical, so further functionalization is required to fulfill valency. Additionally, addition of the first chlorine atom to the ring results in an increase of p character for all carbon atoms in the hexagonal ring, and therefore covalently binding another chlorine atom and changing one of the carbon atoms to sp³-like is favorable. This effect is absent in the cases where two chlorine atoms are bound to separate rings, as with 1,4, 1,6, and 1,8 functionalization. In these cases, the binding energy varies dramatically, ranging from -0.95 to -0.65 eV, and appears to be mostly dependent on direction of functionalization where chiral arrangements are generally less stable than circumferential or diagonal arrangements. In addition, the bond lengths for these cases are significantly different than cases where two chlorine atoms are bound to the same ring, with C-Cl bond lengths increasing to 1.88-1.91 Å (figure 4.5(a)). These bond lengths are also similar to the case of mono-functionalization, further demonstrating the effect of multiple functional groups on the same hexagonal ring. Overall, it is shown that the neutral chlorine atom is most favorably adsorbed in pairs bound to the same ring as these species have the strongest binding. Tube length plays an insignificant role in these neutral species where nearly identical binding energies are observed between 2-unit and 5-unit long systems (figure 4.4(a)).

4.4.2. Charged Systems: Preferential Binding on Separate Rings

Charged systems exhibit the trends as previously described for neutral systems (figure 4.4(b)). The binding energy of a single charged chlorine atom to a 2-unit long (6,2) SWCNT is -0.88 eV, and the stability decreases dramatically when a second charged chlorine atom is bound to the tube (figure 4.4(b)). Slightly positive binding energies are observed for two chlorine atoms

in close proximity to each other. This effect is reduced as the distance between chlorine atoms increases, with negative binding energies being observed for the 1,6- and 1,8-functionalization cases. However, as with neutral tubes, the C-Cl bond length increases in cases where two chlorine atoms are far apart from each other (figure 4.5(c)). Mullikan charge analysis indicates that the charge in these systems is predominantly localized on the carbon atoms where functionalization occurs. Therefore, the binding energy of charged chlorine to the SWCNT in the system is heavily dependent on the proximity of the negative charges as opposed to the strength of interaction between the chlorine atoms and the SWCNT. This effect can be further observed when comparing the longer tubes. Unlike with neutral tubes, there is a substantial increase in stability when the length of a tube is increased for charged cases: the difference in binding energy per chlorine atom going from 2-unit to 5-unit long SWCNTs changes by about -0.3 eV and -0.5 eV for the monochlorinated and dichlorinated cases respectively. This difference is due to the increased delocalization of the negative charge as the size of the SWCNTs increase. Overall, it can be concluded that binding of chlorine ions to CNTs likely occurs at very low concentrations, with a very large distance between functionalization sites.

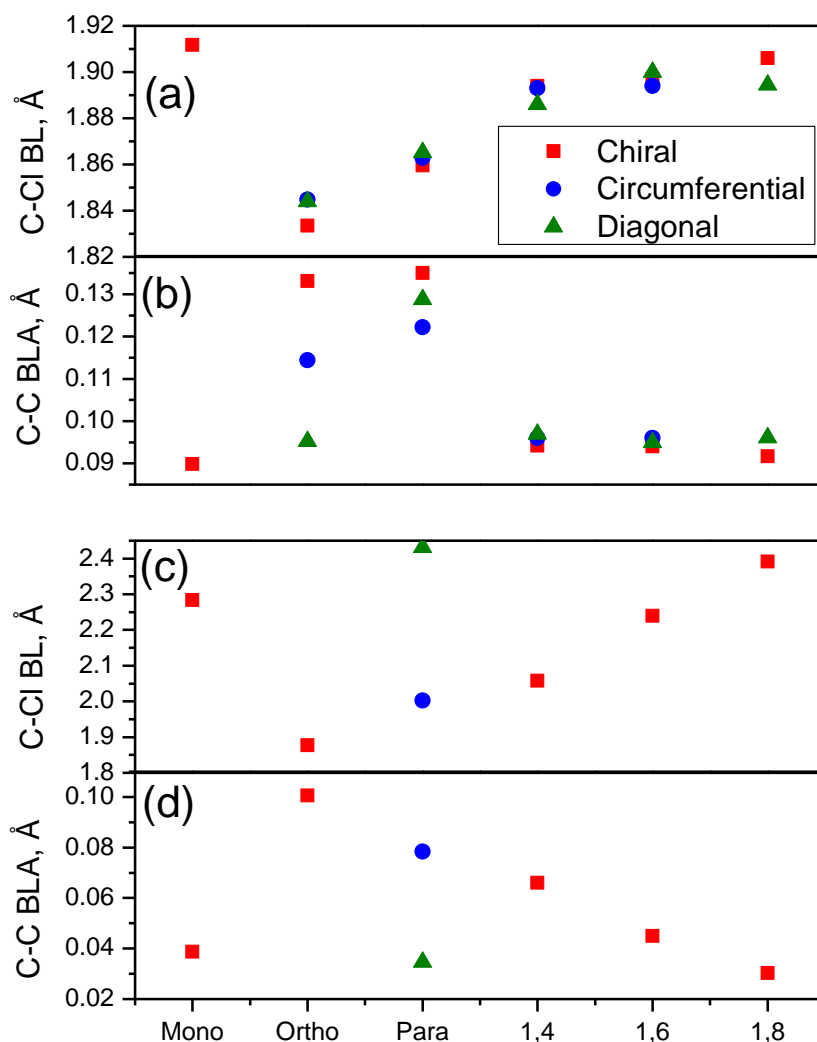


Figure 4.5. Bond length data for all 2-unit chlorinated finite tube arrangements optimized with PBE1 functional and 6-31G* basis set. Panels a and b describe the bond character of neutral chlorinated tubes, while panels c and d describe the bond character of charged tubes. Panels a and c show the C-Cl bond length with respect to the Cl arrangement, and panels b and d show the C-C bond length alternation with respect to the Cl arrangement. Bond length alternation is the average difference between the C-C bonds adjacent to the chlorine defect, which are expected to be elongated, and C-C bonds two bonds away from the chlorine defect, which are expected to be shortened. The top panel shows the data for neutral cases and the bottom panel shows charged cases. For neutral cases, the bond lengths for arrangements where Cl are bonded to different rings are similar to the monochlorinated case, while cases where Cl are bonded to the same ring show much smaller C-Cl bonds and generally much greater bond length alternation. For charged cases, a similar trend appears, where dichlorinated cases become more like monochlorinated case as the Cl separation increases. The main outlier is the diagonal para arrangement, which shows much weaker bonding than other arrangements with 2 Cl atoms bonded to the same ring.

4.5. Analysis of Electronic Structure & Electron Density

4.5.1. Neutral SWCNTs

4.5.1.1. *Molecular Orbitals and Density of States*

The density of states is also notably changed by functionalization of the SWCNT with chlorine atoms. This is especially true of the ortho-Ch, para-Cir, and Para-Di cases. Figure 4.6 shows the density of states for the strongest binding charged and neutral chlorine arrangements on both 2-unit and 5-unit tubes. Binding a pair of neutral chlorine atoms to a 2-unit (6,2) SWCNT results in the occupied frontier molecular orbitals entering the HOMO-LUMO gap (figure 4.7). The depth to which they enter the gap is dependent on the specific configuration of functionalization. Analysis of the molecular orbitals for this additional state in all arrangements reveal it is localized around the chlorine defect. However, the exact nature of this state varies somewhat between different arrangements, with increasing delocalization of the LUMO as the spacing between chlorine atoms increases (table 4.1). Increasing the distance between chlorine functionalization results in a decreased HOMO-LUMO gap (figure 4.6). The gap energies range from 1.84 eV for the circumferential ortho arrangement to 1.25 eV for the diagonal 1,8 arrangement, compared to 2.03 eV for the pristine tube. Mono-chlorination has very little effect on the energy of the HOMO-LUMO, decreasing it marginally to 1.93 eV and not resulting in the introduction of any additional mid-gap states. The dramatic difference is due to the fact that the lowest energy electron configuration for neutral monochlorinated tubes is a doublet configuration. The electronic structure of neutral chlorinated tubes is consistent for 2-unit tubes and infinite tubes optimized with PBC (see figure 4.7), although the size of the HOMO-LUMO gap is smaller for the systems calculated with PBC and the PBE functional than for the finite

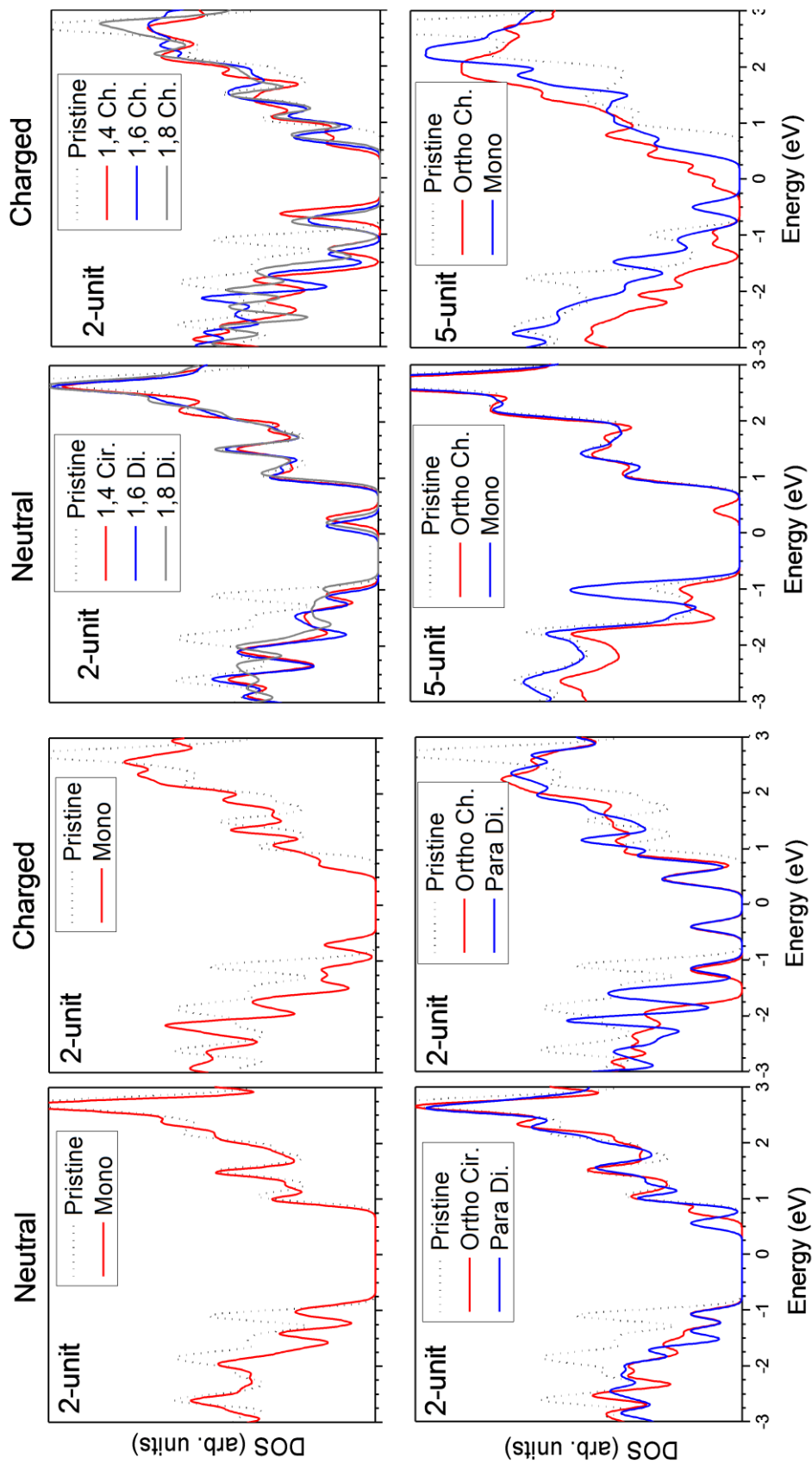


Figure 4.6. Density of states of selected chlorinated tubes generated by broadening about the states using a Gaussian function of linewidth of 0.06 eV. The zero energy for charged and pristine tubes is the center of the HOMO-LUMO gap. For neutral tubes, the DOS was aligned with higher energy states in the conduction band of the pristine tube. The top row shows tubes functionalized with neutral Cl, and the bottom row shows tubes functionalized with charged Cl. The tubes functionalized with a pair of neutral Cl atoms show the introduction of an unoccupied state in the band gap. This state gets closer to the Fermi energy the greater the separation of Cl atoms. Charged cases show a much greater change in band structure, but distinctly show occupied states near the conduction band, particularly in the longer tubes.

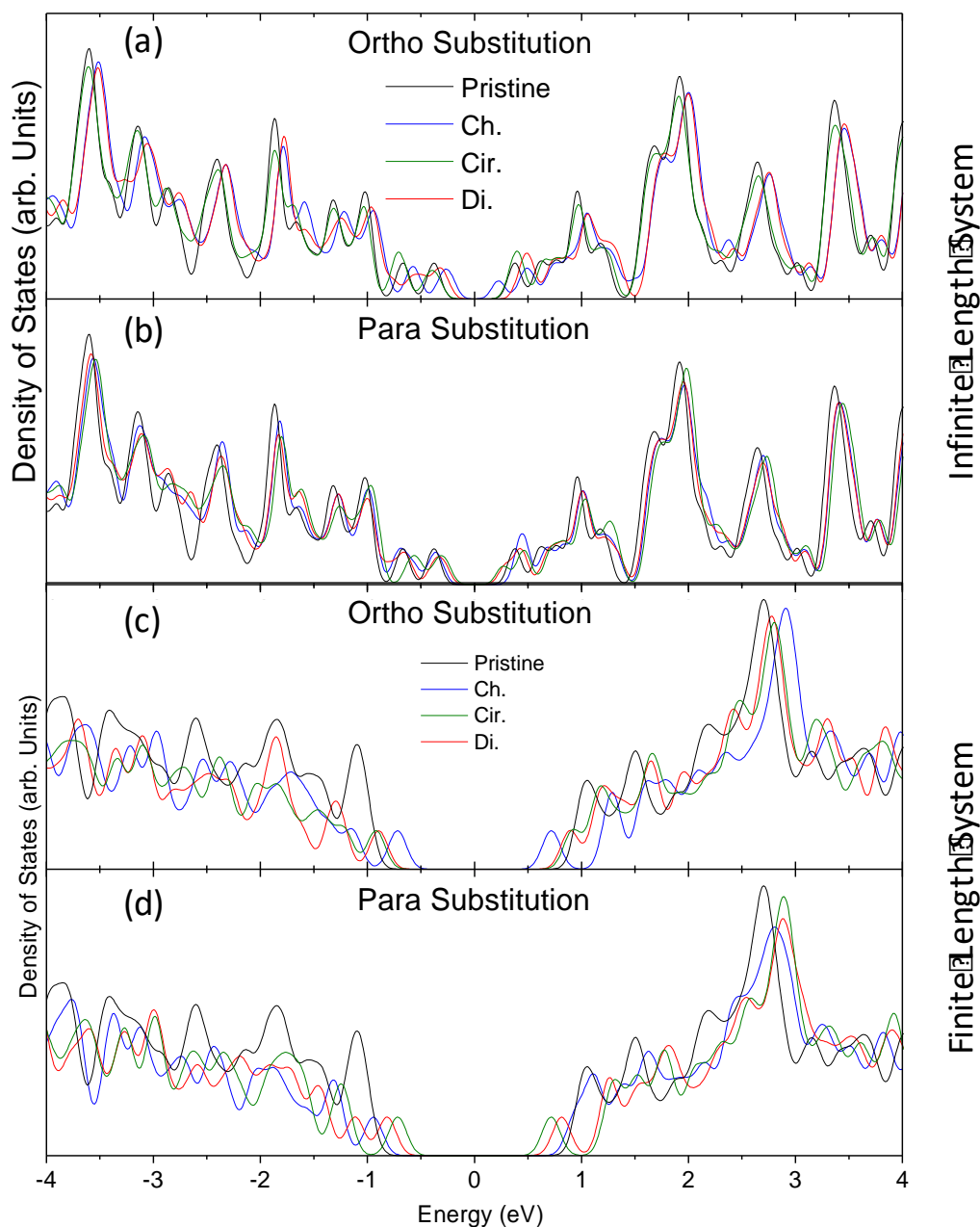
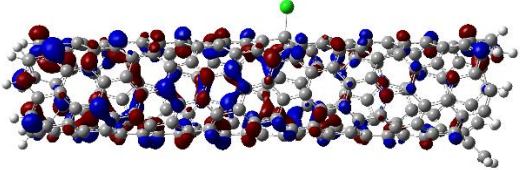
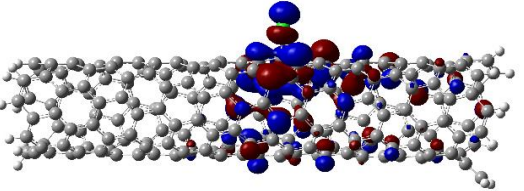
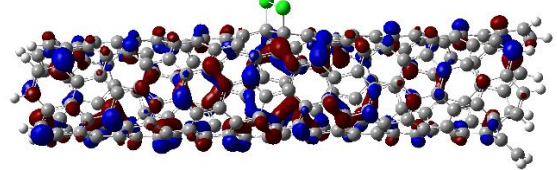
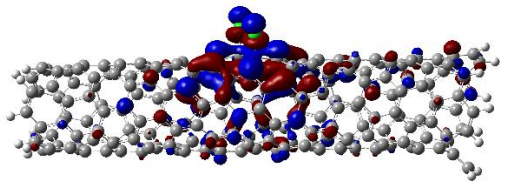
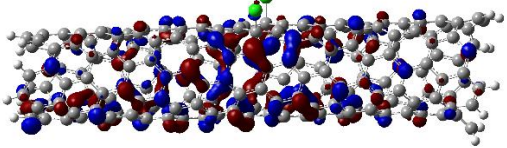
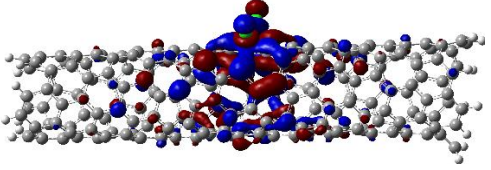
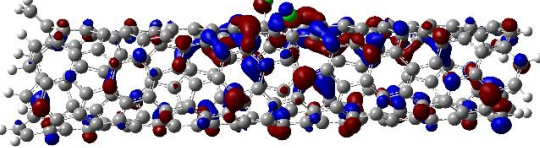
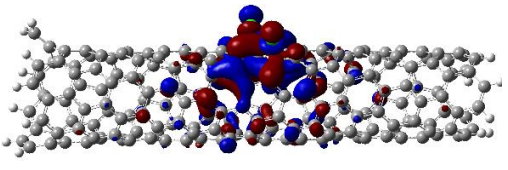
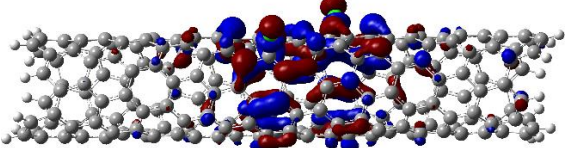
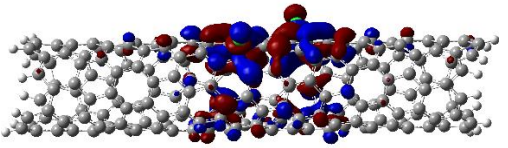
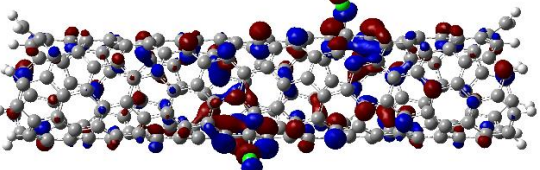
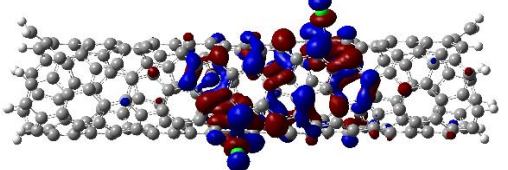


Figure 4.7. (a) Density of States (DOS) for neutral dechlorinated SWCNTs with PBC calculated using PBE functional and PAWS basis set. The top panel is for ortho substitution, and the bottom panel is for para substitution. For ortho substitution, the HOMO-LUMO gap decreases from functionalization with chlorine atoms along the chiral axis. (b) For para substitution, circumferential and diagonal functionalization results in a decreased gap. (c) Density of States (DOS) for neutral finite tubes calculated using PBE1 functional and 6-31G* basis set. The top panel is for ortho substitution, and the bottom panel is for para substitution. For ortho substitution, the HOMO-LUMO gap decreases from functionalization with chlorine atoms along the chiral axis. (d) For para substitution, circumferential and diagonal functionalization results in a decreased gap.

Table 4.1. Molecular orbitals for the HOMO and LUMO of the chlorinated neutral finite SWCNTs optimized with PBE1 functional and 6-31G* basis set plotted with an isovalue of 0.02. Notable is the significant localization of the electron density around the chlorine atoms in the LUMO of the neutral species, showing that this state is primarily chlorine and defect character.

	HOMO	LUMO
Mono $E_{\text{gap}} = 1.93$		
Ortho Cir. $E_{\text{gap}} = 1.84$		
Para Di. $E_{\text{gap}} = 1.63$		
1,4 Cir. $E_{\text{gap}} = 1.36$		
1,6 Di. $E_{\text{gap}} = 1.27$		
1,8 Di. $E_{\text{gap}} = 1.25$		

systems calculated with the PBE1 functional due to the increased delocalization from the hybrid functional. The frontier molecular orbitals from the 2-unit neutral tube clearly shows that new states are not generated in the gap, but instead the HOMO and LUMO from the pristine SWCNT enter the gap upon functionalization (figure 4.8). These orbitals are defect-based but are delocalized across the entire length of the SWCNT in HOMO. However, in the LUMO electron density resides on the defect itself and is even withdrawn onto the chlorine group due to its slight

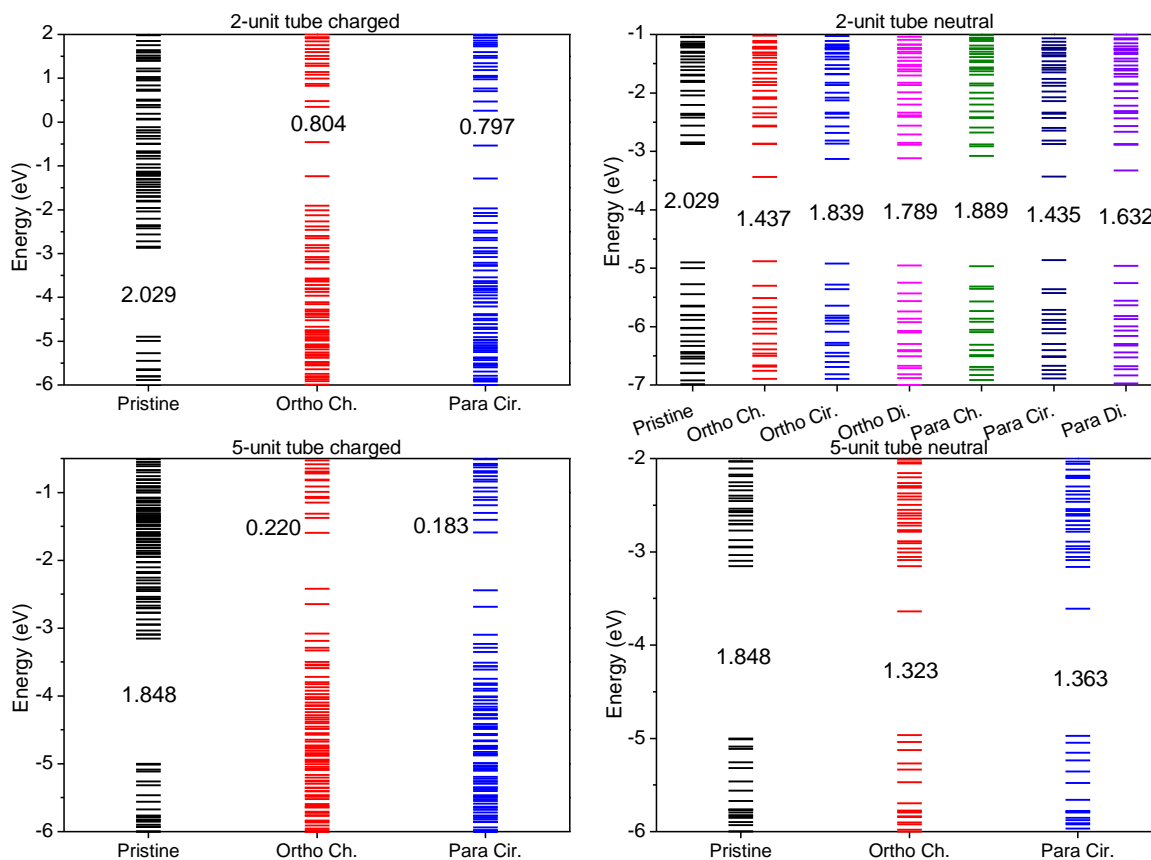


Figure 4.8. Molecular orbital diagram for chlorine doped SWCNTs calculated using PBE1 functional and 6-31G* basis set. The number in each diagram indicates the band gap for each arrangement. P doping is clearly observed for neutral chiral ortho and circumferential and diagonal para configurations. N doping is clearly observed in all charged cases. This is consistent in both the long capped systems (5 SWCNT units) as well as the short capped systems (2 SWCNT units).

electronegativity. As such, a transition from the HOMO to the LUMO would be predominantly charge-transfer in nature.

4.5.1.2. Projected Density of States

To further validate the electron localization in the frontier molecular orbitals and through the valence and conduction bands, projected density of states (pDOS) were generated for the extended conjugated region of carbon atoms on the SWCNT as well as on the chlorine atoms. Using this analysis, it is shown that the chlorine contributes to states predominantly deep in the

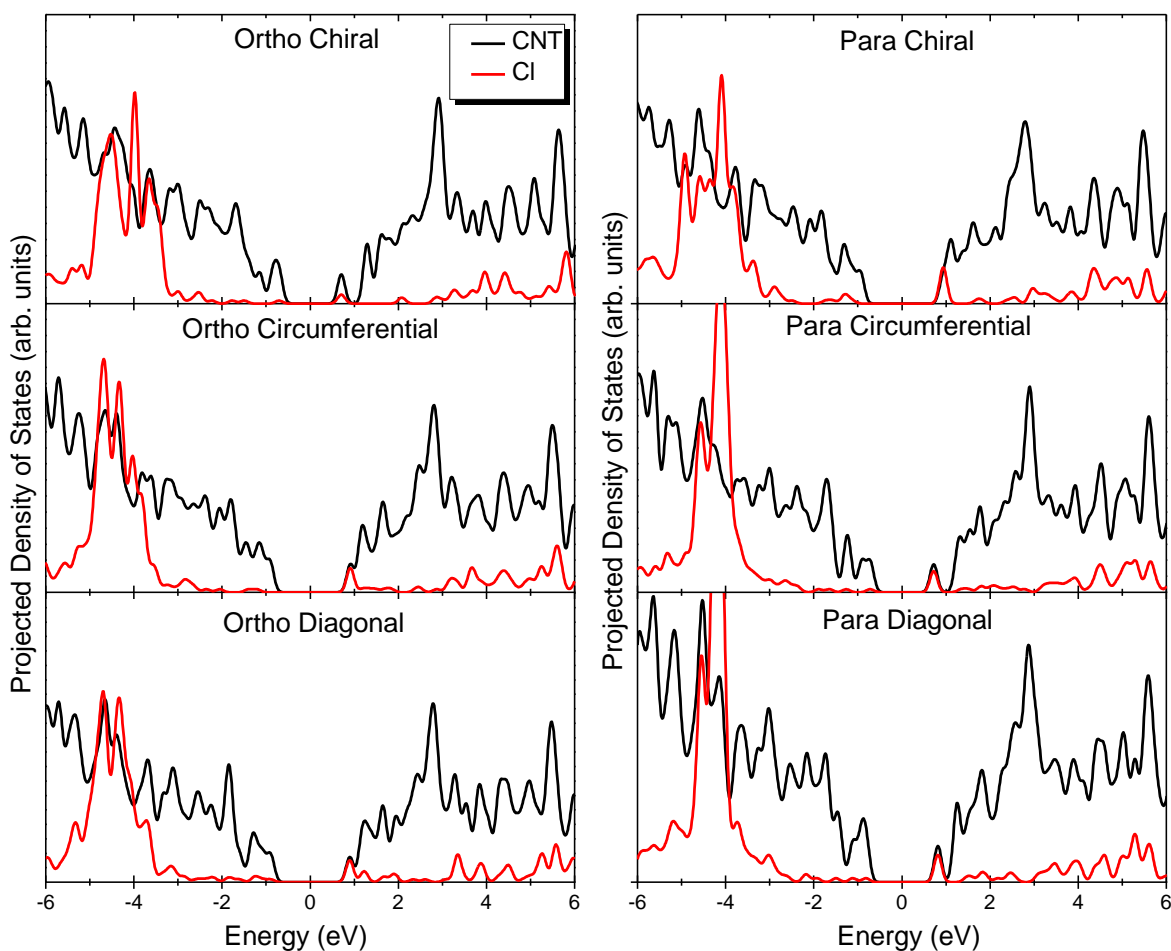


Figure 4.9. Projected density of States (pDOS) for neutral finite tubes calculated using PBE1 functional and 6-31G* basis set. The Cl DOS was multiplied by 10 to better illustrate the contribution of Cl, due to the much larger number of carbon atoms. The left panels are for ortho substitution, and the right panels are for para substitution. For all configurations, the states with the strongest chlorine influence are located deep in the valence band, although there is significant contribution to the LUMO from Cl.

valence band. However, there is always significant contribution from the chlorine atoms in the LUMO (lowest energy state in the conduction band, figure 4.9). This contribution is highest for species with the widest gap and lowest with the narrowest gap. For neutral chlorinated SWCNTs, the gap is closed the most in the cases where more electron density is located on the SWCNT rather than the chlorine. These species also exhibit the greatest localization of electron density around the defect site in the HOMO (table 4.1).

4.5.2. Charged SWCNTs: The Emergence of n-Doped Behavior

In the charged systems, the defect state introduced by chlorine atom functionalization becomes occupied and resides near the valence band (figure 4.6), dramatically reducing the size of the HOMO-LUMO gap and causing the HOMO to be localized around the chlorine defect and the LUMO to be localized around the edges of the tube (table 4.2). This DOS of the functionalized charged tube resembles an n-doped system due to the proximity of the additional occupied state and the conduction band. In 2-unit tubes, the size of the HOMO-LUMO gap

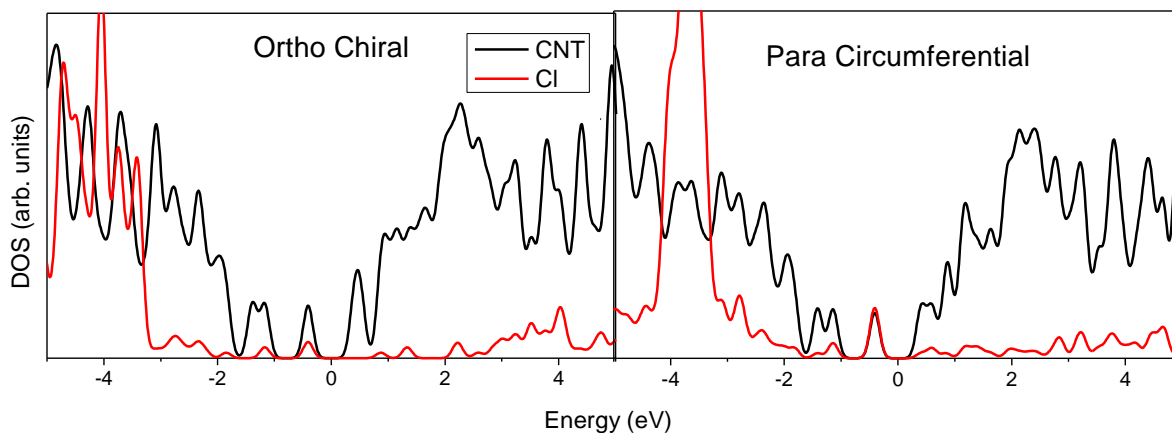


Figure 4.10. Projected density of States (pDOS) for charged finite tubes calculated using PBE1 functional and 6-31g* basis set. The Cl DOS was multiplied by 10 to better illustrate the contribution of Cl, due to the much larger number of carbon atoms. The pDOS shows a substantial Cl contribution in states well below the band gap. However, there is also significant Cl contribution in the HOMO, especially in the circumferential para configuration.

increases with increased separation of chlorine atoms, with a gap of 0.79 eV for the chiral ortho arrangement and a gap of 1.45 eV for the chiral 1,8 arrangement (figure 4.6). The behavior of charged mono-chlorinated tubes are very similar, although somewhat less pronounced, with a HOMO-LUMO gap energy of 1.42 eV. As with neutral cases, behavior is consistent between 2-unit and 5-unit tubes. With 5-unit dichlorinated tubes, the n-doped nature of the system becomes very apparent, with occupied states clearly present above the gap, and a HOMO-LUMO gap of only 0.220 eV for the chiral ortho arrangement. For all charged species, the molecular orbitals show the emergence of a significant sub-gap as the result of the introduction of the occupied state near the conduction band (figure 4.8). The HOMO in all cases becomes localized on the SWCNT defect, as evidenced by both the molecular orbitals (table 4.2) as well as the pDOS (figure 4.10). The electron density in the LUMO becomes localized distant from the defect site: it isn't clear if this is attributed to end group effects or not.

Table 4.2. Molecular orbitals for the HOMO and LUMO of charged chlorinated finite tubes optimized with PBE1 functional and 6-31g* basis set, plotted with an isovalue of 0.02. The HOMO is localized around the Cl atoms and the sp^3 defect, while the LUMO is localized on the edges of the tube. The HOMO of the charged chlorinated tubes is very similar to the LUMO of the neutral chlorinated tubes, showing that this state introduced by chlorination becomes occupied by the addition of a charge.

	HOMO	LUMO
Mono $E_{\text{gap}} = 1.42$		
Ortho Ch. $E_{\text{gap}} = 0.80$		
Para Di. $E_{\text{gap}} = 0.79$		
1,4 Ch. $E_{\text{gap}} = 1.22$		
1,6 Ch. $E_{\text{gap}} = 1.35$		
1,8 Ch. $E_{\text{gap}} = 1.45$		

4.6. Absorption Spectra

4.6.1. Neutral Species: Reduced Gaps → Lower Energy Emission

The absorption spectra calculated from TDDFT of the neutral chlorinated SWCNTs is presented in figure 4.11(a). The primary absorption peak observed in pristine tubes is found at about 1.9 eV with an oscillator strength of 0.612 for 2-unit tubes, and around 1.7 eV with an oscillator strength of 8.99 for 5-unit tubes. This is due to the significant reduction of the HOMO-LUMO gap, resulting in a bright π - π^* of lower energy. This is a common observation in systems where the lowest energy transitions predominantly originate from a HOMO-LUMO transition. For dichlorinated tubes, two main changes from the spectrum of the pristine tube are observed. First, there is a significant decrease in intensity of the brightest transition, reducing the oscillator strength to around 0.4 for 2-unit tubes and about 1.3 for 5-unit tubes (figure 4.11(a)). Second, there is an introduction of lower energy bright transitions due to defect-based changes in the electronic structure. The intensity of these states is very low for the monochlorinated tube with an oscillator strength of 0.018 for the most intense state, but is relatively bright in dichlorinated tubes, particularly when two chlorine atoms are bound to the same carbon ring due to the same effect.

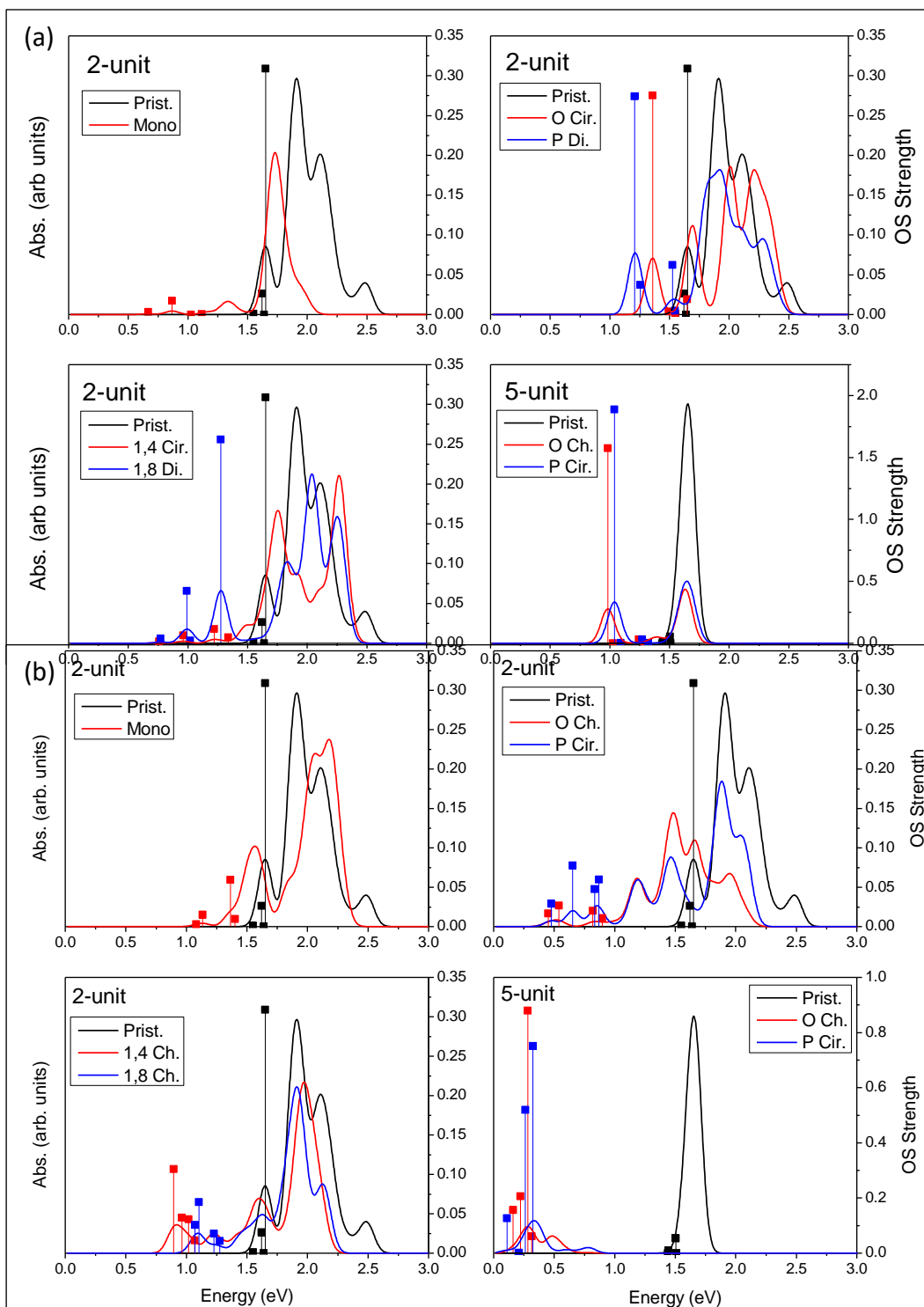


Figure 4.11. (a) Calculated absorption spectra of selected neutral chlorinated SWCNTs. Peaks were broadened about the transition using a Gaussian function with line width 0.04 eV., and (b) Calculated absorption spectra of selected charged chlorinated tubes. Peaks were broadened about the transition using a Gaussian function with line width 0.04 eV.

4.6.2. Charged Species

The calculated absorption spectra for charged chlorinated tubes are shown in figure 4.11(b). The spectra are similar to those for neutral chlorinated tubes, with primary differences in the energy and intensity of the additional red-shifted transitions. For 2-unit tubes the lowest energy transition occurs at about 0.5 eV when two chlorine atoms are on the same ring, and ~0.8-1.0 eV when two chlorine atoms are on different rings, with oscillator strengths of ~0.25-0.1. The energy and intensity of the lower energy transitions raises for tubes where both chlorine atoms are located on different rings than on the same ring, a trend which is opposite of that for neutral tubes. This is due to the presence of the midgap chlorine-localized defect state in dichlorinated tubes at lower energy when the two chlorine atoms are attached to different rings, decreasing the energy of the HOMO-LUMO gap when the state is unoccupied in the neutral cases but increasing the energy of the HOMO-LUMO gap when the state is occupied in charged cases. 5-unit charged dichlorinated tubes exhibit similar absorption properties to 2-unit tubes, except the energy of the low energy transitions is lower (~0.2 eV) and the intensity is greater (~0.5-1.0). Optical properties of the monochlorinated charged case are very similar to the monochlorinated neutral case. Overall, charged chlorinated tubes exhibit fewer low intensity transitions than neutral chlorinated tubes, reducing the applicability of their optical properties.

4.7. Effects of Increasing Cl Concentration

Higher concentrations of chlorine atoms bound to the SWCNT sidewall were tested using multiple pairs of neutral chlorine atoms bound in the circumferential para position on a 2-unit tube. Charged cases with higher concentration were not considered because data with charged mono and di-chlorinated systems indicates that higher concentrations are unlikely to be stable

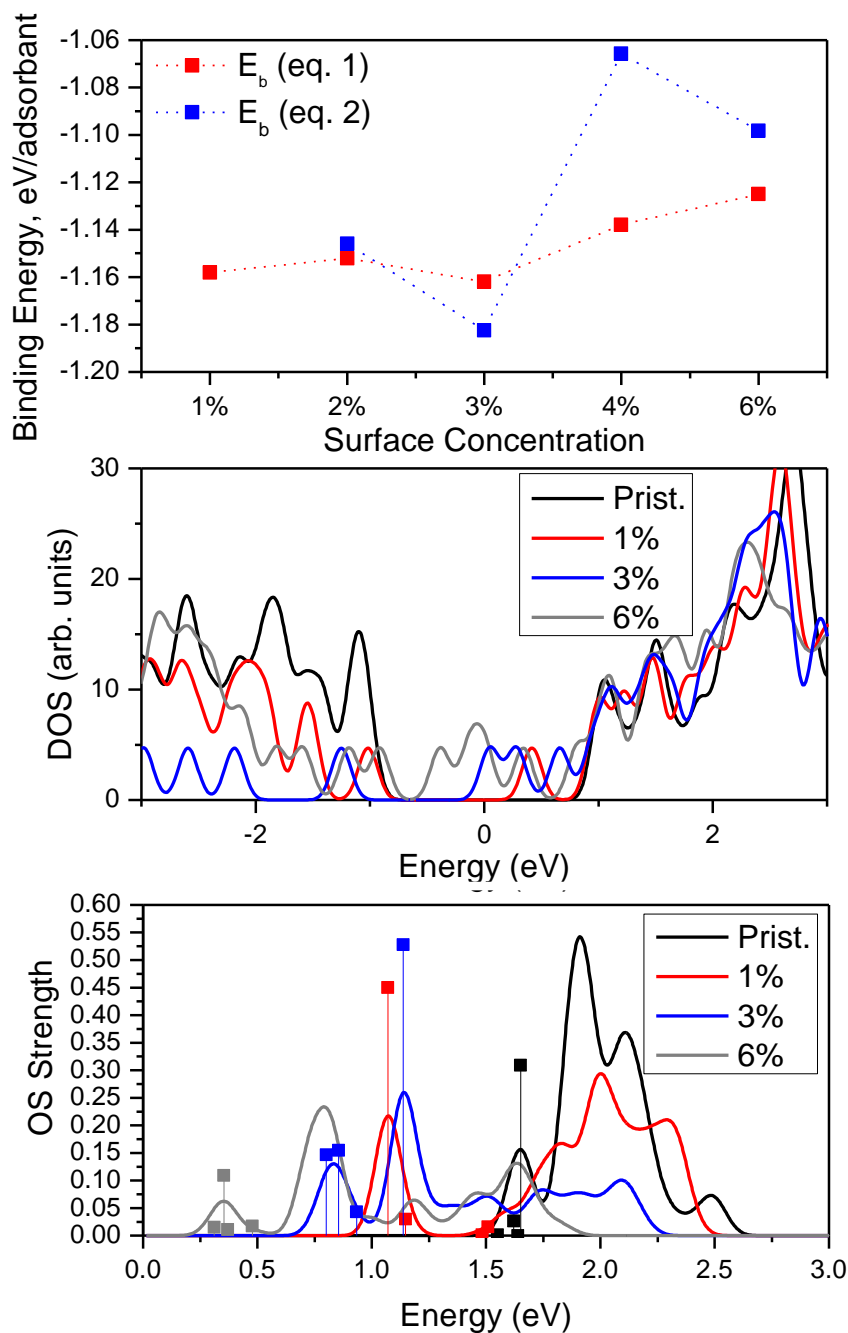


Figure 4.12. (a) Binding energy of chlorine on a CNT with respect to chlorine concentration. Binding energy was determined for tubes optimized with PBE1 functional and 6-31G* basis set. Concentration was increased by binding multiple Cl pairs in circumferential para configuration in different locations on the tube. (b) Density of states for chlorinated 2-unit finite tubes optimized with PBE1 functional and 6-31G* basis set with varying surface concentrations of chlorine. DOS was generated by broadening around the states with a Gaussian function with a linewidth of 0.06 eV. DOS for the chlorinated tubes were shifted to align with the first two unoccupied peaks in the pristine tube. (c) Absorption spectra for chlorinated 2-unit finite tubes optimized with PBE1 functional and 6-31G* basis set with varying surface concentrations of chlorine.

due to the significant charge build up from further functionalization, and therefore optimized geometries of these systems could not be obtained.

4.7.1. Effects of Chlorine Concentration on Binding Energy

Increasing chlorine concentration has a relatively small effect on the binding energy, with the binding energy per chlorine atom only increasing slightly as the concentration is increased (figure 4.12(a)). Notably, the binding of additional chlorine atoms was energetically favorable for all concentrations observed, with binding energies for additional chlorine pairs on an already chlorinated tube ranging from -1.19 to -1.06 eV per additional chlorine atom. Binding energies are likely dependent on the exact position of chlorine pairs on the tube, and the arrangements observed are likely not the most stable configurations. However, the data obtained suggests that relatively high chlorine concentrations should be obtainable.

4.7.2. Density of States: Higher Chlorine Concentrations Closes the Gap

The density of states of selected chlorinated tubes with different chlorine concentrations are shown in Figure 4.13. As the chlorine concentration increases, the number of mid-gap states added from chlorination increases, resulting in a dramatically smaller HOMO-LUMO gap, down to 0.53 eV when the chlorine concentration is 6%. Increasing chlorine concentration effectively increases the doped electronic character of dichlorinated tubes.

4.7.3. Optical Features of Increasing Chlorine Concentration

Calculated absorption spectra for selected chlorinated tubes with different chlorine concentrations are shown in figure 4.12(c). Increasing the chlorine concentration leads to an increase in the number of low energy transitions, and a decrease in the energy of the first transition as a result of closing the HOMO-LUMO gap. Overall, the optical features for

dichlorinated tubes become more predominant as the chlorine concentration is increased, indicating a high chlorine concentration is likely desirable for practical applications.

4.8. Conclusions

For neutral systems, chlorine binding is most favorable with two chlorine atoms bound to the same ring of the SWCNT sidewall, while binding two chlorine atoms to different rings gives rise to bond character resembling that of singly chlorinated SWCNTs. For increased concentrations of chlorine, the binding energy per chlorine atom is slightly increased meaning high degrees of chlorination should be possible. With charged cases, the chlorine binding energy is most favorable for monochlorinated tubes, and is dramatically less favorable for dichlorinated tubes due to the localization of charges on a single ring. The chlorine binding energy becomes

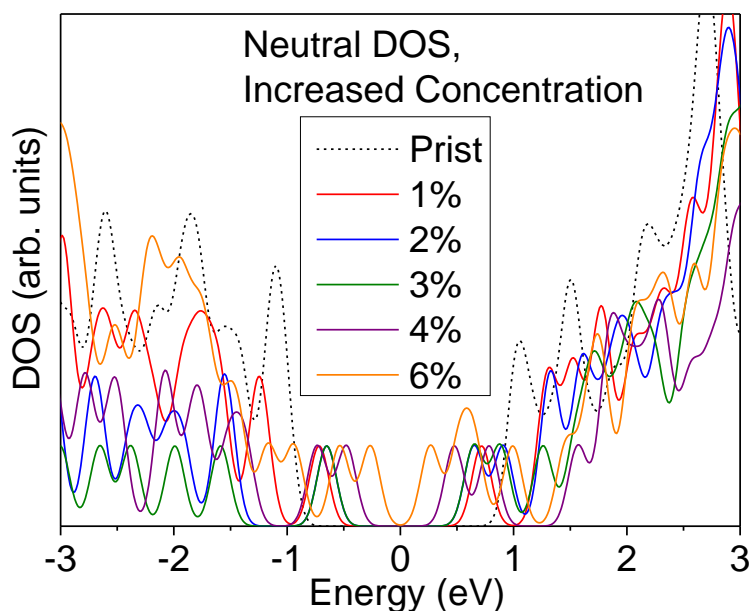


Figure 4.13. Density of states for neutral 2-unit finite tubes calculated with PBE1 functional and 6-31G* basis set with varying Cl surface concentrations. Higher Cl concentrations shows an increase in midgap states.

more favorable for dichlorinated tubes as the distance between chlorine atoms increases, and all cases were much more favorable as the length of the tube increased. Additionally, the bond character has almost no correlation with the binding energy of the system. Therefore, we conclude that the favorability of chlorine binding for charged systems is primarily influenced by the extent of charge delocalization, and chlorine ions likely bind to SWCNTs only in very low concentrations.

Binding of neutral chlorine to the CNT causes the introduction of unoccupied midgap states, therefore resulting in an electronically doped system. In the case of charged nanotubes, these states become occupied thereby raising the fermi energy and creating an n-doped material. As the chlorine concentration is increased, the number of midgap states increases, furthering the extent of doping. The calculated absorption spectra of all cases show a decrease in the intensity of the most intense transition and an introduction of low energy transitions. These states are lower energy in charged systems; however, the intensity is also much lower. Overall, the neutral chlorinated SWCNTs look very promising for application due to ease of modifying the electronic and absorption properties by changing the chlorine concentration. Charged systems are less practical for these applications due to the decreased absorption intensity and the relative inability to control properties through concentration due to the instability of systems with higher concentrations.

4.9. References

- (1) Frey, J. T.; Doren, D. J. *TubeGen 3.4*; University of Delaware: Newark DE, 2011.
- (2) Perdew, J. P.; Burke, K.; Ernzerhof, M. Generalized Gradient Approximation Made Simple. *Phys. Rev. Lett.* **1996**, 77 (18), 3865–3868.

- (3) JP Perdew, K. B. ERRATA:Generalized Gradient Approximation Made Simple. *Phys. Rev. Lett.* **1996**, *77* (18), 3865–3868.
- (4) Blöchl, P. E. Projector Augmented-Wave Method. *Phys. Rev. B* **1994**, *50* (24), 17953–17979.
- (5) Kresse, G.; Joubert, D. From Ultrasoft Pseudopotentials to the Projector Augmented-Wave Method. *Phys. Rev. B* **1999**, *59* (3), 1758–1774.
- (6) Kilina, S.; Tretiak, S. Excitonic and Vibrational Properties of Single-Walled Semiconducting Carbon Nanotubes. *Adv. Funct. Mater.* **2007**, *17* (17), 3405–3420.
- (7) Stewart, J. J. P. *MOPAC2009*; Stewart Computational Chemistry: Colorado Springs, CO, USA, 2008.
- (8) Dewar, M. J. S.; Zoebisch, E. G.; Healy, E. F.; Stewart, J. J. P. AM1: A New General Purpose Quantum Mechanical Molecular Model. *J. Am. Chem. Soc.* **1985**, *107* (13), 3902–3909.
- (9) Kilina, S.; Ramirez, J.; Tretiak, S. Brightening of the Lowest Exciton in Carbon Nanotubes via Chemical Functionalization. *Nano Lett.* **2012**, *12* (5), 2306–2312.
- (10) Frisch, M. J.; Trucks, G. W.; Schlegel, H. B.; Scuseria, G. E.; Robb, M. A.; Cheeseman, J. R.; Scalmani, G.; Barone, V.; Mennucci, B.; Petersson, G. A.; et al. *Gaussian 09*; Gaussian, Inc.: Wallingford, CT, USA, 2009.
- (11) Kresse, G.; Furthmüller, J. Efficient Iterative Schemes for Ab Initio Total-Energy Calculations Using a Plane-Wave Basis Set. *Phys. Rev. B* **1996**, *54* (16), 11169–11186.
- (12) Kresse, G.; Furthmüller, J. Efficiency of Ab-Initio Total Energy Calculations for Metals and Semiconductors Using a Plane-Wave Basis Set. *Comput. Mater. Sci.* **1996**, *6* (1), 15–50.
- (13) Kresse, G.; Hafner, J. Ab Initio Molecular-Dynamics Simulation of the Liquid-Metal Amorphous-Semiconductor Transition in Germanium. *Phys. Rev. B* **1994**, *49* (20), 14251–14269.

- (14) Kresse, G.; Hafner, J. Ab Initio Molecular Dynamics for Liquid Metals. *Phys. Rev. B* **1993**, *47* (1), 558–561.
- (15) Erbahar, D.; Berber, S. Chlorination of Carbon Nanotubes. *Phys. Rev. B* **2012**, *85* (8), 085426.
- (16) Saha, S.; Dinadayalane, T. C.; Murray, J. S.; Leszczynska, D.; Leszczynski, J. Surface Reactivity for Chlorination on Chlorinated (5,5) Armchair SWCNT: A Computational Approach. *J. Phys. Chem. C* **2012**, *116* (42), 22399–22410.
- (17) Adamo, C.; Barone, V. Toward Reliable Density Functional Methods without Adjustable Parameters: The PBE0 Model. *J. Chem. Phys.* **1999**, *110* (13), 6158–6170.
- (18) Lee, C.; Yang, W.; Parr, R. G. Development of the Colle-Salvetti Correlation-Energy Formula into a Functional of the Electron Density. *Phys. Rev. B* **1988**, *37* (2), 785–789.
- (19) Becke, A. D. Density-Functional Exchange-Energy Approximation with Correct Asymptotic Behavior. *Phys. Rev. A* **1988**, *38* (6), 3098–3100.
- (20) Becke, A. D. Density-functional Thermochemistry. III. The Role of Exact Exchange. *J. Chem. Phys.* **1993**, *98* (7), 5648–5652.
- (21) Chai, J.-D.; Head-Gordon, M. Systematic Optimization of Long-Range Corrected Hybrid Density Functionals. *J. Chem. Phys.* **2008**, *128* (8), 084106.
- (22) Chai, J.-D.; Head-Gordon, M. Long-Range Corrected Hybrid Density Functionals with Damped Atom–atom Dispersion Corrections. *Phys. Chem. Chem. Phys.* **2008**, *10* (44), 6614.
- (23) Hehre, W. J.; Stewart, R. F.; Pople, J. A. Self-Consistent Molecular-Orbital Methods. I. Use of Gaussian Expansions of Slater-Type Atomic Orbitals. *J. Chem. Phys.* **1969**, *51* (6), 2657–2664.

- (24) Collins, J. B.; von R. Schleyer, P.; Binkley, J. S.; Pople, J. A. Self-Consistent Molecular Orbital Methods. XVII. Geometries and Binding Energies of Second-Row Molecules. A Comparison of Three Basis Sets. *J. Chem. Phys.* **1976**, *64*, 5142–5151.
- (25) Gill, P. M. W.; Johnson, B. G.; Pople, J. A.; Frisch, M. J. The Performance of the Becke—Lee—Yang—Parr (B—LYP) Density Functional Theory with Various Basis Sets. *Chem. Phys. Lett.* **1992**, *197* (4–5), 499–504.
- (26) Clark, T.; Chandrasekhar, J.; Spitznagel, G. W.; Schleyer, P. V. R. Efficient Diffuse Function-Augmented Basis Sets for Anion Calculations. III. The 3-21+G Basis Set for First-Row Elements, Li–F. *J. Comput. Chem.* **1983**, *4* (3), 294–301.
- (27) Krishnan, R.; Binkley, J. S.; Seeger, R.; Pople, J. A. Self-consistent Molecular Orbital Methods. XX. A Basis Set for Correlated Wave Functions. *J. Chem. Phys.* **1980**, *72* (1), 650–654.
- (28) Hehre, W. J.; Ditchfield, R.; Pople, J. A. Self—Consistent Molecular Orbital Methods. XII. Further Extensions of Gaussian—Type Basis Sets for Use in Molecular Orbital Studies of Organic Molecules. *J. Chem. Phys.* **1972**, *56* (5), 2257–2261.
- (29) Ditchfield, R.; Hehre, W. J.; Pople, J. A. Self-Consistent Molecular-Orbital Methods. IX. An Extended Gaussian-Type Basis for Molecular-Orbital Studies of Organic Molecules. *J. Chem. Phys.* **1971**, *54*, 724–728.
- (30) Hariharan, P. C.; Pople, J. A. The Influence of Polarization Functions on Molecular Orbital Hydrogenation Energies. *Theor. Chim. Acta* **1973**, *28* (3), 213–222.
- (31) Jones, R. O.; Gunnarsson, O. The Density Functional Formalism, Its Applications and Prospects. *Rev. Mod. Phys.* **1989**, *61* (3), 689–746.

- (32) Hellman, A.; Razaznejad, B.; Lundqvist, B. I. Potential-Energy Surfaces for Excited States in Extended Systems. *J. Chem. Phys.* **2004**, *120* (10), 4593–4602.
- (33) Martin, R. L. Natural Transition Orbitals. *J. Chem. Phys.* **2003**, *118* (11), 4774.
- (34) Rappe, A. K.; Casewit, C. J.; Colwell, K. S.; Goddard, W. A.; Skiff, W. M. UFF, a Full Periodic Table Force Field for Molecular Mechanics and Molecular Dynamics Simulations. *J. Am. Chem. Soc.* **1992**, *114* (25), 10024–10034.
- (35) Yanai, T.; Tew, D. P.; Handy, N. C. A New Hybrid Exchange–correlation Functional Using the Coulomb-Attenuating Method (CAM-B3LYP). *Chem. Phys. Lett.* **2004**, *393* (1–3), 51–57.
- (36) Barone, V.; Cossi, M.; Tomasi, J. Geometry Optimization of Molecular Structures in Solution by the Polarizable Continuum Model. *J. Comput. Chem.* **1998**, *19* (4), 404–417.
- (37) Cossi, M.; Rega, N.; Scalmani, G.; Barone, V. Energies, Structures, and Electronic Properties of Molecules in Solution with the C-PCM Solvation Model. *J. Comput. Chem.* **2003**, *24* (6), 669–681.
- (38) Humphrey, W.; Dalke, A.; Schulten, K. VMD – Visual Molecular Dynamics. *J. Mol. Graph.* **1996**, *14*, 33–38.

5. DEDUCING THE ORIGIN OF RED-SHIFTED OPTICAL FEATURES IN CARBON NANOTUBES FUNCTIONALIZED WITH ARYL GROUPS

5.1. Motivation

Functionalization of single-walled carbon nanotubes (SWCNTs) has been shown to modify their electronic and optical properties, thereby increasing the range of applications in which they can be used. Recent experimental studies have shown that covalent aryl functionalization of (6,5) SWCNTs introduces a number of emission features in the infrared region of the electromagnetic spectrum, thereby increasing their utility as single photon sources (SPS) for telecommunications application. Despite this promise, the origin of these red-shifted emission features is unknown. In the preceding chapter, it was shown that the electronic structure and corresponding energies of optical features are dependent on the configuration of functionalization for di-chlorinated species. In this chapter, the role of configuration of chemical functionalization of (6,5) SWCNTs with aryl derivatives is explored using the same techniques. It is shown that the specific isomer geometry – the relative position of functional groups on the carbon-ring of the nanotube – is critical for controlling the energies and intensities of optical transitions introduced by functionalization, while the dielectric environment and the chemical composition of functional groups play less significant roles. The predominant effects on optical properties as a result of functionalization conformation are rationalized by exciton localization on the surface of the SWCNT near the dopant sp^3 -defect but not onto the functional group itself. This research is seminal in explaining the origin of the multiple emission bands observed in experiment and suggests control of functional orientation as a strategy for tuning infrared emission energies.

5.2. A Menagerie of Functionalization Configurations

5.2.1. Synthetic Considerations

Arylation of aromatic compounds, including SWCNTs,¹⁻³ can be achieved using water-soluble aryl diazonium salts. One of the possible scenarios of such a reaction with the SWCNTs has been suggested to occur as a two-step reaction.⁴ In this section, the plausible functionalization configurations are presented from a synthetic point of view.

5.2.1.1. Dissociation of Diazonium Salt to Diatomic Nitrogen & an Electrophilic Aryl Species

In the first step of the reaction, the diazonium salt dissociates into diatomic nitrogen group (N_2) and an aromatic carbocation. The nitrogen gas will bubble off the reaction mixture and leave as a gas. The aromatic carbocation is then left behind to further react with the SWCNT. This aromatic group is able to place the positively charged carbon at positions either ortho (the adjacent positions) or para (the positions across the ring from) with respect to the bromine group. However, steric constraints dictate that further addition of this species will only occur for the intermediate para intermediate. As such, only the products generated from the intermediate where the positive charge is placed on the ring at the position para to bromine will be considered.

5.2.1.2. Generation of a Reactive Carbocation Intermediate on the SWCNT

In the second step of the reaction, the aryl cation is quickly physisorbed to the outer tube surface of the SWCNT. A relatively strong interaction between the nanotube and cation via π - π stacking allows for electron transfer from the tube to the diazonium molecule forming a charge-transfer transition complex.⁵ The complex then decomposes in a rate-limiting step into N_2 gas and aryl radical, forming a mixture of covalently and noncovalently bound products, where the large majority of the sample population is attributed to the covalently functionalized SWCNTs

by aryl derivatives.⁴ Figure 5.1 illustrates the formation of the product at the second step of this path: reaction of the conjugated hexagonal lattice of the SWCNT with an electrophilic species, such as the carbocation generated in reaction with common diazonium salt derivatives, results in carbocation species, where the positive charge can be thought of as localized on the position adjacent to the site of addition of the aryl group (ortho configuration). Resonance can allow this positive charge to be placed on the para- site, as well. However, localization of the positive charge on the meta- site with respect to the aryl attachment is not feasible owing to general chemical rules.

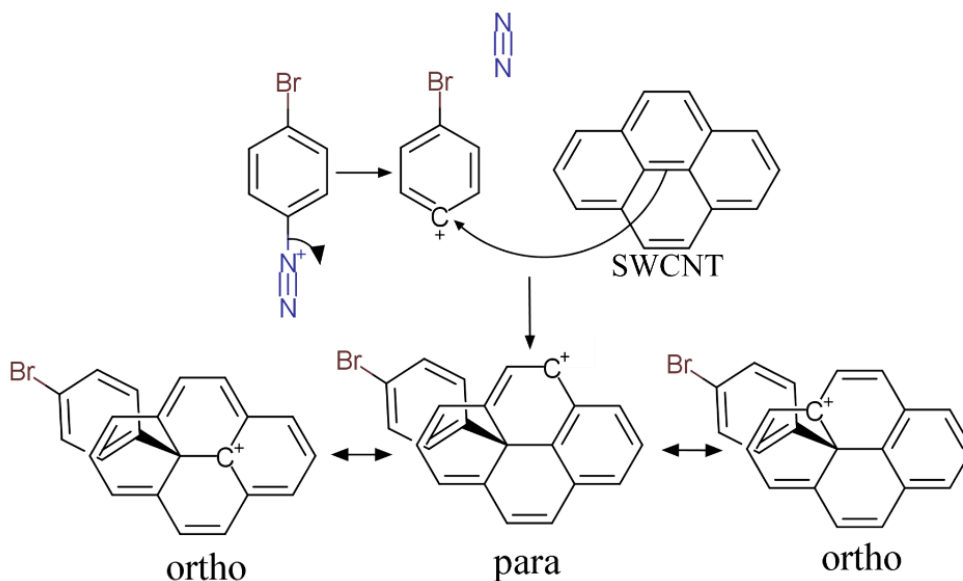


Figure 5.1. Reaction mechanism between a SWCNT and electrophilic species generating reactive carbocations.

5.2.1.3. Formation of Product from Addition of Nucleophilic Species

In the final step of the reaction, the positively charged site of the carbon-ring is saturated by either a second aryl bromide group, hydrogen, or OH⁻ group, resulting in the products presented in figure 5.2(b). These adducts are viable choices for functionalization of SWCNTs in

an aqueous environment. Due to the generation of an electrophilic carbocation with charge localization on sites only ortho or para from the addition in step 2, only configurations with further addition at these sites are plausible. This results in the generation of product where two groups functionalize the SWCNT in positions either ortho or para with respect to each other.

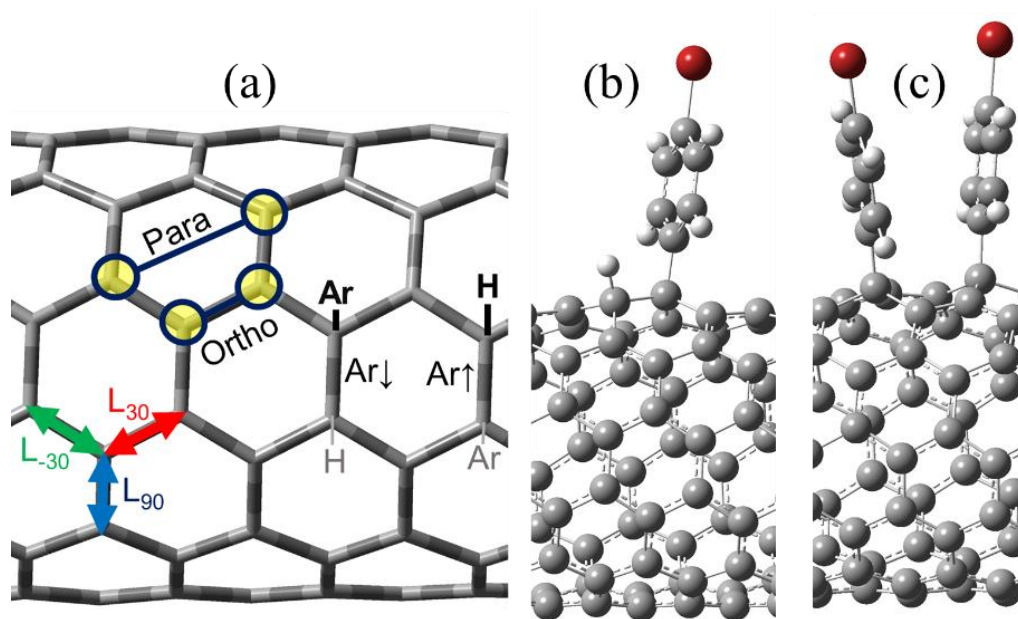


Figure 5.2. Possible orientations of functional groups with respect to the (6,5) SWCNT axis. (a) Ortho denotes functionalization on adjacent carbon atoms, while para refers to functionalization in the (1,4) positions on the same hexagonal ring. L_{30} , L_{90} , and L_{-30} refers to bonds that lie along a vector 27° , 87° , and -33° from the SWCNT axis, respectively. $Ar\uparrow$ and $Ar\downarrow$ refer to the order of functionalization along a chosen vector. Sample representations of a SWCNT functionalized with an aryl bromide group and a hydrogen along the ortho L_{30} bond in the $Ar\uparrow$ configuration (b) and two aryl bromide groups in the para L_{30} configuration (c).

5.2.1.4. Functionalization at the Same Hexagonal Ring

The carbocation generated in the second step of the reaction is relatively unstable, and therefore the third step adding a nucleophilic species would be expected to happen quickly. As a result, the resonance stabilization that would place the charge in hexagonal rings other than the

one where the addition of the aryl species occurred is not expected to occur. As a result, only functionalization adding both groups on the same hexagonal ring of the SWCNT are considered in this chapter (figure 5.2(a)).

5.2.1.5. Bridging Synthetic and Computational Considerations

In addition to the synthetic considerations, there are some theoretical reasons that additions of functional groups to SWCNTs must occur in pairs. Unless the system is considered to be charged, the intermediate result of functionalization with a single aryl group in calculations is an open shell system with a single unpaired electron. These radical species are considered to be very unstable, and generation of a more stable closed shell system requires bonding an additional group at a different carbon atom. As such, all functionalization in this chapter will involve functionalization at different sites on the SWCNT.

5.2.2. Non-equivalent Bonds in Chiral SWCNTs

Due to the chiral angle present in semiconducting SWCNTs where $n > m \neq 0$, three distinct types of bonds emerge with differing angles with respect to the SWCNT axis. These directions are labeled L_{30} , L_{90} , and L_{-30} where the subscript describes the approximate angle between a vector lying along the bond and the SWCNT axis. In the case of the (6,5) SWCNT explored here, these angles are more precisely 27° , 87° , and -33° for L_{30} , L_{90} , and L_{-30} respectively (figure 5.2(a)). For the purpose of calculating electronic and optical properties of functionalized SWCNTs, functionalization along all three types of bonds must be considered.

5.2.3. Interchange of Two Functional Groups

One further structural modification that must be acknowledged is the possibility for the interchange of the two functional sites in the SWCNT. Swapping two functional sites for non-equivalent functional pairs (ie. the aryl-H configurations) results in distinct geometries for all

chiral SWCNTs, and as such these geometries will be considered here as well. Viewing a SWCNT in a perspective that results in a horizontal tube axis allows every carbon atom to either reside at the “top” or the “bottom” of a hexagonal ring. Either the top or the bottom of the hexagonal ring is functionalized with an aryl group to generate “Ar↑” and “Ar↓” configurations respectively. The remaining position is functionalized with the opposing species. It is notable that through considering this interchange, this study implicitly considers the differences between the functionalization of left and right handed SWCNT. Considering all these possible structure modifications results in 12 distinct aryl-H and 6 distinct di-aryl configurations. The geometric parameters of these configurations are summarized in figure 5.2(a).

5.2.4. Functionalization with Different Groups

In addition to modifying the position of functionalization to SWCNTs, a number of different chemical species can be used. To explore the inductive and resonance effects such modifications, a series of groups were utilized. These include alkyl groups with differing lengths as well as degrees of electron withdrawing, aryl groups that can contribute electrons to the SWCNT through resonance, divalent species where two carbon atoms in the SWCNT are bonded

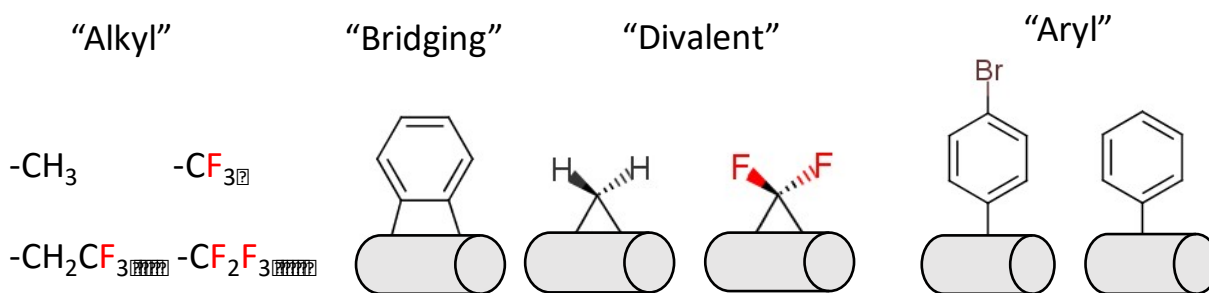


Figure 5.3. Functional groups considered in this chapter. For monovalent non-bridging species, a second location on the SWCNT was functionalized with a hydrogen group to maintain a closed-shell system.

to the same atom, and a “bridging” group where the functionalization occurs through interaction with the SWCNT through two aryl atoms (figure 5.3). The impact of these functional groups is known through experiment.

5.3. Computational Methodology

5.3.1. Generation & Optimizing of Functionalized SWCNT Geometries in Vacuum

The pristine SWCNT was created with (6,5) chirality to a length of ~12 nm by generating 3 unit cells with Tubgen 3.4 software.⁶ To fulfill the vacancies of all terminal carbon atoms, the ends of the SWCNT were capped with hydrogen atoms in all positions according to the capping scheme reported previously.^{7,8} The geometry of the pristine SWCNT was then optimized sequentially by first using UFF⁹ molecular mechanics followed by AM1¹⁰ semi-empirics, and finally density functional theory (DFT) with a CAM-B3LYP¹¹ functional and 3-21G basis set in vacuum. This methodology has been shown to be in reasonable agreement with experimental data.^{12,13} Once the pristine SWCNT geometry was optimized, this structure was then functionalized in the positions previously described. To generate the starting geometries, the torsion angle between the SWCNT and aryl group was adjusted such that the plane containing all the atoms in the aryl group and a vector connecting the SWCNT carbon atoms vicinal to each functional group were perpendicular, figure 5.2(b) and (c). The resulting functionalized SWCNTs were then optimized using the same step-wise methodology previously described. All geometry optimizations were performed using Gaussian-09, version E.01 software.¹⁴

5.3.2. Solvent Dependent Geometries: a Marginal Role

The geometries resulting from the vacuum calculations were utilized as starting points for geometry optimization in the dielectric environment of three solvents of increasing polarity including heptane ($\epsilon=1.9113$), acetonitrile ($\epsilon=35.688$), and water ($\epsilon=78.3553$). The effect of the solvent was introduced implicitly using the conductor-like polarizable continuum model (CPCM)¹⁵ as implemented in Gaussian-09. Due to the negligible difference between both the geometry and relative energetics of the optimized geometries in vacuum and solvent (table 5.1), all further excited state calculations were performed using those structures optimized in vacuum.

Table 5.1. Relative total energies with respect to the lowest energy structure and corresponding electrostatic dipole moments (shown in parenthesis) of aryl-H configurations calculated using the CAM-B3LYP functional and STO-3G basis in vacuum and different solvents.

<i>Configuration</i>			<i>Relative Total Energy in eV (Dipole in Debye)</i>			
			<i>Vac</i>	<i>Heptane</i>	<i>Acetonitrile</i>	<i>Water</i>
<i>Ortho</i>	<i>Ar</i> ↑	<i>L</i> ₃₀	0.0985 (0.64)	0.0987 (0.72)	0.0990 (0.86)	0.0990 (0.86)
		<i>L</i> ₉₀	0.3432 (0.29)	0.3432 (0.41)	0.3430 (0.70)	0.3430 (0.72)
		<i>L</i> ₋₃₀	0.0011 (0.41)	0.0012 (0.47)	0.0013 (0.61)	0.0013 (0.62)
	<i>Ar</i> ↓	<i>L</i> ₃₀	0.0974 (0.61)	0.0976 (0.68)	0.0977 (0.84)	0.0977 (0.85)
		<i>L</i> ₉₀	0.3438 (0.40)	0.3439 (0.49)	0.3437 (0.72)	0.3437 (0.73)
		<i>L</i> ₋₃₀	0.0000 (0.33)	0.0000 (0.40)	0.0000 (0.59)	0.0000 (0.60)
<i>Para</i>	<i>Ar</i> ↑	<i>L</i> ₃₀	0.2459 (0.30)	0.2457 (0.40)	0.2455 (0.66)	0.2455 (0.67)
		<i>L</i> ₉₀	0.3160 (0.66)	0.3135 (0.78)	0.3105 (1.02)	0.3104 (1.03)
		<i>L</i> ₋₃₀	0.4773 (0.56)	0.4765 (0.67)	0.4755 (0.91)	0.4755 (0.93)
	<i>Ar</i> ↓	<i>L</i> ₃₀	0.2462 (0.37)	0.2459 (0.45)	0.2456 (0.67)	0.2456 (0.68)
		<i>L</i> ₉₀	0.3164 (0.57)	0.3138 (0.70)	0.3107 (1.00)	0.3106 (1.01)
		<i>L</i> ₋₃₀	0.4775 (0.60)	0.4767 (0.71)	0.4756 (0.93)	0.4756 (0.94)

5.3.3. Molecular Orbitals

Molecular orbital diagrams were generated by extracting the energies of ground-state orbitals directly from the Gaussian calculations. To visualize electron density, the molecular orbitals (MOs) for the resulting geometries of both pristine and aryl functionalized SWCNTs were generated using CAM-B3LYP functional and 3-21G basis set results and visualized by applying isosurface with an isovalue of 0.008 using Visual Molecular Dynamics (VMD) software.¹⁶ The results are also compared to those calculated by STO-3G basis set.

5.3.4. Determination of Optical Properties with TDDFT

To simulate the optical characteristics, the vertical excitations for 15 states were calculated using TDDFT from the ground state optimized geometries in vacuum and then recalculated in the dielectric environment of the three solvents. The profiles of absorption spectra were generated by broadening about the optical transitions using a Gaussian function of linewidth 0.01 eV weighted by the oscillator strength of the transition. To obtain the fluorescence spectra, the excited-state geometry is optimized,¹⁷ whereby the lowest singlet excitation energy is calculated within the linear response theory framework.¹⁸ Both the absorption and emission spectra calculations were performed using the same functional and basis set as for the geometry optimization. Natural transition orbital (NTO) analysis¹⁹ was then performed to obtain the electron-hole pairs of one-electron orbitals that contribute to each optically active transition of a specific excited state, as implemented in Gaussian-09 software. For absorption, analysis was performed for both the lowest energy bright states as well as the bright states representing E_{11} in the pristine SWCNT. For emission, only the lowest energy bright states were of interest.

5.3.5. Quantification of Vibrational Reorganization

The calculation of reorganization energies is accomplished using the DFT and TDDFT calculations for each species in this chapter. Calculating the reorganization energy in the ground state (ΔE_1) is accomplished using single point energy calculations for each the ground and excited state geometries:

$$\Delta E_1 = \text{reorganization energy in ground state} = E_{S_1}^{SP} - E_{S_0}^{SP} \quad (\text{Equation 5.1})$$

With the reorganization in the ground state, the lowest-energy transitions for TDDFT from each the ground state geometry (E_{abs}) and the excited state geometry (E_{emis}) are used to determine the reorganization energies in the excited state.

$$\Delta E_2 = \text{reorganization energy in excited state} = E_{\text{abs}} - (E_{\text{emis}} + \Delta E_1) \quad (\text{Equation 5.2})$$

Summation of these two quantities will give the full energy that goes into reorganization in the system. See figure 5.4 for a schematic of these quantities.

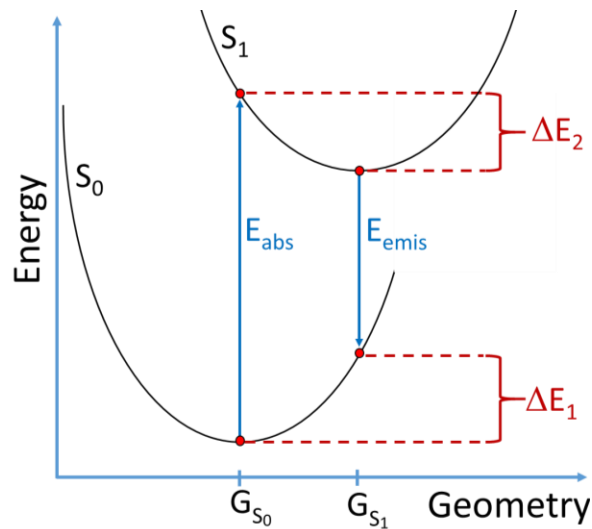


Figure 5.4. Representation of the theoretical potential energy surfaces for ground and first-excited states in the defected SWCNT systems.

5.3.6. Calculation of Radiative Lifetimes

The method of estimation of radiative lifetimes through Einstein coefficients is frequently used^{20,21}. This method relies on the consideration of a steady-state two level system which is undergoing stimulated emission (both facilitated by electromagnetic radiation (ER)) and spontaneous emission of the generated excitations. Borrowing the energy density for the ER for Plank's law and performing an analysis of populations using Boltzmann's distribution, the rates of transitions between the excited states and ground states can be acquired²². The resulting equation describing radiative emission is given by:

$$\tau = \frac{4\pi^2 c^3 \epsilon_0 m_e}{f_{ij} \omega^2 e^2} \quad (\text{Equation 5.3})$$

where c is the speed of light, ϵ_0 is the permittivity of free space, m_e is the mass of an electron, e is the elementary charge, and f_{ij} and ω are the oscillator strength and angular frequency of the transition respectively.

5.3.7. Determination of the Bond Character of Functionalization

Natural bond analysis²³ was performed for the purpose of characterizing the bond character in the region of functionalization. The analysis was performed as implemented by the Gaussian09 software package on specifically the bond between the SWCNT and the functional group for all species with different functional groups.

5.4. Relative Stabilities and Geometries of Binding Configurations

5.4.1. Indistinguishable Stabilities for Left vs. Right SWCNTs

Different functionalization of SWCNTs with an aryl derivative and hydrogen result in similar total energies for all Ar \uparrow and Ar \downarrow configurations considered (figure 5.5). The observed difference between the total energies of Ar \uparrow and Ar \downarrow indicates that these structures are indistinguishable at normal conditions. Assuming the absence of environmental effects such as the presence of surfactants, this indicates the aryl functionalization provides no selectivity between the left- and right-handed (6,5) SWCNT.

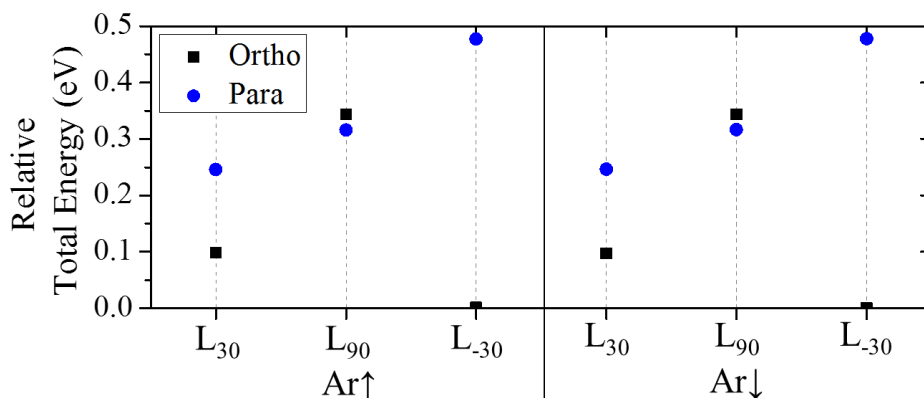


Figure 5.5. Relative total energies of each functionalized configuration with respect to the lowest energy isomer for (a) aryl-H and (b) di-aryl structures optimized with the CAM-B3LYP functional and STO-3G basis set in vacuum. Black squares represent ortho configurations, while blue circles represent para configurations.

5.4.2. Ortho vs. Para: Relative Similarities in Binding Energies

The differences in total energies between various ortho and para isomers of aryl-H configurations are more noticeable, with all computed energies falling within a 0.1-0.4 eV range from the most stable ortho L₋₃₀ configuration, figure 5.6(a). When both functional groups are the same in di-aryl structures, the most stable configuration becomes para L₉₀, being different

from ortho L₋₃₀ by ~0.05 eV, while the energy difference range between all ortho and para isomer structures varies from 0.05 eV to 0.6 eV. In general, binding with the second aryl group instead of hydrogen slightly increases the total energies of all ortho configurations, while it also weakly stabilizes the para conformations, although the changes are relatively small in all cases.

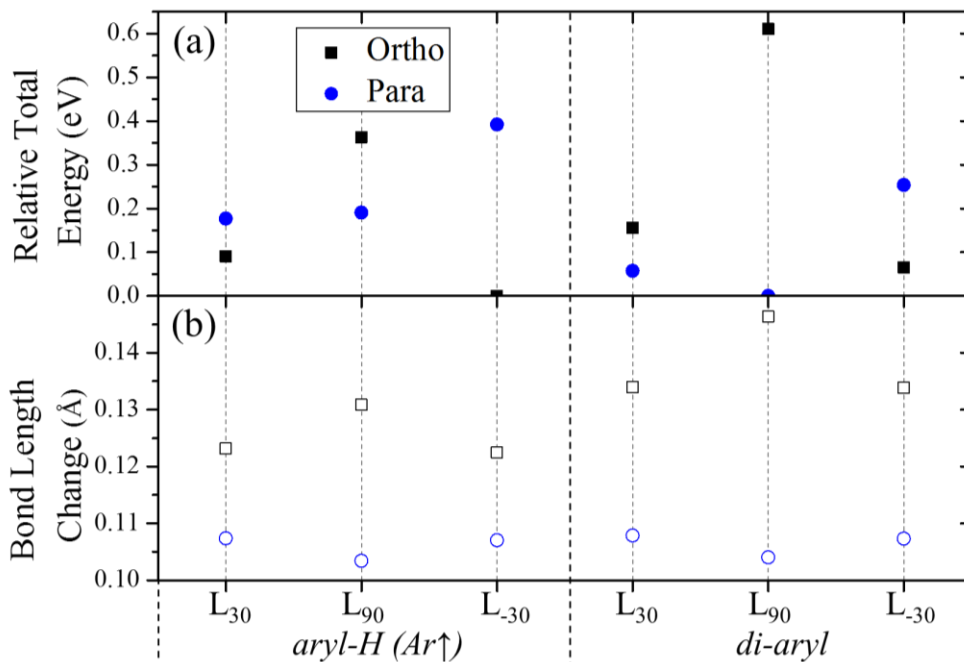


Figure 5.6. Dependence of structural and energetic changes on the functional group conformation calculated in vacuum using CAM-B3LYP functional and 3-21G basis set. (a) Relative total energies of functionalized isomers with respect to the most stable structure compared between (6,5) SWCNT functionalized with an aryl bromide group and a hydrogen (aryl-H) and two aryl bromide groups (di-aryl). (b) The averaged difference between Carbon-Carbon bond lengths adjacent to aryl functionalization and those in the pristine SWCNT. Black squares represent ortho configurations, while blue circles represent para configurations.

5.4.3. Basis Set Dependence: Slight Stabilization with Larger Basis w/o Change in Trends

Increasing in the basis set size, from STO-3G to 3-21G, somewhat reduces the energies of the para configurations, while the energy of ortho structures insignificantly change both in aryl-H and di-aryl structures as shown in figure 5.7. Overall, an increase in the basis set has a qualitatively minor effect on both the geometry of the system. This is in agreement with prior

calculations for OH-functionalized (9,0) nanotubes using B3LYP/3-21G that show a maximum of 0.3% difference in bond lengths compared to B3LYP/6-31G* results.²⁴ This minor effect on the geometry carries over to electronic structure, as will be presented in a further section.

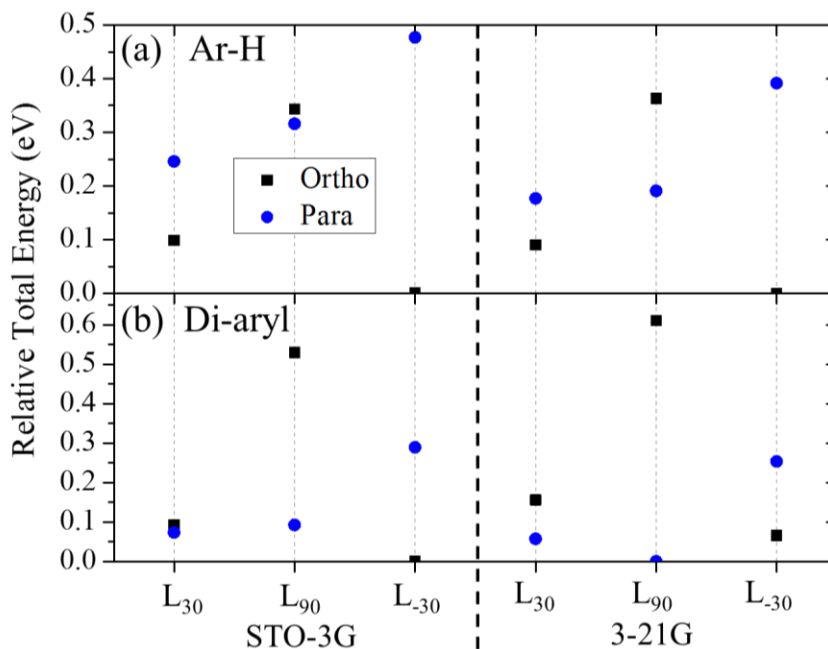


Figure 5.7. Relative total energies of each configuration with respect to the lowest energy structure for (a) Ar↑ aryl-H configurations and (b) diaryl configurations. The panel on the left and right compares the results obtained by STO-3G and 3-21G basis sets, respectively. Black squares represent ortho configurations, while blue circles represent para configurations.

5.4.4. Geometrical Characteristics as a result of Functionalization

5.4.4.1. Computed Geometrical Deviation from Pristine

For ortho configurations, the bond lengths adjacent to the aryl functional group are elongated significantly more than for para configurations as shown in figure 5.6(b). In these cases, the greatest elongation is observed along the axis of functionalization due to the concurrent disruption of the sp^2 -hybridization from both carbon atoms in that direction. The remaining two bonds become lengthened over the pristine SWCNT to a similar degree (table 5.2)

leading to the sp^3 -defect at the conjugated structure of the nanotube. Figure 5.6(b) shows that the average bond disruption is the most significant for ortho functionalization along L_{90} , coinciding with the highest energy among ortho structures, figure 5.6(a). Additionally, the disruption of sp^2 hybridization is observed to be greater in di-aryl functionalized SWCNTs than for aryl-H functionalization. This is accompanied by the corresponding increase in the total energies for all ortho functionalized species. In contrast, para configurations exhibit significantly less elongation of bond lengths, indicating a lower degree of sp^2 disruption in the region local to functionalization for both aryl-H and di-aryl structures. Additionally, the smaller elongation is nearly uniform across all para-isomers, which coincides with a consistent energy difference between the various para configurations (≤ 0.2 eV), as compared to those of the ortho structures (up to 0.6 eV). However, the smaller degree of sp^2 distortion does not always provide the lowest energy configuration, resulting in para isomers having in most cases larger energy than ortho isomers, except for L_{90} , where ortho structures have significant changes in the bond lengths. Thus, some moderate sp^2 distortion, like in the ortho L_{-30} configuration, efficiently stabilizes both aryl-H and di-aryl structures.

5.4.4.2. Experimental Expectations

It is reasonable to suggest that computation of a larger number of unit cells in the SWCNT model, covered with a similar number of functional sites (i.e. modeling a lower concentration of functionalization), might yield an even smaller energy difference between various functionalization geometries. As such, it would be inappropriate to conclude that the ortho L_{30} for aryl-H and para L_{90} for di-aryl are the most thermodynamically probable configurations of the defect position for (6,5) nanotube samples. Additionally, absent from these considerations is the kinetic component, which is driven by thermal fluctuations and is affected by solvent and surfactant molecules covering the tube surface. The latter affects collisions between molecules during the dissociation reaction of diazonium salts into N_2 gas and aryl radical forming a mixture of covalently and noncovalently bound products.⁴ Since it is known that aryl diazonium salts have very complicated chemistry in solutions due to the variety of reaction pathways with a large number of potential intermediate products, we assume that all 12 aryl-H or 6 di-aryl isomers can co-exist in experimental samples.

Table 5.2. Carbon-Carbon bond lengths (in Å) adjacent to aryl functionalization structure for Ar↑ aryl-H and di-aryl isomers calculated using the CAM-B3LYP functional and either the STO-3G basis set in vacuum. The highlighted lengths indicate those bonds that underwent the maximum elongation after functionalization.

		Pristine (6,5)	Ar-H L_{30}	Ar-H L_{90}	Ar-H L_{30}	Di-aryl L_{30}	Di-aryl L_{90}	Di-aryl L_{30}
<i>Ortho</i>	L_{30}	1.442	1.594	1.541	1.549	1.619	1.547	1.549
	L_{90}	1.436	1.550	1.635	1.554	1.562	1.668	1.561
	L_{30}	1.442	1.556	1.537	1.596	1.551	1.545	1.621
<i>Para</i>	L_{30}	1.442	1.549	1.546	1.553	1.549	1.548	1.552
	L_{90}	1.436	1.554	1.558	1.554	1.556	1.56	1.555
	L_{30}	1.442	1.554	1.547	1.550	1.553	1.545	1.551

5.4.5. Solvent Independence for Geometries & Relative Stabilities

The geometry optimizations performed in the different dielectric environment of solvents ranging from the non-polar heptane to very polar water results in no noticeable structural and energetic difference between defect conformations (figure 5.8 and table 5.1). This can be

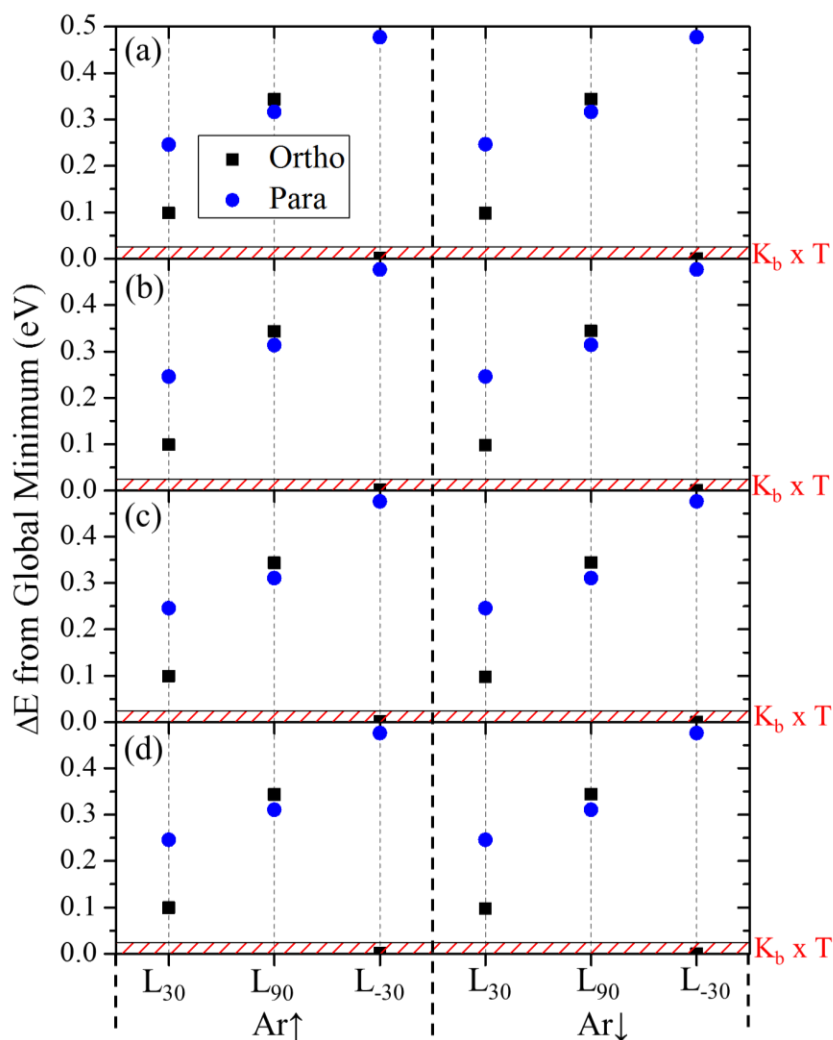


Figure 5.8. Relative total energies of each functionalized configuration with respect to the lowest energy isomer for aryl-H configurations optimized in a dielectric environment equivalent to (a) vacuum, (b) heptane, (c) acetonitrile, and (d) water using the CAM-B3LYP functional and STO-3G basis set. Black squares represent ortho configurations, while blue circles represent para configurations. The red box at the bottom of each panel represents the amount of energy available at room temperature (298K).

rationalized by the nonpolar character of the nanotube, while different isomer conformations of polar functional groups result in a small electrostatic dipole moment of the entire system (≤ 1 Debye) in all solvents. While the total electrostatic dipole moment of the functionalized nanotubes increases with the solvent polarity (by 0.1-0.3 Debye), its relative change between the different conformations stays nearly the same (figure 5.9 and table 5.1), which explains the insensitivity of the defect conformations to the solvent. As such, any difference in properties of aryl functionalized SWCNT samples observed in different solvents is likely not due to structural changes induced by the environment, but can be associated with a different response of the intrinsic electronic structure that is expected to be more sensitive to dielectric effects.

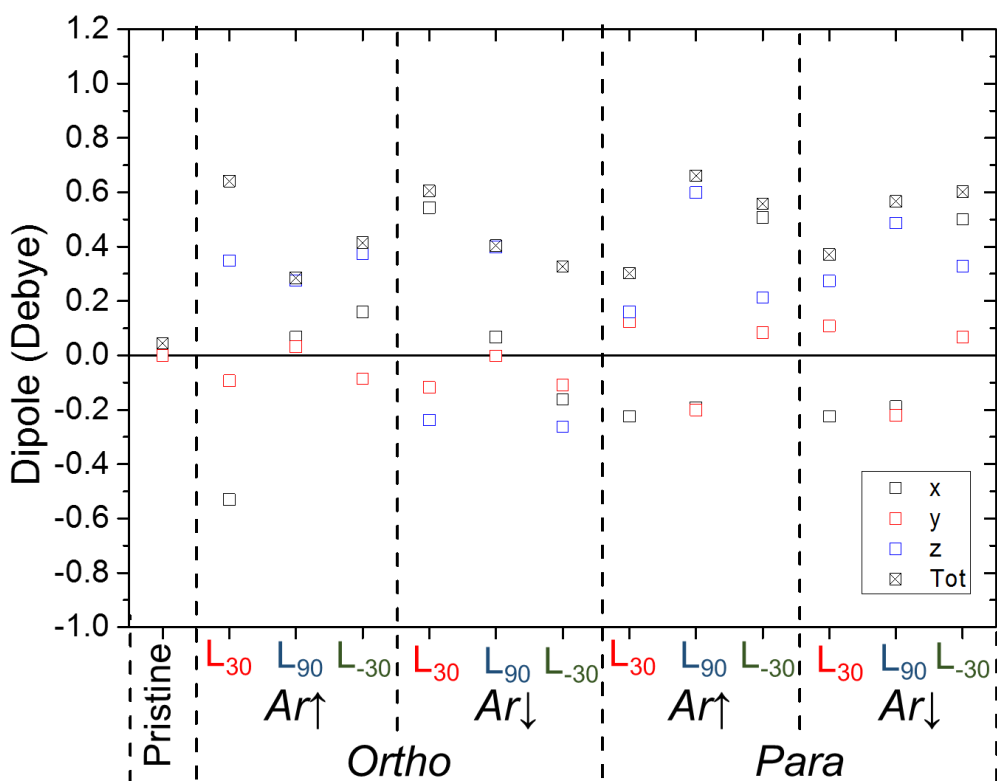


Figure 5.9. Electrostatic dipole moment and its x, y, and z components for aryl-H configurations calculated using the CAM-B3LYP functional and STO-3G basis set in vacuum.

5.5. Electronic Structure Heavily Dependent on Functionalization Configuration

5.5.1. Configuration Effects on Electron Localization

The electron localization in the frontier molecular orbital in the vicinity of the defect plays a significant role in modulating the precise energetics of the orbitals and therefore the gap between the highest occupied molecular orbital (HOMO) and lowest unoccupied molecular orbital (LUMO). For example, the HOMO (and LUMO) of the para L_{30} species exhibits electron delocalization along the entire axis of the SWCNT and the largest energy gap among para isomers for both aryl-H and di-aryl structures, figure 5.10. In contrast, the para L_{-30} species shows significant orbital localization around the defect site and the smallest energy gap for para isomers calculated in vacuum. For the ortho isomer, the trend is opposite, showing the most delocalized frontier orbitals for L_{-30} and having the largest energy gap, while L_{30} exhibits the

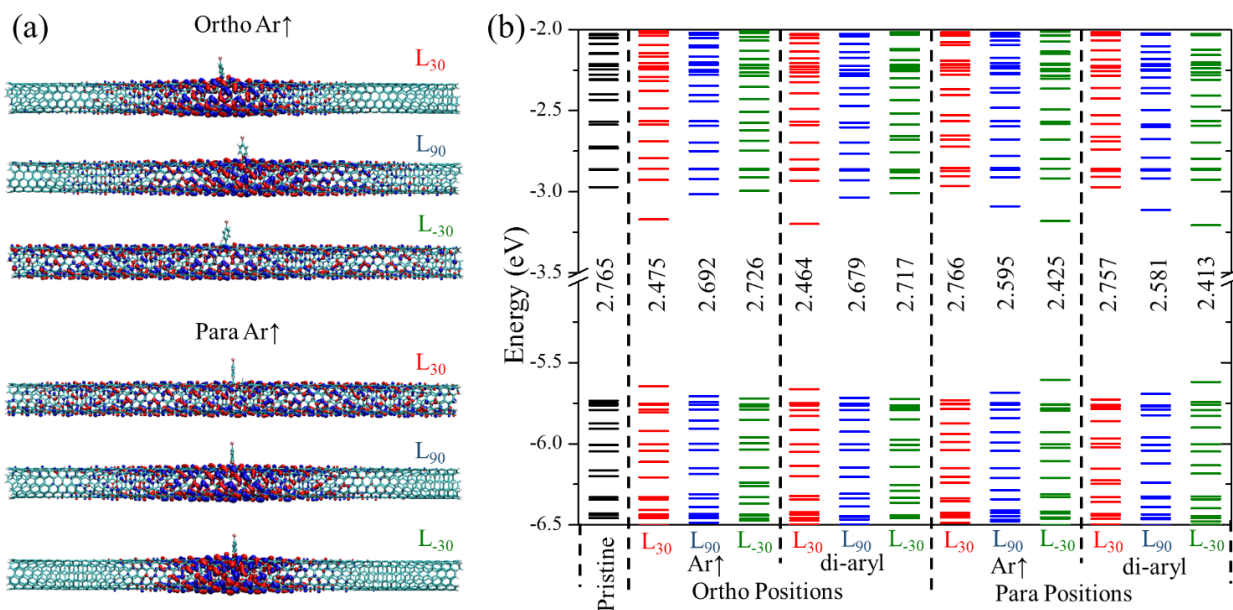


Figure 5.10. The ground state electronic structure comparing Ar \uparrow aryl-H and di-aryl functionalized (6,5) SWCNT in vacuum. Highest occupied molecular orbitals (HOMOs) (a) and the electronic level diagram (b) for functional groups bounded along a vector 27° (L_{30}), 87° (L_{90}), and -33° (L_{-30}) from the SWCNT axis. The values placed between the HOMO and LUMO are the HOMO-LUMO gaps in eV.

most localized orbitals and the smallest energy gap among all ortho structures. L_{90} is in the intermediate range of orbital delocalization and the HOMO-LUMO energy for both ortho and para structures. Overall, the degree of electron localization/delocalization correlates well with the trends of the energy gap and almost perfectly mirrors ortho L_{30} , L_{90} , and L_{-30} to para L_{-30} , L_{90} , and L_{30} , where the lowest HOMO-LUMO gap and the strongest orbital localization is observed for ortho L_{30} and para L_{-30} , while the largest energy gap and the largest degree of delocalization corresponds to ortho L_{-30} and para L_{30} .

5.5.2. Origin of Configuration Dependence: Splitting of Degenerate Molecular Orbitals

Overall, all functionalized SWCNTs have a smaller energy gap than the pristine (6,5) nanotube as shown in figure 5.10(b). Isomer structures with the highest degree of HOMO and LUMO delocalization (ortho L_{-30} and para L_{30}) exhibit only slight differences from the energy gap of the pristine tube, while conformations with highly localized character of their frontier orbitals (ortho L_{30} and para L_{-30}) have a significantly reduced HOMO-LUMO gap. For a hypothetical infinite-length pristine SWCNT, it is expected that the HOMO and LUMO would exhibit double degeneracy. Slight deviation from this expectation is shown in the computations of the pristine (6,5) system, likely due to end-group effects (figure 5.11(b)). However, the sp^3 -defect in the functionalized nanotube completely lifts this degeneracy, resulting in a large splitting between the HOMO and HOMO-1 and LUMO and LUMO+1. As a result, the HOMO is destabilized and the LUMO is stabilized, which decreases the HOMO-LUMO gap in all functionalized structures compared to the pristine tube, which is the most pronounced in isomers having more localized character in their frontier orbitals around the defect site. As with geometries and stabilities, very little difference is observed for $Ar\uparrow$ versus $Ar\downarrow$ configurations

(figure 5.11(a)), reflecting on the similarity between the electronic structure of right handed and left-handed chiral SWCNTs.

5.5.3. Functional Group Independence on Electronic Structure

All these trends are identical for both aryl-H and di-aryl structures. Moreover, the substitution of H by an OH group results in no noticeable changes in the electronic structure of the functionalized SWCNTs, as shown in figure 5.12. It is important to note that even for strongly localized orbitals, the charge density is spread over the part of the tube around the defect site rather than localized on the functional group. This feature of orbital localization underscores

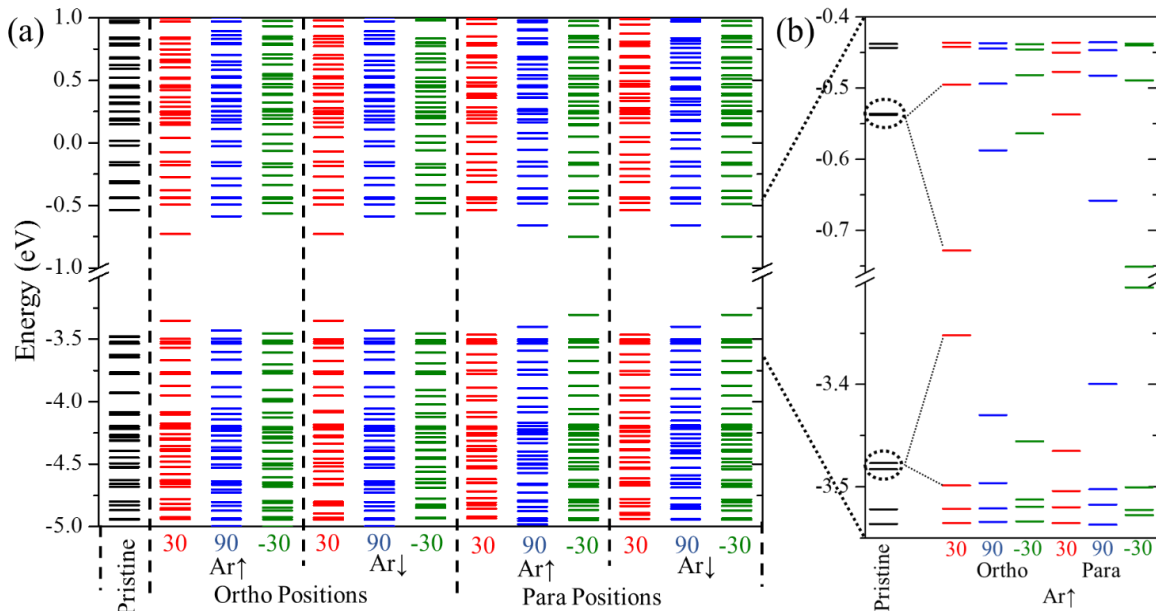


Figure 5.11. Molecular orbital diagrams for 12 aryl-H conformations calculated by the CAM-B3LYP functional and STO-3G basis set in vacuum. (a) The electronic levels in the range of -5.0 to 1.0 eV. (b) Electronic levels at the reduced energy region with only several frontier molecular orbitals of Ar \uparrow configurations. Due to functionalization, the sp^3 -defect at the tube surface breaks the degeneracy of frontier orbitals of the nanotubes resulting in destabilization of the HOMO and stabilization of the LUMO. As a result, the energy gap of functionalized SWCNTs is smaller than in pristine (6,5) nanotube. The decrease in the energy gap is more pronounced in isomer structures with higher degree of localization around the defect site.

the insensitivity of the frontier molecular orbitals of the SWCNT to the chemical composition of the second functional group attached to the same carbon-ring of the tube as the 4-bromobenzene. The position of the functional groups plays a predominant role in governing the electronic structure, while chemical composition of the functional group is secondary.

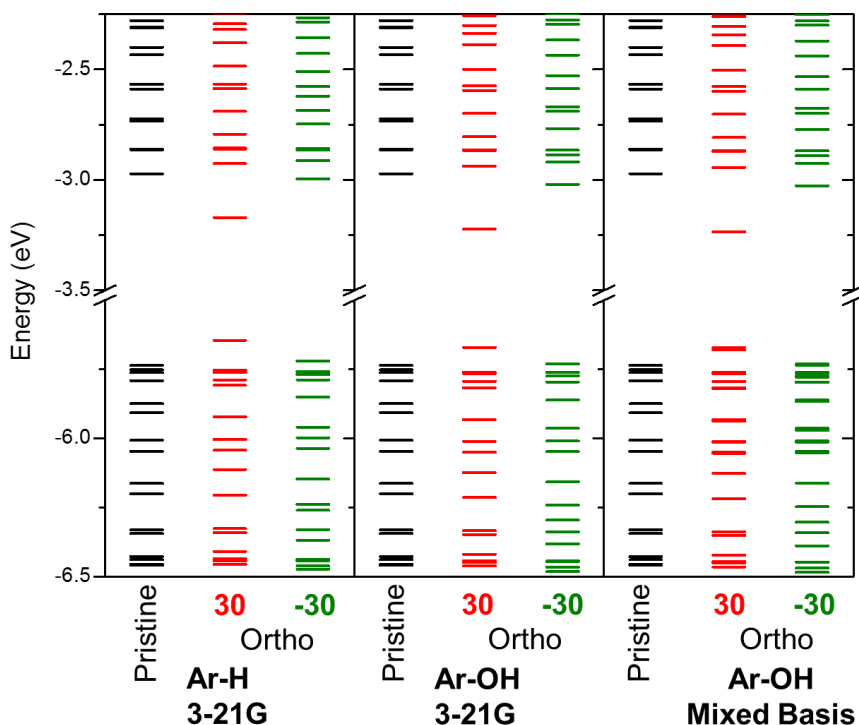
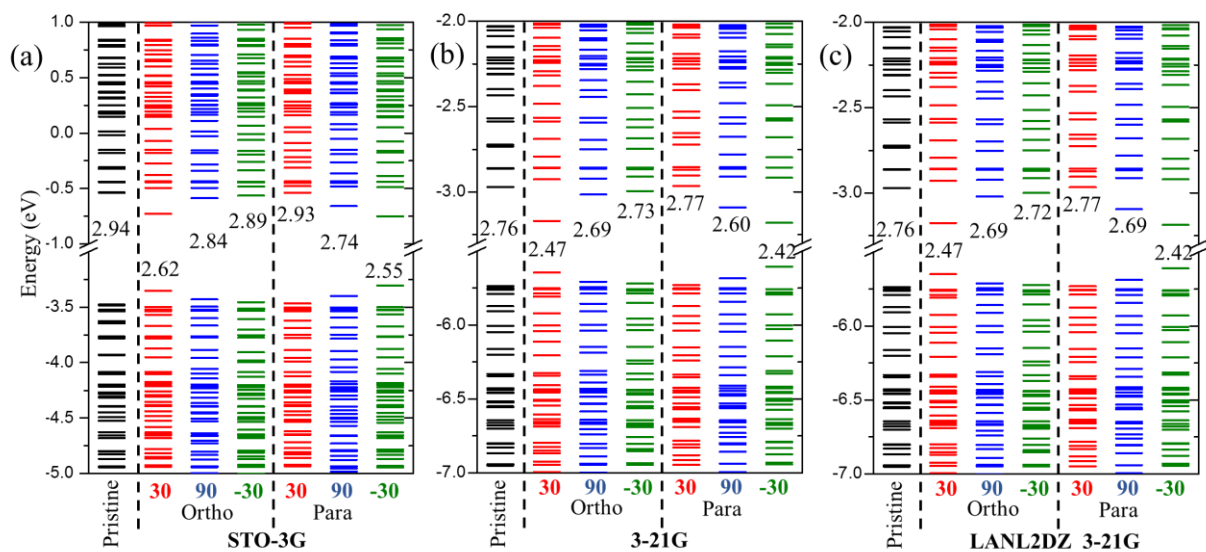


Figure 5.12. Comparison of the molecular orbital diagram of the pristine (6,5) SWCNT and covalently functionalized (6,5) SWCNT by aryl bromide and hydrogen (Ar-H) and aryl bromide and OH (Ar-OH) covalently attached to a single carbon-ring at the tube surface in ortho L_{30} and ortho L_{-30} positions. Calculations are performed using CAM-B3LYP functional and 3-21G basis set and compared to the similar calculations performed with extended mixed basis with 6-31G* basis set used for OH, LANL2DZ for Br atom in aryle bromide group, and 3-21G applied to all other atoms in the system. Neither the increase in the basis set nor the substitution of H to OH-group results in any noticeable change in the electronic structure of the functionalized SWCNT. Thus, the electronic structure of the SWCNT is not sensitive to the chemical composition of the second functional group attached to the same carbon-ring of the tube surface as the aryl bromide. Instead, the position of the functional groups (L_{30} vs. L_{-30}) has a significant effect on the molecular orbitals of the functionalized nanotubes.

5.5.4. Basis Set Dependence: Similar Trends

Overall, an increase in the basis set has a qualitatively minor effect on electronic structure (figure 5.13), which agrees with conclusions from previous literature reports.^{13,24} The results in this chapter demonstrate that increasing the basis set from STO-3G to 3-21G uniformly redshifts the energy gap and excitation energies by a maximum of about 0.2 eV, regardless of isomer geometries, figure 5.14. With the E₁₁ absorption features shifted to match, the energies of E₁₁* becomes nearly indistinguishable. Previous work has shown that a further increase of the basis to 6-31G and 6-31G* insignificantly affects optical transitions of pristine nanotubes.^{12,13} Thus, the qualitative physical picture obtained from these current calculations is not affected by the methodology. Overall, the difference in total energies of the isomer configurations of functionalized SWCNTs is due to the local disruption of the sp²-hybridization in the region of functionalization, as well as the resulting effects on electron delocalization across the entire system.



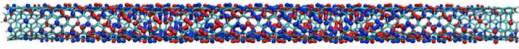
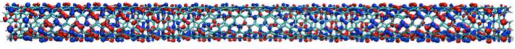
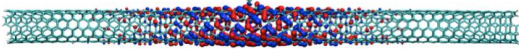
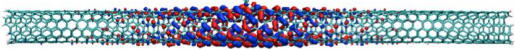
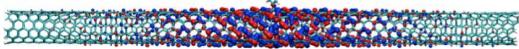
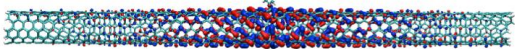
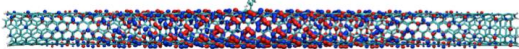
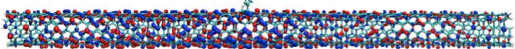
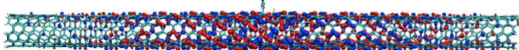
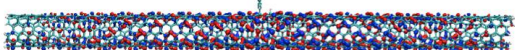
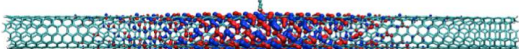
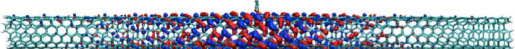
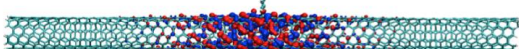
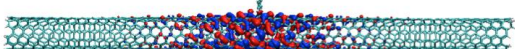
	STO-3G	3-21G
Pristine	 -3.4768 eV	 -5.7361 eV
Ortho L ₃₀	 -3.3522 eV	 -5.6450 eV
Ortho L ₉₀	 -3.4300 eV	 -5.7079 eV
Ortho L ₋₃₀	 -3.4556 eV	 -5.7207 eV
Para L ₃₀	 -3.4651 eV	 -5.7296 eV
Para L ₉₀	 -3.3995 eV	 -5.6850 eV
Para L ₋₃₀	 -3.3054 eV	 -5.6056 eV

Figure 5.13. The ground state electronic structure diagrams for Ar \uparrow conformations of aryl-H functionalized (6,5) SWCNT calculated by CAM-B3LYP functional and (a) STO-3G basis set, (b) 3-21G basis set, and (c) the mixed basis set with LANL2DZ used for Br atom and 3-21G for all other atoms of the system in vacuum. The stated values are the energy gaps in eV. (d) Images of the related highest occupied molecular orbitals (HOMO) calculated by similar methods.

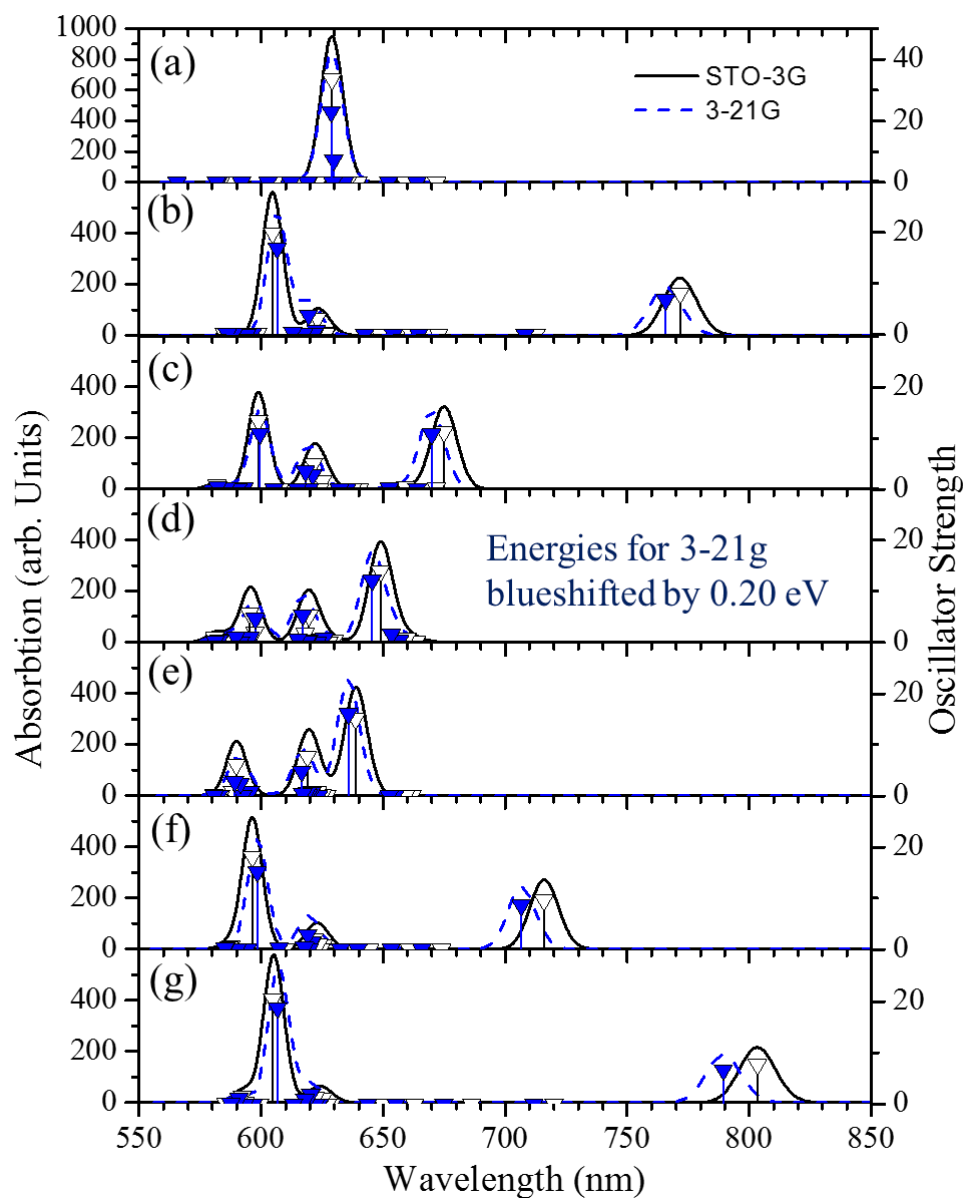


Figure 5.14. Absorption spectra of the (a) pristine (6,5) SWCNT, and its functionalized counterpart with the (b) ortho L_{30} , (c) ortho L_{90} , (d) ortho L_{-30} , (e) para L_{30} , (f) para L_{90} , and (g) para L_{-30} $Ar\uparrow$ conformations calculated in vacuum using CAM-B3LYP and either STO-3G (black lines) or 3-21G basis sets (blue lines). The vertical black lines correspond to the optical transitions with the height related to their oscillator strength, which values are shown at the right Y-axis. Spectra calculated by 3-21G were consistently blueshifted by 0.20 eV to coincide in E_{11} peak with those obtained by STO-3G basis set.

5.6. Optical Properties Arising from Functionalization

5.6.1. The Introduction of Defect-Localized Low Energy Features

The dependence of the ground state electronic structure on the sp^3 -defect position also governs the optical properties of functionalized (6,5) nanotubes, as illustrated in figure 5.14. In the absorption spectrum of the pristine nanotube calculated in vacuum, the lowest energy peak is

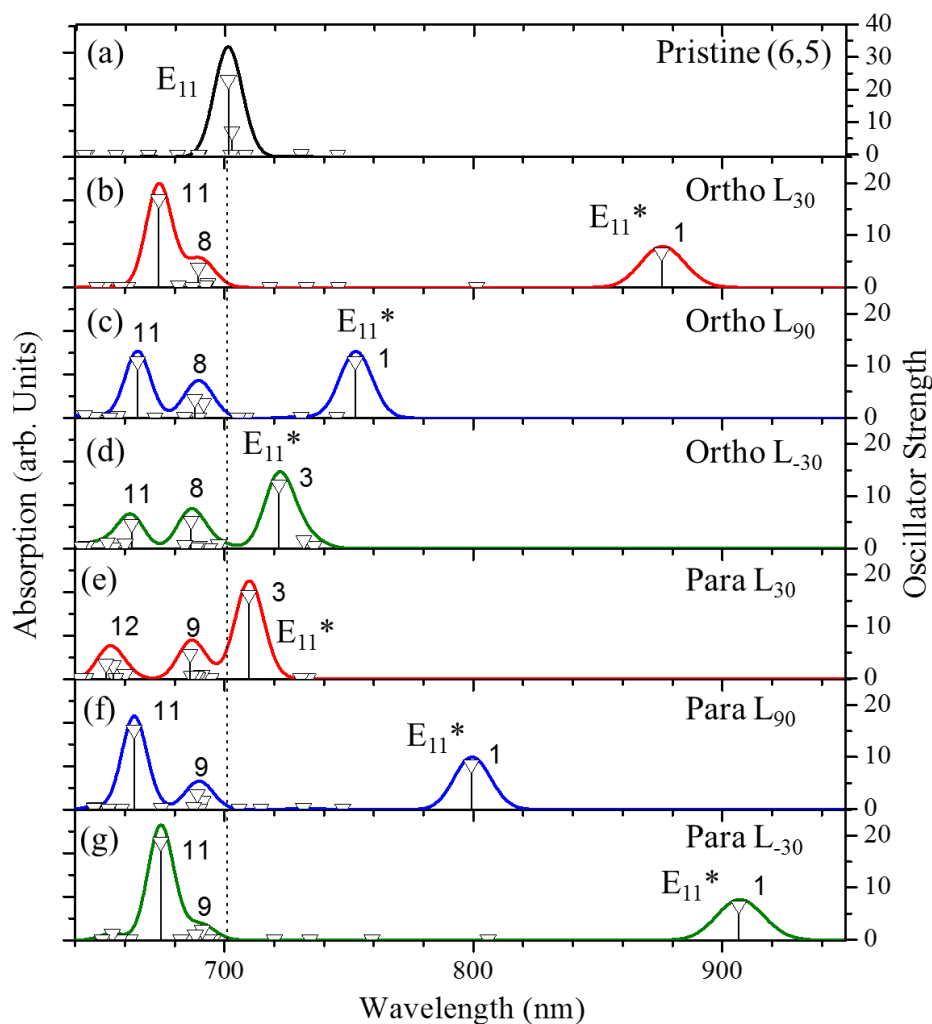


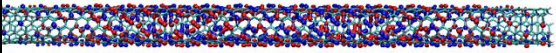
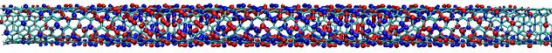
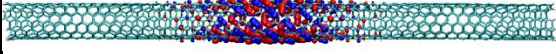
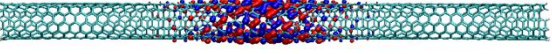
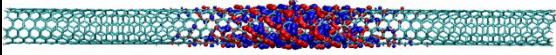
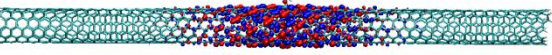
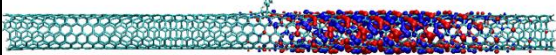
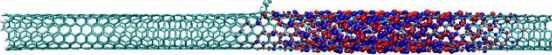
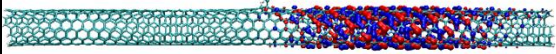
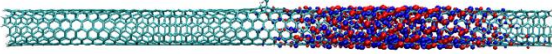
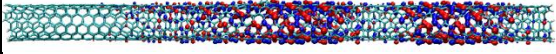
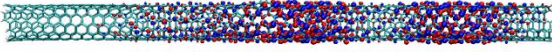
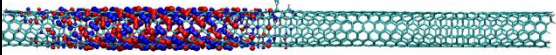
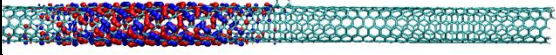
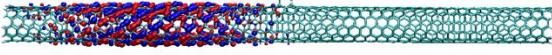
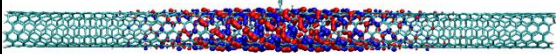
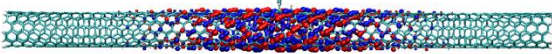
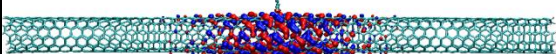
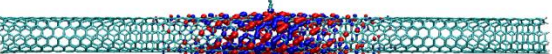
Figure 5.15. Absorption spectra of the pristine (6,5) SWCNT (a), and its functionalized counterpart in ortho L_{30} (b), ortho L_{90} (c), ortho L_{-30} (d), para L_{30} (e), para L_{90} (f), and para L_{-30} (g) $Ar\uparrow$ conformations calculated in vacuum. The vertical black lines correspond to the optical transitions with the height related to their oscillator strength, which values are shown at the right Y-axis. The dashed line indicates the reference point for the energy of the E_{11} transition in the pristine SWCNT.

observed at ~ 700 nm, with the main contribution being from the optically active $\pi \rightarrow \pi^*$ transitions (states 5 and 6 in figure 5.15(a)). The NTOs demonstrate exciton density delocalized across the entire length of the SWCNT, table 5.3. This peak is assigned to the E_{11} band. Note that the energy of E_{11} is expected to be blue shifted compared to the experimental peaks, due to unphysical density functional, limited basis set, and the confinement effect of the finite-size tube model.¹² Functionalization introduces new defect-based optical transitions at much lower energy ranges from the original E_{11} band (labeled E_{11}^* in figure 5.15). The degree of red shifts of E_{11}^* from E_{11} bands depends on the precise position of the sp^3 -defect, following the trends in their ground state energy gaps. Thus, the greatest red shifts are observed for para L_{-30} and ortho L_{30} , followed by para L_{90} and ortho L_{90} , figure 5.15(b), (g) and (c), (f), respectively. For these isomer conformations, the lowest-energy transition is optically active and originates predominantly from the transition between the HOMO and LUMO, demonstrating noticeable localization of NTOs around the defect site as shown in table 5.3.

5.6.1.1. Delocalized Higher Energy States with Familiar Nodal Structure

Conversely, only slight red shifts in the lowest energy absorption peaks are observed for ortho L_{-30} and para L_{30} , figure 5.15 (d) and (e). In these cases, however, the first two lowest energy transitions are optically forbidden (dark states), similar to the pristine nanotube. These dark transitions have highly delocalized $\pi \rightarrow \pi^*$ character, with the orbital density spread over the tube surface, but with some slight preferential localization over one side of the tube with respect to the defect, Table 5.3. This preferential localization over one side of the nanotube is due to the asymmetry of the defect position, which is not located directly at the middle of the tube. This asymmetry in the geometry translates to the excited state orbitals. The NTOs contributing to the optically active lowest-energy E_{11}^* band (transition 3 in figure 5.15 (d) and (e)) of ortho L_{-30} and

Table 5.3. Natural transition orbitals (NTOs) representing the photoexcited electron-hole pair contributing to the lowest energy transition S_1 in the E_{11}^* absorption band of aryl-H (Ar \uparrow) structures and compared to the brightest transition in the E_{11} absorption band of pristine (6,5) SWCNT in vacuum. The left column presents information on the transition number and its oscillator strength. Only the NTO pairs that dominantly contribute to the optical transition are shown, with the percent of their contribution depicted at the bottom of each NTO image. In these cases, a few electron-hole pairs have to be taken as a linear combination to correctly describe the optical transition.

		Hole	Electron
Pristine	S_6		
	$f=33.5$	91%	
Ortho	L30		
	S_1		
	$f=8.0$	93%	
	L90		
	S_1		
	$f=11$	80%	
Ortho			
		35%	
	L-30		
S_1			
$f=0.1$	29%		
Ortho			
		10%	
	Para	L30	
S_1			
$f=0.0$	32%		
Para			
		30%	
Para	L90		
	S_1		
$f=9.6$	89%		
Para	L-30		
	S_1		
$f=7.7$	94%		

para L₃₀ exhibit localization around the defect site, similar to the optically allowed S₁ transitions in other isomer conformations, table 5.3. However, in comparing this S₃ exciton to the strongly red-shifted and optically active S₁ states in para L₃₀ and ortho L₋₃₀, one can notice its higher degree of delocalization. Enhanced delocalization of the S₃ excitonic state in ortho L₋₃₀ and para L₃₀ also correlates with its slightly ‘brighter’ nature (higher oscillator strength), than S₁ in para L₃₀ and ortho L₋₃₀ having more pronounced localization around the defect site. Highly delocalized NTOs are observed for bright transitions at the higher-energy band for all isomer configurations (transitions 8-12 in figure 5.15), as illustrated in table 5.4 and 5.5. These transitions are assigned to the main E₁₁ band because of their completely delocalized $\pi \rightarrow \pi^*$ character similar to those in pristine SWCNT. However, the functionalization splits E₁₁ into two less intense and blue-shifted peaks, compared to the E₁₁ band in the pristine nanotube, figure 5.15. The degree of this splitting and relative intensity of peaks in the E₁₁ band depends on the defect position. The least blue-shifted peak in E₁₁ formed by transitions S₈ and S₉ has its energy and intensity nearly independent of the isomer conformations. This can be rationalized by their NTOs being delocalized over the entire tube but having a node at the defect position, figure 5.5. Because the exciton density has minimal contribution from the defect site, the energy of these transitions is not so much affected by the isomer geometries. Conversely, the excitons in the most blue-shifted peak in the E₁₁ band (S₁₁ and S₁₂) have two nodes and three maxima in their density around the defect site and close to the tube edges, making the energy and intensity of these transitions more sensitive to the isomer conformations, as well as to the edge effects. The nodal structure of excitons originates from the wavefunction confinement due to the finite-size tube model. This nodal structure has the same physical meaning as a characteristic standing wave feature related to its k-vector.^{12,25} Thus, the delocalized excited states can be considered as

Table 5.4. Natural transition orbitals (NTOs) representing the photoexcited electron-hole pair contributing to the bright transitions in the first peak in the split E_{11} absorption band of aryl-H (Ar \uparrow) structure. The left column presents information on the transition number, its oscillator strength, and the percent of the NTO pair contributing to the transition. Calculations are performed using CAM-B3LYP and STO-3G basis set.

		Hole	Electron
Ortho	L ₃₀ S_8 $f=3$ 39%		
	20%		
	L ₉₀ S_8 $f=5$ 57%		
	24%		
	18%		
	L ₋₃₀ S_8 $f=5$ 46%		
30%			
12%			
Para	L ₃₀ S_9 $f=8$ 30%		
	27%		
	L ₉₀ S_9 $f=2$ 30%		
	27%		
	L ₋₃₀ S_9 $f=1$ 28%		
	24%		

Table 5.5. Natural transition orbitals (NTOs) representing the photoexcited electron-hole pair contributing to the brightest transitions in the second peak in the split E_{11} absorption band of aryl-H ($Ar\uparrow$) structures. The left column presents information on the transition number and its oscillator strength and the percent of the NTO pair mostly contributing to the transition.

		Hole	Electron
Ortho	L30		
	S ₁₁		
	f=20		
	30%		
	24%		
	23%		
	L90		
	S ₁₁		
	f=13		
42%			
28%			
20%			
Para	L-30		
	S ₁₁		
	f=6		
	45%		
	29%		
	L30		
	S ₁₂		
	f=6		
	22%		
18%			
18%			
L90			
S ₁₁			
f=18			
27%			
25%			
19%			
L-30			
S ₁₁			
f=20			
27%			
24%			
24%			

standing waves in quasi-1D structures,²⁶ where the nodes are related to the exciton momenta, k . Consequently, the zero-node state is associated with the $k=0$ exciton in the infinite nanotube limit, which has stronger interaction with the defect at the tube center causing its dramatic red shift. States having one or more nodes belong to the same excitonic band as the respective zero-node exciton, but have higher values of the momentum and higher energies.

5.7. Optical Properties for Different Rotational Conformation and Solvents

Since the lowest energy optical transitions in functionalized SWCNT are localized around the defect site, it is imperative to determine the degree of interaction between the electron density located on the SWCNT near the defect and the electron density on the defect itself and qualify how this interaction affects optical properties. This interaction is expected to have some dependence on the precise rotational position of the aryl group with respect to the SWCNT axis. To explore this effect, the potential energy surface (PES) at different rotation angles about the C-C bond between the aryl group and SWCNT were calculated along with the absorption spectra of aryl-H isomers with the aryl group conformations corresponding to the minimal and maximal energies along this PES (figure 5.16). Additionally, solvent effects must be considered.

5.7.1. Most Stable Dihedral Conformations

The conformation with the aryl group is perpendicular to the SWCNT axis allows stability in the system due to the additional space available between the ortho hydrogen atoms of the aryl group and the SWCNT (figure 5.16(a)). Additionally, the aryl group in this position allows for the maximum overlap due to the closer proximity of the two π systems. For all para configurations, this results in the minimum total energy of the system occurring when the aryl group is perpendicular to the SWCNT axis. However, for ortho configurations the conformation

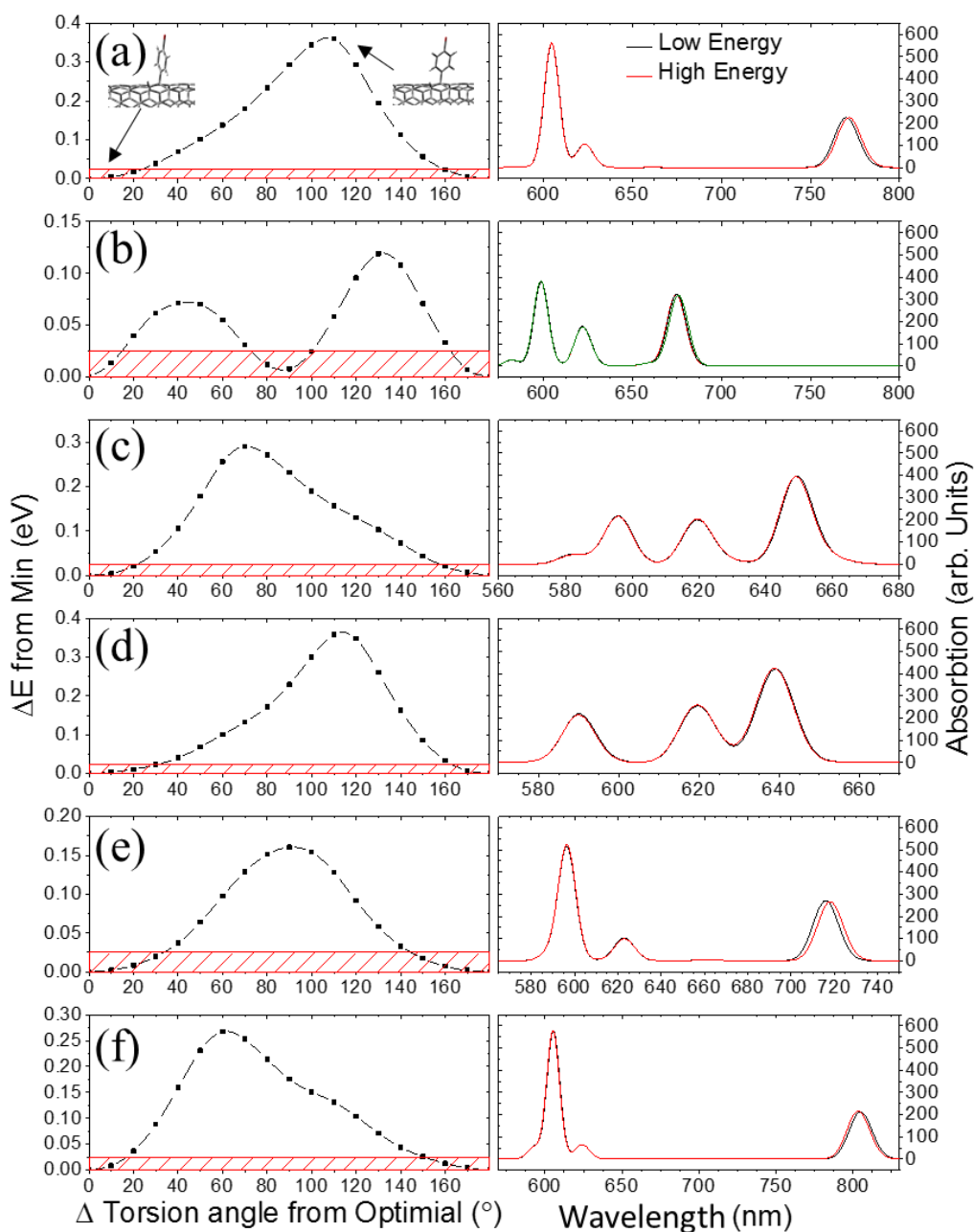


Figure 5.16. Potential energy surface (PES) as a function of rotational angle about the C-C bond between the aryl bromide group and (6,5) SWCNT for different aryl-H configurations (left panels) and absorption spectra calculated for geometries corresponding to the lowest energy (red curve) and to the highest energy (black curve) of the PES (right panels). (a) ortho L₃₀, (b) ortho L₉₀, (c) ortho L₋₃₀, (d) para L₃₀, (e) para L₉₀, and (f) para L₋₃₀ Ar[↑] conformations in vacuum. Because PES of the ortho L₉₀ isomer in (b) shows two local minima and maxima, four spectra are shown with the blue and green lines depicting the spectra of ortho L₉₀ geometries at the second local minimum (torsion angle ~90°) and the second maximum (torsion angle ~130°), respectively. Since all curves in right panels nearly coincide, the absorption spectra are independent on the torsional angle between the aryl and the nanotube for all defect structures.

of the aryl group favors maximizing the distance between the ortho hydrogen of the aryl group and the hydrogen atom functionalizing the SWCNT and is therefore highly dependent on the positions of functionalization. The favored orientation for these species favors the aryl group to be perpendicular to the vector pointing toward the hydrogen atom on the SWCNT.

5.7.2. A Significant Rotational Barrier

All potential energy surfaces for rotation about the C-C bond between the aryl group and SWCNT are substantial but on the same order of magnitude of the energy available at room temperature. Since the position of the aryl group and the hydrogen atom on SWCNT in the ortho L_{90} configuration are located along the curvature of the SWCNT, additional space is allowed between the two groups. As such, this is the only configuration with more than one local minimum in the potential energy surface. Despite the relatively high rotational barriers, the vertical excitations from geometries in either the minimum or maximum of the PES are nearly identical. As such, the overlap between the electron density in the π systems of the SWCNT and the aryl group has very little effect on the optical features and therefore consideration of this rotation would be insufficient to justify any temperature dependence of experimental spectra. This observation further validates the relative similarities of electronic structure between aryl-H and di-aryl species.

5.7.3. Rotational Conformation has Little Influence on Optical Characteristics

The absorption spectra obtained for these different geometries in either the minimum or maximum of the PES, are nearly identical. As such, the overlap between the exciton density in the π -systems of the SWCNT and the aryl group has negligible effect on the optical properties. This observation further validates the relative similarities of electronic structures between aryl-H, aryl-OH, and di-aryl systems (figure 5.16).

5.7.4. Insignificant Bathochromic Shifts due to Small Static Dipoles

Computation of the excitation energies in a dielectric environment of increasing polarity reveals small bathochromic shifts for absorption in all the structures studied, figure 5.17. The E_{11} absorption band of the pristine (6,5) SWCNT exhibits a red shift of ~ 30 meV when computed in hexane versus vacuum. However, increasing the polarity of the solvent over the wide range of $\epsilon=1.9$ for hexane to $\epsilon=78.4$ for water only results in a slight increase of the energy of optical transitions, while acetonitrile ($\epsilon=35.7$) as solvent has a similar effect on transitions as water. Identical trends are observed for the E_{11} absorption band of all functionalized nanotubes, where the maximal shifts are not more than 30 meV in ortho L_{30} and para L_{-30} structures, and are nearly zero for ortho L_{-30} and para L_{30} isomers.

Likewise, the bathochromic shifts for the E_{11}^* absorption band of all functionalized nanotubes are also found to be small on comparing spectra in vacuum and water, with the largest shifts of ~ 40 meV corresponding to the E_{11}^* of ortho L_{30} and para L_{-30} , while nearly no shifts of E_{11}^* are found with respect to the main E_{11} band for ortho L_{-30} and para L_{30} isomers, Fig. 5. As with total energies, this negligible solvent effect can be attributed to the relatively low electrostatic dipole moments of these systems (figure 5.9 and table 5.1). For all species, the calculated static dipoles are less than 0.6 Debye, with the smallest dipole moments of ortho L_{-30} and para L_{30} configurations exhibiting diminishing bathochromic shifts. As such, only small perturbations in electronic structure and optical properties are observed as the result of the dipole-dipole interactions with the environment. These results coincide with previous studies of (6,2) SWCNT covalently functionalized by aryls that have also shown negligible solvent effects on the absorption spectra of functionalized SWCNT.²²

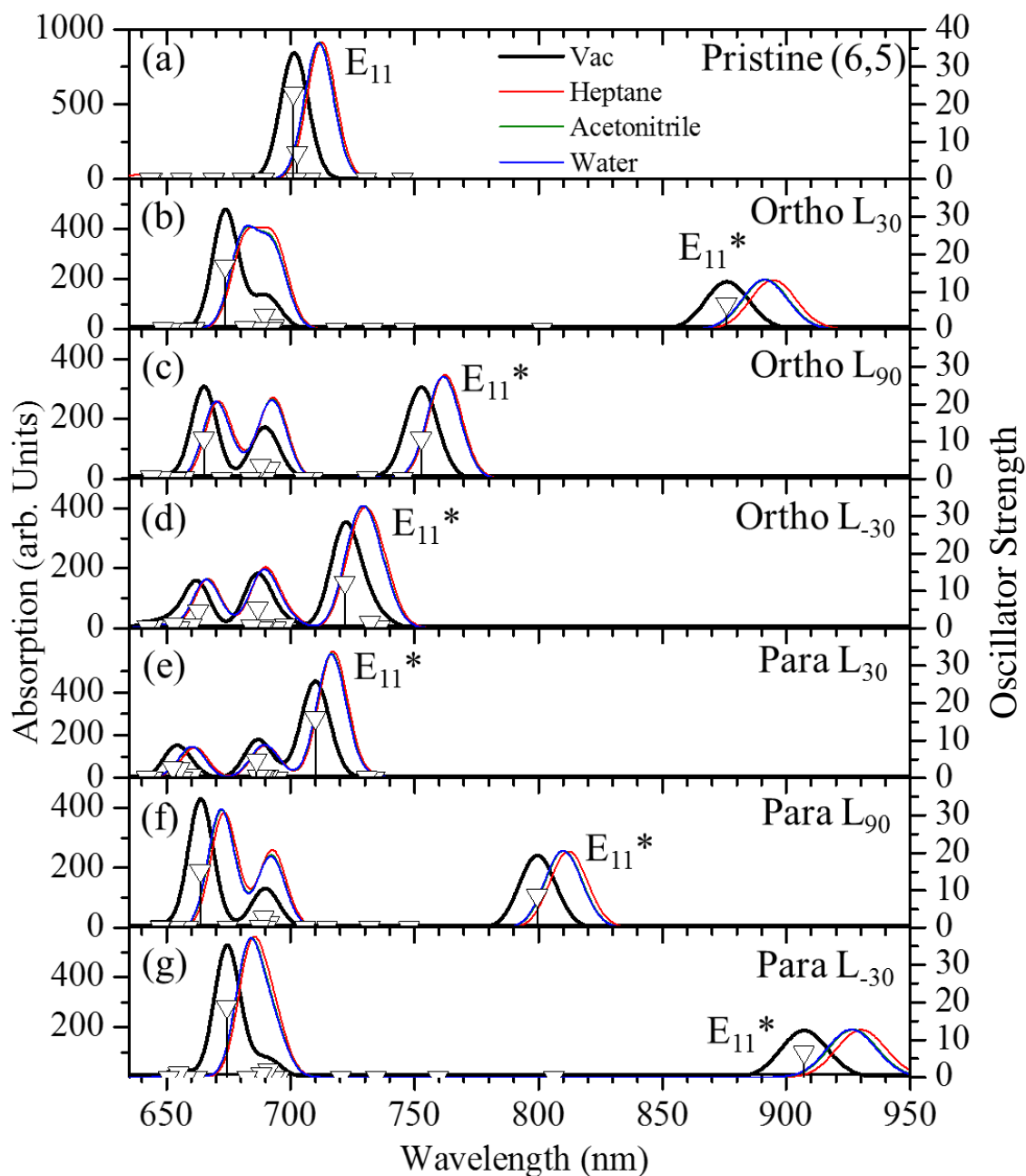


Figure 5.17. Absorption spectra calculated using the CAM-B3LYP functional and 3-21G basis set in vacuum (black lines) and in the dielectric environment of heptane (red lines), acetonitrile (green lines), and water (blue lines) for pristine (6,5) SWCNT and its functionalized counterpart with aryl-H configurations. Note that the results for acetonitrile and water coincide, so that the green line (acetonitrile) is covered by the blue line (water) and is not seen. The vertical black lines correspond to the optical transitions in vacuum with their height related to the transition oscillator strength, which values are shown at the right Y-axis. In all cases, the E_{11} band has diminishing bathochromic shift in different solvents. The most red-shifted E_{11}^* band associated with the defect shows more noticeable bathochromic shift, but still very small.

5.8. Emission Features: Trending with Absorption

5.8.1. Emission Energies

Energetic trends in emission features of the functionalized (6,5) SWCNTs in vacuum and solvent are consistent with those of the lowest energy absorption band E_{11}^* , while showing just slightly more pronounced bathochromic shifts. The magnitude of the bathochromic shifts of the emission energy in different solvents also depends on the defect configuration in the same way as for the transitions in the E_{11}^* absorption band. The full optical features including absorption and emission are presented in figure 5.18. The mirroring trends between the E_{11}^* absorption band and the emission states justifies that calculations of the lowest states in absorption spectra provide a qualitatively correct description of the PL in SWCNTs and functionalized SWCNTs.

5.8.2. Stokes Shifts due to Vibrational Reorganization

While the trends in absolute energies of absorption and emission have been shown to be identical, the Stokes shifts fall in the range between 5 and 168 meV, depending on the defect conformation, and follow similar trends as found for the bathochromic shifts in varying solvents. Negligible Stokes shifts are found for the ortho L_{-30} and para L_{30} configurations, which also display the least redshifted emission energies with solvent. Conversely, the largest Stokes shifts are found for the ortho L_{30} and para L_{-30} configurations, which have the most red-shifted emission. Substantial values of Stokes shifts in the presence of ortho L_{30} and para L_{-30} defects can be understood in terms of vibrational reorganization due to deformation of the nanotube geometry upon exciton trapping at the defect site upon photoexcitation.²⁷ These reorganization energies are discussed in a further section.

5.8.3. Exciton Localization in the Excited State

Due to the relatively small vibration reorganization energy between absorption and emission geometries, the NTOs contributing to the emission states demonstrate similar character as that found for the lowest energy excitons in the E_{11}^* absorption band, but with enhanced localization around the tube center for both pristine and functionalized SWCNTs, as illustrated in table 5.5. Emission states for the ortho L_{-30} and para L_{30} configurations show a low degree of

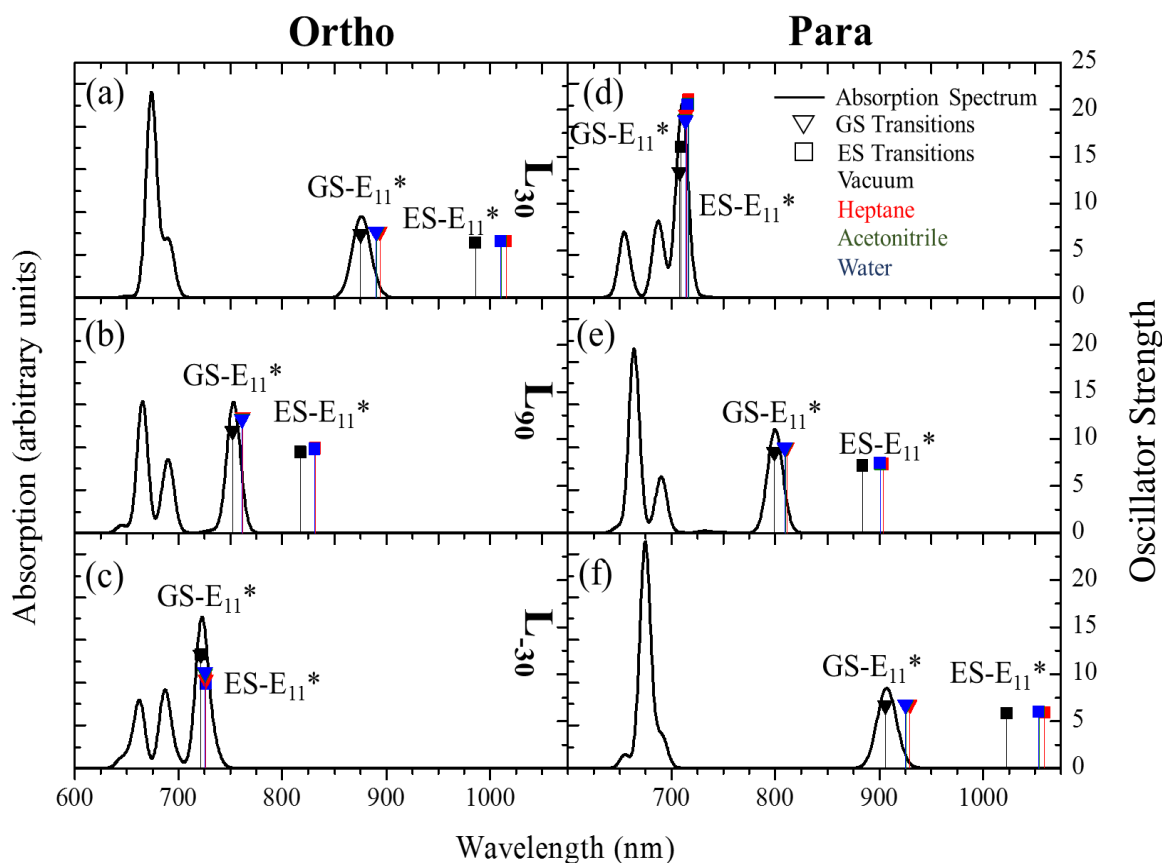


Figure 5.18. Absorption and emission transitions of the Ar-H isomers calculated in various solvents. (a) ortho L_{30} , (b) ortho L_{90} , (c) ortho L_{-30} , (d) para L_{30} , (e) para L_{30} , and (f) para L_{-30} configurations. The black curves are absorption spectra in vacuum. Vertical lines with symbols of black, red, green, and blue colors represent the lower energy optically active transitions in the E_{11}^* band of functionalized SWCNTs in vacuum, heptane, acetonitrile, and water, respectively. The height of the vertical lines corresponds to the values of the oscillator strength of these transitions, shown at the right Y-axis. Triangles depict the lowest energy transitions contributing to the absorption (calculated at the ground state, GS, geometry) and squares the emission (calculated at the optimized excited state, ES, geometry).

exciton localization around the defect site. The NTOs contributing to the E_{11}^* absorption band for these species show a delocalization pattern similar with those of the pristine tube, rationalizing the negligibly small Stokes shifts in these systems. In contrast, ortho L_{30} and para L_{30} structures show noticeably increased localization around the defect site, compared to their excitons in the E_{11}^* absorption band and, consequently, have the largest Stokes shifts. Such a substantial vibrational reorganization energy between the excited and ground state of SWCNTs in the presence of a fluorescent defect agrees well with experimental and computational reports for (6,5) SWCNTs functionalized with various aryl derivatives.

Table 5.6. Natural transition orbitals (NTOs) representing the photoexcited electron-hole pair contributing to the lowest energy emission state of aryl-H ($Ar\uparrow$) structures and compared to the emission state of pristine (6,5) SWCNT in vacuum. The left column represents information on the state number and its oscillator strength. Only the NTO pairs that dominantly contribute to the transition (>60 %) are shown.

		Hole	Electron
Ortho	Pristine $S_9, f=34$		
	L30 $S_1, f=7$		
	L90 $S_1, f=9$		
Para	L-30 $S_3, f=12$		
	L30 $S_3, f=11$		
	L90 $S_1, f=8$		
	L-30 $S_1, f=8$		

Similar to the absorption results, the ortho L₋₃₀ and para L₃₀ configurations with the least red-shifted emission energies have two optically dark lowest energy states with the third state being emitting. Therefore, the emission of these isomers is expected to be the least intense among all other defect conformations due to the ‘trapping’ of the excitation in the optically inactive lowest energy states. However, this weakly emissive peak is close in energy to the E₁₁ main band and, therefore, would be hard to resolve in experimental samples. In contrast, the most red-shifted emission states from ortho L₃₀ and para L₋₃₀ are expected to be significantly distinct from the emission peaks associated with the ortho L₉₀ and para L₉₀ conformations. As such, the experimental photoluminescence (PL) spectra of functionalized (6,5) SWCNTs, where defects associated with functional groups are naturally present in various isomer conformations, is expected to have several well-pronounced emission features. These correspond to the most redshifted E₁₁* band of ortho L₃₀ and para L₋₃₀, followed by the less red-shifted E₁₁* bands of L₉₀ and para L₉₀, and the wide main E₁₁ band close in its energy to the E₁₁ band of the pristine SWCNT. These theoretical predictions agree well with recent experimental data.

5.9. Reorganization Energies & Radiative Lifetimes

5.9.1. Configuration Dependent Reorganization Energies

Previous studies have demonstrated reorganization energies in aryl-functionalized SWCNTs with a magnitude on the order of ~100 meV²⁷. These energies play a non-negligible role in red shifting the emission spectra have significant variance dependent on the configuration of functionalization and have been eluded to by the previously discussed stokes-shifts and similarity between the absorption and emission excitons. The reorganization energies fall into two very distinct “classes” for aryl functionalized SWCNTs with different functionalization configurations (figure 5.19). For species with very little red-shift where the E₁₁ and E₁₁* exhibit

practically the same energy and localization (ie. ortho L_{-30} and para L_{30}) only very small reorganization energies are observed (<30 meV). This is due to the very similar degrees of delocalization between the pristine SWCNT and the functionalized systems. In both cases, the exciton is delocalized across the entire system. Since the exciton occupies nearly the entire length of the SWCNT and therefore lies predominantly on the pristine portion in even the functionalized case, the exciton appears very “similar” independent of functionalization. Little vibration reorganization is involved in transforming the exciton in the pristine SWCNT to the exciton in the functionalized species. However, species with a more significant red-shifted

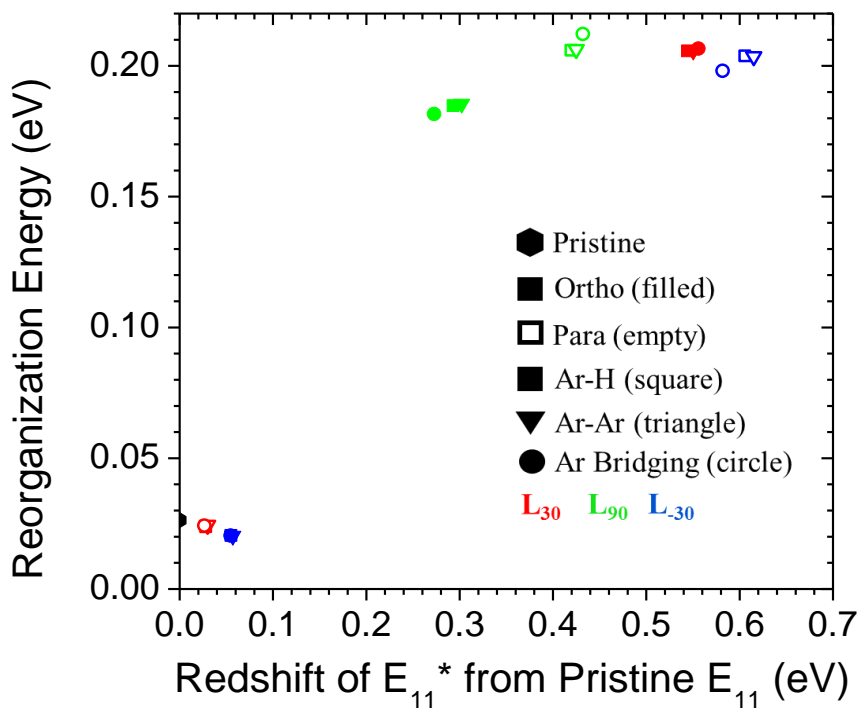


Figure 5.19. Calculated reorganization of different functionalization configurations with respect to the SWCNT axis compared to the energetic shift of the E_{11}^* transition from the E_{11} transition of the pristine SWCNT. In this figure, the hexagon represents the pristine SWCNT, filled points represent ortho, empty points represent para, squares, triangles, and circles represent Ar-H, Ar-Ar, and Aryl bridging configurations respectively, and red, green, and blue represent L_{30} , L_{90} , and L_{-30} respectively.

emission show significantly increased vibrational reorganization on the order of 200 meV. These substantially larger values reflect the fact that the E_{11} and E_{11}^* look very different. In other words, the exciton is formed on the pristine portion of the SWCNT and subsequently is localized on the defect site. This process is accompanied by a reduction in energy in the form of vibrational reorganization.

5.9.2. Radiative Lifetimes: More Closely Correlated with Red Shifts

The transition dipoles of the functionalized SWCNTs only slightly varies over all species, where the most redshifted species have slightly lower transition dipoles. It therefore comes as no surprise that lower transition dipoles generally result in higher lifetimes since the radiative lifetime is inversely proportional to the oscillator strength (figure 5.20(a)). The calculated lifetimes are more affected by the redshift from E_{11} , and effect originating from the frequency of the transition squared term in the denominator. Since these variables are interrelated for a given chemical species, there is great deal of variance where those species that exhibit practically no redshift from E_{11} show lifetimes of less than four nanoseconds while species with significant redshifts have lifetimes of over 10 nanoseconds (figure 5.20(b)). Despite the functionalization configuration dependence of lifetimes, little effect is observed as the result of changing the functional group. Aryl-H, diary, and bridging structures form clusters of points on the curve of redshift vs lifetime, and the trend is nearly linear. This is the natural consequence of invariance in energies of the optical features or electron localization due to the specific chemical species of functionalization (discussed in greater detail in the next section).

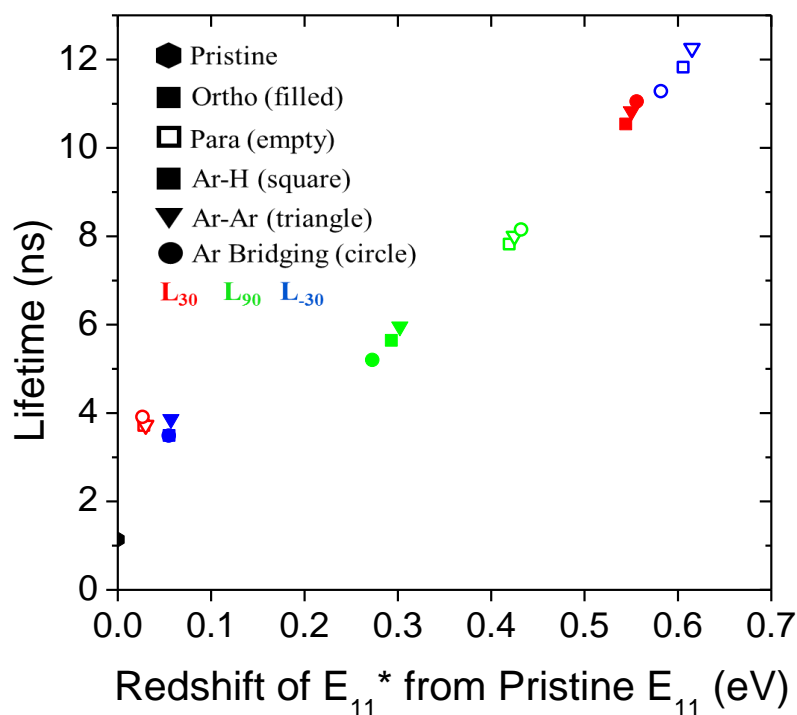
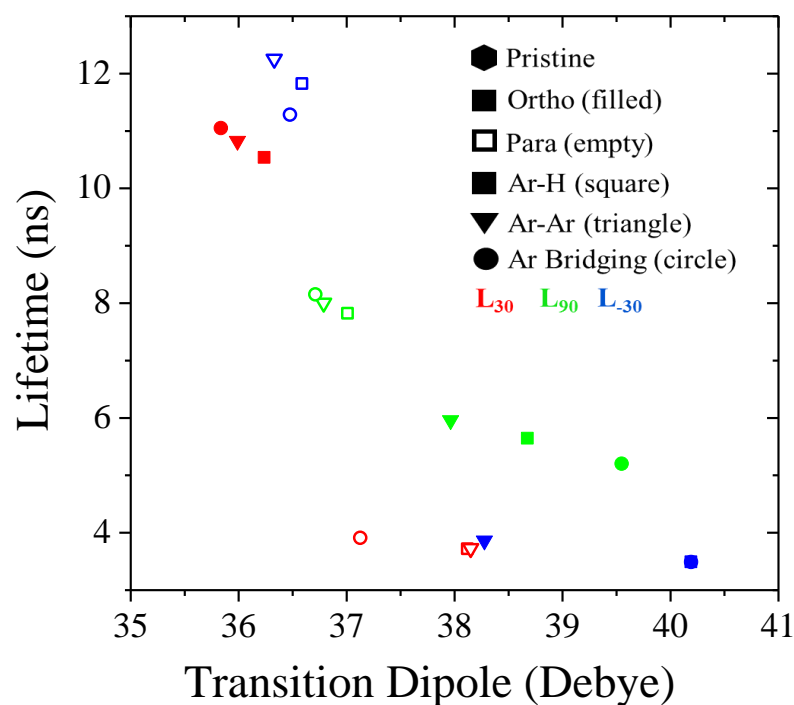


Figure 5.20. Calculated radiative lifetime of different functionalization configurations with respect to the SWCNT axis as a function of (a) transition dipole, and (b) redshift of emission features. Filled points represent ortho, empty points represent para, squares, triangles, and circles represent Ar-H, Ar-Ar, and Aryl bridging configurations respectively, and red, green, and blue represent L₃₀, L₉₀, and L₋₃₀ respectively.

5.10. Role of the Chemical Species of Functionalization

It has been experimentally shown that functionalization of (6,5) SWCNTs with different groups of different electron withdrawing and donating character results in slight shifts of emission features in the range from 1100 to 1200 nm. As shown previously in this chapter, little effect is observed from functionalization with different groups as compared to changing the configuration. The focus of this section is the justification of the experimentally observed redshifts based on the localized structure from of changing the chemical species.

5.10.1. Functional Stabilities

Functionalization with different species results in very little changes in the overall trends. For all monovalent non-bridging species, the ortho L_{30} analogue is the most stable due to the relatively minimal disruption to sp^2 hybridization in those species (figure 5.21). The least stable ortho configuration is the one that puts the connectivity between the two functional groups nearly radial with respect to the SWCNT axis (ortho L_{90}). However, in this trend breaks down when the bridging species is used where this becomes the most favorable binding configuration. This is likely due to optimal bond lengths in systems with the introduced rigidity of the bond along the edge of the six-membered ring. Due to the angle strain required for functionalization of positions across from the hexagonal ring to form the para species, only the ortho configurations are energetically stable for monovalent functional groups. As a result, para species failed to optimize using the DFT procedure.

5.10.2. Electronic Structure due to Different Functionalization

As previously discussed, the most stable HOMO and unstable LUMO results for the pristine (6,5) SWCNT as compared to their functionalized counterparts (figure 5.22). For practically all configurations, functionalization with methyl results in the most destabilized

HOMO. Integrating electronegative atoms such as fluorine and bromine into the functional group results in less destabilization of the HOMO. This effect is most pronounced where electrons are most delocalized. For example, the integration of the trifluoromethane group result in practically no destabilization in the HOMO for ortho L₋₃₀ and para L₃₀. This effect is much less pronounced for ortho L₃₀ and para L₋₃₀. This is the likely the result of slight changes in

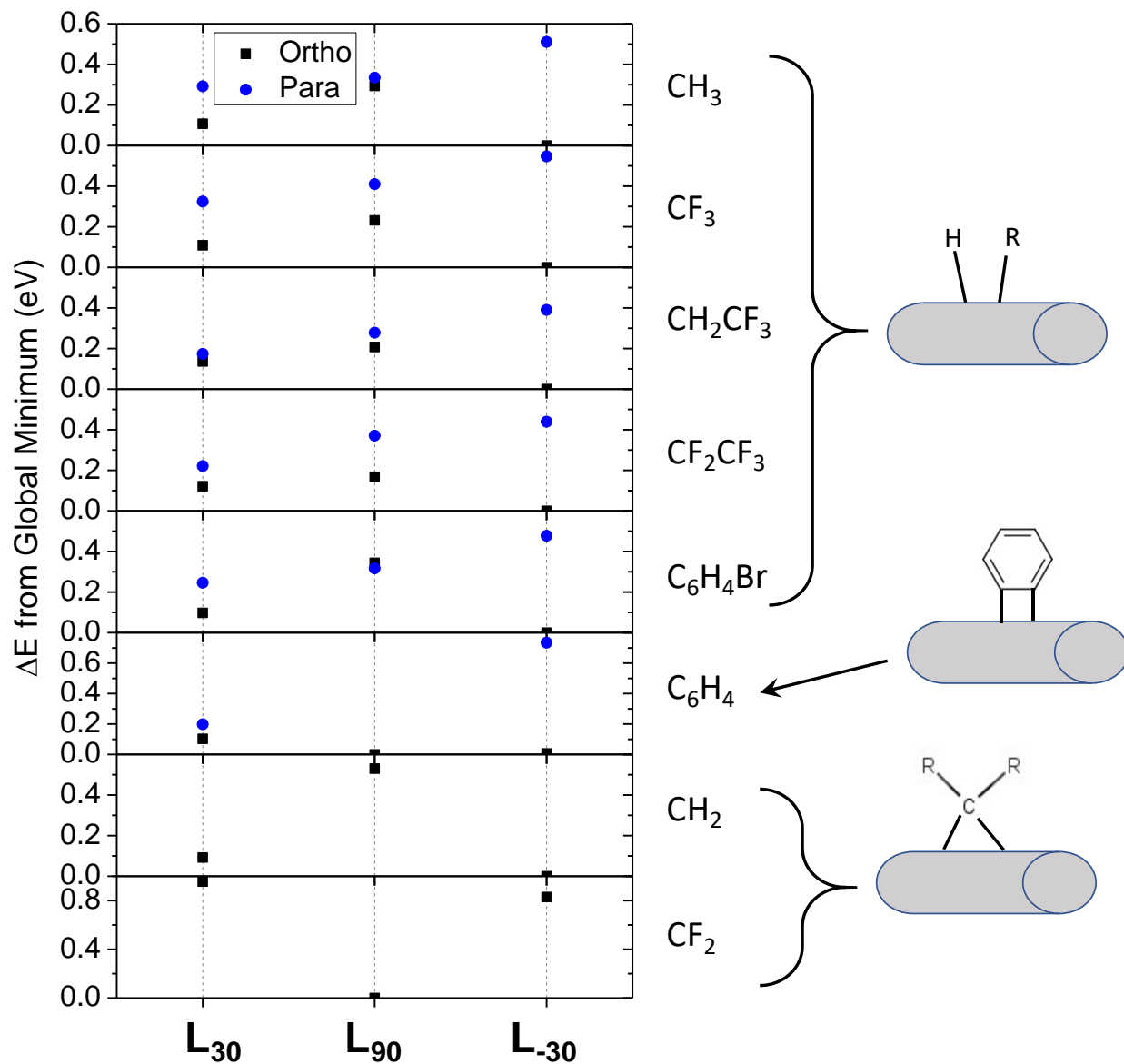


Figure 5.21. Stabilities of (6,5) SWCNTs functionalized with different chemical species.

electron localization as previously discussed in the context of different functional configurations. Electron localization as the result of functional configuration destabilizes the HOMO, but to a lower degree where electronegative groups are present. Additionally, divalent species are met with much less destabilization of the HOMO due to the hybridization in the connecting atom. Despite all these effects in the HOMO, the stabilization as the result of using different groups is very small (<0.02 eV) and almost completely negated by the symmetrical stabilization in the LUMO. As a result, the HOMO-LUMO gaps remain unchanged.

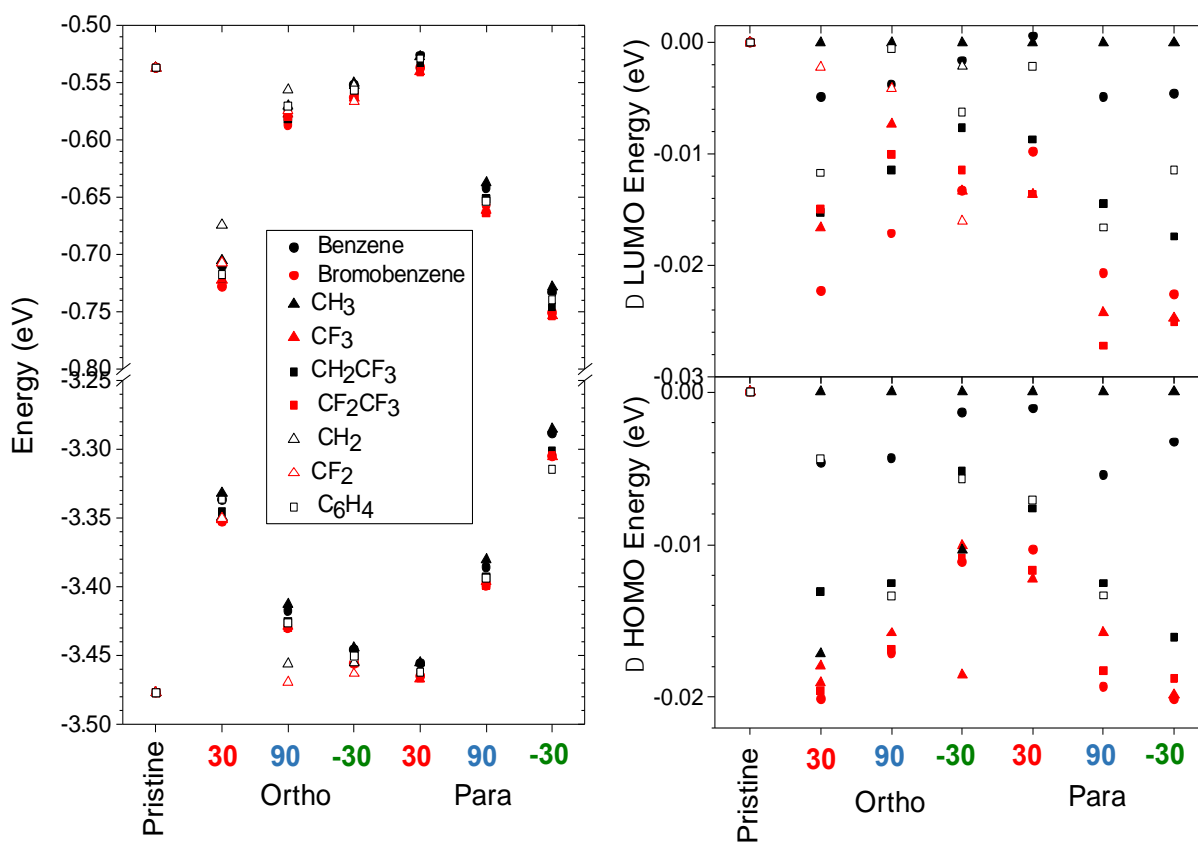


Figure 5.22. The electronic structure for (6,5) SWCNTs functionalized with different chemical groups. (a) Represents the energies of the HOMO and LUMO for each species. The break in the plot is at the HOMO-LUMO gap. For nearly all species, functionalization with methyl is the highest energy in both the HOMO and LUMO (b) Difference in energies for the MO of the species functionalized with the different species versus that functionalized with methyl.

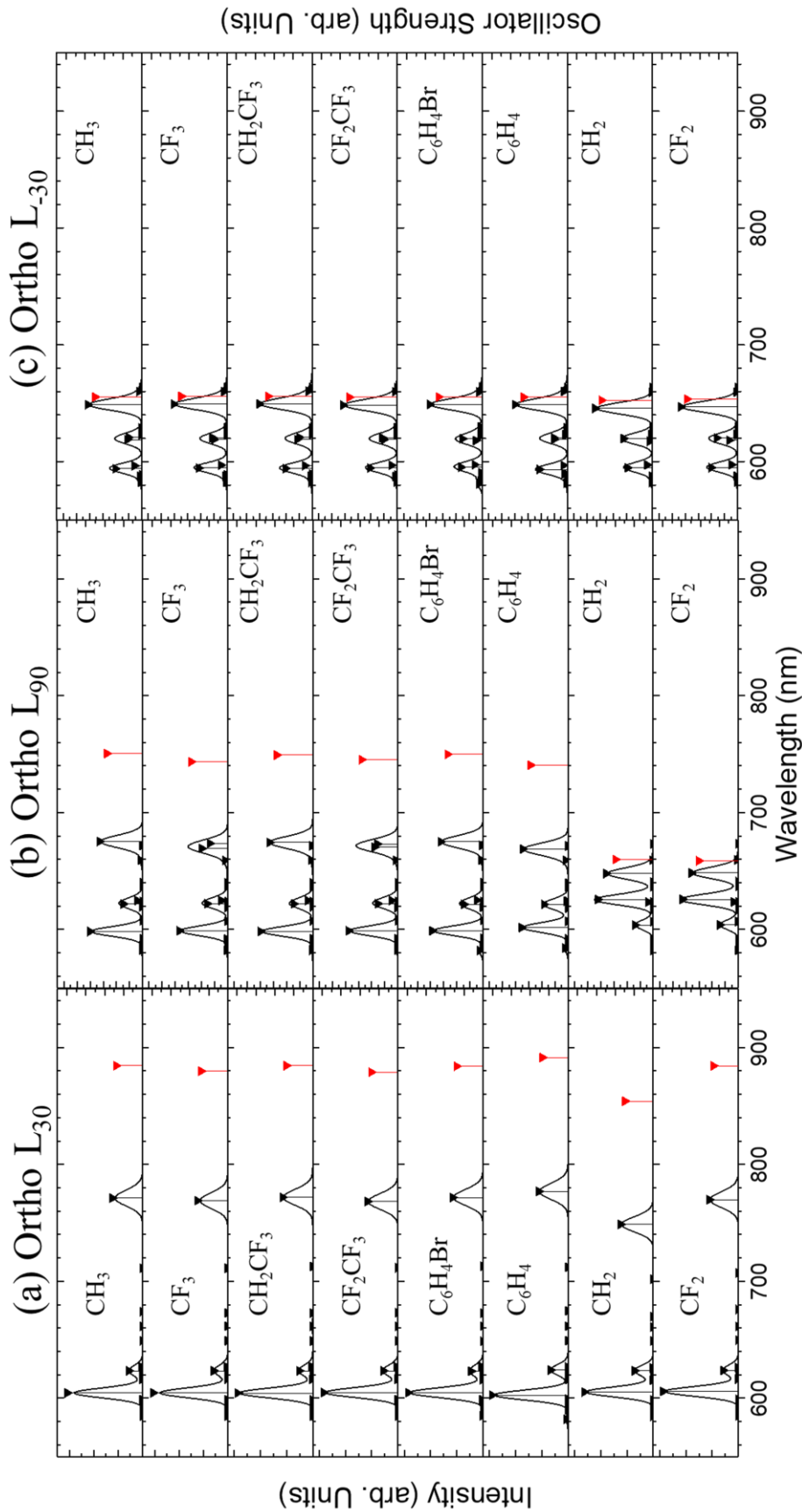


Figure 5.23. Optical properties of all structures in this chapter. Black vertical droplines represent the absorption oscillators, and the solid black curve is for those lines broadened by a Gaussian curve of linewidth 0.01 eV to simulate the absorption spectra. The calculated energies of emission features are represented by red drop lines.

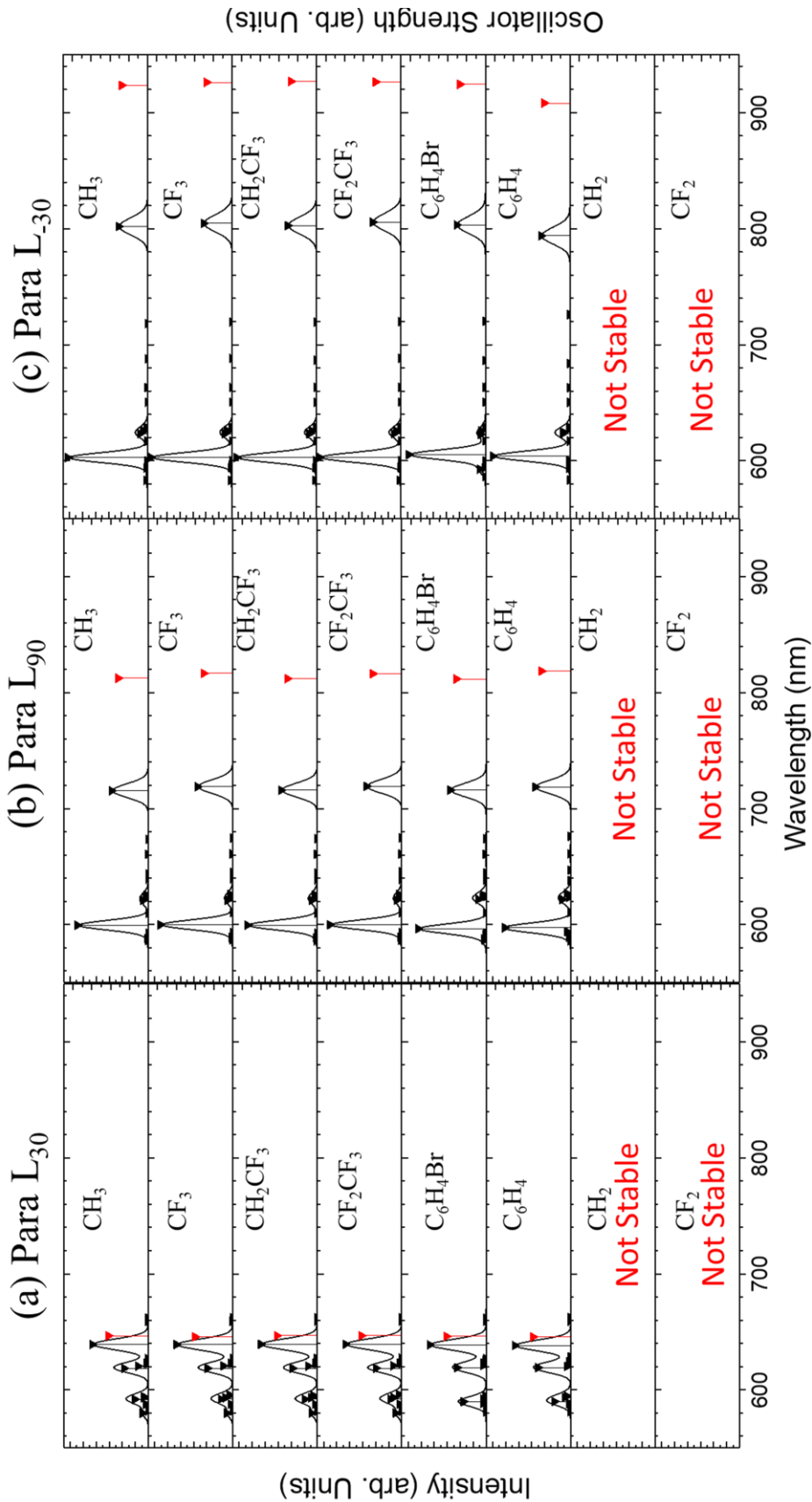


Figure 5.24. Optical properties of all structures in this chapter. Black vertical droplines represent the absorption oscillators, and the solid black curve is for those lines broadened by a Gaussian curve of linewidth 0.01 eV to simulate the absorption spectra. The calculated energies of emission features are represented by red drop lines.

5.10.3. Optical Properties from Different Functionalization

As with aryl functionalized previously presented, the predominant bright optical transition is between the HOMO and LUMO in systems functionalized with other groups. The result is trends in optical features including absorption and emission that are identical to those previously discussed for bromobenzene independent of chemical functionalization (figure 5.23 for ortho, figure 5.24 for para functionalized species). The only exception is for divalent species, where optical features are significantly blue-shifted over their monovalent counterparts. Due to the relatively small variation in the electronic structure, the range of optical features from SWCNTs functionalized with different groups is very tight (only a few nanometers for different species). As a result of this, it is likely that inclusion of surfactant and solvent effects would result in the observation of significantly different trends. Due to this, the trends are not in agreement with experiment and are of little value. However, characterization of the trends in the context of bond character as a result of functionalization are much more useful and presented in the next section.

5.10.4. Natural Charge and Bond Character Due to Different Functionalization

To characterize the effects of functionalization with different species, the natural bond analysis was performed on the bond between the SWCNT and the functional group itself. Through this technique, the natural charge on the bonded atom as well as the bond character was characterized. Both of these were performed for the bonding atom in the SWCNT. These parameters were compared to the experimental redshift obtained by the Wang group who has previously attributed redshifts to the inductive effects induced by the electronegative of the atoms in the functional group.²⁸ This is directly related to the natural charge on the connecting atom as a more electron withdrawing functional group induces a less negative (or more positive)

charge on the adjacent SWCNT atom. The natural charges for the alkyl species (from most negative to most positive) trend $\text{CH}_3 > \text{CH}_2\text{CF}_3 > \text{CF}_3 > \text{CF}_2\text{CF}_3$ (figure 5.25) regardless of functionalization configuration. The trend forms an asymptotically decreasing trend from least electron withdrawing to most electron withdrawing species, as represented by the dashed blue lines in figure 5.25. In addition to the alkyl groups, the aromatic groups with electron withdrawing and donating tendencies fall on the trend almost perfectly, only exhibiting slightly stronger redshifts for the same natural charges on the binding atoms. However, the divalent

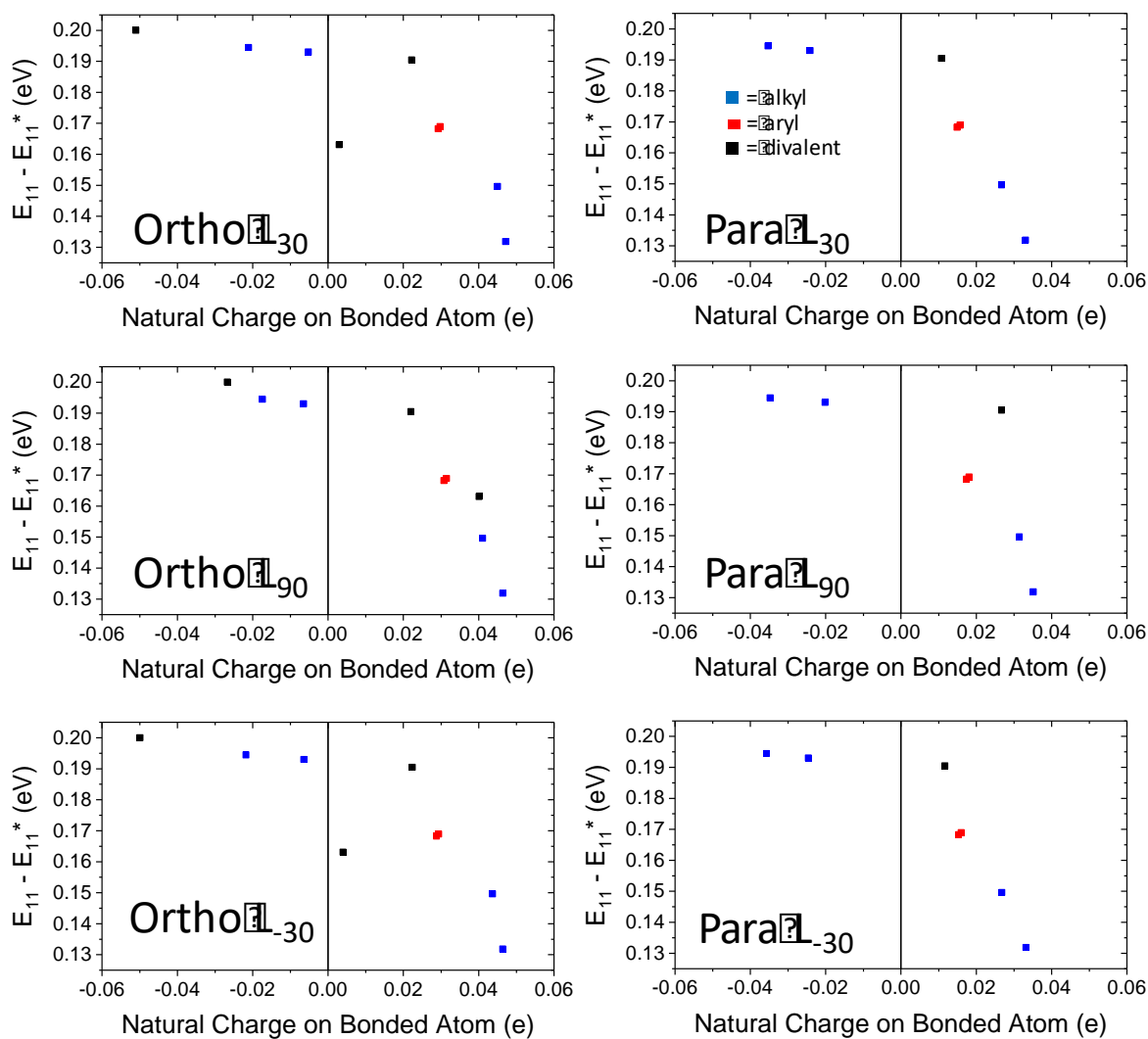


Figure 5.25. Natural charge analysis as a function of experimental redshift for the functionalized species.

species are not in line with the trend. For CF_2 , where the electronegativity is high, the values for redshift per natural charge is higher than the trend for alkyl species. For CH_2 where electron withdrawing doesn't play a role, it falls lower. The single bridging species with monovalent connectivity falls on the line as well (figure 5.25). This shows that, as the Wang group already have shown, the inductive effects play a role in red shifting emission features due to functionalization. However, this isn't the singular effect that must be considered since the divalent species don't fall directly on the trend. To deduce the origin of these discrepancies between monovalent and divalent species requires analysis of the s-character in the must be considered (figure 5.26). The deviations from the trend are the result of increasing s-character of the bonded atom. This is due to the rigidity in the bond angles and distances enforced by the requirement that a single atom in the functional group be bonded to two carbon atoms in the

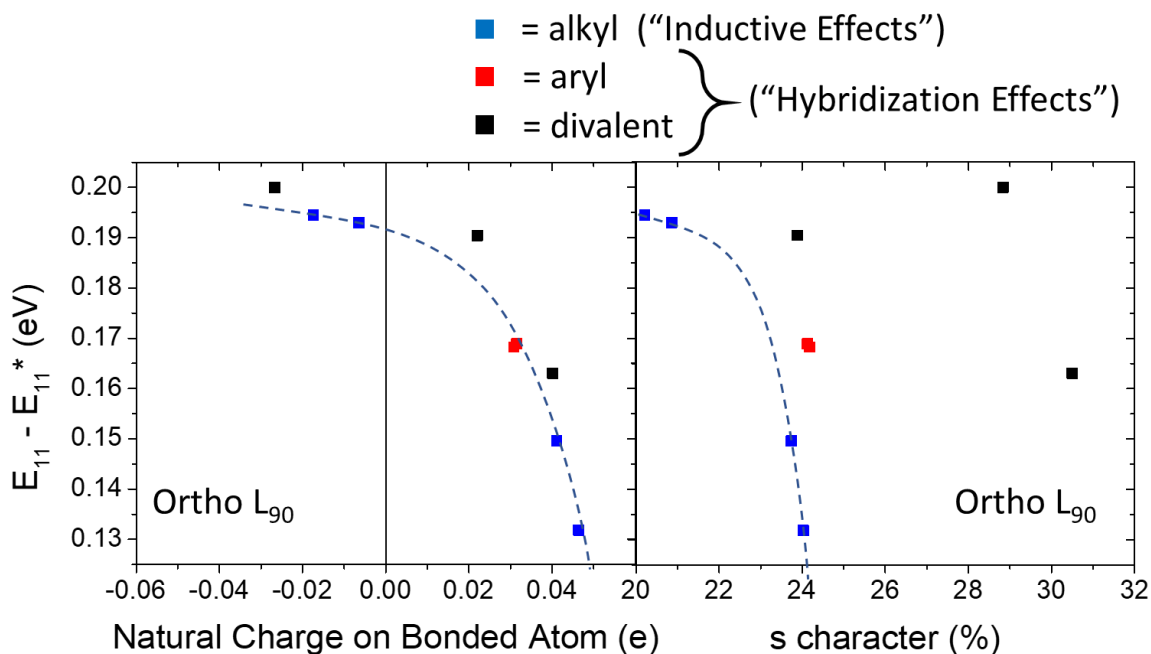


Figure 5.26. (a) Natural charge on the carbon atom adjacent to functionalization versus red shift of the species, and (b) s character versus red shift. The dashed blue lines indicate the asymptotically decreasing trend for the alkyl groups with varying degrees of electron donating/withdrawing ability.

SWCNT. This demonstrates that while inductive effects of the functional groups has a substantial role on redshifts, their consideration alone isn't enough. Additionally, the bond character in the region of functionalization must be considered.

5.11. Conclusions

Synthetic considerations dictate that covalent functionalization of SWCNTs can produce more than one defect site, and computations require at least two carbon atoms at the SWCNT surface be functionalized in order to avoid the formation of open-shell or charged systems. Such functionalization can occur along three distinct directions with respect to the defect site and at either ortho or para positions on a single ring. All isomers arising from different binding positions of the covalently bound 4-bromobenzene at a single carbon-ring of the (6,5) SWCNTs result in significant distortion of the sp^2 -conjugation of the SWCNT and formation of an sp^3 -defect on the nanotube surface. The largest disruption of the hexagonal sp^2 -hybridized network from the pristine SWCNT occurs between the two functional sites oriented along bonds nearly perpendicular to the nanotube axis, L_{90} , for ortho functionalization leading to the highest total energy of these conformations. All para configurations exhibit a noticeably lower degree of sp^2 disruption than do ortho isomers. However, a smaller degree of sp^2 distortion does not always provide the most stable configuration, typically resulting in para isomers having higher total energy than ortho isomers. We conclude that a moderate sp^2 distortion, like in ortho L_{30} and ortho L_{30} , is optimal for stabilization of structures. Nonetheless, the energy differences between all these functional conformations are relatively low, indicating the plausibility of co-existence of several different defect geometries in experimental samples.

Substitution of one of two 4-bromobenzene groups bound to a single carbon ring at the nanotube surface by either H or OH⁻ groups has very similar effects on the electronic structure

and optical response of the functionalized SWCNT. This is rationalized by the fact that the ground and excited state orbitals associated with the defect completely originate from the SWCNT, rather than from the functional group itself. By the same reason, the rotation of the aryl group about the C-C bond with respect to the nanotube also has negligible effect on the optical spectrum of the system. Overall, functionalization of the carbon ring of the nanotube by an aryl derivative and hydrogen is a valid model for the sp^3 -defect on the tube surface. Swapping of the position of the aryl group and hydrogen atom to the 'top' or the 'bottom' of the hexagonal ring of the nanotube leaves the total energies and electronic structure of functionalized SWCNTs virtually unchanged. Thus these structures are indistinguishable at normal conditions, which means that the aryl functionalization does not provide any selectivity between the left- and right-handed (6,5) SWCNT absent the effects of surfactants.

While the chemical composition (-H, -OH, -aryl) of the functional group bound to the second carbon position of the carbon ring being considered has less effect on the photophysical properties of the nanotube, the energy and intensity of the lowest energy optical transitions are very sensitive to the specific isomer geometry. Thus, the appearance of the red-shifted optically allowed E_{11}^* band in absorption spectra of the functionalized SWCNTs is the result of excitation localization around the sp^3 defect, which determines the degree to which the lower energy excitons depend on the defect conformation. The isomers having the strongest localization of their frontier orbitals around the defect exhibit the largest redshifts of their E_{11}^* band, while structures with a smaller degree of orbital localization have the least redshift of the E_{11}^* peak, with respect to the main E_{11} band of the pristine SWCNT. Optically active excitons contributing to these peaks are delocalized over the entire nanotube, but have nodes either at the defect position or in-between the defect and the nanotube edges. Such a nodal structure for the excitons

has the same physical meaning as a characteristic standing wave feature related to its k-vector in the infinitely long quasi-1D nanotube. This demonstrates that both E_{11} and E_{11}^* bands in functionalized nanotubes are derivatives of the lower energy bright E_{11} excitonic band of the pristine SWCNT.

Solvent effects present another important factor potentially affecting emission energies. Very small bathochromic shifts of E_{11}^* (up to ~40 meV) and E_{11} (up to ~30 meV) are observed for both absorption and emission due to the very small electrostatic dipole moments present in the functionalized SWCNTs. Relaxation of the excited state enhances electron and hole localization around the tube center for both pristine and functionalized SWCNTs. The higher the degree of exciton trapping at the defect site the larger is the Stokes shift (ranging from 5 meV to 168 meV), following similar trends as for the bathochromic shifts in varying solvents. Therefore, the largest Stokes shifts are observed in the isomers having the most red-shifted emission with the most localized character of their excited charge densities (ortho L_{30} and para L_{-30}), while cases of negligible Stokes shifts correspond to configurations having the least redshifted emission energies and the most delocalized excitonic orbitals (ortho L_{-30} and para L_{30}). This trend is rationalized by occurrence of a more pronounced difference in the excitonic states upon excited state relaxation in ortho L_{30} and para L_{-30} than for ortho L_{-30} and para L_{30} isomers. Despite substantial vibrational reorganization between the excited and ground state of SWCNTs in the presence of a fluorescent defect, we have observed the mirroring trends between the E_{11}^* absorption band and the lowest energy emission states for all defect conformations. This justifies that calculations of the lowest states in absorption spectra provide qualitatively correct descriptions of the PL in both SWCNTs and functionalized SWCNTs. Thus, for saving computational time, the optimization of the excited state can be omitted and conclusions on the

trends in emission transitions can be made based from the lowest energy absorption peak. Furthermore, for reduced computational expense, use of a small basis set (eg. STO-3G) is justified, since numerically expensive simulations using the larger 3-21G basis produces the same trends across all calculated observables apart from uniform red-shifts (~ 0.2 eV) for optical transition energies.

The calculations presented in this chapter predict that in nanotube samples where defects associated with functional groups are naturally present in the various available isomer conformations, the PL spectra of functionalized (6,5) SWCNTs are expected to exhibit three well pronounced emissive peaks: the most red-shifted E_{11}^* band of ortho L_{30} and para L_{-30} , followed by the less red-shifted E_{11}^* band of L_{90} and para L_{90} , and the wide main E_{11} band mixed with E_{11}^* of ortho L_{-30} and para L_{30} isomers, with the last being very close in its energy to the E_{11} band of the pristine SWCNT. We note that this expectation is corroborated by recent experimental results, displaying just such diversity in emission spectral features.²⁹⁻³² Importantly, for the first two cases, the lowest energy transition contributing to red-shifted emission is optically allowed, in contrast to that of the pristine SWCNT. Thus, the covalent functionalization of SWCNT allows for efficient radiative recombination of the excitons that ordinarily would have recombined non-radiatively in pristine SWCNTs.

In addition to resulting in redshifts in emission, functionalization along different axes results in a significant range of reorganization energies and lifetimes. Changing the functional groups plays a significantly smaller role in changing the optical features, but does result in localized changes in bond character that tend to shift the emission features over a range of about 100 nm. The insights provided in this chapter help explain the mechanisms that are responsible

for such changes in the lowest energy excitonic band make envisioned applications of SWCNTs in optoelectronics, sensing, and imaging technologies more feasible.

5.12. References

- (1) Bahr, J. L.; Yang, J. P.; Kosynkin, D. V.; Bronikowski, M. J.; Smalley, R. E.; Tour, J. M. Functionalization of Carbon Nanotubes by Electrochemical Reduction of Aryl Diazonium Salts: A Bucky Paper Electrode. *J. Am. Chem. Soc.* **2001**, *123*, 6536–6542.
- (2) Kim, W. J.; Usrey, M. L.; Strano, M. S. Selective Functionalization and Free Solution Electrophoresis of Single-Walled Carbon Nanotubes: Separate Enrichment of Metallic and Semiconducting SWNT. *Chem. Mater.* **2007**, *19*, 1571–1575.
- (3) Nair, N.; Kim, W. J.; Usrey, M. L.; Strano, M. S. A Structure-Reactivity Relationship for Single Walled Carbon Nanotubes Reacting with 4-Hydroxybenzene Diazonium Salt. *J. Am. Chem. Soc.* **2007**, *129*, 3946–3954.
- (4) Usrey, M. L.; Lippmann, E. S.; Strano, M. S. Evidence for a Two-Step Mechanism in Electronically Selective Single-Walled Carbon Nanotube Reactions. *J. Am. Chem. Soc.* **2005**, *127*, 16129–16135.
- (5) Ramirez, J.; Mayo, M. L.; Kilina, S.; Tretiak, S. Electronic Structure and Optical Spectra of Semiconducting Carbon Nanotubes Functionalized by Diazonium Salts. *Chem. Phys.* **2013**, *413*, 89–101.
- (6) Frey, J. T.; Doren, D. J. *TubeGen 3.4*; University of Delaware: Newark DE, 2011.
- (7) Kilina, S.; Tretiak, S. Excitonic and Vibrational Properties of Single-Walled Semiconducting Carbon Nanotubes. *Adv. Funct. Mater.* **2007**, *17* (17), 3405–3420.

- (8) Sharma, A.; Gifford, B. J.; Kilina, S. Tip Functionalization of Finite Single-Walled Carbon Nanotubes and Its Impact on the Ground and Excited State Electronic Structure. *J. Phys. Chem. C* **2017**, *121* (15), 8601–8612.
- (9) Rappe, A. K.; Casewit, C. J.; Colwell, K. S.; Goddard, W. A.; Skiff, W. M. UFF, a Full Periodic Table Force Field for Molecular Mechanics and Molecular Dynamics Simulations. *J. Am. Chem. Soc.* **1992**, *114* (25), 10024–10035.
- (10) Dewar, M. J. S.; Zoebisch, E. G.; Healy, E. F.; Stewart, J. J. P. AM1: A New General Purpose Quantum Mechanical Molecular Model. *J. Am. Chem. Soc.* **1985**, *107* (13), 3902–3909.
- (11) Yanai, T.; Tew, D. P.; Handy, N. C. A New Hybrid Exchange–correlation Functional Using the Coulomb-Attenuating Method (CAM-B3LYP). *Chem. Phys. Lett.* **2004**, *393* (1–3), 51–57.
- (12) Kilina, S.; Badaeva, E.; Piryatinski, A.; Tretiak, S.; Saxena, A.; Bishop, A. R. Bright and Dark Excitons in Semiconductor Carbon Nanotubes: Insights from Electronic Structure Calculations. *Phys. Chem. Chem. Phys.* **2009**, *11* (21), 4113.
- (13) Kilina, S.; Kilin, D.; Tretiak, S. Light-Driven and Phonon-Assisted Dynamics in Organic and Semiconductor Nanostructures. *Chem. Rev.* **2015**, *115* (12), 5929–5978.
- (14) Frisch, M. J.; Trucks, G. W.; Schlegel, H. B.; Scuseria, G. E.; Robb, M. A.; Cheeseman, J. R.; Scalmani, G.; Barone, V.; Mennucci, B.; Petersson, G. A.; et al. *Gaussian 09*; Gaussian, Inc.: Wallingford, CT, USA, 2009.
- (15) Cossi, M.; Rega, N.; Scalmani, G.; Barone, V. Energies, Structures, and Electronic Properties of Molecules in Solution with the C-PCM Solvation Model. *J. Comput. Chem.* **2003**, *24* (6), 669–681.

- (16) Humphrey, W.; Dalke, A.; Schulten, K. VMD – Visual Molecular Dynamics. *J. Mol. Graph.* **1996**, *14*, 33–38.
- (17) Furche, F.; Ahlrichs, R. Adiabatic Time-Dependent Density Functional Methods for Excited State Properties. *J. Chem. Phys.* **2002**, *117* (16), 7433–7447.
- (18) Van Caillie, C.; Amos, R. D. Geometric Derivatives of Density Functional Theory Excitation Energies Using Gradient-Corrected Functionals. *Chem. Phys. Lett.* **2000**, *317* (1–2), 159–164.
- (19) Martin, R. L. Natural Transition Orbitals. *J. Chem. Phys.* **2003**, *118* (11), 4775.
- (20) Chen, J.; Schmitz, A.; Kilin, D. S. Computational Simulation of the P-n Doped Silicon Quantum Dot. *Int. J. Quantum Chem.* **2012**, *112* (24), 3879–3888.
- (21) Kilina, S.; Ramirez, J.; Tretiak, S. Brightening of the Lowest Exciton in Carbon Nanotubes via Chemical Functionalization. *Nano Lett.* **2012**, *12* (5), 2306–2312.
- (22) Hilborn, R. C. Einstein Coefficients, Cross Sections, f Values, Dipole Moments, and All That. *Am. J. Phys.* **1982**, *50* (11), 982.
- (23) Foster, J. P.; Weinhold, F. Natural Hybrid Orbitals. *J. Am. Chem. Soc.* **1980**, *102* (24), 7211–7218.
- (24) Wongchoosuk, C.; Udomvech, A.; Kerdcharoen, T. The Geometrical and Electronic Structures of Open-End Fully Functionalized Single-Walled Carbon Nanotubes. *Curr. Appl. Phys.* **2009**, *9*, 352–358.
- (25) Kilina, S.; Tretiak, S.; Doorn, S. K.; Luo, Z.; Papadimitrakopoulos, F.; Piryatinski, A.; Saxena, A.; Bishop, A. R. Cross-Polarized Excitons in Carbon Nanotubes. *Proc. Natl. Acad. Sci. U. S. A.* **2008**, *105* (19), 6797–6802.

- (26) Wu, C.; Malinin, S. V.; Tretiak, S.; Chernyak, V. Y. Exciton Scattering and Localization in Branched Dendrimeric Structures. *Nat. Phys* **2006**, *2*, 631–635.
- (27) Kim, M.; Adamska, L.; Hartmann, N. F.; Kwon, H.; Liu, J.; Velizhanin, K. A.; Piao, Y. M.; Powell, L. R.; Meany, B.; Doorn, S. K.; et al. Fluorescent Carbon Nanotube Defects Manifest Substantial Vibrational Reorganization. *J. Phys. Chem. C* **2016**, *120*, 11268–11275.
- (28) Kwon, H.; Furmanchuk, A.; Kim, M.; Meany, B.; Guo, Y.; Schatz, G. C.; Wang, Y. Molecularly Tunable Fluorescent Quantum Defects. *J. Am. Chem. Soc.* **2016**, *138* (21), 6878–6885.
- (29) He, X.; Gifford, B. J.; Hartmann, N. F.; Ihly, R.; Ma, X.; Kilina, S. V.; Luo, Y.; Shayan, K.; Strauf, S.; Blackburn, J. L.; et al. Low-Temperature Single Carbon Nanotube Spectroscopy of Sp^3 Quantum Defects. *ACS Nano* **2017**.
- (30) Maeda, Y.; Minami, S.; Takehana, Y.; Dang, J.-S.; Aota, S.; Matsuda, K.; Miyauchi, Y.; Yamada, M.; Suzuki, M.; Zhao, R.-S. Tuning of the Photoluminescence and Up-Conversion Photoluminescence Properties of Single-Walled Carbon Nanotubes by Chemical Functionalization. *Nanoscale* **2016**, *8*, 16916–16921.
- (31) Shiraki, T.; Shiraishi, T.; Juhász, G.; Nakashima, N. Emergence of New Red-Shifted Carbon Nanotube Photoluminescence Based on Proximal Doped-Site Design. *Sci. Rep.* **2016**, *6*, 28393.
- (32) He, X.; Hartmann, N. F.; Ma, X.; Kim, Y.; Ihly, R.; Blackburn, J. L.; Gao, W.; Kono, J.; Yomogida, Y.; Hirano, A. Tunable Room-Temperature Single-Photon Emission at Telecom Wavelengths from Sp^3 Defects in Carbon Nanotubes. *Nat. Photonics* **2017**, nphoton. 2017.119.

6. CHIRALITY DEPENDENCE ON FUNCTIONALIZED CARBON NANOTUBE & ANALYTICAL SHIFT

6.1. Motivation

In the previous chapter, it was shown that functionalization of (6,5) single-walled carbon nanotubes (SWCNTs) results in the introduction of significantly redshifted emission features in the infrared region due to configuration-dependent exciton confinement in the vicinity of the defect site. Such chemical modification increases their promise for use as single-photon sources in telecommunications applications, and therefore they have recently been the subject of intense experimental and computational interest. However, the computed energies of optical features are higher than experiment due to the artificial confinement in finite systems as well as methodical errors such as self-correlation in the density functional and a finite basis set size. These errors can't be corrected by a simple constant-energy shift to optical features of all species because the confinement errors are expected to affect species with strong exciton localization to a smaller degree than species with significant exciton delocalization. As such, a proper scheme for correcting for errors needs to consider the methodology errors and confinement errors independently and in species-dependent manner.

In this chapter, the chirality dependence of such introduction in low energy emission features will be explored. Additionally, a scheme for analytically correcting for both confinement and methodologies independently is developed using density functional theory (DFT) and time-dependent density functional theory (TDDFT) to calculate the energies of optical features on systems of different lengths. The dependence of these two variables is correlated using a linear regression as well as Kuhn's formula, and the dependence of SWCNT chirality on the method is explored. Additionally, the correction is developed using two different

density functionals that have previously been demonstrated to produce different degrees of exciton localization. Application of this the model provides remarkable agreement with experimental energies of optical features and will prove invaluable for further computations of functionalized SWCNT optical features.

6.2. Computational Methodology

6.2.1. Details on the Computational Systems

All DFT and TDDFT calculations were performed using Gaussian 09¹ software in vacuum. Single walled carbon nanotubes of (5,4), (6,5), (9,1) and (11,0) chirality one to four unit-cells in length were constructed using Visual Molecular Dynamics (VMD) software². The dangling bonds at the end of the SWCNT computational cell were passivated with a mixture of hydrogen and methylene groups in schemes that have been previously shown to eliminate mid-gap trap states and properly approximate the scaling-relationships for infinite length systems.³ The pristine SWCNTs were then functionalized with aryl and hydrogen groups in para positions (those across the six-membered ring from each other) along the three distinct orientations with respect to the SWCNT axis (denoted L_x , L_{x+60} , and L_{x-60} where the subscript indicates the approximate angle between the vector connecting the two functionalized carbon atoms and the SWCNT axis⁴, figure 6.1)). For the purpose of comparing functionalization configurations across different chirality tubes, the smallest and largest positive angle with respect to the axis of the SWCNT are labeled (+) and (++), while the negative angle with respect to the SWCNT axis is labeled (-). In the previous chapter, it was shown that for (6,5) the para functionalized positions cover the extremes of exciton localization where for L_{30} is nearly completely delocalized and exhibits practically no red-shift of E_{11}^* from E_{11} while L_{-30} is localized in a region approximately 4 nm around the defect site and exhibits a strong ~400nm nm red shift. As

such, only para species were considered for the purpose of developing a scheme for correcting emission energies as the result of confinement.

6.2.2. Density Functional Choice: Comparison of Localization

The geometry of all structures were optimized using range-corrected CAM-B3LYP⁵ density functional and a STO-3G basis set^{6,7} as has been shown effective for predicting transition energies of functionalized SWCNTs^{4,8,9}. It is notable that while previous calculations using B3LYP predict emission energies more consistent with experiment, CAM-B3LYP was shown to better described the electron delocalization in SWCNTs near the ends.¹⁰ Since the objective of the study is to predict properties explicitly considering localization, the optical properties were

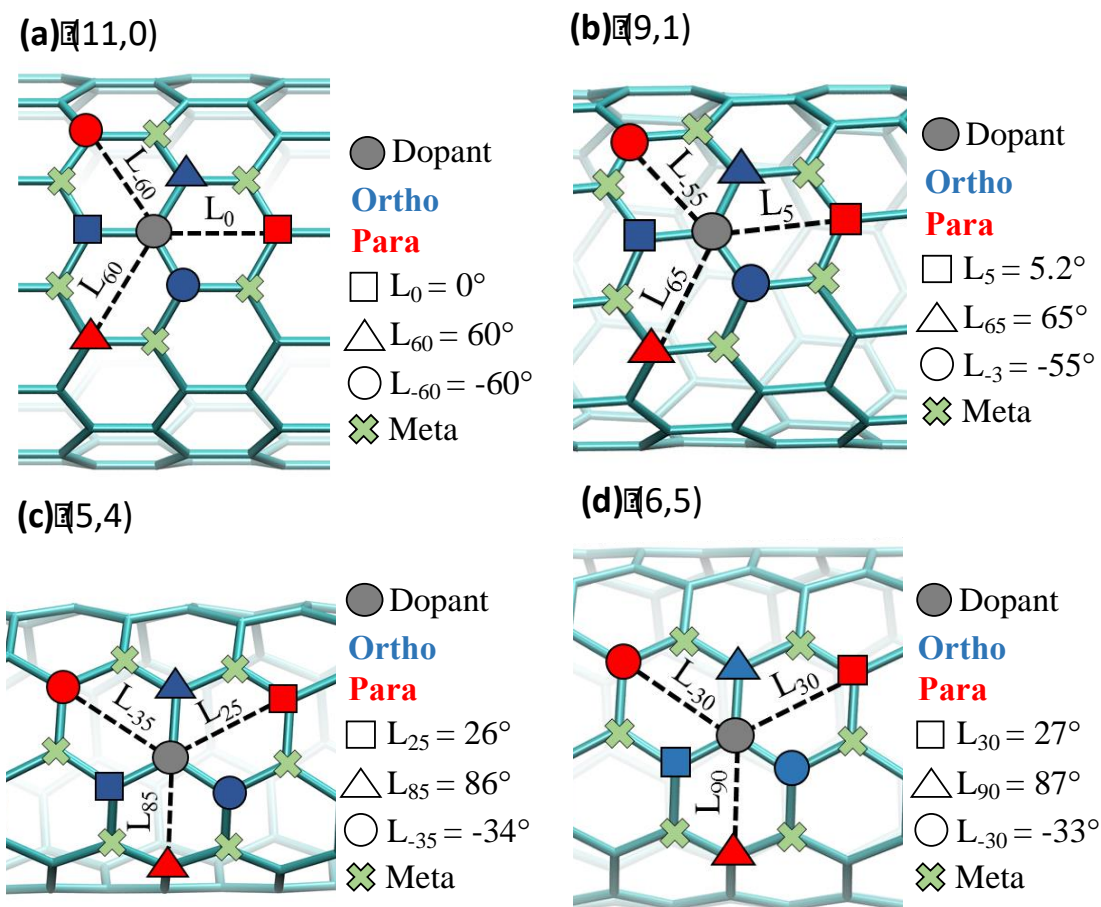


Figure 6.1. Configurations of functionalization for the different chiralities of SWCNTs explored in this chapter.

calculated using both CAM-B3LYP⁵ and B3LYP¹¹⁻¹³ density functionals. The optical properties were calculated for the six functional configurations presented in figure 6.1 for all chiralities in the same way as described in chapter 6.

6.2.3. Computing Length Dependence

To establish the correlation between optical features and different length unit cells, vertical transitions were calculated for 15 excited states from the ground state optimized geometries of all para functional configurations. This methodology is possible for systems up ~16 nm in length given the current state of computational technology. However, excited state optimized geometries required to model emission features are significantly more expensive. As such, all three functional configurations and pristine SWCNTs were optimized in the excited state using TDDFT for three unit cells only, which is the maximum size system for which excited state geometries of functionalized systems could be attained given current computational limitations. The emission energies were determined by calculating the vertical transitions from the excited state geometries in the same way as described for ground state transitions.

6.2.4. Scheme for Shifting Energies of Computed Emission Features

In order to correct for confinement errors, the absorption energies need to be obtained for infinite length systems (called $E_{11}^*(\infty)$) displaying varying degrees of exciton delocalization. This is accomplished by establishing the relationship between E_{11}^* and the inverse length ($1/L$) for the finite systems and extrapolating the values of the hypothetical infinite-length counterparts. This extrapolation was performed using both a simple linear regression and Kuhn's formula for describing optical features in one-dimensional conjugated polymers. To fit the data to curve for the linear method, the following equation for a standard linear regression was used:

$$E_{11}^* \text{ Energy} = m \frac{1}{N} + b \quad (\text{Equation 6.1})$$

where E_{11}^* Energy is the lowest energy bright transition for functionalized species, N is the length of the SWCNT system in unit cells, m is taken as the slope of the line, and b is taken as the intercept. For fitting to the Kuhn method, the following equation was used:

$$E_{11}^* \text{ Energy} = A \sqrt{1 + B \cos\left(\frac{\pi}{N+1}\right)} \quad (\text{Equation 6.2})$$

where A and B are fitting parameters. The values for $E_{11}^*(\infty)$ are then extrapolated by considering the limits as N goes to infinity.

6.2.5. Determining the Impact of Confinement vs. Methodology Errors

The values for $E_{11}^*(\infty)$ were correlated to the computed red-shifts for emission ($E_{11}^* - E_{11}$) for the range of species exhibiting different exciton localization. To account for the combined effect of confinement and methodology errors, the resulting curves are shifted by a constant energy value that results in alignment of the E_{11}^* for the infinite length computed system with zero redshift with the experimentally observed E_{11} values (a proper procedure since E_{11}^* for zero redshift is simply E_{11}). Calculated emission values of ($E_{11}^* - E_{11}$) for the finite 3-unit cell systems can then be used to interpolate the expected E_{11}^* emission energies using the resulting corrected correlation.

The resulting scheme for correcting optical transition energies is analyzed to determine the relative contributions of methodology error vs confinement error affects the computed results for each species. For the systems with the most localized excitons, it can be assumed that the confinement error no longer plays a role in longer systems due to the invariance in transition energies with increasing system length. The magnitude of the methodology error ($\Delta E_{\text{methodology}}$) can be predicted by assuming it is the sole source of error in these systems and simply finding

the difference between the energy of the emission transitions as calculated and as shifted using the linear method:

$$\Delta E_{methodology} = E_{11}^*_{calculated} - E_{11}^*_{linear} \text{ (for most localized species)} \text{ (Equation 6.3)}$$

Since the methodology error is assumed to be constant across all species, it is trivial to determine the magnitude of the confinement error ($\Delta E_{confinement}$) for each species:

$$\Delta E_{confinement} = E_{11}^*_{calculated} - E_{11}^*_{linear} - \Delta E_{methodology} \text{ (Equation 6.4)}$$

This method allows the degree of methodology and confinement error to be evaluated independently.

6.3. Influence of Chirality

6.3.1. Relative Stabilities: Trends within Near-Armchair vs Near-Zigzag Chiralities

As presented for (6,5) in the previous chapter, the most stable (6,5) species is for ortho(-) functionalization. This observation translates to the other near-armchair (5,4) species as well (figure 6.2). For (5,4), the energies of nearly all species are destabilized, likely due to the smaller diameter and therefore increased exciton localization. However, the trends in total energies are identical, indicating the same chemical explanations presented in the previous chapter apply for all near-armchair species independent of functional configuration.

For the near-zigzag and zigzag species, the ortho(+) species becomes the most stable. In zigzag species this configuration lies nearly exactly along the SWCNT axis, allowing the aryl group to form a conformation with the planar aryl group perpendicular to the SWCNT axis. This configuration allows the maximum distance between the hydrogen atom functionalizing the SWCNT and those on the edge of the aryl group, a configuration shown in chapter 6 to be the most favorable for aryl-functionalized SWCNTs. Nearly all species exhibit opposite trends as compared to the near armchair species. However, as with (6,5), no functionalization

configurations have outlandishly high total energies and can be deemed unstable. For (11,0), the total energies suggest the equivalence of the ++ and – positions. These two functional configurations would be expected to become chemically similar in zigzag species due to symmetry.

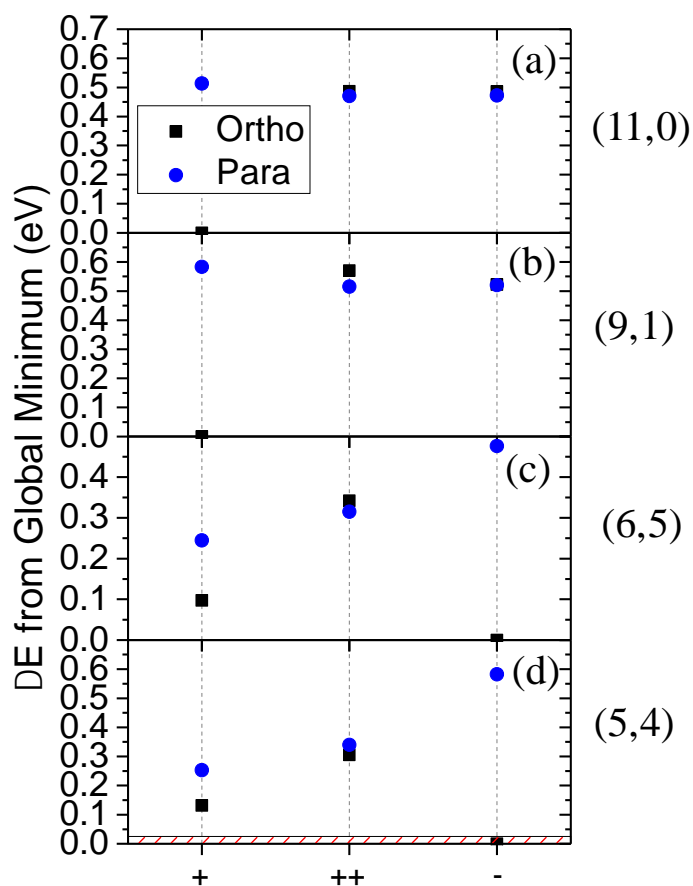


Figure 6.2. Relative stabilities for functional configurations of different chiralities including (a) (11,0), (b) (9,1), (c) (6,5), and (d) (5,4). All values were acquired by subtracting the total energy of the individual chirality and functionalization configuration from the lowest energy value for that particular chirality.

6.3.2. Optical Features: Dependence on Functionalization Configuration

6.3.2.1. Optical Features for E_{11} : Diameter Dependence from Across Axis Localization

For all chiralities of SWCNT, the energies of the optical features is highly dependent on the configuration of functionalization (figure 6.3). The energy of E_{11} is inversely proportional to the diameter of the SWCNT, as would be expected for systems exhibiting confinement in the directions perpendicular to the SWCNT axis. As such, the (11,0) chirality has E_{11} optical features for pristine at about 700 nm while (5,4) E_{11} optical features appear at near 550 nm. These optical features of pristine systems will be explored in much greater detail in a further section. The (6,5) and (9,1) chiralities have the same diameter, and therefore both exhibit E_{11} transitions at about 640 nm. All functionalized species are met with breaking of degeneracy for E_{11} as well as a slight blue shift. As with the (6,5) discussed in the previous chapter, this is an artifact of artificial confinement due to the use of finite SWCNT systems.

6.3.2.2. E_{11}^* Optical Features: Configuration Dependence due to Localization Along the Axis

Additionally, the same range of energies is observed for the optical features of functionalized species. As in the previous chapter, the redshift induced by functionalization is the result of exciton localization about the defect site. This suggests similar localization as the result of functionalization is expected for these chiralities with the same diameter. Despite this, trends are nearly reverse between the near armchair (6,5) and near zigzag (9,1) chiralities (figure 6.4). For example, in (6,5), the para(-) species exhibits the strongest redshifts. However, for (9,1) this species has practically no red shifts. Similar reverse trends are observed across all functionalization configurations. Stoke shifts are also very similar to what was previously

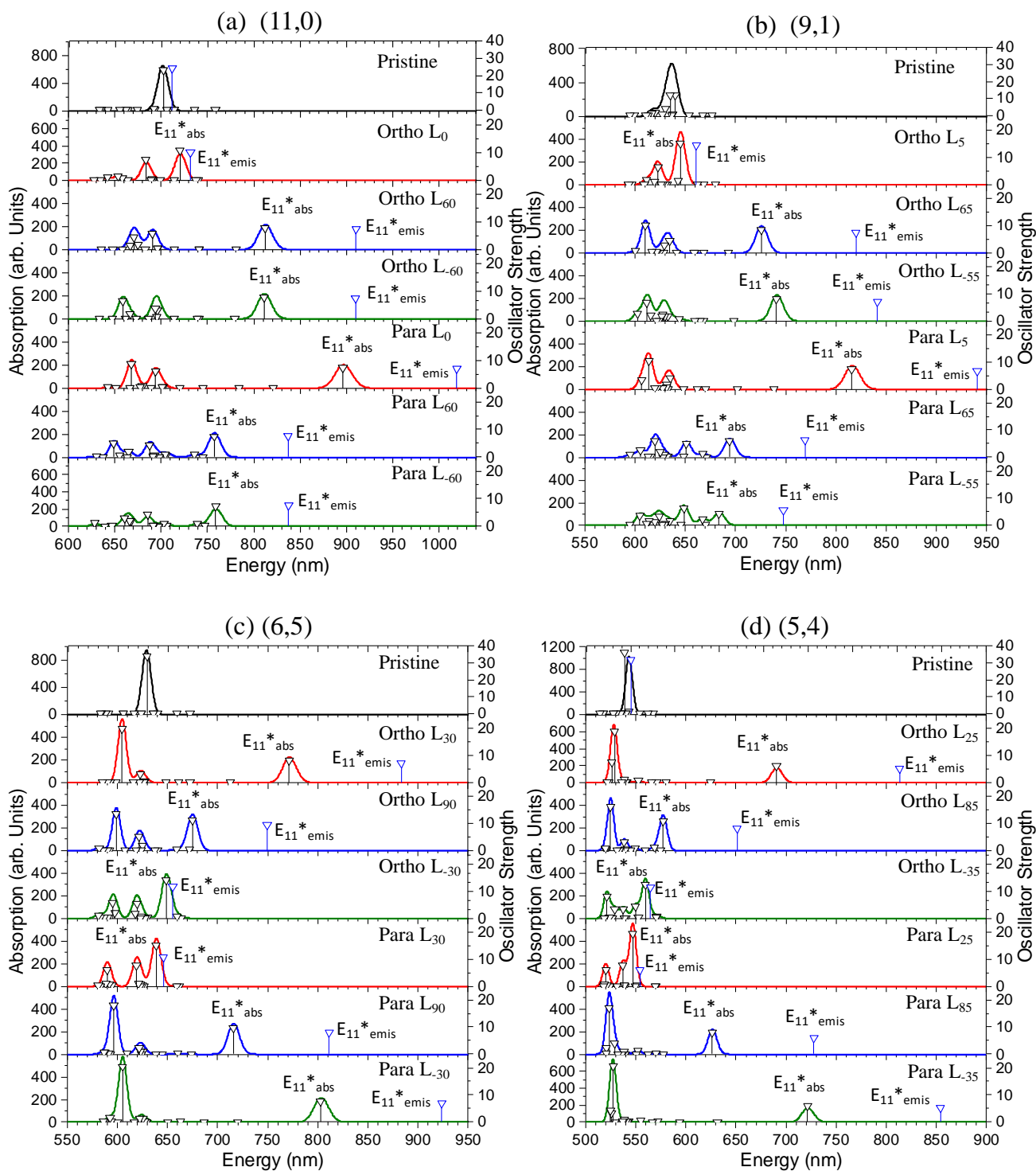


Figure 6.3. Full optical properties for functionalized (a) zigzag (11,0), (b) near-zigzag (9,1), (c) near-armchair (6,5), and (d) near-armchair (5,4) SWCNTs. The black droplines represent the absorption transitions, the blue droplines represent emission transitions, and the solid lines the simulated absorption spectrum acquired by broadening absorption oscillators with a linewidth of 0.01 eV.

discussed for (6,5), where more redshifted emission features exhibit Stokes shifts of ~ 200 nm, an effect that is negligible for the species with no redshifts (figure 6.3).

As with total energies, the optical features are very similar for (++) and (-) functionalized species of the zigzag (11,0) chirality due to the symmetry in the system. This applies for both ortho and para configurations.

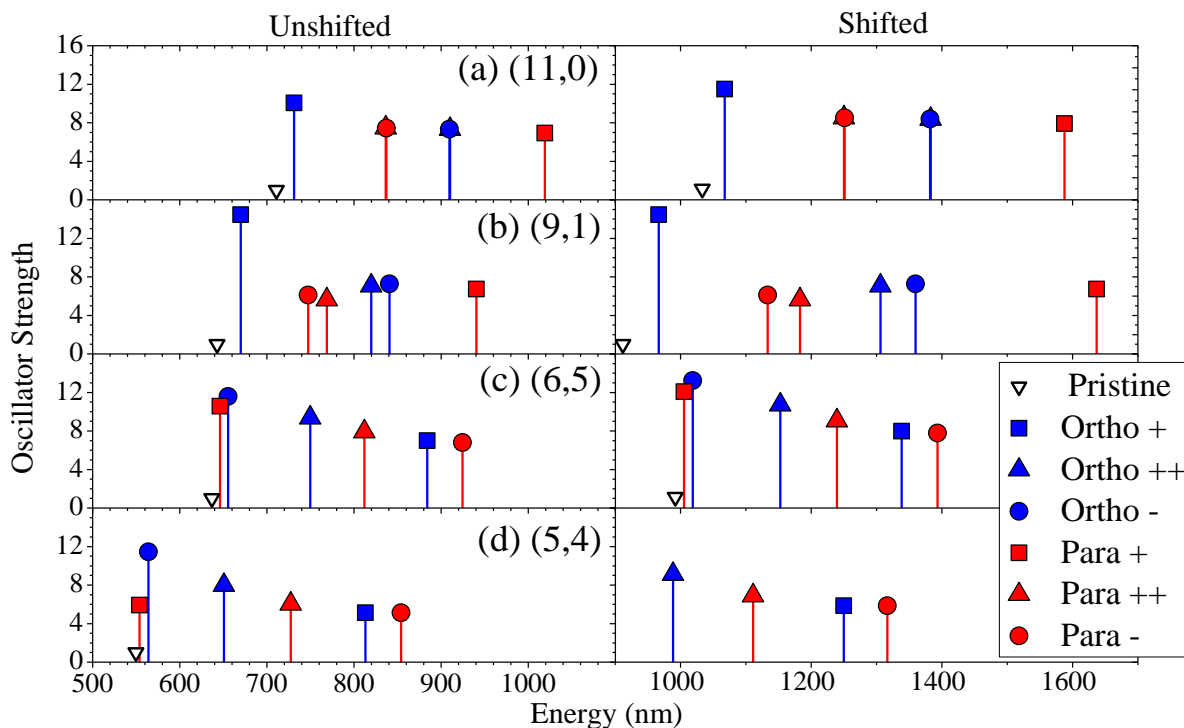


Figure 6.4. Energies of emission features for functionalized (a) zigzag (11,0), (b) near-zigzag (9,1), (c) near-armchair (6,5), and (d) near-armchair (5,4) SWCNTs. The unshifted values are for three unit-cells of SWCNT as calculated using CAM-B3LYP/STO-3G methodology. Shifted values are as corrected using the scheme presented in section 7.2.4 of this chapter.

6.3.3. Conclusions of Influence of Chiralities

Chirality plays a substantial role in the relative stabilities as well as energies of the optical features of SWCNTs functionalized in different orientations. Given a single chirality, trends for the properties of ortho and para features are reverse. Additionally, the near-zigzag and near-armchair systems exhibit opposite trends. Chiralities within the class (ie. Both near zigzag

or both near armchair) are governed by the same effects, and therefore the chiral angle is the most important variable for predicting the trends. The diameter of the SWCNT serves to shift all emission features by the well-established relationship of inverse length but doesn't affect the overall trends with respect to functional configuration.

6.4. Analytical Shift of Functionalized SWCNT Energies

In the previous two chapters and section, it has been shown that the energies of optical transitions of functionalized SWCNTs are highly dependent on the functional configuration and SWCNT chirality due to exciton localization about the defect site. A lot of information has been deduced from these calculations involving the physicality of the systems, and these calculations have been used to predict and explain experimental observations. Despite this, there is still a significant mismatch between the energies predicted by the presented methodologies and experimental observations. As such, it is important to develop a correction for manipulating the calculated values to better match experiment. Such a correction scheme needs to consider the errors introduced by methodology (ie errors due to using a finite basis set and inaccurate density functional) and confinement (ie the error introduced due to using a finite computational cell) separately since the latter errors will affect calculations involving localized excitons to a smaller degree. In this section, the results from a novel approach for doing just that are presented.

6.4.1. Length Dependence of Computational Cells

The slopes of trends correlating length vs calculated optical features are highly dependent on localization in the system and hence the specific functional configurations as well as the chirality of the SWCNT and functional position. For all chiralities explored, the greatest slope is observed for the pristine SWCNT in the absence of defect induced localization (figures 6.5-6.8, left panels). Functionalization results in a localized exciton and, and therefore the effect of

changing the length of the system becomes less significant and the slope decreases. Previous reports have shown that the exciton in the Para L₃₀ functionalization configuration in (6,5) SWCNT is delocalized across the entire length of SWCNT (almost to the same degree as pristine), and therefore using a small finite computational cell would introduce a large degree of confinement error and increasing the computational length would have a significant effect on the energies of the calculated optical features. Conversely, the Para L₋₃₀ functionalization

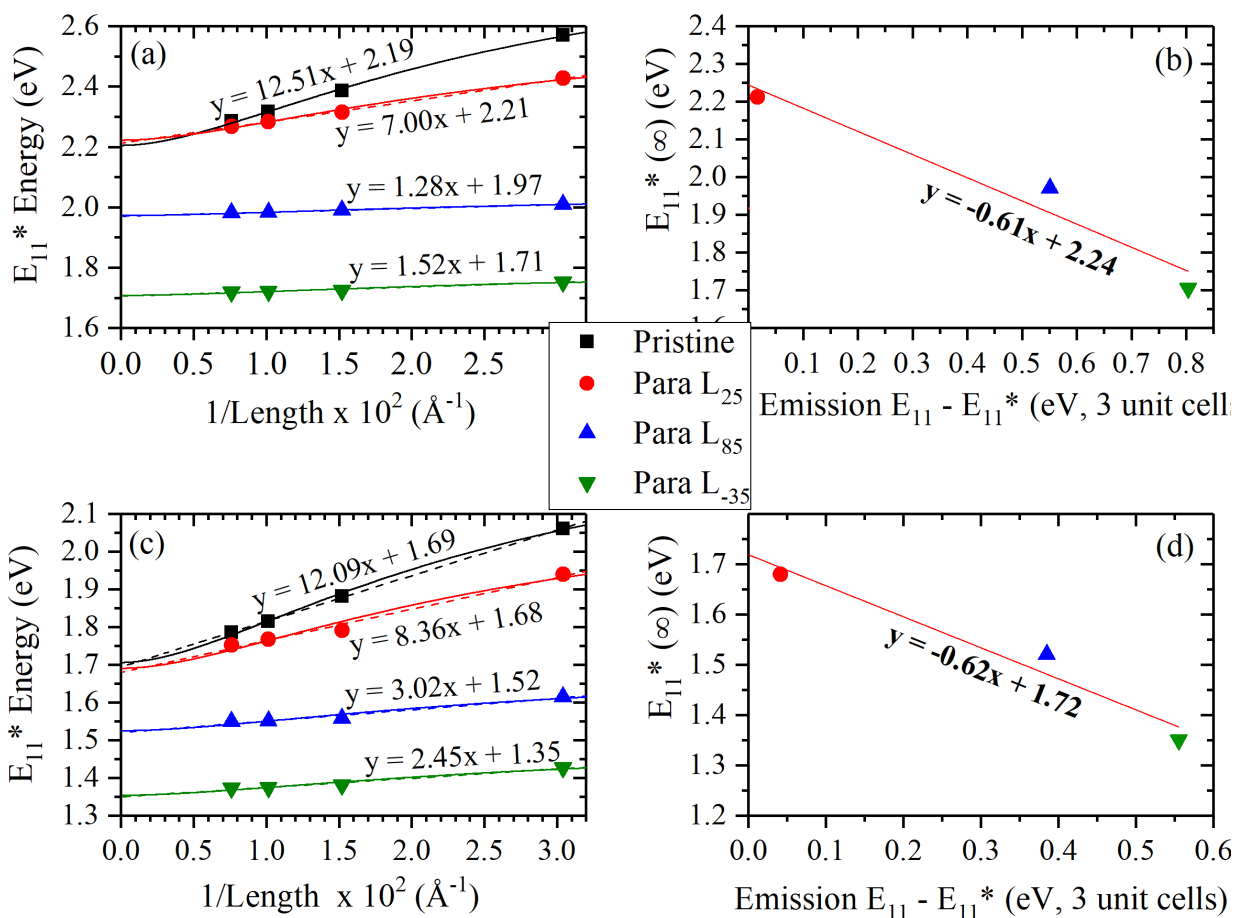


Figure 6.5. Regressions for emission energies of different length functionalized (5,4) systems using CAM-B3LYP (panels a and b) and B3LYP (panels c and d). The dashed and solid regression lines in the left panels represents the fit using the linear method and Kuhn's method respectively, and the formula listed is for the linear fit. The right panels contain the least-squares linear regression between the emission energies extrapolated for the infinite length systems versus the red-shift in the 3-unit cell long systems.

exhibits strong exciton localization about the defect site, and therefore the length of the computational cell would be expected to play a much less significant role on the energy of optical features (figure 6.6(a)). This effect translates to other chiralities as well. The slope for the functionalized near-armchair (5,4) system is slightly higher than (6,5) for the functionalization configurations with the least localized excitons and slightly lower than (6,5) for

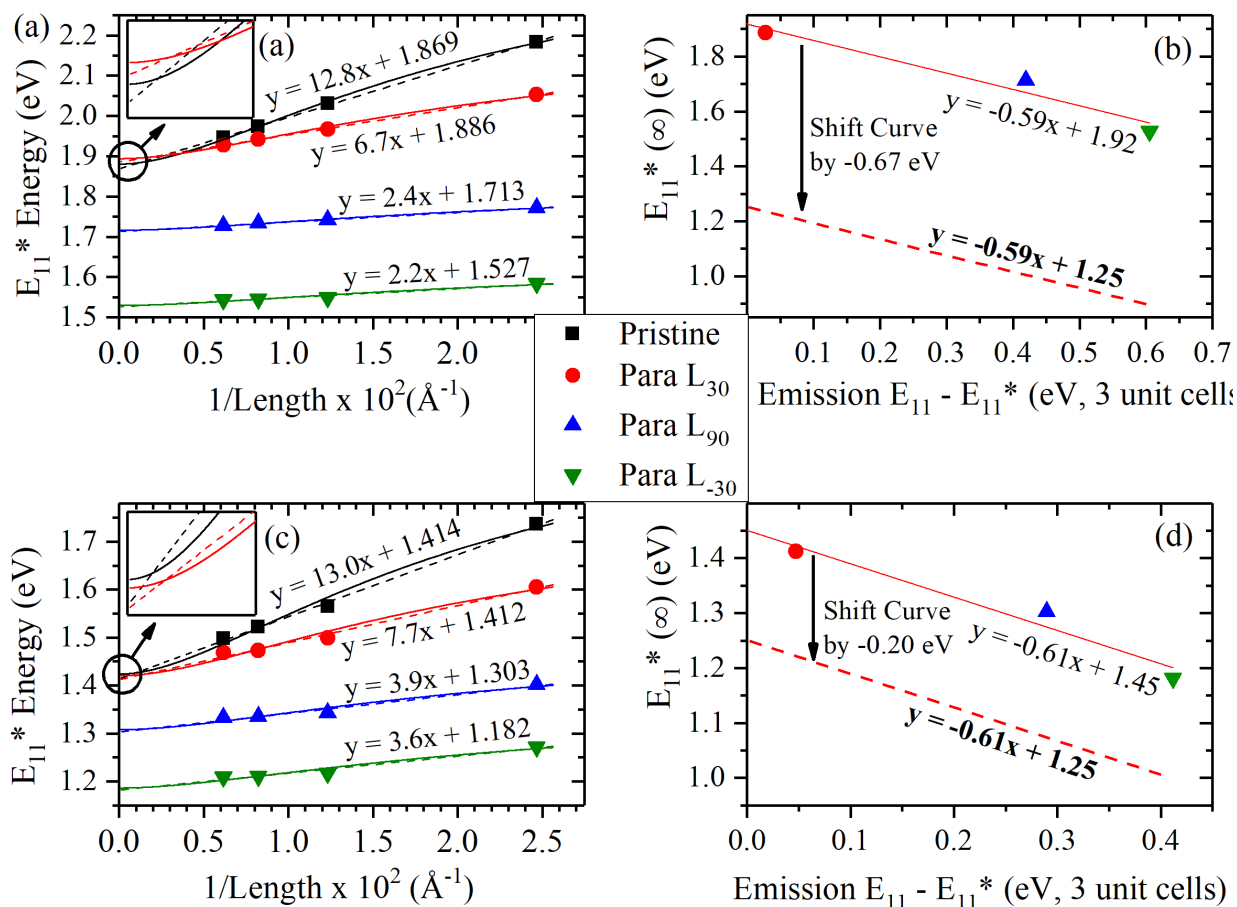


Figure 6.6. (a) Correlation between unit cell length and E_{11}^* energy for different functional configurations of aryl-functionalized (6,5) SWCNTs computed using the CAM-B3LYP density functional. The inset represents the region centered around where the most delocalized species intersect the y-axis. Dashed and solid lines represent the least-squares linear regression of the data points and the fit using Kuhn's formula respectively. (b) Computed red-shifts for the emission of the 3-unit cell systems computed with the CAM-B3LYP density functional correlated to the expected $E_{11}^* (\infty)$ values from panel (a) using a least-squares linear regression. (c) and (d) represent the same data as panels (a) and (b) respectively when calculated using B3LYP density functional.

most localized cases (figure 6.5(a)). The trends of shallower slopes for the most localized species is also observed for the near-zigzag systems as well, where the species that produces the highest exciton localization and the greatest red shift in emission features are reverse to that of near-armchair SWCNTs. Due to the symmetry, the emission energies for (++) and (-) configurations in (9,1) become nearly degenerate and the dependence on different length SWCNTs becomes very similar when the CAM-B3LYP functional is used. For (11,0), this effect becomes even more pronounced and the slopes become congruent. Deviation from this

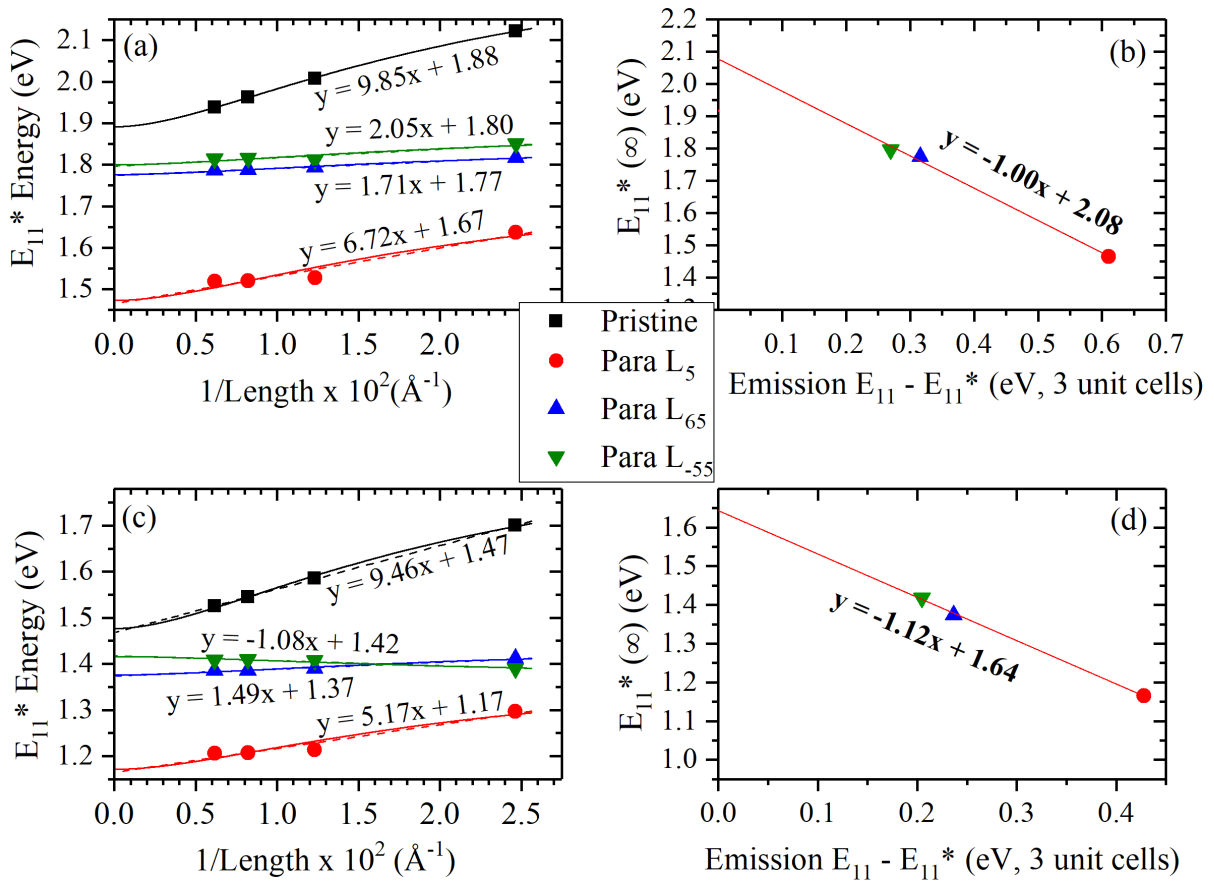


Figure 6.7. Regressions for emission energies of different length functionalized (9,1) systems using CAM-B3LYP (panels a and b) and B3LYP (panels c and d). The dashed and solid regression lines in the left panels represents the fit using the linear method and Kuhn's method respectively, and the formula listed is for the linear fit. The right panels contain the least-squares linear regression between the emission energies extrapolated for the infinite length systems versus the red-shift in the 3-unit cell long systems.

trend is only observed from the most localized (11,0) system (figure 6.8(a)), in which case the slope is slightly negative due to lower energy in the shortest system likely due to end-effects where electron density is forced onto the SWCNT caps in such a short system. This deviation is accentuated when further localization is induced from the use of the CAM-B3LYP functional over B3LYP (figure 6.8(c)). For all chiralities, the energy of the optical features is expected to reach saturation once the length of the unit cell reaches the exciton size. This expectation is observed for the most localized species in all chiralities as elongation of the system beyond three

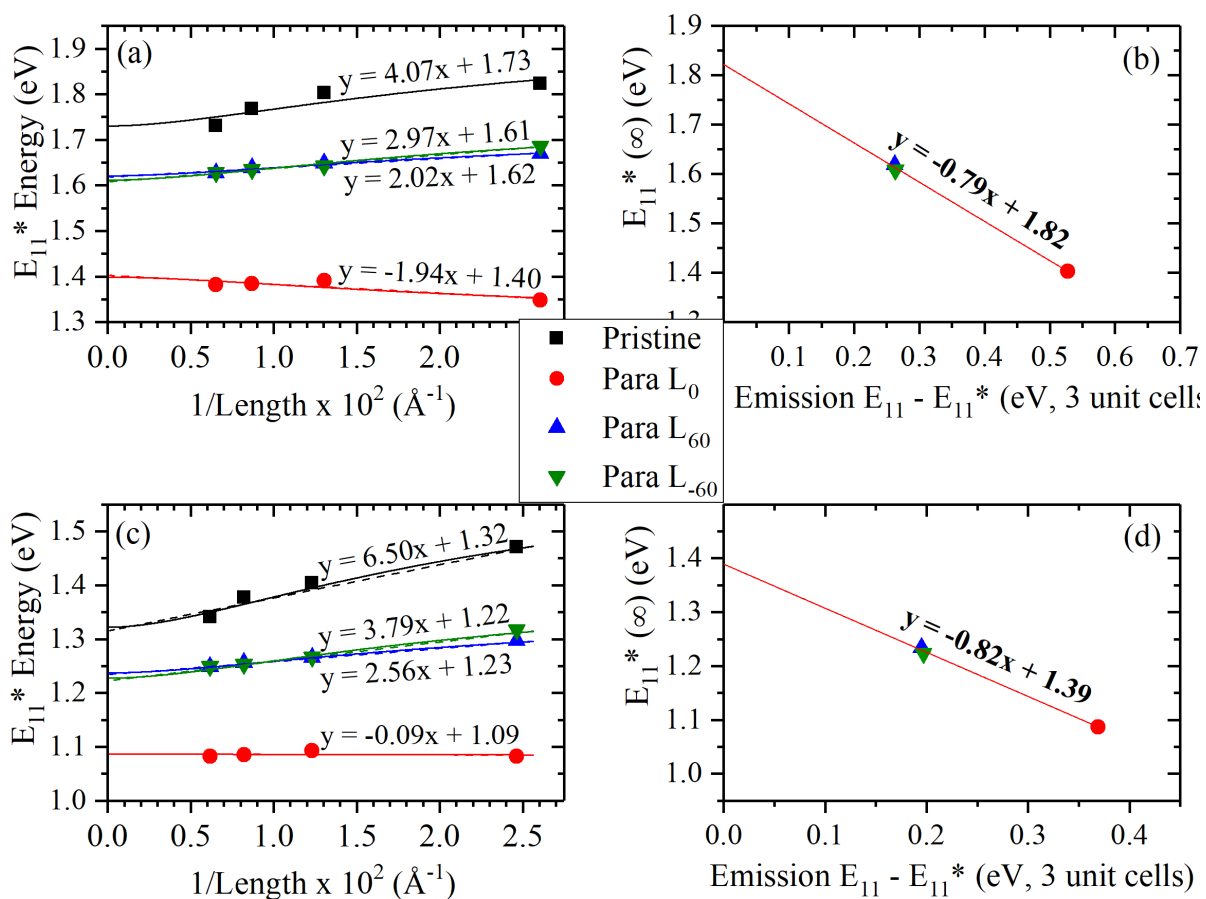


Figure 6.8. Regressions for emission energies of different length functionalized (11,0) systems using CAM-B3LYP (panels a and b) and B3LYP (panels c and d). The dashed and solid regression lines in the left panels represents the fit using the linear method and Kuhn's method respectively, and the formula listed is for the linear fit. The right panels contain the least-squares linear regression between the emission energies extrapolated for the infinite length systems versus the red-shift in the 3-unit cell long systems.

unit cells is met with insignificant changes in transition energies (figures 6.5-6.8, left panels). In addition to slopes, the values for extrapolated energies of optical features at infinite length systems are consistent with previously shown where localized systems produce lower energy optical features than delocalized systems. The only deviation from these trends is observed for CAM-B3LYP results in near-armchair systems, where the energy of pristine E_{11}^* drops below that of Para L_{30} (inset of figure 6.6(a)). However, this anomaly is very small (crossover of $<0.02\text{eV}$) and disappears completely when the computations are performed using the B3LYP functional (inset of figure 6.6(c)).

6.4.2. Density Functional Dependence of Length Dependence

A recent report has demonstrated the density functional dependence in the degree of charge localization in both anionic and cationic pristine (6,5) SWCNTs. These systems exhibit a maximum charge density near the central portion of the SWCNT when calculated with CAM-B3LYP while a more evenly spread charge distribution is observed when the calculations are performed using B3LYP¹⁴. In the present chapter, the variance in the slope of E_{11}^* energies for different length systems using different methodologies demonstrates that these observations in charged systems can be extended to neutral pristine small diameter SWCNTs. The slopes of the trends for (5,4), (6,5) and (9,1) chiralities are nearly the same using either methodology indicating the exciton is localized across the entire length of the SWCNT independent of the methodology used. In the case of the larger zigzag (11,0), it is observed that the slope is reduced by using the CAM-B3LYP functional due to localization. Despite this overall independence of density functional for pristine SWCNTs, the CAM-B3LYP slope is universally smaller than is observed with B3LYP for functionalized systems. The difference in slopes is greatest for the species where exciton localization about the defect site is strongest and much smaller for species

with less localized excitons (figure 6.9). This effect is the result of a more localized exciton using the range-corrected CAM-B3LYP density functional than for just using the hybrid B3LYP. Since the additional delocalization using B3LYP allows the exciton to be in closer proximity to the caps of the SWCNT than for CAM-B3LYP, greater confinement errors would be expected using the former methodology.

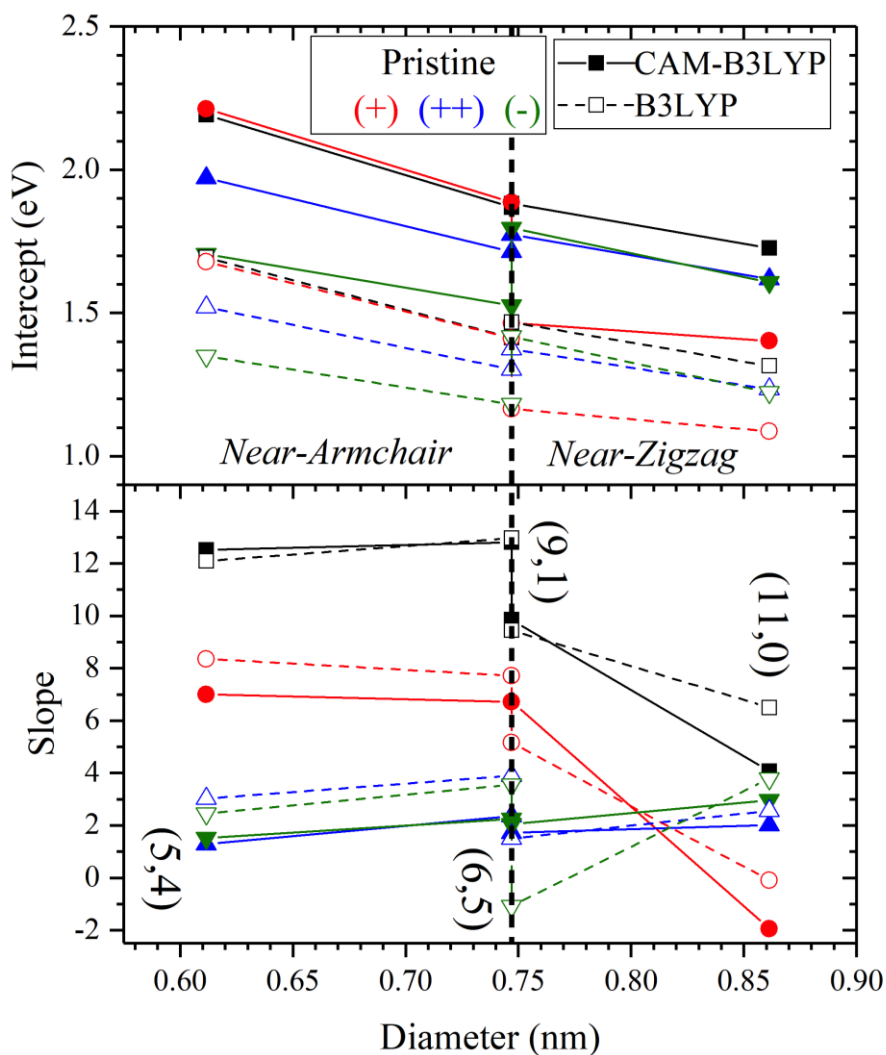


Figure 6.9. Linear fitting parameters for the different SWCNTs of different lengths and functionalization configurations. Solid points and lines represent the parameters acquired from CAM-B3LYP results, and open points and dashed lines represent the parameters from B3LYP.

6.4.3. Linear Regression vs Kuhn

To account for confinement errors, the infinite length absorption transition energies are extrapolated from the calculations performed from different length systems. Kuhn's formula (equation 2) is generally the most physical fit for this purpose. However, in the limits of small lengths, Kuhn's formula exhibits linear behavior and therefore a much simpler linear regression can be used as an approximation where computations were performed on relatively short systems without sacrificing a significant degree of accuracy. The predicted transition energies in the current study differ only slightly using either the linear regression or a fit to Kuhn's formula to determine the magnitude of confinement errors (figures 6.5-6.8, left panels), with a magnitude of only about 15 meV in the most deviant cases. Additionally, the method for performing the linear regression becomes less important for species with excitons that exhibit strong localization due to either functionalization configuration or computational methodology. For example, the difference in transition energies using Kuhn's formula versus a linear regression is most significant for the pristine species with a completely delocalized exciton (figure 6.10). Pristine SWCNTs show a greater difference between using the two fitting methods for CAM-B3LYP results, and nearly all functionalized species show a greater dependence on fitting method using results from the more delocalized B3LYP density functional that is less pronounced in the species with localized excitons (figure 6.10). Kuhn's formula nearly universally predicts slightly lower transition energies for infinite systems due to its asymptotic behavior for long lengths for near-armchair systems (near the y-axis in figures 6.5-6.8). Due to these similarities in transition energies predicted using either Kuhn's formula or the much simpler least squares linear regression, all further results will be discussed using the latter fitting method.

6.4.4. Methodology vs. Confinement Errors

The degree to which methodology errors versus confinement errors affect the calculated transition energies is strongly dependent on all factors governing localization about the defect and therefore the specific density functional and functionalization configuration. The overestimation of HOMO-LUMO gaps and transition energies using CAM-B3LYP has been well documented and is observed in the current study regardless of chirality or configuration of functionalization (figure 6.11). The methodology error is 0.4 to 0.6 eV for all chiralities using this density functional. Much smaller methodology errors of 0.05 to 0.15 eV are observed when B3LYP is used. In addition, the magnitude of confinement error is greater for all chiralities when CAM-B3LYP is used. This accounts for about half of the total error in near-armchair systems

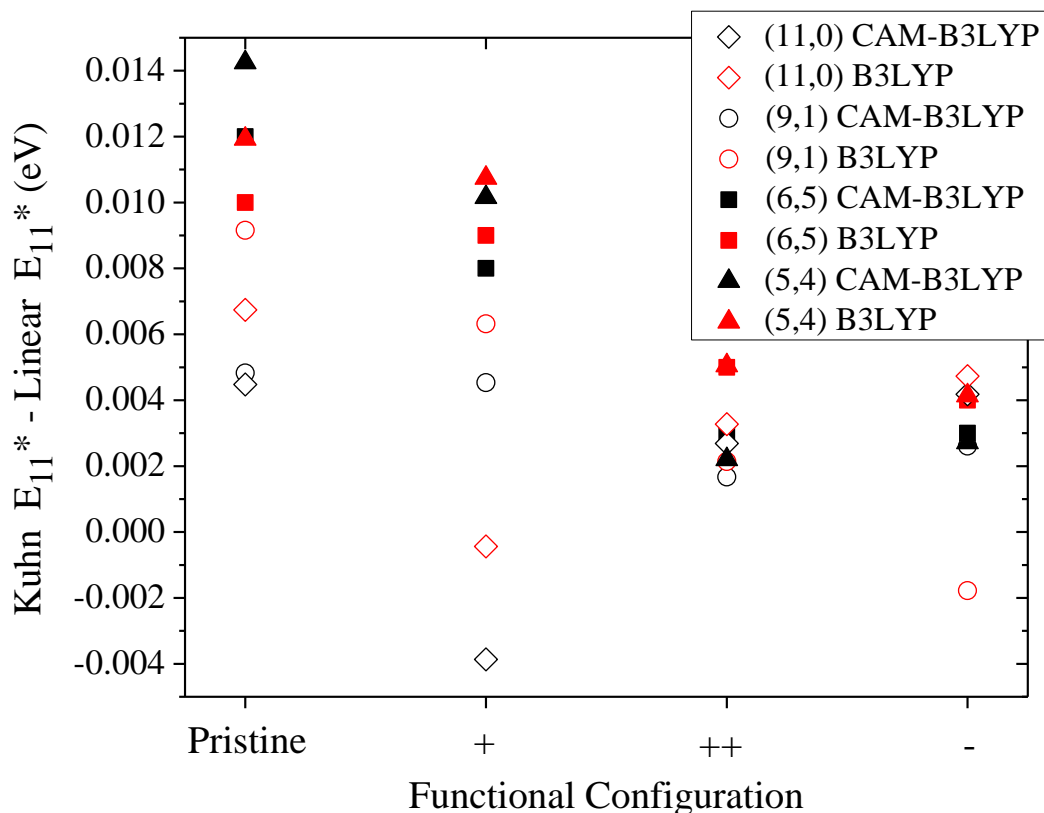


Figure 6.10. Difference between predicted E_{11}^* using either a linear regression or the Kuhn formula for correlating the effect of exciton localization on energy shifts. Black and red points represent optical features using the CAM-B3LYP and B3LYP density functional respectively.

with delocalized excitons and results in significant blue shifts in these systems and becomes less important where the most red-shifted transitions are observed in systems with localized excitons. However, when the calculations are performed using B3LYP, the difference in magnitude of the two types of error is much less pronounced. In this case, methodology error exceeds confinement error for the most localized cases and confinement error dominates for delocalized systems. For the near-zigzag (9,1) and zigzag (11,0) functionalized SWCNT the methodology error always exceeds the confinement errors, demonstrating increased localization in these systems for all functional configurations (figure 6.11). Only a slightly reduced confinement error is observed with the near-zigzag systems when the regression is performed with Kuhn fitting, and differences between the breakdown of error in all other system is similar independent of fitting technique (figure 6.11).

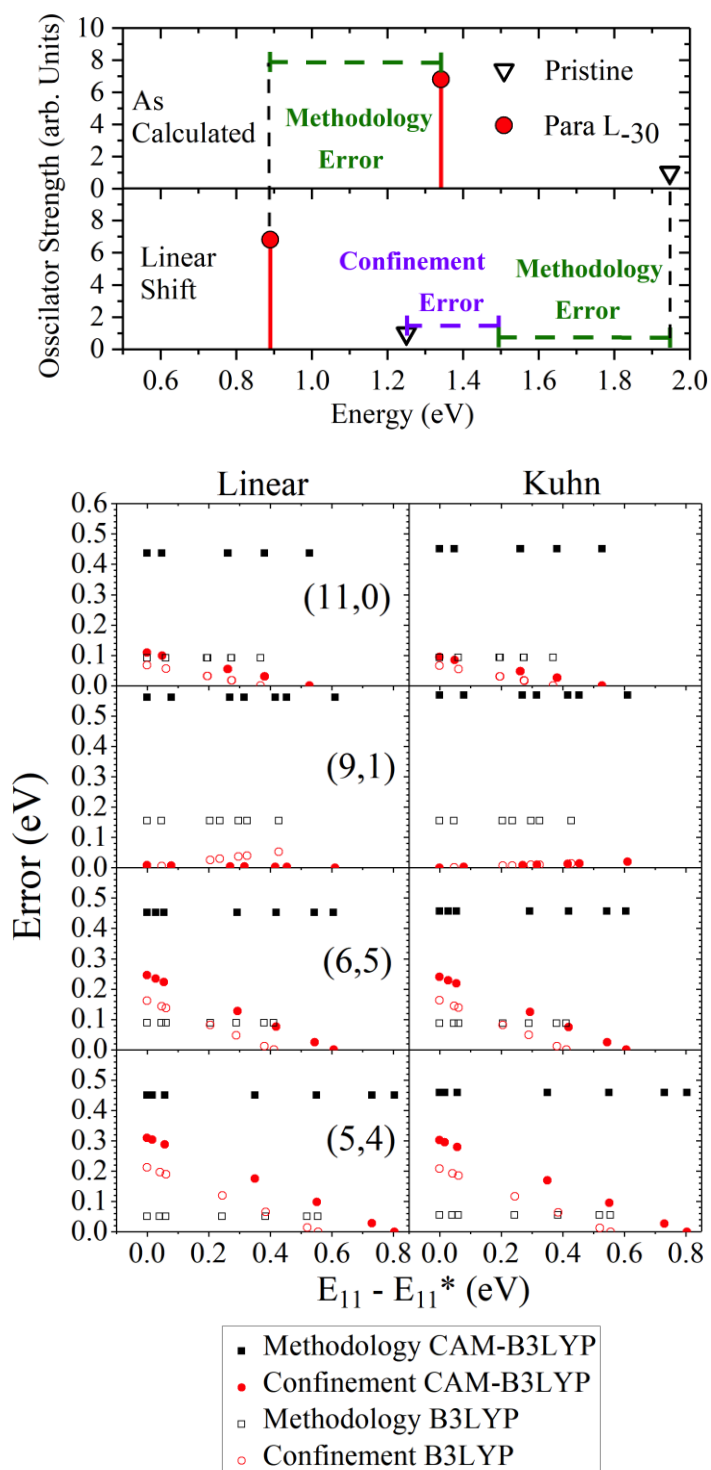


Figure 6.11. Confinement error vs methodology error in systems exhibiting different degrees of exciton localization and red-shifts. The greatest exciton delocalization is observed in pristine for all chiralities, while the species with strongest exciton localization is chirality dependence.

6.4.5. Accuracy of 3-unit Cells vs. Extrapolated Energies

Trends for the values of the aforementioned infinite length transition energies (correlating to exciton localization) versus the E_{11} to E_{11}^* red-shift in emission are performed using a simple linear regression (figures 6.5-6.8, left panels). The y-intercepts of these trends represents the E_{11} transition for the infinite length pristine system (where E_{11}^* is red-shifted from E_{11} by zero) and varies across different diameter tubes consistent with exciton confinement in the directions perpendicular to the SWCNT axis. The (11,0) systems have the least confinement in these directions independent of functionalization and therefore exhibits the smallest transition energies. Conversely, the (5,4) systems exhibit the strongest confinement and have the greatest transition energies. This method provides E_{11} energies that are similar to those taken directly from the computations with three unit-cell long systems but are slightly lower due to the increased correction for confinement (figure S9a). The experimental E_{11} values for the SWCNTs exhibit the same degree of diameter dependence as the computed results, with slight differences on the trend depending on whether they are near-armchair or near-zigzag. This behavior is not well captured in the computed results from three unit cells and becomes much more evident when transition energies are extrapolated as demonstrated from the sudden shift in trends going from (11,0) to (9,1) and from (6,5) to (5,4) (figure 6.12(a)). The difference in transition energies predicted using the two methods is due to additional delocalization along the axial direction allowed in the longest 4-unit cell long systems that are part of the regression, range from 0.04 to 0.14 eV independent of the density functional, and are diameter dependent where larger diameter SWCNTs have smaller differences than larger diameters due to exciton localization (figure 6.12(b)). The slopes of the regressions reflect the degree to which confinement versus methodology errors affect the computed results. A slope near one indicates that confinement

error plays little role compared to methodology errors (as in the (9,1) chiral systems). As such, a simple constant energy shift in these systems is very similar to the method presented here where the sources of error are considered independently. As the slope decreases from one, more of the error becomes attributed to confinement and a greater subtraction of error is required from the constant energy shift for systems with a localized exciton (as in the near-armchair systems). These effects are simultaneously considered by first shifting the curve to align the y-intercepts with the experimental values for E_{11} and subsequently interpolating the energies of the emission

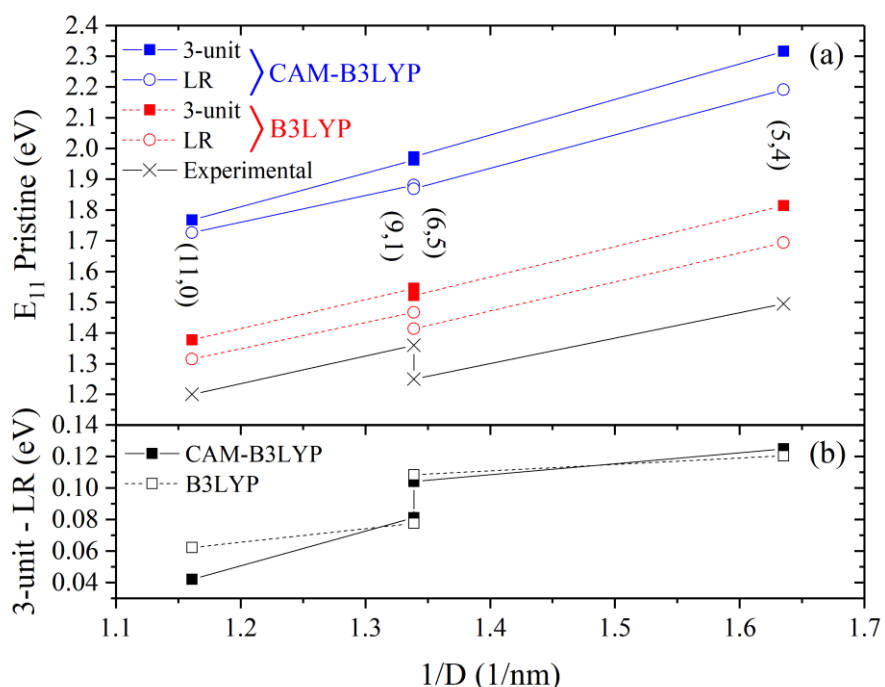


Figure 6.12. (a) Calculated E_{11} energies for pristine SWCNTs of different diameter and chirality, including (11,0), (9,1), (6,5), and (5,4). Solid square points represent the energies as calculated using three unit cell computational cells, while the open circles represent the energies extrapolated from the infinite length linear regressions (LR) of length dependence of E_{11} . Blue and red points represent those calculated using CAM-B3LYP versus B3LYP respectively. Black (x) points represent the experimental values to which all trends were shifted for the purpose of correcting the computed values. (b) Difference between the E_{11} as calculated from three unit cell long systems versus the linear regression, using either CAM-B3LYP (open data points) or B3LYP (closed data points).

features using calculated values for red-shifts of emission features from the three-unit cell systems.

6.4.6. Shifted Emission Energies: Comparison with Experimental Values

Previous studies have attributed diversity of energies of emission features for functionalized SWCNTs to the existence of the distinct chemical configurations calculated in this report. However, due to the combined effect of confinement and methodology errors, practically all of the most red-shifted uncorrected emission energies calculated for functionalized SWCNTs with CAM-B3LYP are at higher energies than the pristine E_{11} . Due to the high methodology errors with this method, these shifts exceed 0.5 eV for all chiralities (figures 6.13(a) and 6.14(a)). A constant energy shift to align the experimental and computational E_{11} results in the calculated emission energies of some of the functional configurations to fall within the experimentally observed range (figures 6.13(b) and 6.14(b)). However, shifting by a constant energy results in overcorrection for the most red-shifted emission features due to the minor role of confinement errors in these systems as compared to the species with delocalized excitons. Due to this, proper shifting schemes involve interpolating energies from the previously formed and corrected regression. Implementation of this strategy results in the significantly improved agreement with experiment regardless of if the regression is performed on infinite E_{11} energies extrapolated using a linear regression or Kuhn's formula (figures 6.13(c&d) and 6.14(c&d)). These observations are consistent for all chiralities with the exception of (9,1), where end group effects are likely still playing a minor role and shifting the computed emission energies. Due to the smaller methodology errors associated with use of the B3LYP density functional, the results calculated using this method initially deviate from experiment by a smaller degree while E_{11} still exhibits a significant blue-shift from experiment of about 0.25 eV. A result of these smaller

methodology errors is relatively good agreement with experiment using a constant energy shift. Despite this, correcting by using the same scaling scheme as previously outlined results in astonishingly good agreement with experiment with all emission features for different configurations falling in the range shown by experiment. While the B3LYP has previously been shown to predict lower degrees of charge localization and the magnitude of confinement error exceeds methodology errors for many species, the method of correcting energies presented in this report independently compensates for each and results in a very good agreement with experiment for emission features of functionalized SWCNTs. As such, the less expensive B3LYP functional can be used in lieu of CAM-B3LYP followed by the energetic correction.

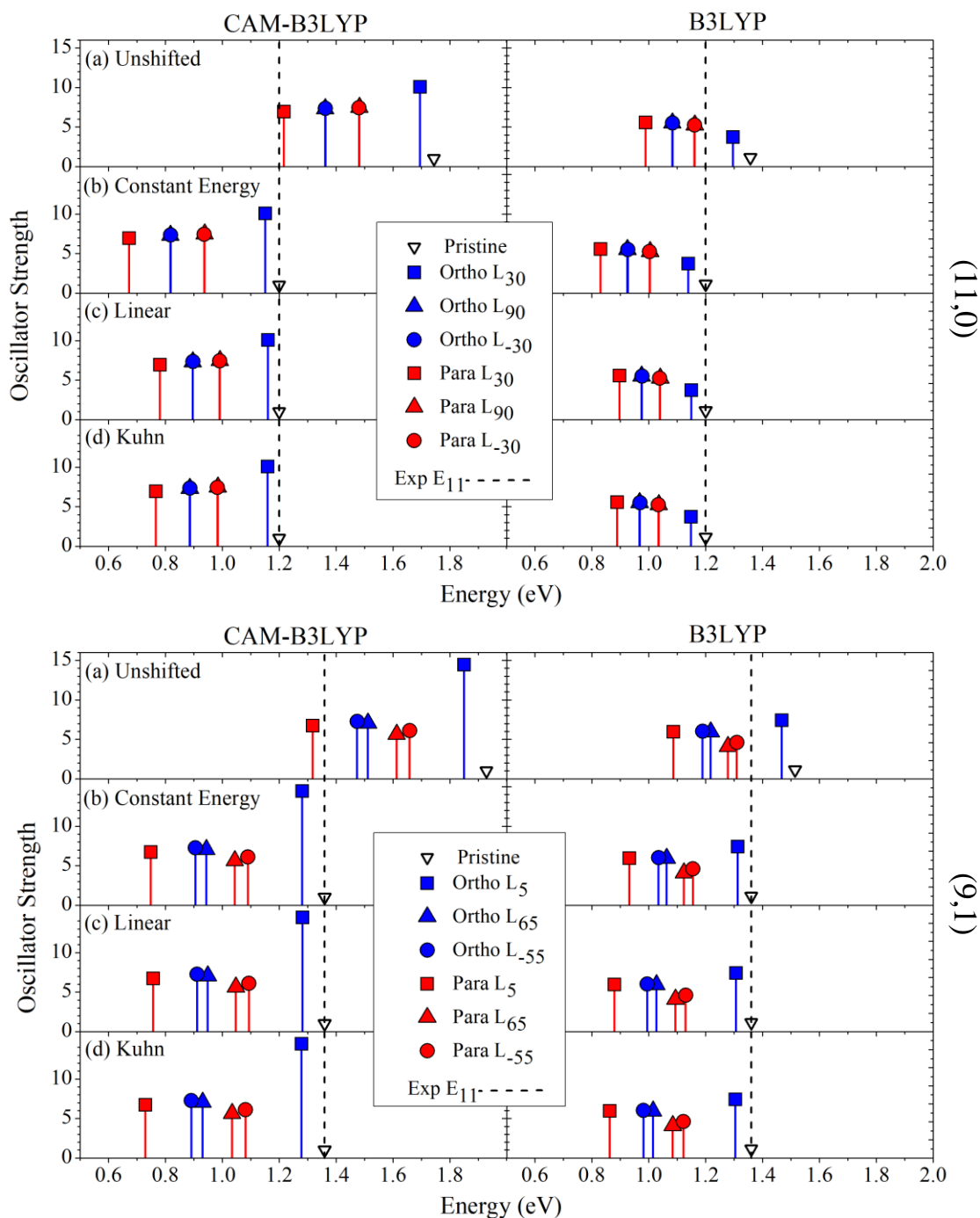


Figure 6.13. Computed energies of E_{11}^* for the six different functional configurations of aryl-functionalized (11,0) (top) and (9,1) (bottom) SWCNTs (a) as calculated using the specified methodology, (b) shifted by a constant energy value, (c) corrected for confinement errors using linear regression to determine the effect of exciton localization on E_{11}^* values, and (d) by using a fit to Kuhn's formula to determine the effect of exciton localization on E_{11}^* values. Square, triangular, and circular markers represent functionalization for different functionalization configurations. Blue markers denote values for ortho functionalization, while red markers denote para. The left and right columns present the results as calculated using CAM-B3LYP and B3LYP respectively. The dashed vertical lines represent the experimental E_{11} values.

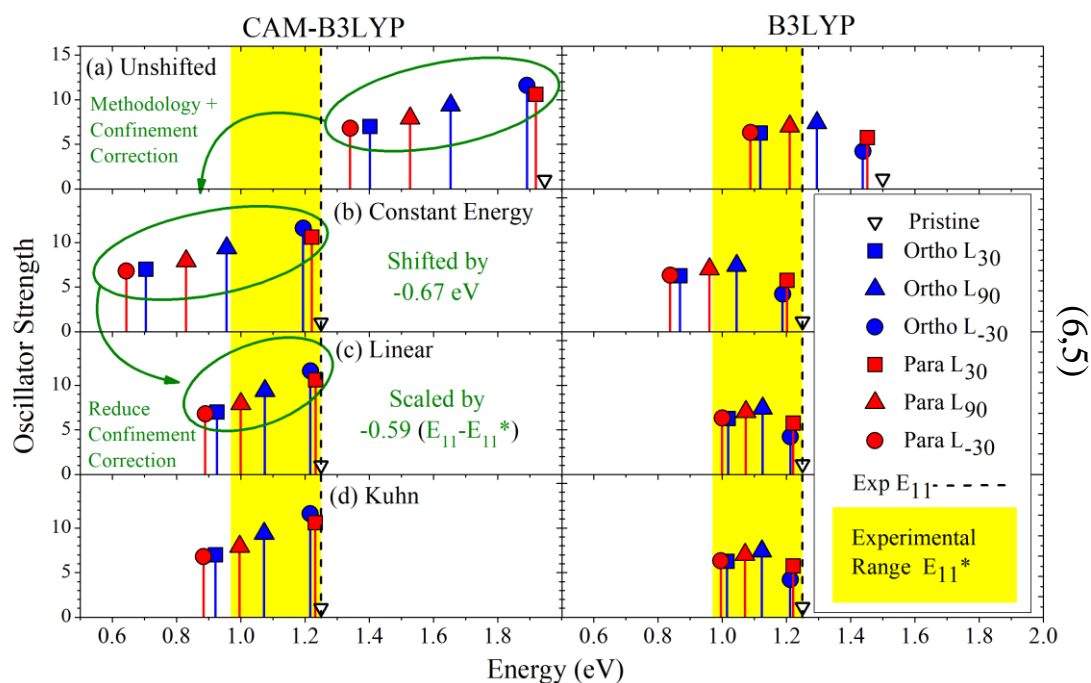
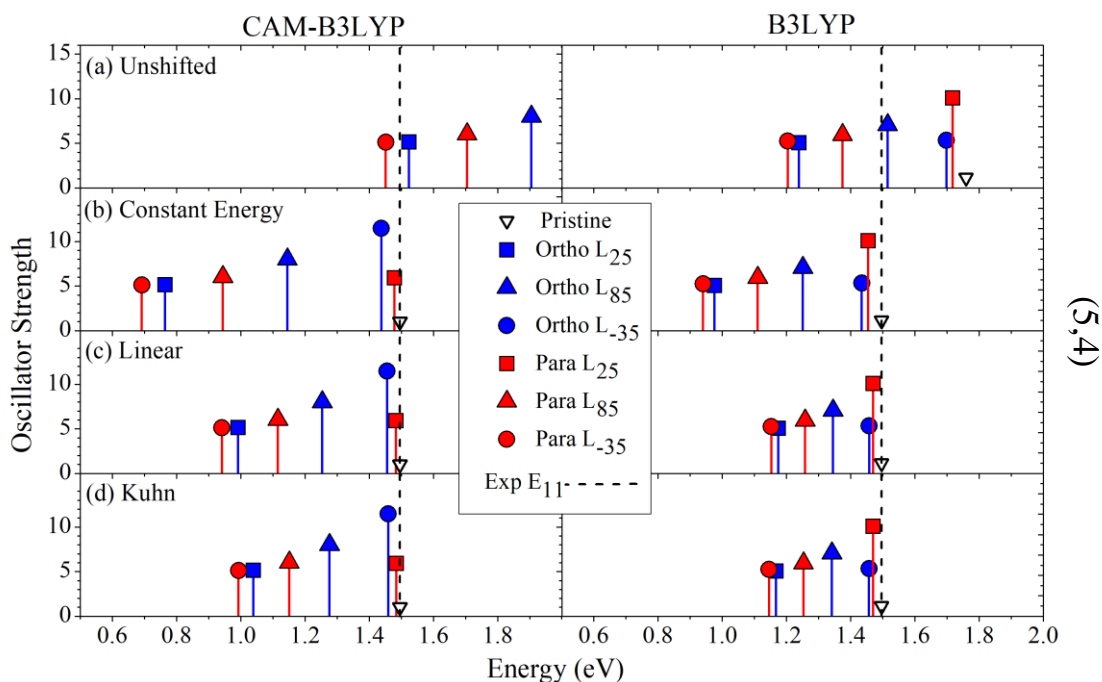


Figure 6.14. Computed energies of E_{11}^* for the six different functional configurations of aryl-functionalized (5,4) (top) and (6,5) (bottom) SWCNTs (a) as calculated (b) shifted by a constant energy value, (c) corrected for confinement errors using linear regression to determine the effect of exciton localization on E_{11}^* values, and (d) by using a fit to Kuhn's formula. The left and right columns present the results as calculated using CAM-B3LYP and B3LYP respectively. The area of the plots highlighted in yellow is the range of energies where emission features were observed experimentally, and the dashed vertical lines represent the experimental E_{11} values.

6.5. Conclusions

SWCNT functionalization introduces configuration dependent redshifted optical features in all chiralities. The degree of redshift for a given configuration changes dependent on the chirality, where the most significant redshift in ortho is observed for functionalization along the axis for zigzag and across the axis for near-armchair. As with (6,5), para configurations exhibit opposite trends. For all chiralities, a significant blueshift is observed in the computed energies as compared to experimental. Adjustment of the energies requires an analytic correction taking into account methodology and confinement errors independently. Such corrections can be applied by computing inexpensive vertical transitions on ground state geometries of different lengths. The length-dependent correlations on resulting absorption features can be developed by using Kuhn's method, but a simpler linear regression provides nearly indistinguishable results. The slopes of such correlations are heavily dependent on the degree of electron localization about the defect site induced by either functional configuration or choice of density functional. At long lengths, further extending the system plays little role in decreasing the energies of transition for the most localized systems. As such, the energy deviations from infinite length systems in these species is solely due to methodology errors and the degree of confinement versus methodology error in all systems can be evaluated. Methodology errors far exceeds confinement error when calculations are performed with the CAM-B3LYP density functional due to stronger localization about the defect site and become approximately equal in magnitude for delocalized systems when the emission energies are calculated with B3LYP. Increasing the length of systems with delocalized excitons beyond three unit cells results in further reduction of energies of optical features exhibiting the role of confinement errors. Due to these species-dependent discrepancies in the

degree of confinement error versus methodology error, a constant energy shift is insufficient for correcting the calculated energies to better match experiment.

The energies of optical features for hypothetical infinite length systems can be extrapolated from the length-dependent trends and subsequently correlated to the red-shift of emission from E_{11} in the computationally feasible three unit-cell long model. A constant energy shift of this curve corrects for both types of error, while preserving the slope compensates for overcorrection due to less confinement error in localized systems. The resulting relationship is used to interpolate the corrected energies of emission features taking into account both types simultaneously. This procedure generates energies of optical features for functionalized (6,5) SWCNTs computed using three unit-cells of that are in remarkably good agreement with recently published experimental results, particularly when the B3LYP density functional is used. While trends of exciton confinement and optical transition energies of different functionalization configurations are opposite depending if the SWCNT chirality is near-armchair or zigzag, and the effect of confinement versus methodology errors follows such trends and therefore the correction scheme presented here works independent of chirality. Since it has previously been shown the predominant factor generating redshifts for emission features is the functionalization configuration and not identity of functional groups, this powerful analytical correction to such energies is derived for each chirality and methodology but can be applied to other functionalities.

6.6. References

(1) Frisch, M. J.; Trucks, G. W.; Schlegel, H. B.; Scuseria, G. E.; Robb, M. A.; Cheeseman, J. R.; Scalmani, G.; Barone, V.; Mennucci, B.; Petersson, G. A.; et al. *Gaussian 09*; Gaussian, Inc.: Wallingford, CT, USA, 2009.

- (2) Humphrey, W.; Dalke, A.; Schulten, K. VMD – Visual Molecular Dynamics. *J. Mol. Graph.* **1996**, *14*, 33–38.
- (3) Kilina, S.; Tretiak, S. Excitonic and Vibrational Properties of Single-Walled Semiconducting Carbon Nanotubes. *Adv. Funct. Mater.* **2007**, *17* (17), 3405–3420.
- (4) He, X.; Gifford, B. J.; Hartmann, N. F.; Ihly, R.; Ma, X.; Kilina, S. V.; Luo, Y.; Shayan, K.; Strauf, S.; Blackburn, J. L.; et al. Low-Temperature Single Carbon Nanotube Spectroscopy of Sp^3 Quantum Defects. *ACS Nano* **2016**.
- (5) Yanai, T.; Tew, D. P.; Handy, N. C. A New Hybrid Exchange–correlation Functional Using the Coulomb-Attenuating Method (CAM-B3LYP). *Chem. Phys. Lett.* **2004**, *393* (1–3), 51–56.
- (6) Hehre, W. J.; Stewart, R. F.; Pople, J. A. Self-Consistent Molecular-Orbital Methods. I. Use of Gaussian Expansions of Slater-Type Atomic Orbitals. *J. Chem. Phys.* **1969**, *51* (6), 2657–2664.
- (7) Collins, J. B.; von R. Schleyer, P.; Binkley, J. S.; Pople, J. A. Self-Consistent Molecular Orbital Methods. XVII. Geometries and Binding Energies of Second-Row Molecules. A Comparison of Three Basis Sets. *J. Chem. Phys.* **1976**, *64*, 5142–5151.
- (8) Kilina, S.; Badaeva, E.; Piryatinski, A.; Tretiak, S.; Saxena, A.; Bishop, A. R. Bright and Dark Excitons in Semiconductor Carbon Nanotubes: Insights from Electronic Structure Calculations. *Phys. Chem. Chem. Phys.* **2009**, *11* (21), 4113–4123.
- (9) Kilina, S.; Kilin, D.; Tretiak, S. Light-Driven and Phonon-Assisted Dynamics in Organic and Semiconductor Nanostructures. *Chem. Rev.* **2015**, *115*, 5929–5978.
- (10) Adamska, L.; Nayyar, I.; Chen, H.; Swan, A. K.; Oldani, N.; Fernandez-Alberti, S.; Golder, M. R.; Jasti, R.; Doorn, S. K.; Tretiak, S. Self-Trapping of Excitons, Violation of

Condon Approximation, and Efficient Fluorescence in Conjugated Cycloparaphenylenes. *Nano Lett.* **2014**, *14* (11), 6539–6546.

(11) Lee, C.; Yang, W.; Parr, R. G. Development of the Colle-Salvetti Correlation-Energy Formula into a Functional of the Electron Density. *Phys. Rev. B* **1988**, *37* (2), 785–789.

(12) Vosko, S. H.; Wilk, L.; Nusair, M. Accurate Spin-Dependent Electron Liquid Correlation Energies for Local Spin Density Calculations: A Critical Analysis. *Can. J. Phys.* **1980**, *58*, 1200–1211.

(13) Becke, A. D. Density-functional Thermochemistry. III. The Role of Exact Exchange. *J. Chem. Phys.* **1993**, *98* (7), 5648–5652.

(14) Adamska, L.; Nazin, G. V.; Doorn, S. K.; Tretiak, S. Self-Trapping of Charge Carriers in Semiconducting Carbon Nanotubes: Structural Analysis. *J. Phys. Chem. Lett.* **2015**, *6* (19), 3873–3879.

7. CLOSING REMARKS

The contributions of this dissertation cover a wide array of areas dealing with single walled carbon nanotube (SWCNT) functionalization. It has been shown that the sidechains in conjugated polymers has a significant role in interacting with SWCNTs. In contrast with the long-held belief of their insignificance and therefore their neglect in computational studies, the length of alkyl sidechains of PFO has been shown to affect the adsorption strength of PFO. While π - π interactions provide the predominant force holding the polymer-SWCNT complex together, the weaker van der Waals interactions between the sidechains and SWCNT cannot be neglected. Future studies involving the strength of binding of conjugated polymers to SWCNTs need to be mindful of these findings and must consider the complex interplay between sterics and favorable π - π stacking that have been demonstrated in this dissertation. For very short sidechains, the π -interactions dominate and the van der Waals interactions between the sidechain and SWCNT serve to slightly increase the adsorption energy. However, as the chain elongates, sterics begins to take effect resulting in the twisting of the polymer backbone and therefore destruction of the π - π overlap. The result is weaker binding despite the additional van der Waals interactions between the sidechain and the SWCNT. This indicates that the neglect of sidechains will result in stronger binding strengths than would be observed in experiment. Additionally, the morphology of experimental systems would not be as ordered as predicted in simulations where sidechains are neglected. These results also suggest the plausible utilization of sidechain length as an additional degree of freedom in efforts to solvate and disperse SWCNTs, thereby advancing the ability of experimental studies to sort SWCNTs into individual chiralities for further functionalization.

The results presented in this dissertation regarding the effect of capping SWCNTs are the first to demonstrate the irrelevance of the inductive effects in specific functional groups in modulating the electronic and optical properties. While functionalization with alcohols, carboxylic acids, and aldehydes results in slight changes in charge density and bond lengths along the terminated edges, these groups play very little role in changing the electronic structure near the HOMO-LUMO gap. Connectivity to very electronegative groups results in a high redistribution of charges along the edge but little change in electronic structure. Much more significant changes in the electronic structure are observed when the number of sp^2 hybridized methylene derivatives are bonded at the caps. This suggests that the capping schemes used in computational studies involving finite-length SWCNT systems need only consider the number of sp^2 hybridized groups bonded at the edges. For the (10,5) SWCNT, two methylene groups are required on the caps to open up the gap. Using only a single methylene group opens up the gap slightly, but not to the degree of two. Additionally, adding more than two methylene groups to the edges results in additional states with electron density located on the edges of the SWCNT being introduced into the gap, thereby reducing it. Perhaps the most important result in this section involved the position dependence of functionalization with the sp^2 hybridized groups. The precise position of functionalization has relatively insignificant role on the HOMO-LUMO gap providing it occurs along the axis following the chirality of the SWCNT. However, functionalization on the other axis results in a greatly reduced HOMO-LUMO gap in the system as a result of introduction of edge-localized states. This information provides guidance for further computational studies involving both pristine and functionalized SWCNTs as a proper capping scheme is a prerequisite to high-quality electronic structure calculations.

With proper capping schemes designed based on the findings in the second chapter, the remainder of this dissertation focused on calculating the electronic structure and optical properties of functionalized SWCNTs. Neutral systems of (6,2) functionalized with chlorine displayed chlorine binding was most favorable with two chlorine atoms bound to the same ring of the SWCNT sidewall while binding two chlorine atoms to different rings results in bond character similar to a singly chlorinated SWCNT. This result is significant as it guides further studies involving functionalization with groups other than chlorine. The binding energy per chlorine atom is only slightly changed with an increasing chlorine surface concentration, meaning high degrees of chlorination should be possible. With charged cases, the chlorine binding energy is most favorable for mono-chlorinated tubes, and is dramatically less favorable for di-chlorinated tubes. The chlorine binding energy becomes more favorable as the distance between chlorine atoms increases, and all cases were much more favorable as the length of the tube increased. This suggests that predominant binding mechanism likely doesn't involve anionic chlorine and chloride ions likely bind to SWCNTs only in very low concentrations. Binding of neutral chlorine to the SWCNT causes the introduction of unoccupied midgap states resembling a p-doped system, suggesting their utility in photovoltaic applications.

The results with chlorine functionalization suggest that the orientation of addition of the functional groups to SWCNTs may impact their electronic and optical properties. This translates to aryl functionalized systems as well. Synthetic considerations dictate that two monovalent species will add to the SWCNT in experiment, thereby generating multiple defect types differing in the orientation of their functional groups. All of the resulting species are of computational interest. Total energies suggest that they are all likely to form with no species being energetically forbidden. The most stable orientation of the aryl group is largely the result

of competing effects of maximal overlap of π orbitals between the aryl group up and SWCNT versus steric hindrance in the multiple functional sites. The electronic structure is significantly modified by functionalization, where the degenerate frontier molecular orbitals move into the gap to different degrees dependent on the orientation of functionalization. This is the result of restricted electron delocalization along the SWCNT axis in these states, an effect that is nearly independent of the chemical identity of the functional group. Due to these changes in the electronic structure, the energies of significantly red-shifted features introduced by functionalization are dependent on the configuration for the functional group. These calculations have justified the presence of a range of emission features in experiment for the first time. Since these emission features are in the range required for telecommunications applications, the importance of the results in this dissertation that explain their presence cannot be understated.

While the calculated emission features span an energetic range that is similar to experimental observations, the energies are significantly blue shifted due to computational errors. While a simple constant-energy shift could be enacted, a better analytic correction was developed in the final chapter of this dissertation that takes into account methodology and confinement errors independently. This novel method requires only computing inexpensive vertical transitions on ground state geometries of different lengths. The slopes of such correlations are heavily dependent on the degree of electron localization about the defect site induced by either functional configuration or choice of density functional. By preserving the slope but shifting the entire correlation, the resulting curve can be used to extrapolate the energies of emission features using only redshifts calculated with finite unit cell systems. Additionally, the degree of methodology errors versus confinement errors in all systems can be

evaluated. The development of this ground-breaking procedure enables direct comparison between theoretically determined and experimental emission energies.

Probably most importantly, the results in this dissertation provide the framework for further advancement of knowledge in the field of functionalized SWCNTs. The demonstration of sidechain length dependence on non-covalent adsorption and covalent functional configuration impacts on energies of emission features guides further experimental efforts in the field. Additionally, justification of proper capping schemes and development of the analytical shifting schemes provide tools for the complementary computational studies. As such, the full value of these contributions will be recognized in the near future.